JUSTUS-LIEBIG-
UNIVERSITÄT
GIESSEN

Dissertation

Chiral symmetry restoration and strangeness dynamics in heavy-ion collisions at FAIR energies

Alessia Palmese

Mai 2017

Justus-Liebig-Universität Giessen
Fachbereich 07
Institut für theoretische Physik

Gütachter: Prof. Dr. Dr. Wolfgang Cassing
Prof. Dr. Claudia Höhne

Zusammenfassung

Diese Arbeit beschäftigt sich mit der Untersuchung chiraler Symmetriewiederherstellung in Schwerionenkollisionen. Das Dileptonenspektrum gilt bis heute als mögliches Signal für die Wiederherstellung der chiralen Symmetrie, da in der chiral restaurierten Phase der Vektor- und Axialvektorstrom übereinstimmen müssen. Allerdings konnten bis heute keine klaren Hinweise für dieses Verhalten gefunden werden. Gitter Quanten-Chromo-Dynamik (QCD) Rechnungen für verschwindendes chemisches Potential weisen darauf hin, dass der chirale Phasenübergang ein Crossover ist mit annähernd derselben kritischen Temperatur wie der des Deconfinement-Phasenübergangs. Die Natur des Phasenübergangs bei endlichem chemischen Potential ist nicht geklärt und wird derzeit theoretisch und experimentell untersucht. Aufgrund des Vorzeichenproblems der Gitter QCD muss von theoretischer Seite her auf effektive Modelle zurückgegriffen werden. Die effektiven Modelle weisen darauf hin, dass der chirale Phasenübergang noch vor dem Deconfinement-Übergang bei niedrigeren Temperaturen liegt. Von experimenteller Seite werden Systeme hoher Dichte in "Niederenergie" Schwerionenkollisionen an Beschleunigeranlagen untersucht: der Relativistic Heavy-Ion Collider (RHIC), die zukünftige Facility for Antiproton and Ion Research (FAIR) sowie die zukünftige Nuclotron-based Ion Collider fAcility (NICA). Die Aufgabe der Schwerionenphysik ist es, Spuren der chiralen Symmetriewiederherstellung aus den gemessenen Spektren zu identifizieren und theoretisch zu verstehen.

In dieser Arbeit analysieren wir die Effekte der chiralen Symmetriewiederherstellung in Schwerionenkollisionen mithilfe des Parton-Hadron-String Dynamics (PHSD) Transportansatzes, welcher zur Beschreibung von Schwerionenkollisionen partonische, hadronische sowie Stringfreiheitsgrade beinhaltet. Diese Arbeit gliedert sich folgendermaßen:

Im Kapitel 1 stellen wir die grundlegenden Eigenschaften von Schwerionenkollisionen mit besonderem Schwerpunkt auf dem Phasendiagramm von QCD Materie vor. Außerdem geben wir einen kurzen Überblick der theoretischen Modelle, die zur Untersuchung von Schwerionenkollisionen verwendet werden.

Im Kapitel 2 wird eine Einführung zu PHSD gegeben. Zunächst stellen wir die theoretischen Grundlagen der relativistischen Vielteilchentheorie vor sowie das Dynamical Quasi-Particle

Modell (DQPM), auf welchem PHSD basiert. Anschließend beschreiben wir die verschiedenen Stufen einer Schwerionenkollisionen im mittleren Energiebereich ($\sqrt{s_{NN}} = 3 - 20\,\mathrm{GeV}$) und die Ergebnisse von PHSD Rechnungen. Zuletzt präsentieren wir die Implementierung der chiraler Symmetriewiederherstellung in die hadronische Teilchenproduktion innerhalb des PHSD Ansatzes.

Kapitel 3 beschäftigt sich mit der Untersuchung von Hyperonproduktion bei niedrigen Energien ($\sqrt{s_{NN}} = 2 - 3\,\mathrm{GeV}$). Die Berücksichtigung der Hyperon-Hyperon-Wechselwirkung ist eine Verbesserung des PHSD Ansatzes für die Mehrfach-Strange-Teilchen-Produktion nahe der Produktionsschwelle. Ein Vergleich zu aktuellen Messdaten der HADES und FOPI Kollaborationen wird mit besonderem Augenmerk auf die (überraschend) großen Multiplizitäten der Ξ Teilchen präsentiert. Die Einbeziehung der Hyperon-Hyperon Wechselwirkung induziert eine Erhöhung der Ξ Multiplizität bei niedrigen Energien, liefert jedoch keine schlüssige Interpretation der HADES Messungen.

Die Rolle der chiralen Symmetriewiederherstellung im Energiebereich $\sqrt{s_{NN}} = 2 - 20\,\mathrm{GeV}$ wird in Kapitel 4 untersucht. Die Strangenesserhöhung bei diesen Energien wird als Signatur der chiralen Symmetriewiederherstellung identifiziert. Es stellt sich heraus, dass die Teilchenmultiplizitäten, Rapiditätsspektren sowie Teilchenverhältnisse -im Gegensatz zu dem geringen Einfluss auf transverse Massenspektren- geeignete Observablen der chiralen Symmetriewiederherstellung sind. Die Abhängigkeit von der nuklearen Zustandsgleichung wird ebenfalls untersucht. Das Hauptresultat besteht aus der Feststellung, dass eine mikroskopische Interpretation des K^+/π^- Verhältnisses durch das Zusammenspiel der chiralen Symmetriewiederherstellung und der Bildung eines Quark Gluon Plasmas (QGP) gelingt.

In Kapitel 5 wird sodann das kollektive Verhalten von Teilchen in Form des direkten Flusses erforscht. Wir berechnen die differentiellen Hadronenspektren der von p+p sowie A+A Kollisionen produzierten Teilchen im Energiebreich $E_{Lab} = 6 - 158\,A\mathrm{GeV}$. Weitern untersuchen wir die Zeitentwicklung der transversalen Impulsspektren von Teilchen und charakterisieren die wichtigsten Kanäle, die für eine Änderung des Impulses während der Dynamik des Systems verantwortlich sind. Zusätzlich adressieren wir die Sensitivität der PHSD Berechnungen vom direkten Fluss von hadronischen Potentialen, experimentellen Cuts und Zentralitätsauswahl. Der direkte Fluss wird für den Energiebereich $\sqrt{s_{NN}} = 3 - 100\,\mathrm{GeV}$ im Vergleich zu den verfügbaren experimentellen Messdaten von STAR, E895 und NA49 präsentiert. Wir stellen fest, dass die PHSD Rechnungen unter Berücksichtigung der chiralen Symmetriewiederherstellung und dem hadronischen Potential eine gute Übereinstimmung mit den experimentellen Messdaten des Proton- und Pionflusses ergeben.

In Kapitel 6 liefern wir Voraussagen für Observablen in ultrarelativistischen Kollisionen im Energiebereich der zukünftigen FAIR und NICA Einrichtungen und untersuchen ihre Ab-

hängigkeit von der chiralen Symmetriewiederherstellung. Hierzu betrachten wir zusätzlich zu den Rapiditätsspektren die Strange-zu-nicht-Strange Teilchenverhältnisse und erforschen diese als Funktionen der Systemgröße und der Zentralität des kollidierenden Systems.
Im letzten Kapitel fassen wir noch offene Fragen innerhalb des PHSD Ansatzes und die Ergebnisse dieser Arbeit zusammen.
Diese Dissertation beinhaltet zwei Anhänge: Der erste liefert eine Einleitung zur chiralen Symmetriewiederherstellung und der zweite widmet sich der Herleitung von Wirkungsquerschnitten für die Hyperon-Hyperon Wechselwirkung innerhalb eines Eich-Flavour-SU(3) hadronischen Models.

Summary

This dissertation is devoted to the study of Chiral Symmetry Restoration (CSR) in Heavy-Ion Collisions (HIC). The dilepton spectroscopy has always been identified as a source of signatures for CSR, since in a chirally restored phase the vector and axial-vector currents should become equal. However, no clear evidence for this phenomenon has been achieved so far. Lattice QCD (lQCD) calculations show that at vanishing baryon chemical potential the CSR takes place as a crossover transition at roughly the same critical temperature as the deconfinement phase transition. The question of CSR and of deconfinement at finite baryon chemical potential has been investigated theoretically and experimentally in the past. In the first context, effective or functional models have to be employed, due to the fermion sign problem of lQCD. These models suggest that CSR occurs prior to deconfinement at a lower temperature. In the second context, many facilities address the dense matter in "low-energy" HIC: the Relativistic Heavy-Ion Collider (RHIC), the future Facility for Antiproton and Ion Research (FAIR) and the future Nuclotron-based Ion Collider fAcility (NICA). The identification of signatures in the final particle distributions and the theoretical understanding of those observables represent the actual tasks of heavy-ion physics.

In this work, we analyze the role of CSR in HIC adopting the Parton-Hadron-String Dynamics (PHSD), a transport approach describing heavy-ion reactions using partonic, hadronic and string degrees-of-freedom. This dissertation is organized as follows:

In Chapter 1 an introduction to the HIC is given with a focus on the main goal of this field, which is the study of the Quantum-Chromo-Dynamics (QCD) phase diagram. We also briefly present the available theoretical approaches that are used to study HIC.

In Chapter 2 we recall PHSD, the theoretical approach adopted in this study. We introduce the relativistic transport theory -upon which PHSD is based- and the Dynamical-Quasi-Particle Model (DQPM) adopted for the partonic phase. We describe the different stages of a HIC and analyze the main features of PHSD when applied to HIC in the intermediate energy regime ($\sqrt{s_{NN}} = 3 - 20\,\mathrm{GeV}$). Furthermore, we present the implementation of CSR in the hadronic particle production within PHSD on the basis of the Schwinger mechanism.

Chapter 3 is devoted to the investigation of the hyperon production at low energies ($\sqrt{s_{NN}} =$

$2-3$ GeV). The extension of PHSD to include hyperon-hyperon scatterings is an improvement of the model concerning the multi-strange particle production close to threshold. A comparison to recent measurements from the HADES and FOPI collaborations is presented, with a special focus on the (surprisingly) large multiplicity of the Ξ particles. The inclusion of the hyperon-hyperon interaction produces an enhancement of the Ξ multiplicity at low energies but does not provide a conclusive interpretation of the HADES measurements.
The role played by CSR in the particle production within the energy range $\sqrt{s_{NN}} = 2-20$ GeV is investigated in Chapter 4. The strangeness enhancement at AGS energies is identified as a signature of the CSR. Particle abundances, rapidity spectra and ratios are suitable observables for CSR, contrary to the transverse mass spectra where the CSR contribution is rather small. The dependence on the nuclear equation of state is also investigated. The main finding is a microscopical interpretation of the excitation function of the K^+/π^+ ratio related both to CSR and to the formation of a Quark Gluon Plasma (QGP).
Chapter 5 is dedicated to a study of the collective behavior of the particles produced in HIC in terms of the directed flow. We investigate the differential hadron spectra produced in p+p and A+A collisions in the energy range $E_{Lab} = 6 - 158$ AGeV. We analyze the time evolution of the transverse momentum of particles and we distinguish the most important channels as sources of changes in momentum during the dynamics. In addition, we address the sensitivity of PHSD calculations of the directed flow on hadronic potentials, experimental cuts and centrality selection. The directed flow of protons and pions is presented in the energy range $\sqrt{s_{NN}} = 3-100$ GeV in comparison with avaliable data from the STAR, E895 and NA49 experiments. We find that the PHSD calculations including CSR and hadronic potential -according to the NL1 parametrization- give a good description of the experimental observations of the proton and pion flows.
In Chapter 6, we provide predictions for observables in relativistic collisions in the energy range of the future FAIR and NICA facilities. The main purpose is to shed further light on the CSR. Thus, in addition to particle rapidity spectra, the strange to non-strange particle ratios are explored as a function of the system size and of the centrality of the colliding system. In this investigation it emerges that the "horn" feature in the excitation function K^+/π^+ ratio disappears in small systems (e.g. $C + C$), while the analogous peak-structure in the excitation function $(\Lambda + \Sigma^0)/\pi$ ratio is independent of the size of the system.
In the final Chapter we summarize the issues addressed in this work within the PHSD framework and the results achieved.
This dissertation includes two appendices: the first provides an introduction to chiral symmetry and the second is dedicated to the derivation of scattering cross-sections for hyperon-hyperon interactions within a gauged flavor SU(3) hadronic model.

Contents

Chapter 1

Heavy-ion collisions

Heavy-ion collisions (HIC) represent the unique experimental way to probe strongly interacting matter under extreme conditions, *i.e.* high temperature and/or density. Often they are labeled "little bangs" in parallelism with the Big Bang of the universe. In fact, during a heavy-ion reaction the temperature and density might reach values comparable to those attained $\approx 10\,\mu$s after the Big Bang. Moreover, the hot and dense system created in the central volume of the collision, called "fireball", expands and cools down analogously to the evolution of the universe. Therefore, the study of HIC allows to explore and extract information about the state and properties of the matter at the early stages of the universe. In this respect, high energy heavy-ion reactions seem to produce a Quark Gluon Plasma (QGP), a phase of the strongly interacting matter where quarks and gluons are not confined into hadrons. The investigation of the QGP is the main goal of the heavy-ion physics, along with the more general study of the Quantum-Chromo-Dynamics (QCD) phase diagram. In this Chapter, an introduction to HIC is provided with a focus on the past, current and future experiments in this field. Moreover, we present the ideas of the QCD phase diagram and briefly describe the available theoretical approaches to study these reactions, with a comparison between these models.

1.1 Introduction

The study of heavy-ion physics relates to about five decades of research. We can trace back its beginning to the '70s with experiments at the Bevatron/Bevalac at the Lawrence Berkeley National Laboratory (LBNL) and at the Synchro-Phasotron at the Joint Institute for Nuclear Research (JINR). The maximum bombarding energy reached by the Bevatron/Bevalac has been $E_{Lab} \approx 2\,$AGeV, while the heavy-ion program at the Synchro-Phasotron studied collision energies of the order of 100 AMeV. The subsequent experiments have been pushed to larger and larger energies with the aim of discovering the QGP. The Alternating Gradient Syn-

chrotron (AGS) [1] at the Brookhaven National Laboratory (BNL) have studied the energies $E_{Lab} = 2 - 11$ AGeV, while the Super Proton Synchrotron (SPS) [2] at *Centre Europeen de la Recherche Nuclaire* (CERN) has addressed the energy interval of $E_{Lab} = 20 - 160$ AGeV. In order to achieve higher center-of-mass energies $\sqrt{s_{NN}}$, the collider configuration has been preferred relative to the fixed target experiments. The Relativistic-Heavy-Ion-Collider (RHIC) [3, 4] at BNL has been the first collider experiment for HIC and it is currently able to span a wide range of center-of-mass energy, *i.e.* $\sqrt{s_{NN}} = 5 - 200$ GeV. It has provided first measurements at $\sqrt{s_{NN}} = 200$ GeV, which indicate that a QGP has been created during the collisions and that it behaves as an almost perfect fluid [5]. However, there are indications that a QGP can be produced also at lower energy, in particular in the SPS regime [6, 7]. The upper limit set by RHIC has been overtaken by the Large Hadron Collider (LHC) [8], which is currently performing collisions at the TeV scale (the maximum energy which has recently been achieved is $\sqrt{s_{NN}}$ =5.02 TeV). Complementary to these high-energy collision programs, some experiments (FOPI [9], KAOS [10] and HADES [11]) have studied low energy reactions ($E_{Lab} \lesssim 2$ AGeV) at the SchwerIonen Synchrotron (SIS) at the *Gesellschaft für Schwerionenforschung (GSI Helmholtzzentrum für Schwerionenforschung)*. Recently, the interest has shifted from high energies to the investigation of intermediate energy regimes ($\sqrt{s_{NN}} = 4 - 11$ GeV) with the aim of exploring systems with large baryon density/chemical potential. In this respect, new heavy-ion facilities are under construction: the Facility for Antiprotons and Ion Research (FAIR) at GSI [12], the Nuclotron-based Ion Collider fAcility (NICA) [13] at the JINR and the Japan Proton Accelerator Research Complex (J-PARC) [14]. At FAIR, fixed target experiments will be performed within the energy range $\sqrt{s_{NN}} = 4 - 9$ GeV, such as the Compressed Baryonic Matter (CBM) experiment [15]. NICA is a collider facility and will carry out experiments at $\sqrt{s_{NN}} = 4 - 11$ GeV. In addition to the new facilities, the beam energy scan (BES) performed at RHIC [16] is currently studying intermediate energies: $\sqrt{s_{NN}} = 5.5, 7.7, 11.5, 19.6, 27, 39, 62.4$ GeV.

The time evolution of a HIC can be represented schematically in Fig. 1.1, from the initial stage, in which two heavy-ions are boosted with bombarding energy E_{Lab} against each other, to the final stage, in which the produced particles hit the detectors. Unfortunately, we cannot have direct access to the collision process via experimental techniques. It is only possible to detect the distributions and spectra of the produced particles, which correspond to the last stage displayed in Fig. 1.1. We can extract information about the previous stages of the collisions identifying some suitable observables and explaining their features and behaviors using theoretical models.

The identification and interpretation of observables represent the major challenges in HIC physics. From the experimental point of view, many technical difficulties have to be addressed,

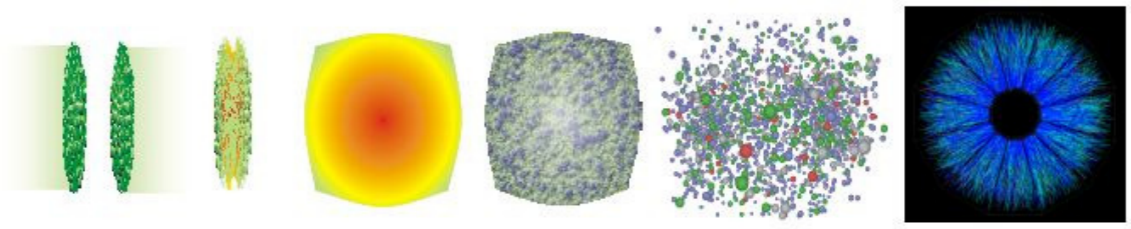

Figure 1.1: Sketch of the time evolution of a heavy-ion collision. Courtesy by Steffen Bass.

mostly related to the intent of reaching high luminosity and to the problem of resolving the high number of detected particles (separation of the background, recognition of many channels etc..). Instead, on the theoretical point of view, the description of these reactions is not easy, since HIC is a strongly interacting many-body system in a non-perturbation regime. We will discuss in detail the available theoretical approaches in Section 1.3.

1.2 The QCD phase diagram

HIC represent a suitable framework to study the in-medium properties of hadrons at high baryon density and the QCD Equation of State (EoS). This consists in the investigation of the QCD phase diagram, where different states of the strong matter and the associated phase transitions are displayed as a function of the net baryon density n (or chemical potential μ_B) and temperature T. In Fig. 1.2 an illustrative plot of the QCD phase diagram is shown. This only represents a qualitative picture, since our knowledge is limited to one point of the diagram at vanishing temperature and at net baryon density $n = n_0$, *i.e.* the state of the nuclei. Fig. 1.2 is based on experimental and theoretical considerations, which are not conclusive and still need to be confirmed with quantitative results. Here, we draw the main features of the QCD phase diagram, which has become more sophisticated during the years compared to the initial version of the diagram proposed by Cabibbo and Parisi in Ref. [17].
The strong matter is characterized by two phases: a hadronic phase at low temperature and density and a QGP phase at large temperature and/or large density. The associated phase transition is considered to be a crossover at low chemical potential and a first order transition at large chemical potential, with a critical point in between matching the two types of transition. Lattice QCD (lQCD), which consists in numerically solving the QCD theory of quarks and gluons on a space-time grid [19, 20], provides robust information about an area of the phase diagram close to the temperature axis. It gives a crossover transition and currently no indications of a critical point have been found with this method. Unfortunately, lQCD calcula-

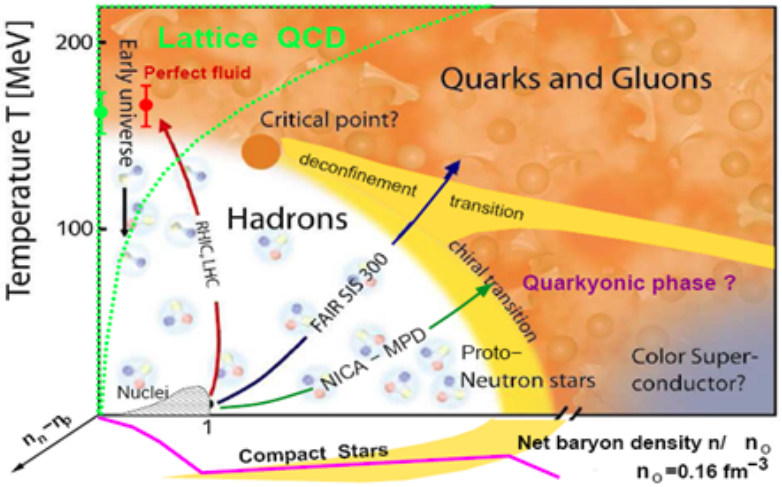

Figure 1.2: Illustrative plot of the QCD phase diagram. The figure is taken from Ref. [18].

tions cannot be performed at finite baryon chemical potential due to the fermion sign problem. There are few methods that allow lQCD to probe $\mu_B \neq 0$ [21], like the Taylor expansion of the thermodynamic quantities in terms of μ_B/T and/or the use of an imaginary chemical potential, but the calculations remain impossible for $\mu_B >> 0$. On the other hand, effective and functional models can be used to describe a larger area of the diagram [22, 23, 24, 25]. In particular, the functional approaches, like Dyson-Schwinger Equations (DSE) [23, 26, 27] and Functional Renormalization Group (FRG) [25], can provide information at finite μ_B, since they are not affected by the fermion sign problem. The downside is that a truncation scheme has to be applied to solve the system of coupled equations. Another possibility is to consider effective Lagrangians which approximate QCD. This is done in the approaches based on the Nambu Jona-Lasinio (NJL) model [28], where the strong interactions are considered as effective point-like interactions between quarks, excluding gluons from the description. This model does not include confinement, which can be incorporated via the coupling of the NJL quarks to a Polyakov loop. This improvement of the model is called Polyakov Nambu Jona-Lasinio model (PNJL) [29].

Apart from deconfinement, the QCD phase diagram is characterized by an additional transition, which is the chiral symmetry restoration. Chiral symmetry is the invariance of a Lagrangian under a transformation of the group $U(N_f)_R \times U(N_f)_L$ (with N_f as the number of flavors), which is approximate for the QCD Lagrangian (see Appendix A). As in case of the deconfinement phase transition, the boundaries of the CSR phase transition line are not well known. Lattice QCD calculations show that at vanishing μ_B the CSR takes place at roughly the same critical temperature and energy density as the deconfinement crossover. At finite baryon chemical potential different effective models support the idea that at finite chemical potential

a partially restored phase is achieved before the deconfinement occurs [28, 30, 31]. In this context, a quarkyonic phase has been proposed as a phase in which the degrees of freedom (partons) are confined in chirally symmetric baryons.

Additionally to the common density/temperature axes, in Fig. 1.2 a third axis is shown as a function of the difference between the neutron and proton densities $n_n - n_p$. In this way, isospin-asymmetric matter is also considered. This condition of the matter is relevant for neutron stars.

As mentioned before, the goal of heavy-ion physics is to map the QCD phase diagram. In particular, high-energy collisions (investigated at LHC and RHIC) probe the low-μ_B area, as highlighted by the red arrow, whereas the intermediate and low energy reactions (investigated at FAIR and NICA) probe the large-μ_B area, as highlighted by the blue and green arrows in the figure. These arrows represent ideal paths in the $T - n$ (or $T - \mu_B$) plane, that the systems created in HIC should follow during the time evolution. The understanding of how the system created in HIC evolves in the $T - n$ (or $T - \mu_B$) plane is not straightforward. Statistical models [32, 33, 34, 35, 36] extract from the final hadronic multiplicities values of temperature and baryon chemical potential that characterize the system at the freeze-out, *i.e.* the stage at which all particle abundances are fixed (see Section 1.3 for details). Each colliding system corresponds to one point in the phase diagram and the line connecting them is called freeze-out line. Hydrodynamical models, that incorporate the equation of state as input, are able to obtain trajectories [37] in the $T - n$ (or $T - \mu_B$) plane, each one associated to one colliding system. However, these models assume that the system is in local equilibrium, a strong assumption which limits the applicability of this type of approach. The comparison between results obtained by hydrodynamical models and experimental observations supports the fact that hydrodynamics provides a good description of the evolution of the fireball created in high-energy collisions (e.g. at RHIC), while it cannot be used in the low energy regime (e.g. at SPS). On the other hand, local equilibrium is not required by transport approaches [7, 38, 39, 40, 41, 42], which describe HIC on a microscopical level in terms of non-equilibrium dynamics. In this framework though, it is problematic to derive macroscopic equilibrium properties and the exact QCD-equation of state is needed to relate the energy and the conserved charges to temperature and to chemical potentials of the system in equilibrium. Moreover, in order to extract information about the QCD phase diagram, one needs to check if the system has reached kinetic equilibration. One possible method to verify this condition is to locally compute the longitudinal and transverse pressures; if they are equal, kinetic equilibrium is established. This has been done using the Ultrarelativistic Quantum Molecular Dynamics (UrQMD) transport model [39] in Ref. [43] and it has been found that at AGS energies kinetic equilibrium is achieved for times larger than ≈ 10 fm/c. Thus, it is in

principle possible to study the phase diagram of the strong matter also adopting transport approaches. In Ref. [44], within the PHSD model, the strangeness production has been analyzed and characterized as a function of T and μ_B adopting an EoS for a non-interacting hadron gas. In this study, the following results emerged. At AGS energies only a few percent of the total strangeness production happens in approximate local thermodynamical equilibrium. The cells, where strange particles are produced in equilibrium, are characterized by values of T which decrease with decreasing bombarding energy E_{Lab}, while the values of μ_B increase with decreasing E_{Lab}. For each colliding system the extracted points in the $T - \mu_B$ plane are spread over a wide area. From these findings, locating a critical point in the phase diagram appears to be difficult to accomplish experimentally.

1.3 Theoretical models

The theoretical study of HIC is not easy since one needs to describe a strongly interacting many-body system in a non-perturbative regime in an initially non-equilibrium state. It is also not conclusively established whether kinetic and chemical equilibria are achieved at some level. Moreover, the theory of the strong interaction (QCD) can be solved using lQCD techniques only in few cases: for static systems and for small values of μ_B. Consequently, we need to rely on effective models to investigate theoretically HIC. The available models are statistical, hydrodynamical and transport approaches. In the following Sections 1.3.1 - 1.3.3 we report the main features of these models, highlighting the advantages and disadvantages.

1.3.1 Statistical models

The statistical or thermal models aim to describe the particle production in HIC as a statistical process in equilibrium. This represents the main assumption of this type of approach. Statistical models do not provide a dynamical description of the collision process but they are limited to the characterization of the final particle multiplicities, that are detected experimentally. Consequently, they are not able to extract physical information about the processes occurring during the collision. The particle production, as considered in this approach, fulfills the conservation laws of the quantum numbers that characterize the analyzed degrees of freedom, *i.e.* baryon number B_i, electric charge Q_i and strangeness S_i. The choice of statistical prescriptions -to follow in HIC- mostly depends on the energy regime. The grand canonical ensemble is used for high collision energies, like those addressed at RHIC and LHC, while the canonical ensemble is suited for low collision energies, like those investigated at SIS and AGS (this prescription is also appropriate to study small systems). In fact, when the produc-

tion of strangeness is suppressed, as at low energies or in p+p collisions, the produced strange particles are strongly correlated and an exact strangeness conservation is required (not only an average conservation). In the following, we only show the statistical formulation of the grand canonical ensemble, but these considerations can be easily extended to the canonical case.
A statistical system is described in terms of its partition function Z, which in case of the grand canonical ensemble is given by:

$$Z(T, V, \mu_Q) = Tr[e^{-\beta(H-\sum_i \mu_{Q_i} Q_i)}], \tag{1.1}$$

where H is the Hamiltonian of the system, T and V are the temperature and volume of the system, respectively, β is $\beta = 1/T$, Q_i are the conserved charges and μ_{Q_i} are the associated chemical potentials.
The Hamiltonian usually adopted for HIC is the one describing a non-interacting hadron gas. Thus, the statistical models, which use this EoS, are referred to as Hadron Resonance Gas (HRG) models. In this picture, the partition function can be factorized in terms of single contributions Z_i associated to each hadron species. Each contribution is given by:

$$\ln Z_i(T, V, \boldsymbol{\mu}) = \frac{V g_i}{2\pi^2} \int_0^\infty \pm p^2 dp \ln[1 \pm \lambda_i \mathrm{e}^{-\beta\epsilon_i}], \tag{1.2}$$

where the label i refers to the hadronic particle, the +(-) sign is associated to fermions (bosons), g_i is the spin-isospin degeneracy factor, $\epsilon_i = \sqrt{p^2 + m_i^2}$ is the energy, $\boldsymbol{\mu} = (\mu_B, \mu_S, \mu_Q)$ is the total chemical potential and λ_i is the fugacity given by:

$$\lambda_i(T, \boldsymbol{\mu}) = \exp\left(\frac{B_i\mu_B + S_i\mu_S + Q_i\mu_Q}{T}\right). \tag{1.3}$$

From the partition function Z, one can derive all thermodynamic properties of the system. For example, the density of the particle i reads:

$$n_i(T, \boldsymbol{\mu}) = \frac{\langle N_i \rangle}{V} = \frac{T g_i}{2\pi^2} \sum_{k=1}^{\infty} \frac{(\pm 1)^{k+1}}{k} \lambda_i^k m_i^2 K_2\Big(\frac{k m_i}{T}\Big), \tag{1.4}$$

where K_2 is the modified Bessel function, the +(-) sign is associated to bosons (fermions). The thermal densities of the particles can be additionally corrected taking into account modifications related to the resonance decays with appropriate branching ratios.
In HIC, the net strangeness is zero and the electric charge is fixed by the colliding nuclei, thus, the partition function (Eq. 1.2) and the associated particle densities (Eq. 1.4) depend on three parameters: V, T, μ_B. The set of free parameters reduce only to T, μ_B if particle ratios are considered instead of absolute particle yields. Several statistical models succeed in describing simultaneously several particle ratios, including pions, kaons and baryons up to Ω,

with a unique set of parameters (T, μ_B) [32, 34, 45, 46, 47]. The extracted values of T and μ_B characterize the system at the freeze out, that is the stage at which all particle multiplicities are frozen. The (T, μ_B) points obtained from the fit of the particle ratios for different colliding systems can be represented in the QCD phase diagram and constitute the freeze-out line. The level of proximity between this line and the line of the deconfinement phase transition is still an open issue. Different statistical models find a common trend of the parameters T and μ_B as a function of the center-of-mass energy $\sqrt{s_{NN}}$ [32, 34, 46]: the temperature increases with increasing $\sqrt{s_{NN}}$ (up to a saturation temperature), while the baryon chemical potential decreases. Despite this, relevant differences in the results emerge among the available models. These are mostly related to the introduction of new fitting parameters, introduced to better describe the particle multiplicities, such as the factor for strangeness suppression γ_S [33], the non-equilibrium fugacities [35] and the separation of freeze-out in multiple freeze-out stages associated to different particle species [36].
The question of the different dynamics of the strange degrees of freedom compared to the particles containing light quarks is a source of uncertainty of the model, which is not able to provide a dynamical description of the collision process. There are other sources of uncertainty in this approach. It is not clear which resonances must be included in the HRG model. The inclusion of the scalar-isoscalar resonance $f_0(500)$, also identified as the σ meson, is still under debate [48]. Moreover, as stated before, HRG models are commonly employed for this approach, but they neglect interactions between particles and mean-field properties of the medium. However, interactions and mean-field effects become relevant in systems with large density [49]. To cope with this, some models implement interactions between particles via excluded volume corrections [50] or through the use of an EoS based on Van der Waals interactions [51].

1.3.2 Hydrodynamical models

The hydrodynamical models describe the hot and dense system created in HIC from a macroscopical point of view, where the relevant variables are thermodynamical quantities like temperature, pressure, densities and currents. They provide a dynamical description of the collision processes under the restrictive assumption of local thermal and chemical equilibria. These assumptions strongly limit the applicability of this approach to the intermediate stage of the collision. In fact, the system does not achieve a local equilibrium instantaneously after the collision contact and at the late stages the system cannot be described as a fluid, since it develops as a dilute gas.
In this approach, the dynamics of the system is ruled by the conservation equations of the energy-momentum tensor $T_{\mu\nu}$ and of currents associated to the relevant charges, such as the

current N_μ associated to the net baryon density:

$$\partial_\mu T^{\mu\nu} = 0, \tag{1.5}$$

$$\partial_\mu N^\mu = 0. \tag{1.6}$$

This system of equations is closed with the inclusion of an EoS that provides information about the chemical potential and temperature of the system. The differential equations are solved locally on a space-time grid, where the macroscopic variables are propagated.
The simplest case is represented by an ideal fluid, whose $T^{\mu\nu}$ and N^μ read:

$$T^{\mu\nu}(x) = [\varepsilon(x) + p(x)]\, u^\mu(x) u^\nu(x) - g^{\mu\nu} p(x), \tag{1.7}$$

$$N^\mu = \rho_B(x)\, u^\mu(x), \tag{1.8}$$

where $\varepsilon(x)$ is the energy density, p is the pressure, $u^\mu = \gamma(1, \mathbf{v})$ is the 4-velocity, $g^{\mu\nu}$ is the metric tensor and $\rho_B(x)$ is the net baryon density.
The advantage of this approach is that the EoS is incorporated in the model as input, so it is in principle possible to connect the experimental observations to the properties of the QCD phase diagram. On the other hand, from the hydrodynamical evolution it is not possible to extract particle multiplicities and spectra in a direct way, due to the break-down of the hydrodynamical description at the so-called freeze-out[1]. A prescription for this final stage has to be introduced in the model for example via a Cooper-Frey formula [52], which gives the phase-space density of hadronic particles in correspondence of a suitable hypersurface (defined on the basis of constant time, constant temperature or constant energy density). The implementation of the Cooper-Frey formula suffers from the problem of negative contributions, *i.e.* particles which move inwards the fireball [53]. In addition, current models are not able to include interactions between the freeze-out particles and the fluid. Thus, a self-consistent realization of the freeze-out and the description of the final stage of the system evolution are still missing within this approach. The definition of the freeze-out boundary and the necessary recipe for the initial stage are the main sources of uncertainty in the hydrodynamical approach, which is consequently unable to describe consistently the entire collision process. Possible prescriptions for the pre-equilibrium stage (before the hydrodynamical evolution) are the Glauber models [54], the Taub-adiabate scheme [55] and initial conditions according to a color glass condensate *ansatz* [56]. Despite the issue of the boundary conditions, hydrodynamical models provide satisfying results for HIC in the high energy regime [57, 58]. The main achievement of the hydrodynamical approach is the successful description of the elliptic flow measured at RHIC [59, 60], supporting the idea that the system behaves almost like a perfect fluid during the

[1] In the context of hydrodynamical models, the freeze-out corresponds to the stage in which hydrodynamical equilibrium ceases.

fireball expansion [5].
The hydrodynamical description is realized in different models, which differ in the number of dimensions considered (1+1, 2+1 and 3+1 dimensional models [61, 62, 63]) and in the number of fluids implemented in the propagation (one-fluid [64] or multi-fluid models [37], the latter describing separately target, projectile and fireball). A recent development of hydrodynamical models is the inclusion of small deviations from equilibrium, that resolves in the use of viscous hydrodynamics [65, 66]. This extension implies the calculation of transport coefficients, bulk and shear viscosity and heat conductivity.
Further progress in this field has been achieved with the creation of hybrid models, which combine hydrodynamical and transport codes [67, 68]. This is accomplished by integrating a transport description for the particles produced after the hydrodynamical evolution of the system. The final hadron cascade is called "after-burner" stage. The development of hybrid models is motivated by the aim of realizing two separate freeze-out stages: a chemical freeze-out and a kinetic freeze-out. New models have implemented transport codes also to describe the pre-equilibrium stage. Unfortunately, although the hybrid models merge hydrodynamical and transport approaches, these ingredients remain independent and not consistently combined. Thus, the final results strongly depend on the prescriptions adopted to match the different ingredients.
We specify that the question of applicability of hydrodynamical models is not limited to the temporal evolution of the collision process, but it also concerns energy considerations [57]. In fact, the time interval in which the condition of local equilibrium is fulfilled progressively decreases as the beam energy decreases. This can be seen via the computation of the Knudsen number, *i.e.* the ratio between the mean free path and the fluid length scale [69]. Thus, the hydrodynamical picture is suitable predominantly at high energies, like top RHIC energies, while it fails at low energies, e.g. in the FAIR and NICA regimes.

1.3.3 Transport models

The transport models are unique as they have the capability to consistently describe the whole time evolution of a HIC. They provide a microscopic description of the particle dynamics occurring in the collision process. In spite of the direct access to the microscopic features of the system, information about macroscopic properties, such as temperature or chemical potential, is not straightforward to derive in transport approaches, especially in relation to the out-of equilibrium dynamics (for a detailed discussion on this issue see Refs. [43, 44]).
This kind of models does not require any assumption about the equilibration of the system. However, to study a system as HIC one needs to solve a system composed of a large number of coupled differential and integral equations of motion. Thus, in order to be able to solve the

transport equations describing many-body interactions, one needs to require at some level a simplification (e.g. type of collisions considered, mean-field approximation etc.).
To illustrate the main features of this approach, we consider the Vlasov Ühling Uhlenbeck (VUU) equation, as a simple starting point. This is a semiclassical extension of the Boltzmann transport equation which includes a mean-field potential and binary collisions of the type $1 + 2 \leftrightarrow 3 + 4$. The VUU equation gives the time evolution of the single-particle phase-space distribution function $f(\mathbf{r}, \mathbf{p}, t)$ and reads in the non-relativistic limit:

$$\left(\frac{\partial}{\partial t} + \frac{\mathbf{p}}{m}\nabla_{\mathbf{r}} - \nabla_{\mathbf{r}}U(\mathbf{r})\nabla_{\mathbf{p}}\right)f(\mathbf{r},\mathbf{p},t) = g\int \frac{d^3p_2}{(2\pi)^3}\frac{d^3p_3}{(2\pi)^3}\frac{d^3p_4}{(2\pi)^3}\,W_{(1+2\to3+4)} \tag{1.9}$$
$$\times (2\pi)^4\delta^3(\mathbf{p}_1 + \mathbf{p}_2 - \mathbf{p}_3 - \mathbf{p}_4)\,\delta\left(\frac{\mathbf{p}_1^2}{2m_1} + \frac{\mathbf{p}_2^2}{2m_2} - \frac{\mathbf{p}_3^2}{2m_3} - \frac{\mathbf{p}_4^2}{2m_4}\right)$$
$$\times [f_3f_4(1 \pm f_1)(1 \pm f_2) - f_1f_2(1 \pm f_3)(1 \pm f_4)],$$

where $\mathbf{p}$ is the particle momentum, $U(\mathbf{r})$ is the self-generated mean-field potential (of single-particle type), g is the spin-isospin particle degeneracy factor, $W_{(1+2\to3+4)}$ is the transition matrix element (squared) for the reaction $1 + 2 \to 3 + 4$, $f_i = f_i(\mathbf{r}, \mathbf{p_i}, t)$ is the short-hand notation for the phase-space distribution function of the particle of type i, the (+) and (-) signs are associated to bosons and fermions and correspond to the Bose enhancement and Pauli blocking factors, respectively. On the right-hand side, the term $f_3f_4(1 \pm f_1)(1 \pm f_2)$ represents the gain term arising from the backward collisions $3 + 4 \to 1 + 2$, while the term $f_1f_2(1 \pm f_3)(1 \pm f_4)$ represents the loss term associated to the forward collisions $1 + 2 \to 3 + 4$. The left-hand side of Eq. 1.9 corresponds to the Vlasov transport equation for particles propagating in the self-generated mean-field potential (in the Hartree-Fock approximation), while the right-hand side represents the collision contribution.
If the system is composed of i particle species, we need to solve a set of i coupled transport equations. A solution of the coupled transport equations can be calculated numerically either assuming a Gaussian particle density distribution or applying a test-particle *ansatz*. The latter replaces the phase-space density with n test-particles according to:

$$f(\mathbf{r},\mathbf{p},t) = \lim_{n\to\infty}\frac{1}{n}\sum_{i}^{n\cdot A}\delta(\mathbf{r} - \mathbf{r}_i(t))\,\delta(\mathbf{p} - \mathbf{p}_i(t)), \tag{1.10}$$

where A is the total particle number given by:

$$A = \int d^3r\int d^3p f(\mathbf{r},\mathbf{p},t). \tag{1.11}$$

For a proper treatment of the HIC, quantum relativistic equations have to be considered; consequently models based on classical Boltzmann-type equations are usually not suited for

strongly-interacting systems. In the latter case one needs to employ the Kadanoff-Baym equations [70] (see Section 2.1 for more details), *i.e.* generalized off-shell transport equations for the Green functions. This is done in the Parton-Hadron-String Dynamics (PHSD) transport approach [7] presented in Chapter 2.

A numerical realization of transport models for HIC starts with an initialization stage, where two colliding nuclei are described on a space-time grid according to a density profile (given for example by Woods-Saxon distributions) with a phase-space distribution. The system is then divided into cells, where particles propagate and interact (according to the implemented transport theory) in line with experimental or phenomenological cross-sections, that are included as input. Usually, transport models are integrated by high-energy event generators like PYTHIA [71], FRITIOF [72, 73] and JETSET [74] to describe hard collisions on the basis of the Lund string model [75]. At low energies, medium effects and hadronic potentials are found to be significant, thus it is important to include also these aspects in the description [49]. The majority of transport codes includes interactions of the type: $2 \leftrightarrow 2$, $2 \rightarrow 3$, $1 \leftrightarrow 2$, whereas three body interactions are neglected. In this respect, we mention that the PHSD transport approach incorporates three-body channels for the production of three mesons from the interaction of a baryon and antibaryon pair both in the strange and non-strange sectors [44, 76]. The actual solution of the transport equation is performed numerically via Monte Carlo simulations. Many transport codes [7, 40] resort to use the parallel ensemble method, that consists in the simulation of N collision events performed in parallel. This allows to compute with good accuracy collective quantities (scalar density, hadron potentials and in-medium properties of particles in general), since the statistical fluctuations are reduced by averaging over the N events. However, this numerical method is computationally demanding. The description of rare processes is also hard to accomplish in transport models. Attempts to overcome this issue involve perturbative treatments, as performed e.g. by the HSD model for the strangeness production at low SIS energies [49].

The most difficult aspects to introduce in transport models is the phase transition between a hadronic and a partonic phase and a suitable description of the partonic phase in a non-perturbative regime in line with lQCD data. Some transport codes model the QCD phase as a parton cascade according to perturbative QCD (pQCD), but RHIC observations of the large elliptic flow support the idea that the hot and dense phase behaves as a strongly coupled QGP, in contrast to pQCD calculations. On the other hand, lQCD, which is a non-perturbative approach, is currently not able to provide dynamical properties of the degrees of freedom. Regarding this issue, the PHSD transport approach describes the partonic phase according to the Dynamical Quasi-Particle Model (DQPM), which reproduces the lQCD equation of state and gives the dynamical properties of quarks and gluons as a function of the scalar or en-

ergy density (an introduction to the DQPM model is given in Section 2.2). The hadronization procedure is also hard to model. One possible method is the quark coalescence [77], which consists of an instantaneous recombination of quark states into hadron states that, however, does not conserve energy. The conservation of energy and momentum is instead a natural outcome of an off-shell model, where particles are described in terms of broad spectral functions. This is the case of PHSD, in which the hadronization scheme follows local covariant transition rates for (qqq), $(\bar{q}\bar{q}\bar{q})$ and $(q\bar{q})$ fusion (see Section 2.3 for more details).
In this work, we make use of the PHSD transport approach, which is capable of consistently describing the whole collision process including both hadronic and partonic phases and ensuring the conservation of energy, momentum and quantum numbers at each stage of the time evolution.

Chapter 2

Parton-Hadron-String Dynamics

Among the different theoretical models that are used to study Heavy-Ion Collisions (HIC), only the transport approaches provide a microscopic and consistent description of the whole dynamics of the collision. The research work presented in this dissertation is based on a transport approach, the Parton-Hadron-String Dynamics (PHSD), which has been developed for the study of strongly interacting systems in- and out-of equilibrium [7, 78]. It contains both hadronic and partonic degrees of freedom, the latter included according to the Dynamical Quasi-Particle Model (DQPM) [79, 80]. The PHSD approach has been tested for different colliding systems (p+p, p+A, A+A) in a wide range of bombarding energy, from SIS to LHC energies, and has been able to describe a large number of experimental observables [81]. In this Chapter, we firstly present the transport theory on which PHSD is based, *i.e.* the Kadanoff-Baym equations for the Green functions [70, 79, 80]. Secondly, we introduce both the PHSD and DQPM approaches and analyze the main features of PHSD in case of heavy-ion collision at intermediate energies ($\sqrt{s_{NN}} = 3 - 20\,\mathrm{GeV}$). Finally, the recent extension of PHSD to incorporate Chiral Symmetry Restoration (CSR) [44, 82] is presented in detail.

2.1 Transport theory: Kadanoff-Baym equations

The PHSD transport approach is based on the Kadanoff-Baym equations, which are off-shell transport equations in phase-space representation describing the time evolution of the degrees of freedom. In this quantum and relativistic theory, the transport equations are applied not to single-particle phase-space distribution functions, as in Section 1.3.3 for the Vlasov Ühling Uhlenbeck (VUU) equation, but to field quanta characterized in terms of the propagators, *i.e.* Green functions G that depend on two time arguments. The single-particle Green functions, defined on the Keldysh-contour (which is shown in Fig. 2.1), can have different arguments depending on how the path is drawn using the branches of the contour. We obtain

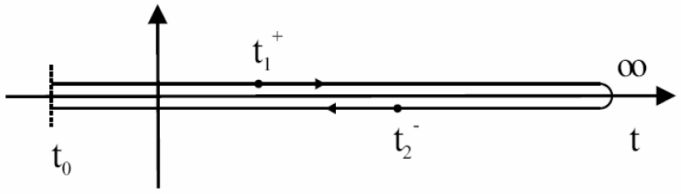

Figure 2.1: The Keldysh-contour for the time integration on a closed path, where the time t_1 is located on the chronological branch (+), while the time t_2 is located on the anti-chronological branch (-). The figure is taken from Ref. [79].

four possibilities for G, which in case of scalar fields $\phi(x)$ are:

$$iG^c(x,y) = iG^{++}(x,y) = \langle\, \hat{T}^c(\phi(x)\phi(y))\,\rangle, \tag{2.1}$$

$$iG^<(x,y) = iG^{+-}(x,y) = \langle \phi(y)\phi(x)\rangle, \tag{2.2}$$

$$iG^>(x,y) = iG^{-+}(x,y) = \langle \phi(x)\phi(y)\rangle, \tag{2.3}$$

$$iG^a(x,y) = iG^{--}(x,y) = \langle\, \hat{T}^a(\phi(x)\phi(y))\,\rangle, \tag{2.4}$$

where $x = (x^0, \mathbf{x})$ and $y = (y^0, \mathbf{y})$ are spatial 4-vectors, the apices + and − refer to the chronological branch and to the anti-chronological branch, respectively, $\hat{T}^c$ is the causal time-ordering operator placing fields at later times to the left and $\hat{T}^a$ is the anti-causal time-ordering operator placing fields at later times to the right. The $G^<(x,y)$ and $G^>(x,y)$ are called Wightman functions. The Green functions (Eqs. 2.1-2.4) can also be written in terms of a 2×2 matrix as follows:

$$G(x,y) = \begin{array}{c} \\ + \\ - \end{array} \begin{array}{c} \begin{array}{cc} + & \quad - \end{array} \\ \begin{pmatrix} G^c(x,y) & G^<(x,y) \\ G^>(x,y) & G^a(x,y) \end{pmatrix} \end{array}. \tag{2.5}$$

In addition, we introduce the retarded G^R and advanced G^A Green functions as follows:

$$G^R(x,y) = G^c(x,y) - G^<(x,y) = G^>(x,y) - G^a(x,y), \tag{2.6}$$

$$G^A(x,y) = G^c(x,y) - G^>(x,y) = G^<(x,y) - G^a(x,y). \tag{2.7}$$

The Kadanoff-Baym equations provide the exact time evolution of the single-particle Green functions and they are expressed by:

$$-(\partial^x_\mu \partial^\mu_x + m^2) G^{R,A}(x,y) = \delta(x-y) + \Sigma^{R,A}(x,x') \odot G^{R,A}(x',y), \tag{2.8}$$

$$-(\partial^x_\mu \partial^\mu_x + m^2) G^{<,>}(x,y) = \Sigma^R(x,x') \odot G^{<,>}(x',y) + \Sigma^{<,>}(x,x') \odot G^A(x',y), \tag{2.9}$$

where the symbol $\odot$ refers to an integration over the intermediate space-time points x' and y' on a closed-time path (according to the Keldysh-contour) and Σ is the self-energy. The

self-energy includes interactions of the Green functions of higher orders and in this sense generates an infinite tower of coupled equations with non-perturbative expansion. From the Dyson-Schwinger equation we can connect the self-energy and the Green function according to:

$$G^{-1}(x,y) = G_0^{-1} - \Sigma(x,y) \tag{2.10}$$

where G_0 is the free Green function.
Once we determine Σ (at least in a suitable order), Eqs. 2.8 and 2.9 define the dynamics of the degrees of freedom. The self-energy can be extracted from the variation of the effective action $\Gamma[G]$ of the considered interaction theory:

$$\Sigma = 2i\frac{\delta\Phi}{\delta G}, \tag{2.11}$$

where Φ is the functional that includes all irreducible diagrams up to infinite order. However, we consider here only the contributions up to the second order in the coupling. This approximation is known as effective 2-particle irreducible (2PI) limit and considers two-particle interactions as irreducible diagrams. In this framework, both mean-field effects and scatterings (at the leading order) are included. We defer the complete derivation of the generalized transport equations from the Kadanoff-Baym equations to Ref. [79] and here report the final result obtained after a first-order gradient expansion of the Wigner transformed[1] Kadanoff-Baym equations. The Wigner transformed Green functions $\overline{G}$ and self-energies $\overline{\Sigma}$ can be written as:

$$\overline{G}^{R,A} = \Re\,\overline{G}^{R} \mp i\overline{A}/2, \tag{2.13}$$

$$\overline{\Sigma}^{R,A} = \Re\,\overline{\Sigma}^{R} \mp i\overline{\Gamma}/2, \tag{2.14}$$

where $\overline{A}$ is the spectral function and $\overline{\Gamma}$ is the width of the particle. In first-order gradient expansion, the spectral function is of relativistic Breit-Wigner form:

$$\overline{A} = \frac{\overline{\Gamma}}{[p_0^2 - \mathbf{p}^2 - m^2 - \overline{\Sigma}^{\delta}(x) - \Re\overline{\Sigma}^{R}(p,x)]^2 + \overline{\Gamma}^2/4} = \frac{\overline{\Gamma}}{\overline{M}^2 + \overline{\Gamma}^2/4}. \tag{2.15}$$

[1]The Wigner transformation consists basically in a relativistic Fourier transform. By applying a Wigner transformation to a space-dependent function $F(x_1, x_2)$, we obtain a function $\overline{F}(p,x)$ which depends on the 4-momentum p and on the mean space-time coordinates x according to :

$$\overline{F}(p,x) = \int_{-\infty}^{+\infty} d^D\Delta x\, e^{i\Delta x_\mu p^\mu} F(x_1 = x + \Delta x/2, x_2 = x - \Delta x/2), \tag{2.12}$$

where $p = (p_0, \mathbf{p})$, $x = (x_1 + x_2)/2$, $\Delta x = x_1 - x_2$ and the index D refers to the space dimensions. We notice that, compared to the classical phase space distribution $f(\mathbf{r}, \mathbf{p}.t)$, the Wigner transform $F(p,x)$ contains the energy p_0 as additional degree of freedom.

The generalized transport equations are given by:

$$2p^\mu \partial_\mu^x i\overline{G}^{<,>} - \{\overline{\Sigma}^\delta + \Re\overline{\Sigma}^R, i\overline{G}^{<,>}\} - \{i\overline{\Sigma}^{<,>}, \Re\overline{G}^R\} = i\overline{\Sigma}^< i\overline{G}^> - i\overline{\Sigma}^> i\overline{G}^<, \tag{2.16}$$

with $\{\overline{F}(p,x), \overline{G}(p,x)\} := \partial_\mu^p \overline{F}(p,x) \cdot \partial_p^\mu \overline{G}(p,x) - \partial_\mu^p \overline{G}(p,x) \cdot \partial_p^\mu \overline{F}(p,x)$, as the relativistic generalization of the Poisson brackets and where $\overline{G}$ and $\overline{\Sigma}$ are purely imaginary quantities after the Wigner transformation and thus hereafter indicated as $i\overline{G}$ $i\overline{\Sigma}$.
In addition, the generalized mass-shell equation is:

$$[p^2 - m^2 - \overline{\Sigma}^\delta - \Re\overline{\Sigma}^R] i\overline{G}^{<,>} = i\overline{\Sigma}\Re\overline{G}^R + \frac{1}{4}\{i\overline{\Sigma}^>, i\overline{G}^<\} - \frac{1}{4}\{i\overline{\Sigma}^<, i\overline{G}^>\}. \tag{2.17}$$

In Eq. 2.16 we identify a structure similar to the VUU equation (Eq. 1.9). On the l.h.s. $p^\mu \partial_\mu^x i\overline{G}^{<,>}$ represents the drift term and the Poisson bracket $\{\overline{\Sigma}^\delta + \Re\overline{\Sigma}^R, i\overline{G}^{<,>}\}$ corresponds to the Vlasov term with local potentials. On the r.h.s., we find the collision terms with the gain contribution represented by $i\overline{\Sigma}^< i\overline{G}^>$ and the loss contribution represented by $i\overline{\Sigma}^> i\overline{G}^<$. On the other hand, the Poisson bracket $\{i\overline{\Sigma}^{<,>}, \Re\overline{G}^R\}$, labeled as back-flow term, does not have any correspondence in the VUU equation. It is associated to the off-shell behavior of the particle propagation in systems out-of equilibrium (it disappears in the limit of on-shell particles) and vanishes in the quasi-particle approximation.
Introducing the distribution function $\overline{N}(p,x)$ by:

$$i\overline{G}^<(p,x) = \overline{N}(p,x)\overline{A}(p,x), \tag{2.18}$$

$$i\overline{G}^>(p,x) = (1 + \overline{N}(p,x))\overline{A}(p,x), \tag{2.19}$$

we can separate the occupation density from the spectral properties. Thus, the generalized transport equations given in Eqs. 2.16 and 2.17 describe the evolution of the Green functions providing information both on the occupation number of particles in terms of $\overline{N}(p,x)$ and on the properties and interactions of the particles in terms of $\overline{A}(p,x)$.
We note that Eqs. 2.16 and 2.17 are not equivalent, even though they are both derived from the first-order gradient expansion of the Kadanoff-Baym equations. In fact, they present a discrepancy due to a second order contribution contained in the term $\{i\overline{\Sigma}^{<,>}, \Re\overline{G}^R\}$. This discrepancy can be solved by replacing the self-energy $\overline{\Sigma}^<$ with $(\overline{G}^<\overline{\Gamma}/\overline{A})$ in the generalized transport equation (Eq. 2.16), which can then be rewritten in the following short-hand way, known as Botermans-Malfliet form [83]:

$$\frac{1}{2}\overline{A}\,\overline{\Gamma}\left[\{\overline{M}, i\overline{G}^<\} - \frac{1}{\overline{\Gamma}}\{\overline{\Gamma}, \overline{M} \cdot i\overline{G}^<\}\right] = i\overline{\Sigma}^< i\overline{G}^> - i\overline{\Sigma}^> i\overline{G}^<, \tag{2.20}$$

where the mass function is defined as $\overline{M} = p^2 - m^2 - \overline{\Sigma}^\delta - \Re\overline{\Sigma}^R$.
Equation 2.20 reproduces the full Kadanoff-Baym dynamics and can be solved numerically

using techniques developed for the classical or semi-classical transport theories. A numerical solution can be obtained within the test-particle *ansatz*, which has been already introduced in Eq. 1.10 of Section 1.3.3. We recall that in this case we consider relativistic off-shell particles; thus the test-particle *ansatz* is extended as follows:

$$\overline{F}(x,p) = i\overline{G}^{<}(x,p) = \frac{1}{N}\sum_{j=1}^{N\cdot A}\delta^{(3)}(\mathbf{x}-\mathbf{X}_j(t))\,\delta^{(3)}(\mathbf{p}-\mathbf{P}_j(t))\,\delta(p_0-\epsilon_j(t)), \tag{2.21}$$

where j is the label referring to each test-particle and the sum over the test-particles is properly normalized to the total number of particles A.
The equations of motion for the test-particle j are given by:

$$\frac{d\vec{X}_j}{dt} = \frac{1}{1-C_{(j)}}\frac{1}{2\epsilon_j}\left[2\vec{P}_j + \vec{\nabla}_{P_j}\mathrm{Re}\overline{\Sigma}^R_{(j)} + \frac{\epsilon_j^2 - \vec{P}_j^2 - M_0^2 - \mathrm{Re}\overline{\Sigma}^R_{(j)}}{\overline{\Gamma}_{(j)}}\vec{\nabla}_{P_j}\overline{\Gamma}_{(j)}\right] \tag{2.22}$$

$$\frac{d\vec{P}_j}{dt} = -\frac{1}{1-C_{(j)}}\frac{1}{2\epsilon_j}\left[\vec{\nabla}_{X_j}\mathrm{Re}\overline{\Sigma}^R_{(j)} + \frac{\epsilon_j^2 - \vec{P}_j^2 - M_0^2 - \mathrm{Re}\overline{\Sigma}^R_{(j)}}{\overline{\Gamma}_{(j)}}\vec{\nabla}_{X_j}\overline{\Gamma}_{(j)}\right] \tag{2.23}$$

$$\frac{d\epsilon_j}{dt} = \frac{1}{1-C_{(j)}}\frac{1}{2\epsilon_j}\left[\frac{\partial\mathrm{Re}\overline{\Sigma}^R_{(j)}}{\partial t} + \frac{\epsilon_j^2 - \vec{P}_j^2 - M_0^2 - \mathrm{Re}\overline{\Sigma}^R_{(j)}}{\overline{\Gamma}_{(j)}}\frac{\partial\overline{\Gamma}_{(j)}}{\partial t}\right] \tag{2.24}$$

where the subscript (j) means that the function is evaluated at the test-particle coordinates $x = (t, \mathbf{X}(t))$ and $p = (\epsilon(t), \mathbf{P}(t))$ and where $C_{(j)}$ is given by:

$$C_{(j)} = \frac{1}{2\epsilon_j}\left[\frac{\partial\mathrm{Re}\overline{\Sigma}^R_{(j)}}{\partial\epsilon_j} + \frac{\epsilon_j^2 - \vec{P}_j^2 - M_0^2 - \mathrm{Re}\overline{\Sigma}^R_{(j)}}{\overline{\Gamma}_{(j)}}\frac{\partial\overline{\Gamma}_{(j)}}{\partial\epsilon_j}\right]. \tag{2.25}$$

The normalization factor $1/(1-C_{(j)})$ in Eqs. 2.22-2.24 represents a Lorentz gamma factor that transforms the time t into the eigentime τ of the particle j: $\tau_j = t/(1-C_{(j)})$. If we change the variable from t to τ_j the gamma factor disappears from the equations of motion.
The theory derived in this Section, which describes relativistic strongly-interacting systems in- and out-of equilibrium, has been successfully employed in PHSD to study HIC including both hadronic and partonic phases.

2.2 Dynamical quasi-particle model

The theoretical description of the partonic degrees of freedom (massive quarks q anti-quarks $\overline{q}$ and gluons g) is realized following the Dynamical-Quasi-Particle Model (DQPM) [79, 80] which reproduces lQCD results in thermodynamical equilibrium and provides the properties of the partons, *i.e.* masses and widths in their spectral functions. The basic idea is

to characterize the interacting quasi-particles with Lorentzian spectral functions A and propagators G:

$$A(\omega, \mathbf{p}) = \frac{2\gamma\omega}{(\omega^2 - \mathbf{p}^2 - M^2)^2 + 4\gamma^2\omega^2}, \tag{2.26}$$

$$G(\omega, \mathbf{p}) = \frac{-1}{\omega^2 - \mathbf{p}^2 - M^2 + 2i\gamma\omega} = \frac{-1}{\omega^2 - \mathbf{p}^2 - \Sigma}, \tag{2.27}$$

with $\omega = p_0$. The dynamical properties, masses M and widths γ of the partons are given by the following expressions (in line with the hard thermal loop relations in the high momentum regime):

$$M^2_{q(\overline{q})}(T) = \frac{N_c^2 - 1}{8N_c} g^2 \left(T^2 + \frac{\mu_q^2}{\pi^2} \right), \tag{2.28}$$

$$M^2_g(T) = \frac{g^2}{6} \left((N_c + \frac{1}{2} N_f) T^2 + \frac{N_c}{2} \sum_q \frac{\mu_q^2}{\pi^2} \right), \tag{2.29}$$

$$\gamma_{q(\overline{q})}(T) = \frac{1}{3} \frac{N_c^2 - 1}{2N_c} \frac{g^2 T}{8\pi} \ln\left(\frac{2c}{g^2} + 1 \right), \tag{2.30}$$

$$\gamma_g(T) = \frac{1}{3} N_c \frac{g^2 T}{8\pi} \ln\left(\frac{2c}{g^2} + 1 \right), \tag{2.31}$$

where $N_c = 3$ refers to the number of colors, $N_f = 3$ refers to the number of flavors, μ_q is the quark chemical potential, T is the temperature, $T_c \approx 158\,\text{MeV}$ is the critical temperature and g^2 is the coupling squared which is approximated by:

$$g^2(T/T_c) = \frac{48\pi^2}{(11N_c - 2N_f) \ln[\lambda^2 (T/T_c - T_s/T_c)^2]}\,. \tag{2.32}$$

We specify that the above expressions of the widths (Eqs. 2.30 and 2.31) are valid for $\mu_q = 0$. In the calculations of the parton widths we take into account the following physical reactions between gluons g and (anti)quarks p:

$$g + g \leftrightarrow g + g, \qquad g \leftrightarrow g + g + g, \qquad g + p \leftrightarrow g + p, \qquad p + p \leftrightarrow p + p,$$
$$g \leftrightarrow g + g, \qquad g \leftrightarrow g + g + g + g, \qquad g \leftrightarrow p + \overline{p}, \qquad p + p \leftrightarrow p + p + g.$$

In Eqs. 2.28-2.32 we identify three independent parameters: λ, T_s and c, that have to be fixed. For this purpose, we compute from DQPM -within the grand canonical ensemble- thermodynamical quantities, such as energy density ε or entropy density s, and then we fit either ε or s in order to reproduce the same quantities calculated in lQCD. This fitting procedure must be applied to a system in thermal equilibrium and it is realized numerically simulating a system

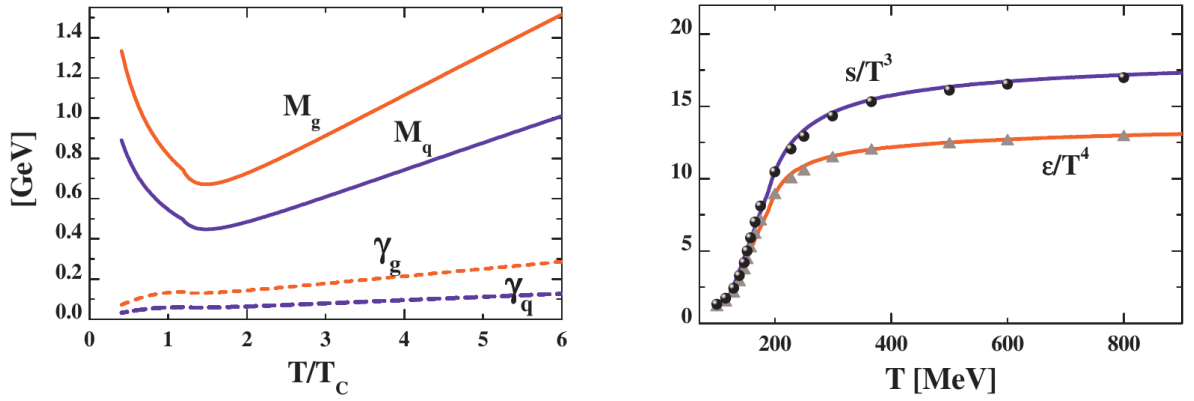

Figure 2.2: (l.h.s.) The effective masses $M_{q,g}$ and widths $\gamma_{q,g}$ as function of the temperature T normalized to T_c. The blue and red lines refer to the quarks and gluons, respectively. (r.h.s.) The normalized entropy density $s(T)/T^3$ in blue and the normalized energy density $\varepsilon(T)/T^4$ in red from the DQPM in comparison with the lQCD calculations from the BMW group [84] in full dots and triangles. The figure is taken from Ref. [78].

of quasi-particles in a box with periodic boundary conditions. The extracted values for the parameters are: $\lambda \approx 2.42$, $T_s \approx 0.56 T_c$ and $c \approx 14.4$. On the r.h.s. of Fig. 2.2 we show the results of the DQPM fit to the energy density and entropy density of the lQCD data from the Budapest-Marseille-Wuppertal (BMW) collaboration and on the l.h.s. the extracted masses and widths of (anti)quarks and gluons. We notice that the dynamical quark masses are larger than the bare quark masses ($m_q^0 \approx 7$ MeV, $m_s^0 \approx 100$ MeV). The strange quark mass is larger than the light quark mass according to $M_s(T) = M_{u,d}(T) + 35$ MeV. This has been fixed empirically by a comparison with experimental data on the K^+/π^+ ratio in central Au+Au collisions at $\sqrt{s_{NN}} = 17.3$ GeV. This fit to the lQCD calculations allows to determine the self-energies of the degrees of freedom, needed to describe the time evolution of the system using the off-shell transport equations, as given in Section 2.1.

The DQPM can also be extended to finite chemical potential μ_q applying a scaling of the temperature $T \to T^*$ according to the following relation (as provided by Eqs. 2.28 and 2.29):

$$T^*(T, \mu_q) = \sqrt{T^2 + \mu_q^2/\pi^2}, \tag{2.33}$$

and defining a critical temperature dependent on μ_q:

$$\frac{T_c(\mu_q)}{T_c(\mu_q = 0)} = \sqrt{1 - \alpha \mu_q^2}, \tag{2.34}$$

with $\alpha \approx 8.79\,\text{GeV}^{-2}$, which is consistent with (or defined by) the lattice curvature at small μ_q. In addition to the dynamical masses and widths, the DQPM also provides the mean-field

potential in which the degrees of freedom propagate. The scalar mean-field potential U_S for quark and antiquarks is given by:

$$U_S(\rho_S) = \frac{dV_p(\rho_S)}{d\rho_S}, \tag{2.35}$$

where ρ_S is the scalar density and V_p is the potential energy density (derived from the energy momentum tensor). Thus, the propagation of a particle j in the system is ruled by the force $F_j = (M_j/E_j)\nabla U_S(x)$.
Recently, the DQPM has been extended to include a dependence of the self-energy on the 3-momentum. This extension of the model, denoted as DQPM* [85, 86], has improved the description of the susceptibilities in line with the lQCD results.

2.3 Description of heavy-ion collisions in PHSD

The Parton-Hadron-String Dynamics is a microscopic covariant dynamical approach developed on the basis of the Kadanoff-Baym equations for the Green functions (see Section 2.1) in phase-space representation in first-order gradient expansion [70, 79, 80]. PHSD has been conceived to describe strongly interacting systems both in- and out-of equilibrium [7, 78]. Therefore, it represents a powerful framework for the description of heavy-ion collisions. In particular, PHSD is capable of describing the full time evolution of these processes, since it includes both hadronic and partonic phases as well as a transition between the associated degrees of freedom. The DQPM (see Section 2.2) is adopted as theoretical model for the partonic degrees of freedom (quarks and gluons) [79, 80]. Here, we focus on how a heavy-ion collision is described within PHSD, analyzing the different stages of the collision process.
The transport calculation is performed on a discretized space-time grid ($\Delta t, \Delta x, \Delta y, \Delta z$), where z correspond to the beam axis and x and y correspond to the transverse directions. The grid sizes Δx and Δy are fixed to 1 fm during the whole simulation. Instead both Δz and $\Delta t = \Delta z/2$ change dynamically in order to optimize the simulation. Initially, they are small ($\Delta z = 1/\gamma$ where γ is the Lorentz factor of the collision), then they increase during the late expansion phase. The numerical realization is also done according to the parallel ensemble method: one single simulation develops as N independent nuclear reactions calculated in parallel. This is extremely important to achieve a reliable evaluation of the spectral properties of the degrees of freedom. The hadrons included in PHSD are the baryonic spin $1/2$ and $3/2$ particles with the corresponding antiparticles and the pseudoscalar 0^- and vector 1^- $SU(4)$ meson states and additionally the axialvector 1^+ a_1 meson.
A nucleus-nucleus collision in PHSD develops as initial hard scattering, followed (depending

on the energy density) by a partonic phase with subsequent hadronization and finally by a hadronic re-scattering phase. These steps are explained in the following.

1. The system is initialized to reproduce two nuclei boosted with bombarding energy E_{Lab} towards each other along the z axis. The test particles of the simulation correspond to the nucleons contained in the colliding nuclei and their distribution in space follows a Woods-Saxon profile:
$$\rho(r) = \frac{\rho_0}{1 + \exp(\frac{r-R}{a})}, \tag{2.36}$$
where r is the radial distance from the center of the nucleus, $R = 1.124\,A^{1/3}$ fm is the nuclear radius (A is the mass number of the nucleus), $a = 0.13$ fm is the surface thickness of the nucleus and $\rho_0 = 0.166\,\text{fm}^{-3}$ is the saturation density of the nuclear matter. The initial configuration in momentum space is fixed according to the Thomas-Fermi approximation, where the phase space density is given by:
$$N(\vec{r}, \vec{p}) \sim \Theta(p_F(\vec{r}) - |\vec{p}|), \tag{2.37}$$
where p_F is the local Fermi momentum. The two nuclei travel against each other with velocity β, fixed by E_{Lab}. The test particles interact in the time step Δt if the impact parameter b satisfies the following relation according to the collision criteria provided in Ref. [87]:
$$b \leq b_{max} = \sqrt{\frac{\sigma_{geom}}{\pi}} \tag{2.38}$$
with σ_{geom} referring to the maximal cross-section, estimated as geometrical cross-section. If particles reach a minimal distance needed to interact, the reaction channel i is chosen via the Monte-Carlo method with a probability $P_i = \sigma_i/\sigma_{geom}$.

2. Primary hard scatterings between nucleons take place and produce excited color-singlet states, denoted by "strings", as described within the FRITIOF Lund model [72, 73] (PYTHIA 6.4 [71] and JETSET 7.3 [74] are incorporated for the production and fragmentation of jets).
A string is composed of two string ends corresponding to the leading constituent quarks of the colliding hadrons and a color flux tube in between. As the string ends recede, virtual $q\bar{q}$ or $qq\bar{q}\bar{q}$ pairs are produced in the uniform color field, causing the breaking of the string. These strings decay into "leading hadrons" and "prehadrons", the latter with a formation time[2] $\tau_f \sim 0.8$ fm/c in the rest-frame of the string. The leading hadrons can re-interact with hadrons almost instantly with reduced cross-sections (according to the

[2]The formation time τ_f is interpreted as the time needed for a hadron to tunnel out of the vacuum and form its own wavefunction.

constituent quark number).

In the string decay, the flavor of the produced quarks is determined via the Schwinger formula [71, 88], which defines the production probability of massive $s\bar{s}$ pairs with respect to light flavor $u\bar{u}, d\bar{d}$ pairs:

$$\frac{P(s\bar{s})}{P(u\bar{u})} = \frac{P(s\bar{s})}{P(d\bar{d})} = \gamma_s = \exp\Big(-\pi\frac{m_s^2 - m_{u,d}^2}{2\kappa}\Big), \tag{2.39}$$

with $\kappa \approx 0.176\,\mathrm{GeV}^2$ representing the string tension and $m_{u,d,s}$ denoting the constituent quark masses for light and strange quarks. If in Eq. 2.39 we employ the constituent quark masses in the vacuum ($m_u \approx 0.35\,\mathrm{GeV}$ and $m_s \approx 0.5\,\mathrm{GeV}$), the production of strange quarks is suppressed by a factor of $\gamma_s \approx 0.3$ with respect to the light quarks. The value $\gamma_s = 0.3$ is the default setting in the FRITIOF routines. The relative production factors in PHSD/HSD have been re-adjusted in 1998 as follows [89]:

$$u : d : s : uu = \begin{cases} 1 : 1 : 0.3 : 0.07 & \text{at SPS to RHIC energies;} \\ 1 : 1 : 0.4 : 0.07 & \text{at AGS energies.} \end{cases} \tag{2.40}$$

The fraction of energy and momentum that the newly produced hadrons acquire at the string decay is defined by the fragmentation function $f(x, m_T)$, which is the probability distribution for a hadron with transverse mass m_T to be produced with an energy-momentum fraction x from the fragmenting string:

$$f(x, m_T) \approx \frac{1}{x}(1 - x^a)\exp(-b\,m_T^2/x)\,, \tag{2.41}$$

where $a = 0.23$ and $b = 0.34\,\mathrm{GeV}^{-2}$ are reliable settings for p+p and p+A collisions [89].

3. In case the local energy density is above the critical value of $\varepsilon_c \sim 0.5\,\mathrm{GeV/fm}^3$, the deconfinement is implemented by dissolving the newly produced hadrons into the massive colored quarks/antiquarks and mean-field energy. The partons are described as off-shell quasi-particles and the DQPM provides their spectral properties, *i.e.* masses and widths as a function of ε. Within the QGP phase, the partons strongly interact (only at high scalar density partons are expected to weakly interact [7]) and propagate in a self-generated mean-field potential. The parton-parton interactions are modeled using the cross-section computed in DQPM (with detailed balance) and they can be distinguished in (quasi-)elastic and inelastic interactions.

   The (quasi-)elastic reactions included in PHSD are:

$$\begin{aligned} &q + q \to q + q, && q + \overline{q} \to q + \overline{q}, && \overline{q} + \overline{q} \to \overline{q} + \overline{q}, \\ &g + g \to g + g, && g + q \to g + q, && g + \overline{q} \to g + \overline{q}, \end{aligned} \tag{2.42}$$

where q, $\overline{q}$, g denote quark, antiquark and gluon, respectively.
The inelastic reactions included in PHSD are:

$$\begin{aligned} q + \overline{q} &\leftrightarrow g, & g &\leftrightarrow q + \overline{q}, \\ q + \overline{q} &\leftrightarrow g + g, & g &\leftrightarrow g + g, \end{aligned} \tag{2.43}$$

where the channels with two gluons in the final state are suppressed due to the large mass of the gluons. Because of this reason, the partonic reactions $g \rightarrow g+g$ and $q+\overline{q} \rightarrow g+g$ are neglected in this work. We specify that the channel $q+\overline{q} \rightarrow g$ is described by a Breit-Wigner cross-section [7] and the corresponding backward reaction, *i.e.* the gluon decay, $g \rightarrow q + \overline{q}$, is characterized by a small suppression of the production of $s + \overline{s}$ compared to the light quark production due to the larger mass of the s quark (see Section 2.2).

4. The expansion of the system is associated to a decrease of the local energy density and, once the local energy density drops below ε_c, the massive colored off-shell quarks and antiquarks hadronize to colorless off-shell mesons and baryons. The hadronization process is defined by covariant transition rates for the fusion of quark-antiquark pairs to mesonic states and three (anti)quarks to (anti)baryonic states. For example, the rate for the quark-antiquark fusion to a meson m with four-momentum $p = (\omega, \mathbf{p})$ at the space-time point $x = (t, \mathbf{x})$ is expressed by:

$$\begin{aligned} \frac{dN_m(x,p)}{d^4x d^4p} =& Tr_q Tr_{\overline{q}}\, \delta^4(p - p_q - p_{\overline{q}})\, \delta^4\left(\frac{x_q + x_{\overline{q}}}{2} - x\right) \omega_q \rho_q(p_q)\, \omega_{\overline{q}} \rho_{\overline{q}}(p_{\overline{q}})\, |v_{q\overline{q}}|^2 \\ & \times W_m\left(x_q - x_{\overline{q}}, \frac{p_q - p_{\overline{q}}}{2}\right) N_q(x_q, p_q)\, N_{\overline{q}}(x_{\overline{q}}, p_{\overline{q}})\, \delta(\text{flavor, color}), \end{aligned} \tag{2.44}$$

where $N_{q,\overline{q}}(x,p)$ is the phase-space density of the (anti)quark at the position x and momentum p, $v_{q\overline{q}}(\rho_p)$ is the effective $q-\overline{q}$ interaction obtained within the DQPM as a function of the local parton (including quarks, antiquarks and gluons) density ρ_p (or energy density) and $W_m(x,p)$ is the dimensionless phase-space distribution of the formed prehadron. In Eq. 2.44, Tr_j is a short-hand operator notation which includes a summation over the discrete quantum numbers (spin, flavor, color) and the spatial and momentum integrations:

$$Tr_j = \sum_j \int d^4x_j \int \frac{d^4p_j}{(2\pi)^4}. \tag{2.45}$$

Moreover, the distribution $W_m(x,p)$ is given by:

$$W_m(\xi, p_\xi) = \exp\left(\frac{\xi^2}{2b^2}\right) \exp\left[2b^2\left(p_\xi^2 - \frac{(M_q - M_{\overline{q}})^2}{4}\right)\right], \tag{2.46}$$

where ξ and p_ξ are the relative quark and antiquark position and momentum, respectively, $\xi = x_q - x_{\overline{q}}$ and $p_\xi = (p_q - p_{\overline{q}})/2$ and b is the width parameter corresponding to the average radius of the meson defined as $b = \sqrt{\langle r^2 \rangle} = 0.66\,\text{fm}$ (in the rest frame of the meson).

The transition rate given in Eq. 2.44 and the phase space distribution in Eq. 2.46 can be easily extended to describe the fusion of three (anti)quarks to a color neutral (anti)baryonic state [7].

We stress that in Eq. 2.44 the presence of the δ(flavor, color) ensures the conservation of the flavor and color quantum numbers. In particular, regarding the color quantum number, the produced hadron is color neutral, but it can be seen as a color dipole as created from a colored $q - \overline{q}$ pair. Moreover, the four-momentum is conserved in each event, thanks to the off-shell nature of both partonic and hadronic degrees of freedom, and the total entropy increases. Once the hadronization occurs, the inverse reaction, *i.e.* the dissolution of hadrons into partons, is suppressed at low energy density by the large masses of the partons according to the DQPM. Furthermore, at low energy density ($\varepsilon < \varepsilon_c$) the hadronization rates are large, due to large values of the associated transition matrix elements. These features drive the system to a pure hadronic phase during the expansion.

5. In the hadronic corona as well as in the late hadronic phase, the particles propagate and interact both elastically and inelastically. The cross-sections for the collisions between baryons, mesons and resonances implemented in PHSD are taken from experimental measurements [90] or based on effective theories when experimental observations are not available (for example in Appendix B we introduce an effective hadronic model to derive the cross-sections for the hyperon-hyperon scattering). The backward reactions are included through detailed balance for all channels. The type of interactions present currently in PHSD are: 2-particle interaction ($2 \leftrightarrow 2$), resonance formation and decay ($1 \leftrightarrow 2$) and 3-to-2 particle interaction between mesons and baryon-antibaryon pair ($3M \leftrightarrow B\overline{B}$). The last type of interaction has been recently extended to the strange sector [44], but no crucial impact has been found in heavy-ion observables at AGS and SPS energies.

PHSD gives the possibility to track the dynamics of the particles and to identify the contribution of the different production mechanisms to the final observables. For example, we are able to disentangle the role played by the QGP phase through the comparison of the PHSD calculations with and without the partonic phase in the system evolution. In fact, in PHSD it is possible to exclude the creation of a QGP from the simulation and, in particular, the pure hadronic phase in PHSD is equivalent to the Hadron-String Dynamics (HSD) model [91].

The PHSD approach can be used to study different colliding systems (p+p, p+A, A+A) in a wide range of bombarding energy (from SIS up to LHC energies) and has provided a good description of a large number of experimental observables, such as charged particle spectra, collective flow coefficients and electromagnetic probes [81]. In the next Section we apply PHSD in the intermediate energy regime and study how the particle dynamics develops.

2.4 PHSD at intermediate energies

In this Section, we provide some plots which illustrate the types of interactions and mechanisms occurring within PHSD in HIC at intermediate energies ($\sqrt{s_{NN}} = 3 - 20$ GeV corresponding to the AGS and SPS regimes). This allows us to better interpret the results which will be reported in the following Chapters 3-6.

Firstly, we quantify the contribution from the QGP phase to the evolution of the system in a heavy-ion collision. This is investigated in terms of the fraction of the partonic energy density ε_p with respect to the total energy density ε_t. The partonic energy density ε_p includes both the energy associated to the partonic degrees of freedom (quarks, antiquarks and gluons) and the mean-field energy. We display on the l.h.s. of Fig. 2.3 the ratio $\varepsilon_p/\varepsilon_t$ as a function of the time rescaled according to the collision time t_{coll} in Pb+Pb collisions at 30 AGeV with different impact parameters ranging from b =1 fm to b =13 fm. The partonic energy fraction sharply increases as a function of time from $t - t_{coll} = 0$ fm/c up to $t - t_{coll} \approx 3.5$ fm/c, then it smoothly drops and vanishes at $t - t_{coll} \approx 10$ fm/c. This behavior (as a function of time) is basically independent on the impact parameter, apart from the very peripheral b =13 fm. The ratio $\varepsilon_p/\varepsilon_t$ for the most peripheral collision ($b = 13$ fm) is almost zero in the whole time interval. The more central collisions are characterized by larger contributions of the partonic phase. In fact, for smaller b the peak of the ratio $\varepsilon_p/\varepsilon_t$ is larger and the time interval in which ε_p is finite is wider. Moreover, the $\varepsilon_p/\varepsilon_t$ curves for $b < 5$ fm follow for $t - t_{coll} < 2$ fm/c the same steep rise and the associated peaks are at the same time. From this analysis, it is clear that partonic degrees of freedom appear in the system at $E_{Lab} = 30$ AGeV in a wide range of centrality (1 fm $\leq b \leq$ 10 fm) and they provide a finite contribution to the energy density of the system. The maximum contribution is associated to the most central collision and it is $\approx 22\%$ of the total energy density.

On the r.h.s. of Fig. 2.3, we study the time evolution of the partonic energy fraction $\varepsilon_p/\varepsilon_t$ in central Pb+Pb collisions ($b = 1$ fm) at different collision energies in the AGS and SPS regimes: $E_{Lab} = 6, 10.7, 30, 60, 100, 158$ AGeV. We observe that a QGP phase is created in the system in all cases investigated here and the time dependence is analogous to that described above for the l.h.s. of Fig. 2.3. At 6 AGeV the energy density carried by the partonic degrees

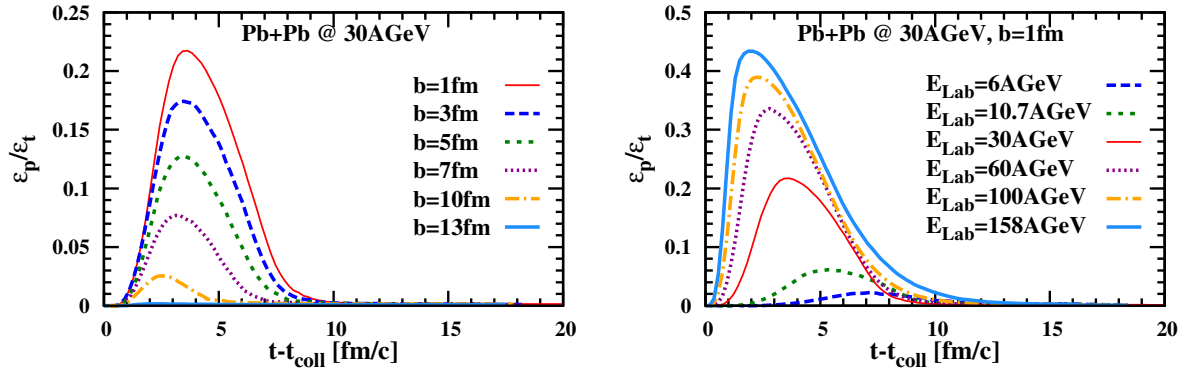

Figure 2.3: The ratio of the partonic energy density ε_p to the total energy density ε_t as a function of the time re-scaled according to the collision time t_{coll} in Pb+Pb collisions at 30 AGeV with different impact parameters on the l.h.s. and in Pb+Pb collisions with impact parameter $b = 1$ fm for different collision energies on the r.h.s..

of freedom is small (the maximum value for the ratio is $\varepsilon_p/\varepsilon_t \approx 2\%$), but not negligible. At this small collision energy the deconfinement phase transition occurs within small droplets in the central cells of the system, where the energy density is large. We identify some features of the ratio $\varepsilon_p/\varepsilon_t$ in correlation with the increase of E_{Lab}:

- the maximum value of $\varepsilon_p/\varepsilon_t$ becomes higher, as a larger volume of the system is reached by the deconfinement phase transition;
- the peak of $\varepsilon_p/\varepsilon_t$ shifts to smaller times and the rise of $\varepsilon_p/\varepsilon_t$ as a function of $t - t_{coll}$ becomes steeper;
- the final hadronization and disappearance of the partonic phase occurs at later times.

We conclude that, within PHSD, the QGP is created at intermediate energies, with a maximum value for the ratio $\varepsilon_p/\varepsilon_t$ of about 42% at the top SPS energies ($E_{Lab} = 158$ AGeV). If we increase even more the collision energy, the partonic contribution to the total energy density becomes larger than the hadronic one. For example, at top RHIC energies the QGP phase at midrapidity contains $\approx 90\%$ of the energy density.

Secondly, we study the behavior of the yields of the most abundant particles as a function of time. We display the number of hadrons in panels (a) and (c) and the number of partons in panel (b) of Fig. 2.4, produced in Pb+Pb collisions at 30 AGeV with impact parameter $b = 1$ fm. Initially, the system is only composed of nucleons, protons and neutrons, from the two colliding nuclei. At about $t \approx 1.5$ fm/c, the two nuclei collide and mesons, strange baryons and partons are created. The number of pions, kaons, $(\Lambda + \Sigma^0)$'s and partons rise

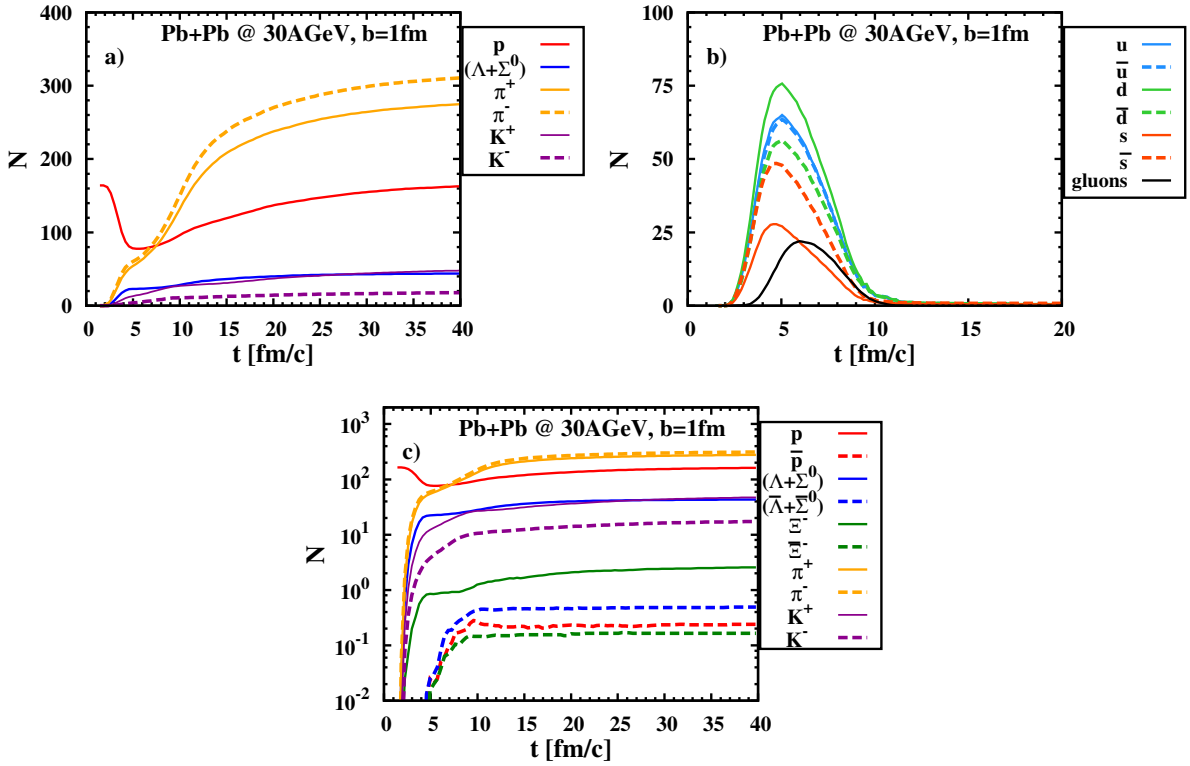

Figure 2.4: The number of the most abundant particles (hadrons in panels (a), (c) and partons in panel (b)) as a function of time in Pb+Pb collisions at 30 AGeV with impact parameter $b = 1$ fm.

steeply within 3 fm/c after the collision. The number of all hadronic particles, apart from the nucleons, increases with increasing time. On the other hand, the number of partons increases up to $t \approx 4$ fm/c for quarks and $t \approx 6$ fm/c for gluons. Then, the abundances of partonic degrees of freedom drop, as the hadronization occurs. The hadronization lasts up to $t \approx 10$ fm/c. We observe that the number of strange quarks, which are not initially present in the system, is smaller than the number of light quarks, both u and d. The panel (c) of Fig. 2.4 shows in addition to baryons also antibaryons ($\overline{p}$, $(\overline{\Lambda} + \overline{\Sigma}^0)$ and $\overline{\Xi}^-$), which appear in the system later than the other particles at $t \geq 5$ fm/c. In fact, differently from mesons, which are produced at the early stages from the string decays, the antibaryons are mainly produced in the hadronization of partons. This emerges also by the fact that the number of $\overline{p}$, $(\overline{\Lambda} + \overline{\Sigma}^0)$ and $\overline{\Xi}^-$ increases up to $t \approx 10$ fm/c, when the hadronization ceases, and then it remains constant. We observe that the $(\Lambda + \Sigma^0)$ particles are produced almost entirely within the time interval 1.5 fm/c $\leq t \leq 4$ fm/c, while the production of mesons lasts longer. In fact, even if the majority of mesons is produced at the early stages ($t < 5$ fm/c), the number of pions and kaons increases also at later times due to the hadronization process, to the hadronic re-scattering and to the resonance decays. The

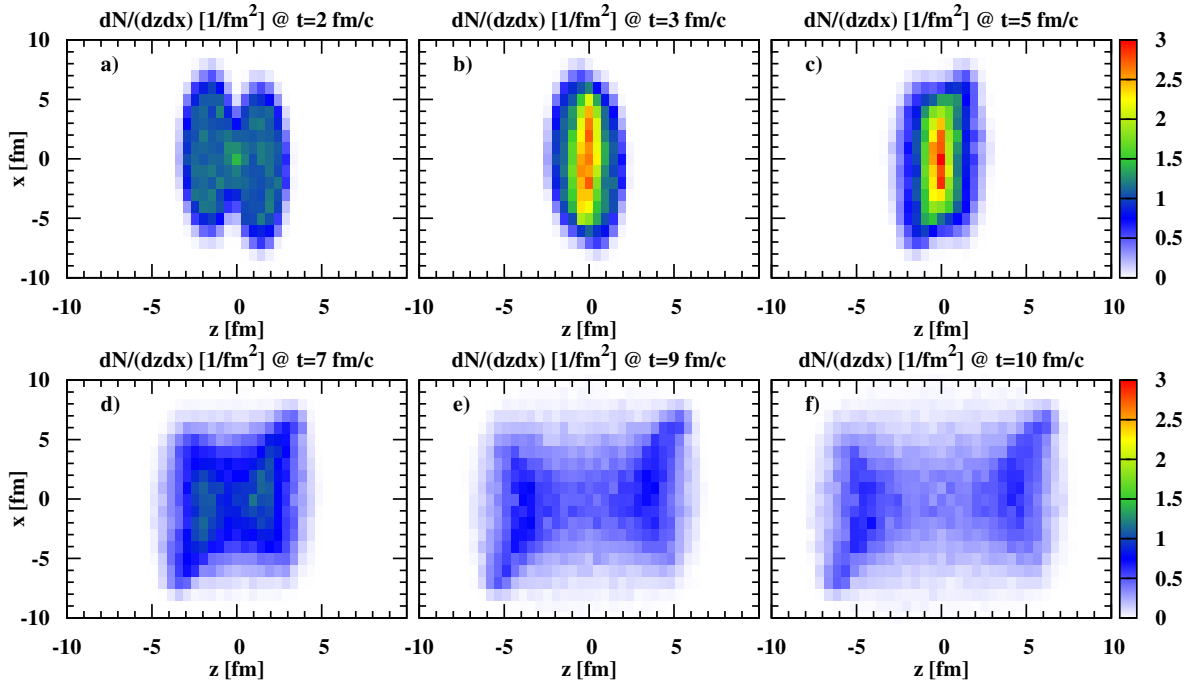

Figure 2.5: The distribution $dN/(dxdz)$ of baryons as a function of x and z (for $y = 0$) at different times t for a central ($b = 1$ fm) Pb+Pb collision at 30 AGeV.

most abundant particles produced in central Pb+Pb collisions at 30 AGeV are pions. There is a small difference between the number of charged pions: the abundance of π^- is larger than the abundance of π^+ by a factor of ≈ 1.1. On the other hand, the difference between the charged kaons is larger: the K^+ are more abundant than the K^- by a factor of ≈ 2. The yield of antibaryons and multi-strange baryons is extremely small. Their final abundances are $N_{\Xi^-} \approx 2.6$, $N_{\overline{p}} \approx 0.24$, $N_{(\overline{\Lambda}+\overline{\Sigma}^0)} \approx 0.49$ and $N_{\overline{\Xi}^-} \approx 0.17$, which are one and two orders of magnitude lower than the K^- yield ($N_{K^-} \approx 17$).

Thirdly, we explore the space distribution of the particle species during the collision process. In Figs. 2.5, 2.6 and 2.7 we show the distribution $dN/(dxdz)$ of baryons, mesons and partons, respectively, in a central ($b = 1$ fm) Pb+Pb collision at 30 AGeV for $y = 0$. The panels (a)-(f) refer to different times ranging from 2 fm/c to 10 fm/c, which are later than the collision time $t_{coll} = 1.55$ fm/c. The reference frame is fixed as follows: the $z-$axis corresponds to the beam axis, the $x-$axis corresponds to the transverse direction in the reaction plane (along which the impact parameter is established), the $y-$axis corresponds to the direction perpendicular to the reaction plane. In panel (a) of Fig. 2.5 it is possible to identify the two colliding nuclei at the early stage of the collisions. In fact, they overlap in a small area at $|z| \approx 0.5$ fm. In panel (b), we observe the system during the stage of maximum compression, when the highest energy densities are achieved. As |z| and $|x|$ decrease, the distribution of baryons increases.

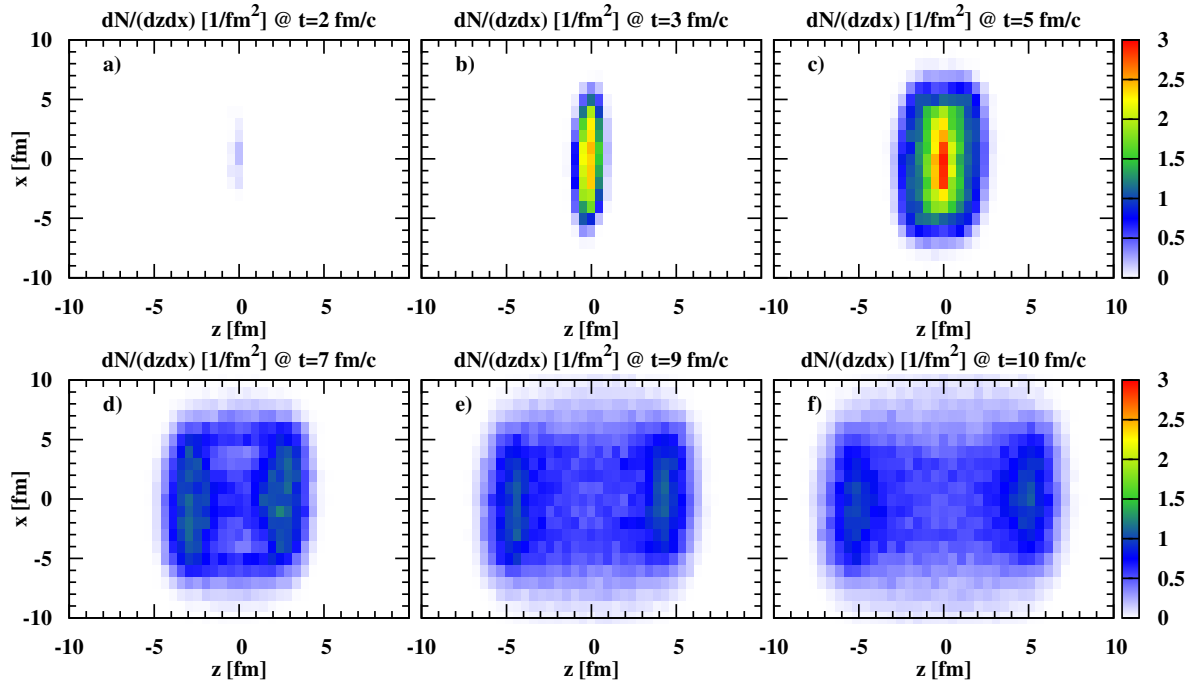

Figure 2.6: The distribution $dN/(dxdz)$ of mesons as a function of x and z (for $y = 0$) at different times t for a central ($b = 1$ fm) Pb+Pb collision at 30 AGeV.

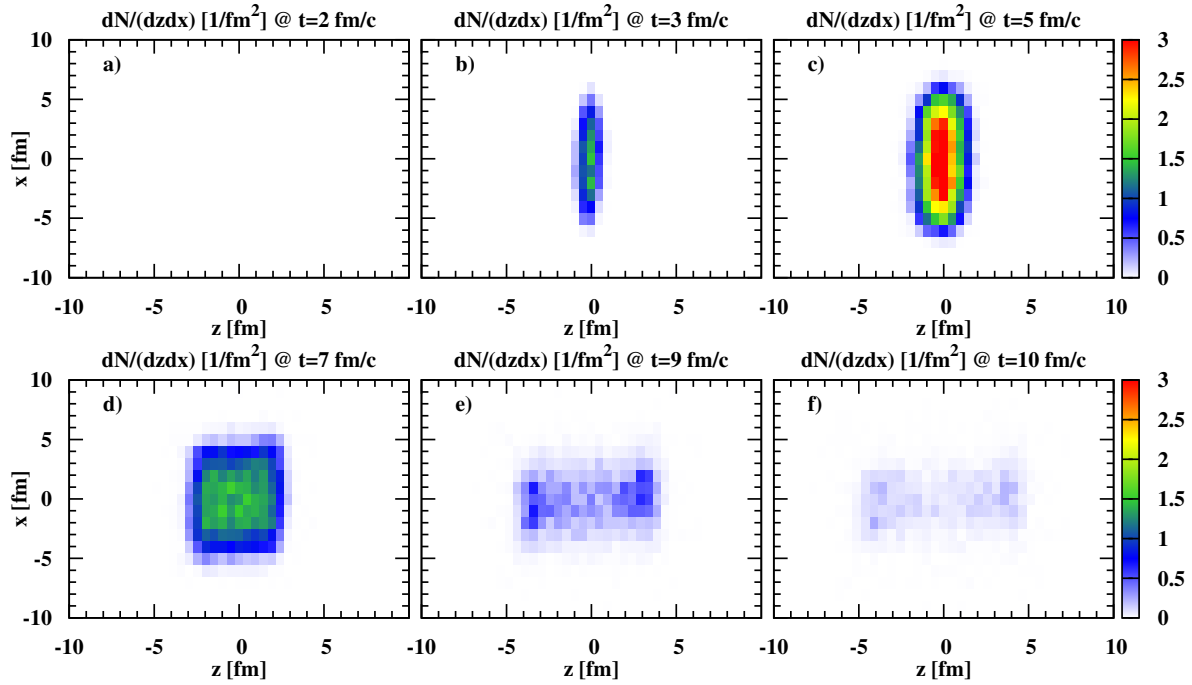

Figure 2.7: The distribution $dN/(dxdz)$ of partons as a function of x and z (for $y = 0$) at different times t for a central ($b = 1$ fm) Pb+Pb collision at 30 AGeV.

This is even more pronounced at $t = 5$ fm/c (panel (c)) where the central cells of the system achieve the largest the baryon densities. During the expansion of the system (panels (d)-(f)), the baryon distribution in the central cells drops. This is not due to a decrease of the number of baryons, but to their spread in a larger volume: at $t = 3$ fm/c the baryons are located in an area with $|z| < 3$ fm and $|x| < 8$ fm, while at $t = 7$ fm/c they are located in an area with $|z| < 5$ fm and $|x| < 8$ fm. It is also possible to track the fragments of the two colliding nuclei that survive the collision. These are represented by the dark blue areas in panels (e) and (f) of Fig. 2.5. Instead, the light blue area in the central part of the $x - z$ plane corresponds to the newly produced baryons.

In Fig. 2.6 we follow the time evolution of the mesons, which appear in the system immediately after the first hard scatterings. In fact, already at $t = 2$ fm/c (panel (a)) the most central cells of the system contain a small number of mesons. While the two colliding nuclei pass through each other (panels (b) and (c)), the distribution $dN/(dxdz)$ of mesons become appreciable, reaching larger values in the most central cells (where the production of mesons is enhanced), and rapidly spreads in a larger volume of the system. In particular at $t = 5$ fm/c, the meson distribution occupies an area comparable to the one of the baryons. After the passage time[3], we observe that $dN/(dxdz)$ of mesons is lager in the area of the system corresponding to the nuclear fragments. This is due to the fact that the baryon density is high and the heavy resonances present in these cells predominantly decay producing mesons. As the system expands ($t \geq 7$ fm/c), the meson density in the most central cells decreases and the mesonic particles occupy a larger and larger volume of the system. Moreover, for the most central part of the system ($|z| < 5$ fm and $|x| < 5$ fm) the distribution of mesons appears to be homogeneous along the transverse direction x and achieve larger values with respect to the distribution of baryons.

In Fig. 2.7 the parton distribution is displayed and it exhibits a time evolution different with respect to both baryons and mesons. The partonic particles are not created immediately after the first nucleon interactions, as it is evident in panel (a), where $dN/(dxdz)$ is zero in all cells. Between $t = 3$ fm/c and $t = 5$ fm/c (panels (b) and (c)), the whole production of partonic degrees of freedom occurs (as discussed above for Fig. 2.4) and the associated $dN/(dxdz)$ increases in the central cells of the system. We observe that $dN/(dxdz)$ achieves the largest values of $3\,\text{fm}^{-2}$ in an area of the system with $|z| \approx 0.5$ fm and $|x| \leq 4$ fm, which is more extended than that for the baryon and meson cases, where the area occupied by the peaks of the distribution is smaller. On the other hand, the total area occupied by partons is smaller compared to baryons and mesons. In particular, it is narrower by about 1fm along the z direction. At the later stages

[3]The nuclear passage time can be estimated in the center-of-mass frame of the collision as $t = d/(\beta\gamma)$, where d is the diameter of the nucleus at rest (we assume a symmetric collision) (panels (d)-(f)), β is the velocity of the nucleus in the center-of-mass frame of the collision and γ is the Lorentz factor of the center-of-mass frame with respect to the system in which one nucleus is at rest (e.g. in the laboratory frame for a fixed target experiment).

(panels (d)-(f)), the expansion of the system has the following effects on the distribution of partons:

- partons propagate in the system occupying more external cells;
- the energy density drops and consequently the hadronization occurs decreasing the average value of $dN/(dxdz)$;
- the region occupied by partons decreases rapidly along the transverse direction x.

At $t = 10$ fm/c (panel (f)) only few cells contain partons, which completely hadronize shortly after.

Finally, we investigate the collision rate dN/dt of Baryon-Baryon (B-B), meson-Baryon (m-B) and meson-meson (m-m) scatterings as a function of time and we study the energy distribution $dN/d\sqrt{s_b}$ as a function of the center-of-mass energy of the colliding particles $\sqrt{s_b}$. This analysis is done to understand which type of reactions dominates in a HIC and to figure out the features of the interactions. On the l.h.s. of Fig. 2.8, we show the rate dN/dt as a function of the time re-scaled according to the collision time t_{coll} in central Pb+Pb collisions ($b = 1$ fm) at $E_{Lab} = 8, 30, 158$ AGeV in panels (a), (b), (c), respectively. A common trend is identified among the energies investigated. At the early stage, the dominant type of collision is the B-B scattering (solid green lines). In particular, each line referring to the B-B interaction shows a pronounced peak, which becomes larger and shifts to smaller times with increasing E_{Lab}. This is explained by the fact that the passage time shortens as the collision energy increases. We specify that the B-B scatterings at the early stage are essentially string interactions. After the passage time, the B-B collision rate rapidly drops: the number of string interactions vanishes, while the number of low-energy reactions remains finite for later times (see Fig. 3.2 and the related discussion for additional details).

The rate of the m-B reactions (dashed red lines) shares some similarities with the one associated to the B-B reactions. At small values of $t - t_{coll}$, dN/dt increases with increasing time reaching a peak (associated to the string interactions) that for $E_{Lab} = 8$ AGeV and $E_{Lab} = 30$ AGeV is at the same time as for the B-B rate. At later times, it decreases during the nuclear passage time and after it rises again exhibiting a second peak, during the hadronic re-scattering. Similarly to the first peak, the second peak shifts to smaller time as the collision energy increases, due to the fact that all the collision processes become faster for larger E_{Lab}. Finally, at late times, the m-B rate drops. At the early stage, dN/dt associated to m-B scatterings is lower than the rate of B-B, while after the passage time it is larger. For example, in case of 158AGeV the m-B rate is larger by about one order of magnitude with respect to the B-B rate for $t > 5$ fm/c. In fact, during the hadronic re-scattering, the system created in heavy-ion

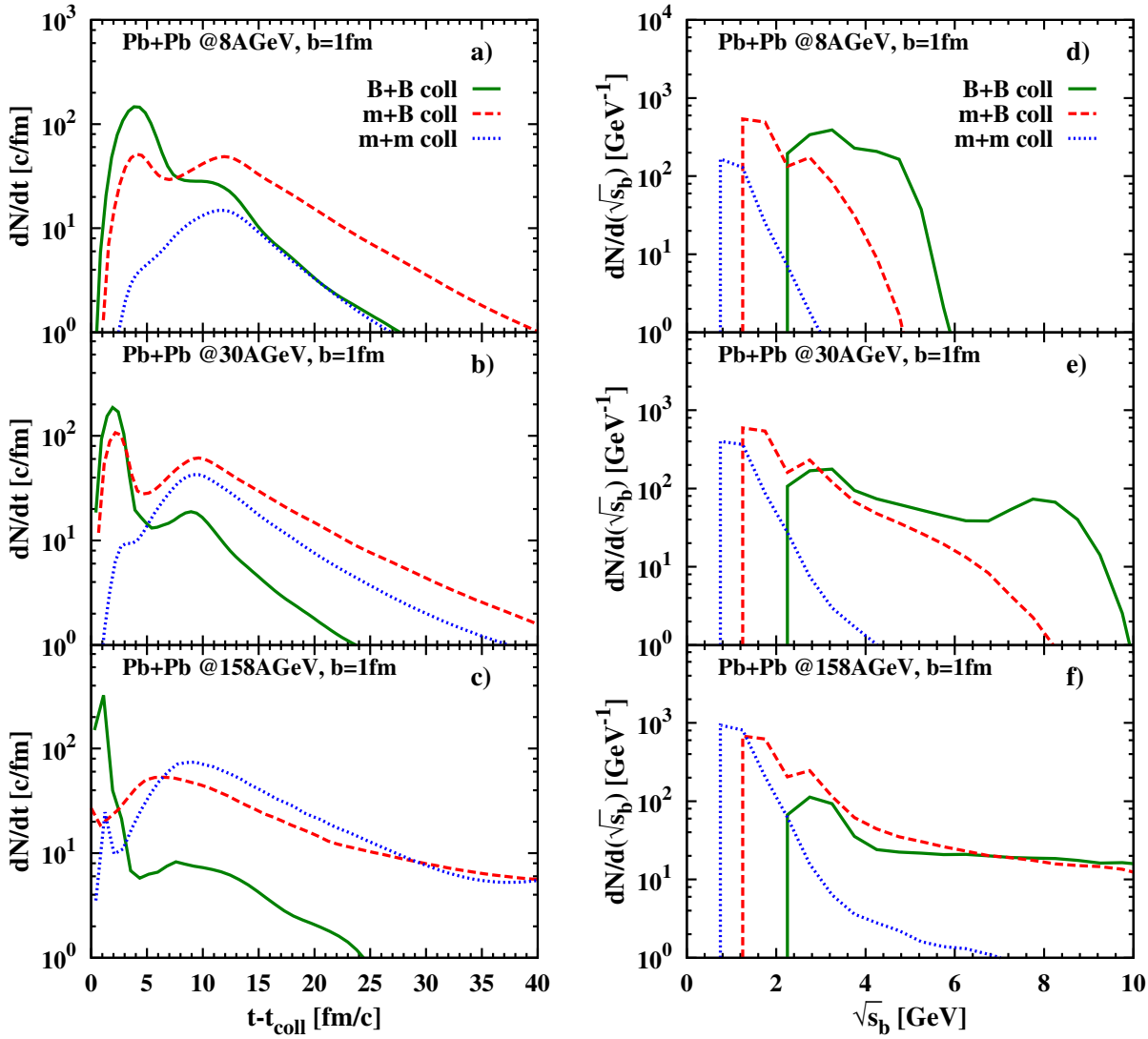

Figure 2.8: (l.h.s.) The collision rate dN/dt as a function of the time re-scaled according to the collision time t_{coll} in Pb+Pb collisions with impact parameter $b = 1$ fm at different collision energies $E_{Lab} = 8, 30, 158$ AGeV in panels (a), (b), (c), respectively. (r.h.s.) The energy distribution $dN/d\sqrt{s_b}$ of the binary scatterings as a function of the center-of-mass energy of the colliding particles $\sqrt{s_b}$. The solid green lines refer to baryon-baryon scatterings, the dashed red lines refer to meson-baryon scatterings and the dotted blue lines refer to the meson-meson scattering.

collisions is characterized by a large multiplicity of mesons and the number of m-B and m-m interactions overshoots the number of B-B interactions. This is more evident at the large collision energy ($E_{Lab} = 158$ AGeV), since the production of mesonic particles is enhanced. For this reason, the rate associated to the m-m reactions (dotted blue lines) increases with E_{Lab}.

Concerning the time evolution of the m-m rate, we observe for $E_{Lab} = 8, 30$ AGeV that dN/dt shows only one peak in the stage of the hadronic re-scattering (essentially in correspondence to the second peak of the m-B rate), while for $E_{Lab} = 158$ AGeV it shows two peaks. In the latter case, the first peak is at the same time of the peak of the B-B rate and the second peak is shortly after the m-B second peak. In general, the rate of m-m collisions rises with time for $t < 10$ fm/c and it smoothly decreases with t for larger times.
On the r.h.s. of Fig. 2.8, we show the distribution $dN/d\sqrt{s_b}$ as a function of $\sqrt{s_b}$ in central Pb+Pb collisions ($b = 1$ fm) at $E_{Lab} = 8$ AGeV and $E_{Lab} = 30$ AGeV in panels (d), (e), (f), respectively. This analysis is performed to understand in which ranges of energy the different interactions are dominant. The three types of interactions acquire a non-vanishing value for $dN/d\sqrt{s_b}$ in the following order: first the m-m reactions at $\sqrt{s_b} \approx 0.8$ GeV, second the m-B reactions at $\sqrt{s_b} \approx 1.2$ GeV and third the B-B reactions at $\sqrt{s_b} \approx 2.2$ GeV. Moreover, we observe the following features:

- the m-m reactions are dominant at low values of $\sqrt{s_b}$;
- the m-B reactions are dominant at intermediate values of $\sqrt{s_b}$;
- the B-B reactions are dominant at larger values of $\sqrt{s_b}$.

These hierarchies are common to all collision energies investigated. Increasing E_{Lab}, the ranges of energy in which the B-B, m-B and m-m scattering are effective become wider. In panel (f), we notice that, due to the high meson multiplicity, the energy distribution associated to the B-B interactions at $E_{Lab} = 158$ AGeV gets larger than the m-B distribution only at large values of $\sqrt{s_b}$ ($\sqrt{s_b} > 8$ GeV).

2.5 Chiral symmetry restoration

The main goal of HIC is the study of the QCD phase diagram, as discussed in Chapter 1, where the properties of the deconfinement phase transition and of chiral symmetry restoration (CSR) are not well known. In this work, our focus is the investigation of CSR, that at vanishing baryon chemical potential is predicted from lQCD to occur as a crossover at about the same critical temperature and energy density of the deconfinement. At finite baryon chemical potential one must rely on effective or functional models, since lQCD calculations cannot be performed due to the fermion sign problem. Different models support the idea that at finite chemical potential a partially chirally restored phase is achieved before the deconfinement occurs [28, 30, 31]. In order to distinguish the two phases of this transition, effective models use the scalar quark condensate $\langle \bar{q}q \rangle$ as an order parameter. As the baryon density and

temperature increase, the scalar quark condensate $\langle\bar{q}q\rangle$ is expected, according to the Hellman-Feynman theorem [92], to decrease from a non-vanishing value in the vacuum to $\langle\bar{q}q\rangle \approx 0$ which corresponds to CSR [93, 94]. This decrease of the scalar quark condensate is expected also to lead to a change of the hadron properties with density and temperature. This means that, for example, in a chirally restored phase the vector and axial vector currents should become equal [95, 96, 97, 98, 99, 100] and, consequently, the ρ and a_1 spectral functions should become identical. On this issue, a final evidence is, however, lacking [101].
Our aim is to include in our transport approach the CSR, as a mechanism that generates a modification of the masses of the quarks according to their coupling with the $\langle\bar{q}q\rangle$ condensate (see Appendix A for details). In the following Sections, we describe how essential aspects of CSR have been incorporated in PHSD and what are the uncertainties in our approach.

2.5.1 Modeling of the chiral symmetry restoration

Here we describe how PHSD has been extended to include CSR in the string decay in a hadronic environment of finite baryon and meson density. The material in this Section has been published in Refs. [44, 82].
In leading order the scalar quark condensate $\langle\bar{q}q\rangle$ can be evaluated in a dynamical calculation as follows [102]:

$$\frac{\langle\bar{q}q\rangle}{\langle\bar{q}q\rangle_V} = 1 - \frac{\Sigma_\pi}{f_\pi^2 m_\pi^2}\rho_S - \sum_h \frac{\sigma_h \rho_S^h}{f_\pi^2 m_\pi^2}\,, \tag{2.47}$$

where σ_h stands for the σ-commutator of the relevant mesons h, $\langle\bar{q}q\rangle_V$ represents the vacuum condensate, $\Sigma_\pi \approx 45\,\mathrm{MeV}$ is the pion-nucleon Σ-term and f_π and m_π are the pion decay constant and pion mass, respectively. Note, however, that the value of Σ_π is not accurately known. A recent analysis points to a larger value of $\Sigma_\pi \approx 59$ MeV [103, 104], while lQCD results suggest a substantially lower value [105]. We have investigated the dependence of our results on the value of Σ_π ranging between $\Sigma_\pi \approx 30\,\mathrm{MeV}$ and $\Sigma_\pi \approx 60\,\mathrm{MeV}$ [106] and we have not found any remarkable sensitivity. Thus, $\Sigma_\pi = 45$ MeV has been chosen as default value in PHSD, since it represents a "world average" among the available calculations (cf. Fig. 3 in Ref. [106]). According to the light quark content, the Σ-term for hyperons is decreased by a factor of 2/3 for Λ and Σ hyperons and by a factor of 1/3 for Ξ baryons. Furthermore, for mesons composed of light quarks and antiquarks, we use $\sigma_h = m_\pi/2$, whereas for mesons with a strange (antistrange) quark we consider $\sigma_h = m_\pi/4$.
In Eq. A.1, the quantities ρ_S and ρ_S^h denote the nucleon scalar density and the scalar density for a meson of type h, respectively. The scalar density of mesons h is evaluated in the

independent-particle approximation as:

$$\rho_S^h(x) = \frac{(2s+1)(2\tau+1)}{(2\pi)^3} \int \mathrm{d}^3p \frac{m_h}{\sqrt{\mathbf{p}^2 + m_h^2}} f_h(x, \mathbf{p}) \,, \tag{2.48}$$

where $f_h(x, \mathbf{p})$ denotes the meson phase-space distribution ($x = (\mathbf{r}, t)$) and s, τ refer to the discrete spin and isospin quantum numbers, respectively.
The vacuum scalar condensate $\langle \bar{q}q \rangle_V = \langle \bar{u}u \rangle_V + \langle \bar{d}d \rangle_V \approx 2\langle \bar{u}u \rangle_V$ can be computed according to the Gell-Mann-Oakes-Renner (GMOR) relation [107, 108, 109],

$$f_\pi^2 m_\pi^2 = -\frac{1}{2}(m_u^0 + m_d^0)\langle \bar{q}q \rangle_V \,, \tag{2.49}$$

providing $\langle \bar{q}q \rangle_V \approx -3.2\,\mathrm{fm}^{-3}$ for the bare quark masses $m_u^0 = m_d^0 \approx 7\,\mathrm{MeV}$.
Finally, in Eq. A.1 the nucleon scalar density ρ_S has to be determined in a suitable model with interacting degrees of freedom. A proper (and widely used) approach is the non-linear $\sigma - \omega$ model for nuclear matter where ρ_S is defined as:

$$\rho_S(x) = \frac{d}{(2\pi)^3} \int \mathrm{d}^3p \frac{m_N^*}{\sqrt{\mathbf{p}_N^{*2} + m_N^{*2}}} f_N(x, \mathbf{p}) \,, \tag{2.50}$$

where m_N^* and p_N^* denote the effective mass and momentum, respectively, $f_N(x, \mathbf{p})$ is the phase-space occupation of the nucleon and the degeneracy factor is d=4.
In fact, in the non-linear $\sigma - \omega$ model the nucleon mass is modified by the scalar interaction with the medium:

$$m_N^*(x) = m_N^V - g_s\sigma(x) \,, \tag{2.51}$$

where m_N^V denotes the nucleon mass in vacuum and $\sigma(x)$ is the scalar field which mediates the interaction between the nucleons and the medium with the coupling g_s.
In order to calculate ρ_S, we need to determine the value of the scalar field $\sigma(x)$ at each space-time point x. This is done via the non-linear gap equation [109, 110]:

$$\begin{aligned} m_\sigma^2\sigma(x) + B\sigma^2(x) + C\sigma^3(x) &= g_s\rho_S(x) \\ &= g_s d \int \frac{\mathrm{d}^3p}{(2\pi)^3} \frac{m_N^*(x)}{\sqrt{\mathbf{p}^2 + m_N^{*2}}} f_N(x, \mathbf{p}) \,, \end{aligned} \tag{2.52}$$

since for matter at rest in Eq. 2.50 we have $\mathbf{p}^* = \mathbf{p}$.
In Eq. 2.52 the self-interaction of the σ-field is included up to the forth order. The parameters g_s, m_σ, B, C are fixed in order to reproduce the values of the nuclear matter quantities at saturation, *i.e.* the saturation density, the binding energy per nucleon, the compression modulus, and the effective nucleon mass. Actually, there are different sets for these quantities that lead

to slightly different saturation properties. We defer a discussion on the related uncertainties of our results to the following Section 2.5.2.
The inclusion of the CSR mechanism in the particle production within PHSD consists essentially in the following: we consider effective masses (see Eq. 2.51) for the dressed quarks in the Schwinger formula (Eq. 2.39) for the string decay in a hot and dense medium. The effective quark masses can be expressed in terms of a scalar coupling to the quark condensate $\langle\bar{q}q\rangle$ in first-order as follows:

$$m_q^* = m_q^0 + (m_q^V - m_q^0)\frac{\langle\bar{q}q\rangle}{\langle\bar{q}q\rangle_V}\,, \tag{2.53}$$

$$m_s^* = m_s^0 + (m_s^V - m_s^0)\frac{\langle\bar{q}q\rangle}{\langle\bar{q}q\rangle_V}\,, \tag{2.54}$$

with $m_q^0 \approx 7\,\text{MeV}$ and $m_s^0 \approx 100\,\text{MeV}$ for the bare quark masses.
In Eqs. 2.54 and 2.53 the effective masses decrease from the vacuum values with decreasing scalar condensate $\langle\bar{q}q\rangle$ to the bare masses. This adaptation of the Schwinger formula in case of a hot and dense medium implies a modification of the flavor production factors in Eq. 2.40. In an simulated nucleus-nucleus collision, PHSD incorporates a dynamical calculation of all these quantities for each cell in space-time:

- the scalar density ρ_S is determined by solving the gap equation (Eq. 2.52) for the σ-field;
- the scalar condensate $\langle\bar{q}q\rangle$ is then computed via Eq. A.1;
- the effective masses m_q^*, m_s^* are calculated according to Eqs. 2.54 and 2.53 and plugged in the Schwinger formula (Eq. 2.39) in order to compute the flavor production ratios for the string decay.

We stress that, once the nucleon scalar density ρ_S and Σ_π are fixed, there is no need for further parameters in PHSD.

2.5.2 Dependence on the nuclear equation of state

In this Section we analyze in more detail the flavor production ratios from the Schwinger formula in the presence of a hot and dense nuclear medium including CSR within PHSD. As mentioned in the previous Section 2.5.1, there are different sets for the parameters g_s, m_σ, B, C in the gap equation (Eq. 2.52). These parameters are fixed within the non-linear $\sigma-\omega$ model in order to reproduce empirical values of nuclear matter quantities at saturation (*i.e.* saturation density, binding energy per nucleon, compression modulus, effective nucleon mass etc.), but non-negligible uncertainties remain. In Table 2.1 we display the values of g_s, m_σ, B, C together with the vector coupling g_v, the vector meson mass m_v, the compression modulus K and the

	NL1	NL2	NL3
g_s	6.91	8.50	9.50
g_v	7.54	7.54	10.95
B (1/fm)	-40.6	50.57	1.589
C	384.4	-6.26	34.23
m_σ (1/fm)	2.79	2.79	2.79
m_v (1/fm)	3.97	3.97	3.97
K (MeV)	380	210	380
m_N^*/m_N	0.83	0.83	0.70

Table 2.1: Parameter sets NL1, NL2 and NL3 for the non-linear $\sigma - \omega$ model employed in the transport calculations from Ref. [110].

ratio between the effective and the bare nucleon mass m_N^*/m_N at saturation density for three sets commonly indicated as NL1, NL2 and NL3 [110]. The sets NL1 and NL3 have the same compression modulus K, but differ in the effective mass m_N^*/m_N at saturation density whereas NL1 and NL2 have the same effective mass, but differ in the compression modulus K. By comparing the results from NL1, NL2 and NL3 we are able to explore separately the effects of the effective mass and the compression modulus. In the context of the string decay, the most important parameter to focus on is the scalar coupling g_s, which is lower for the NL1 and NL2 sets with respect to the corresponding value in the NL3 set.

In Fig. 2.9 we plot the nucleon scalar density ρ_S (in panel (a)), the ratio between the scalar quark condensate and its value in the vacuum $\langle\bar{q}q\rangle/\langle\bar{q}q\rangle_V$ (in panel (b)), the light and strange quark effective masses m_q^*, m_s^* (in panel (c)) and the production probability γ_s (in panel (d)) as a function of the energy density ε. An analogous dependence of these quantities is observed as a function of the baryon density ρ_B, since the energy density ε in leading order is just $\varepsilon \approx m_N\rho_B$. We find that all quantities plotted in Fig. 2.9 show indistinguishable results for NL1 (green dashed lines) and NL2 (thin orange lines) since the scalar density ρ_S essentially depends on the effective nucleon mass which is very similar for NL1 and NL2 when plotted as a function of ε. The results shown in Fig. 2.9 are obtained at vanishing temperature $T = 0$, but all the following considerations can be extended to a more realistic picture at finite temperature (finite meson density). Moreover, the plots shown in Fig. 2.9 represent a helpful illustration of the consequences of CSR in the PHSD results for heavy-ion collisions.

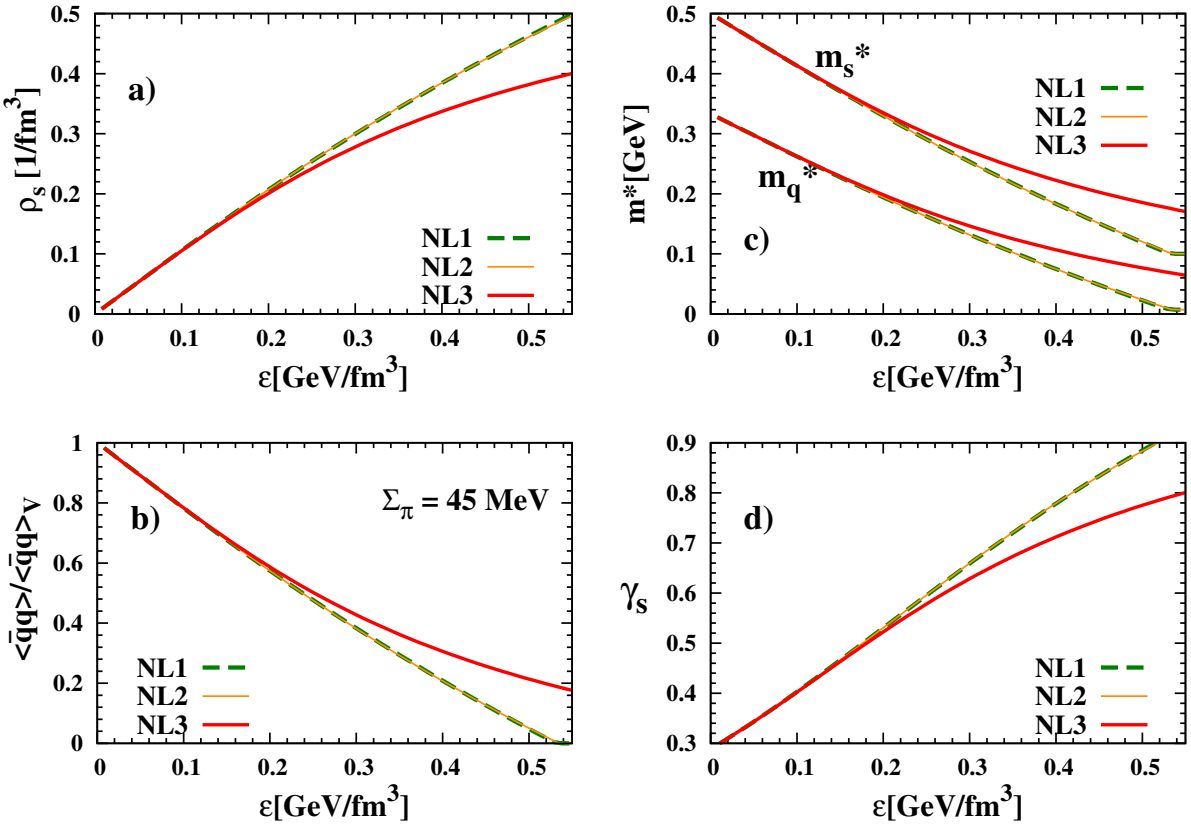

Figure 2.9: The nucleon scalar density ρ_S in panel (a), the ratio between the scalar quark condensate and its value in the vacuum $\langle\bar{q}q\rangle/\langle\bar{q}q\rangle_V$ in panel (b), the light and strange quark effective masses m_q^*, m_s^* in panel (c), and the production probability of massive $s\bar{s}$ pairs relative to light flavor production γ_s in panel (d) as a function of the energy density ε for the parameter sets NL1 (dashed green lines), NL2 (thin orange lines) and NL3 (red solid lines) at temperature $T = 0$ and with Σ_π=45 MeV.

The energy density ε here is calculated within the non-linear $\sigma - \omega$ model by:

$$\varepsilon = U(\sigma) + \frac{g_v^2}{2m_v^2}\rho_N^2 + d\int \frac{\mathrm{d}^3p}{(2\pi)^3}\, E^*(\mathbf{p})\left(N_f(\mathbf{p}) + N_{\bar{f}}(\mathbf{p})\right), \tag{2.55}$$

with

$$E^*(\mathbf{p}) = \sqrt{\mathbf{p}^2 + m_f^{*2}}, \tag{2.56}$$

$$U(\sigma) = \frac{m_\sigma^2}{2}\sigma^2 + \frac{B}{3}\sigma^3 + \frac{C}{4}\sigma^4, \tag{2.57}$$

where ρ_N represents the nucleon density and $N_f(\mathbf{p})$ and $N_{\bar{f}}(\mathbf{p})$ are the particle/antiparticle occupation numbers at fixed momentum $\mathbf{p}$, respectively, with effective mass m_f^* and associated

degeneracy factor d.

The scalar density ρ_S increases with increasing energy density ε as displayed in panel (a) of Fig. 2.9. We find a moderate sensitivity to the nuclear equation of state for $\varepsilon \lesssim 0.5$ GeV/fm^3 (energy range corresponding to the hadronic phase in PHSD). In fact, the lines referring to the parameter sets NL1/NL2 and NL3 show a very similar behavior as a function of ε, but the NL3 (solid line) set is always characterized by lower values of the scalar density ρ_S relative to the NL1 or NL2 parametrizations (dashed lines). This is due to the larger value of the effective nucleon mass m_N^* in case of the NL1 and NL2 parameter sets. In panel (b) of Fig. 2.9 we study the energy dependence of the ratio $\langle\bar{q}q\rangle/\langle\bar{q}q\rangle_V$. At $\varepsilon = 0$ the scalar condensate corresponds to the vacuum value $\langle\bar{q}q\rangle_V$ and for fixed Σ_π=45 MeV it decreases almost linearly with increasing energy density and for the NL1 and NL2 parameter sets nearly vanishes for the critical energy density $\varepsilon_c \approx 0.5$ GeV/fm^3. In this case, the order between NL1/NL2 and NL3 results is reversed: the NL3 parametrization for the nuclear EoS shows higher values of the scalar quark condensate with respect to the NL1 or NL2 sets. This feature can be easily explained looking at the definition of the ratio $\langle\bar{q}q\rangle/\langle\bar{q}q\rangle_V$ in Eq. A.1. At $T = 0$, there are no thermal mesons, thus the last term of Equation A.1 vanishes and the ratio is entirely fixed by the scalar density ρ_S. Hence, higher values of ρ_S correspond to lower values of $\langle\bar{q}q\rangle/\langle\bar{q}q\rangle_V$. Therefore, the NL1 and NL2 parametrizations are characterized by lower values of the scalar quark condensate with respect to the NL3 parameter set. It follows that the light and strange quark effective masses m_q^*, m_s^* in panel (c) of Fig. 2.9 show a very similar dependence on the energy density. At vanishing energy density ε, the quark effective masses are equal to their vacuum values, $m_q \approx 0.33$ GeV and $m_s \approx 0.5$ GeV; with increasing ε the quark masses decrease in line with the scalar quark condensate up to their bare values $m_s^0 \approx 100$ MeV and $m_q^0 \approx 7$ MeV for vanishing $\langle\bar{q}q\rangle/\langle\bar{q}q\rangle_V$. The decrease of both m_q and m_s is approximately linear in energy density where the slope associated to the light quark is flatter in comparison to the strange quark mass. Concerning the comparison between the different choices for the nuclear equation of state, we find also for these masses a non-negligible sensitivity and the same hierarchy as for the scalar quark condensate (the results associated to NL1/NL2 are always below the corresponding results for NL3).

In panel (d) of Fig. 2.9 the strangeness ratio γ_s (referring to the hadronic particle production via the string decay, described by the Schwinger formula in Eq. 2.39) is shown as a function of energy density for the three parameter sets. The factor γ_s increases from the vacuum case ($\gamma_s \approx 0.3$) with increasing energy density up to values of $\gamma_s \approx 0.8 - 0.9$ for $\varepsilon \approx \varepsilon_c$. Thus, the production of a $s\bar{s}$ pair relative to a light quark pair is no longer suppressed close to the phase boundary for CSR as it is in vacuum. The reason of this increase is the steeper decrease of the effective strange quark mass (with energy density) in comparison to the effective light quark

mass as mentioned above. Furthermore, the NL1 and NL2 parametrizations give larger values of γ_s than the NL3 parametrization due to a faster change of the masses with ε (see panel (c) of Fig. 2.9).

This scheme for CSR in the string decay mechanism is applied not only to the light and strange quarks, but also to diquark combinations that are produced in the fragmentation of the string and lead finally to baryon-antibaryon pairs. For example, the default JETSET[4] ratios fix the diquark mass in the vacuum, e.g. a light diquark mass in vacuum of m^V_{uu}= 0.65 GeV leads to a suppression of a light diquark pair relative to a light quark-antiquark pair by a factor of:

$$\frac{P(uu\bar{u}\bar{u})}{P(u\bar{u})} \approx 0.07\,. \tag{2.58}$$

Instead, for the creation of a diquark *su* one employs $m^V_{su} \approx 0.725$ GeV which leads to the ratio for a *su*-diquark pair relative to a light *uu*-diquark pair of:

$$\frac{P(su\bar{s}\bar{u})}{P(uu\bar{u}\bar{u})} \approx 0.4\,. \tag{2.59}$$

The Schwinger mechanism of string decay in vacuum thus requires the following dressed vacuum masses (included in the default JETSET): $m^V_u \approx 0.35$ GeV, $m^V_s \approx 0.5$ GeV, $m^V_{uu} \approx 0.65$ GeV, $m^V_{su} \approx 0.725$ GeV and $m^V_{ss} \approx 0.87$ GeV to comply with experimental observation in nucleon-nucleon collisions. The production probability of diquark combinations does not change very much in the dense medium and since $m^0_{su} - m^0_{uu} \approx m^0_s - m^0_u$, the bare diquark masses m^0_{uu} can be fixed and give $m^0_{uu} \approx 0.5$ GeV, $m^0_{su} \approx 0.593$ GeV and $m^0_{ss} \approx 0.763$ GeV.

The explicit variations of the quark and diquark flavor ratios with the energy density are displayed for $T = 0$ in a hadronic environment on the l.h.s. of Fig. 2.10 and show that the diquark ratios change only very moderately with the energy density whereas the s/u ratio steeply rises with ε.

This increase of the s/u ratio is, however, limited to the hadronic phase, as it is visible on the r.h.s. of Fig. 2.10, where both the hadronic phase and the QGP phase are considered. We recall that in PHSD above $\varepsilon_c \approx 0.5\,\mathrm{GeV/fm^3}$ hadrons dissolve in partonic degrees of freedom and mean-field energy and we remark that in the QGP phase strings cannot be formed anymore due to a vanishing string tension. As displayed on the r.h.s. of Fig. 2.10, the s/u factor shows an increase for $\varepsilon < \varepsilon_c$ and for $\varepsilon \geq \varepsilon_c$ it drops to the value $\sim 1/3$ (fixed by comparison with the strangeness production at RHIC and LHC energies observed experimentally). In the partonic phase the s/u ratio remains constant as a function of the energy density. Consequently, we can identify a "horn" structure in the s/u ratio as a function of ε, where the initial increase

[4]JETSET [74, 111] is a program simulating string fragmentations based on the Lund string model for the QCD deconfinement.

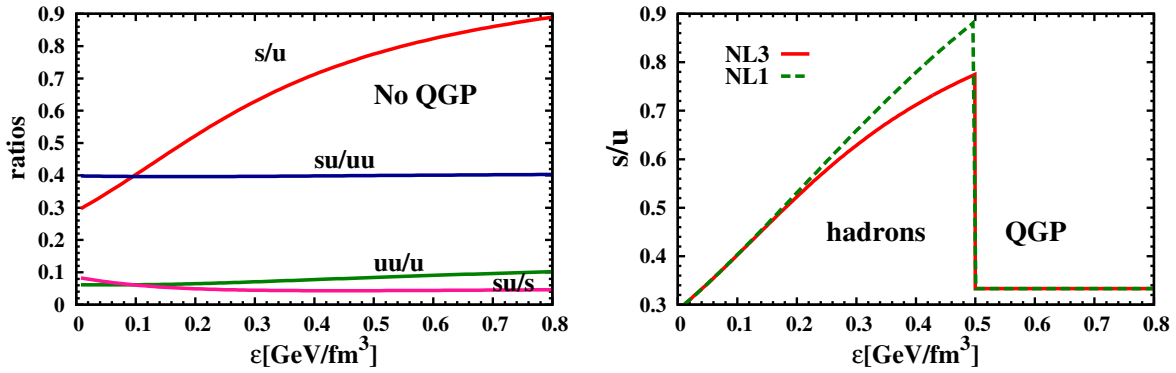

Figure 2.10: (l.h.s.) The quark and diquark ratios in the string decay (hadronic environment) as a function of the energy density ε as evaluated within the non-linear $\sigma - \omega$ model for the parameter set NL3 for $T = 0$. (r.h.s.) The strangeness ratio s/u in the string decay as a function of the energy density ε as evaluated within the non-linear $\sigma - \omega$ model for the parameter sets NL3 and NL1 at $T = 0$. For $\varepsilon < 0.5\,\mathrm{GeV/fm^3}$ the system is composed of hadronic degrees of freedom, while for $\varepsilon > 0.5\,\mathrm{GeV/fm^3}$ the system is composed of partonic degrees of freedom

is related to CSR in the hadronic phase and the subsequent sharp drop is associated to the formation of the QGP.

We have found that the major consequence of the restoration of chiral symmetry emerges as an energy-dependent increase of the strange to non-strange particle production in the hadronic phase. We, thus, expect that CSR modifies the particle abundances and spectra from heavy-ion collisions, where an increasing energy density ε in the overlap region can be achieved with increasing bombarding energy. Our investigation of these effects on experimental observables is deferred to Chapter 4.

Chapter 3

Strange particle production at low energies

The production of hyperons has always been of great interest in Heavy-Ion Collisions (HIC), especially since their abundance can be a sensitive observable for the formation of the Quark Gluon Plasma (QGP). Recent measurements from the HADES [112, 113] and FOPI[114, 115] collaborations have drawn the attention on the strange particle yields at low energies, in particular on the hyperon production close to threshold. In the low energy regime, $\sqrt{s_{NN}} = 2 - 3\,\text{GeV}$, the production of hyperons is not seen as a signature for the creation of a QGP, because the system cannot achieve large energy densities. Most likely it is a probe for the equation of state and an indicator of in-medium properties of hadrons in matter. The transport models, as PHSD and UrQMD, were so far unable to describe the surprisingly large multiplicities of the Ξ and ϕ particles measured by the HADES collaboration. This open issue pushed the transport approaches to improve the multi-strange particle production at low energies and this Chapter is devoted to the progress accomplished in this context within PHSD.

3.1 Flavor exchange reactions

The strange particle production in HIC fulfills the conservation laws, for example strangeness must always be produced in $s - \bar{s}$ pairs. Consequently, in nucleon-nucleon ($N + N$) collisions there are strict energy thresholds $\sqrt{s_{th}}$ associated to the hyperon production, which correspond basically to the sum of the masses of the particles involved in the interaction:

$$\text{for } \Lambda: \quad \sqrt{s_{th}}^{\Lambda} = m_N + m_{\overline{K}} + m_{\Lambda} = 2548\,\text{MeV}, \tag{3.1}$$

$$\text{for } \Xi: \quad \sqrt{s_{th}}^{\Xi} = m_N + 2 * m_{\overline{K}} + m_{\Xi} = 3240\,\text{MeV}, \tag{3.2}$$

where m_N is the nucleon mass, $m_{\overline{K}}$ is the antikaon mass, m_Λ is the Λ mass and m_Ξ is the Ξ mass.
In nucleus-nucleus ($A + A$) collisions there are few mechanisms that allow hyperons to be produced below threshold:

- In the medium the hadrons undergo modifications of their properties, e.g. the mass. The change of the mass of kaons shifts the production thresholds.
- The nucleons, seen as bound states in the nuclei, have an associated Fermi momentum, which can increase the center-of-mass energy of two colliding nucleons with respect to the center-of-mass energy of the two nuclei (when the nucleon momentum is anti-parallel to the projectile momentum).
- The nucleon might interact not only with a single nucleon of the other nucleus, but also with a composite object, like an α particle.
- The necessary energy to overcome $\sqrt{s_{th}}$ can be achieved via multiple scatterings involving nucleons, produced hadrons and resonances.

The multi-strange baryon production is found in Ref. [116] to be only marginally affected by the in medium effects on the kaon properties, while on the other hand it is more sensitive to the magnitude of the cross-sections of flavor exchange reactions, which happen as secondary interactions in $A+A$ collisions. This multi-step production process for the hyperon production proceeds with the following stages:

Λ and Σ production	$\Longrightarrow$	Ξ production	$\Longrightarrow$	Ω production
$N + N \rightarrow N + \overline{K} + Y$		$Y + \overline{K} \leftrightarrow \Xi + \pi$		$\Xi + \overline{K} \leftrightarrow \Omega + \pi$
$\pi + N \leftrightarrow \overline{K} + Y$		$Y + Y \leftrightarrow \Xi + N$		$\Xi + \Xi \leftrightarrow \Omega + Y$
$N + \overline{K} \leftrightarrow Y + \pi$.				

The single-strange baryons, Λ and Σ, are produced in the first step either via primary nucleon-nucleon collisions or via secondary flavor exchange meson-baryon reactions. The Ξ and the Ω can be produced through the flavor exchange reactions both by meson-baryon and baryon-baryon scatterings in the second and third step, respectively. Recently, the HADES collaboration measured surprisingly high Ξ^- yields [112, 113] below $\sqrt{s_{th}}^{\Xi}$ at odds with theoretical predictions. The main reason for the low multiplicity of Ξ^- in the available transport approaches was proposed to be the absence of Baryon-Baryon (B-B) flavor exchange reactions of the type $Y + Y \leftrightarrow \Xi + N$ in the hadronic re-scattering [117], while the contribution of the meson-Baryon (m-B) interactions of the type $Y + \overline{K} \leftrightarrow \Xi + \pi$ is negligible at low energy

[117, 118] (the m-B flavor exchange reactions play an important role at AGS and SPS energies where the abundance of mesons is much larger). Moreover, these m-B flavor exchange reactions are included in the PHSD model and they do not provide Ξ^- yields comparable with the measured data. Thus, the inclusion of the $Y + Y$ interaction represents an important extension of the PHSD model where so far the hyperons have been taken into account in the B-B dynamics only in the string fragmentation and in 3-body strangeness production channels, *i.e.* $NN \to NYK$, $NN \to \Delta YK$, $N\Delta \to NYK$, $\Delta\Delta \to NYK$.

To incorporate these reaction channels in PHSD, the associated scattering cross-sections are required. In fact, within a transport model the scattering cross-sections are employed as input. In case of elementary binary collisions, available experimental cross-section are used in PHSD [90]. Unfortunately, direct experimental observations are not accessible for all reaction channels. Thus, the transport approaches need to rely on effective theories for the missing cross-sections, for example for the Hyperon-Hyperon ($Y + Y$) interactions. In PHSD, we choose to employ for these reactions the cross-sections calculated in Ref. [117], where a gauged flavor SU(3)-invariant hadronic Lagrangian in the Born approximation is used. This is consistent with the cross-sections for the scatterings $Y + \overline{K} \leftrightarrow \Xi + \pi$ already included in PHSD. The reader can find more details on this model [117] in the Appendix B. The parametrizations for the cross-sections of the forward reactions $YY \to N\Xi$ are:

$$\sigma_{\Lambda\Lambda\to N\Xi} = 37.15\frac{p_N}{p_\Lambda}(\sqrt{s} - \sqrt{s_0})^{-0.16} mb, \tag{3.3}$$

$$\sigma_{\Lambda\Sigma\to N\Xi} = 25.12(\sqrt{s} - \sqrt{s_0})^{-0.42} mb, \tag{3.4}$$

$$\sigma_{\Sigma\Sigma\to N\Xi} = 8.51(\sqrt{s} - \sqrt{s_0})^{-0.395} mb, \tag{3.5}$$

with p_N as the initial nucleon momentum and p_Λ as the final momentum of the Λ, both expressed in the center-of-mass frame of the collision; $\sqrt{s_0}$ is the minimum energy needed for the reaction to occur:

$$\sqrt{s_0} = Max[(m_{\Lambda,\Sigma} + m_{\Lambda,\Sigma}), (m_N + m_\Xi)]. \tag{3.6}$$

The cross-sections for the backward reactions $YY \leftarrow N\Xi$ are computed applying the detailed balance, and are expressed by the following relations (taken at the same $\sqrt{s}$):

$$\sigma_{N\Xi\to\Lambda\Lambda} = \frac{1}{4}\left(\frac{p_\Lambda}{p_N}\right)^2 \sigma_{\Lambda\Lambda\to N\Xi}, \tag{3.7}$$

$$\sigma_{N\Xi\to\Lambda\Sigma} = \frac{3}{4}\left(\frac{p_\Lambda}{p_N}\right)^2 \sigma_{\Lambda\Sigma\to N\Xi}, \tag{3.8}$$

$$\sigma_{N\Xi\to\Sigma\Sigma} = \frac{9}{4}\left(\frac{p_\Sigma}{p_N}\right)^2 \sigma_{\Sigma\Sigma\to N\Xi}, \tag{3.9}$$

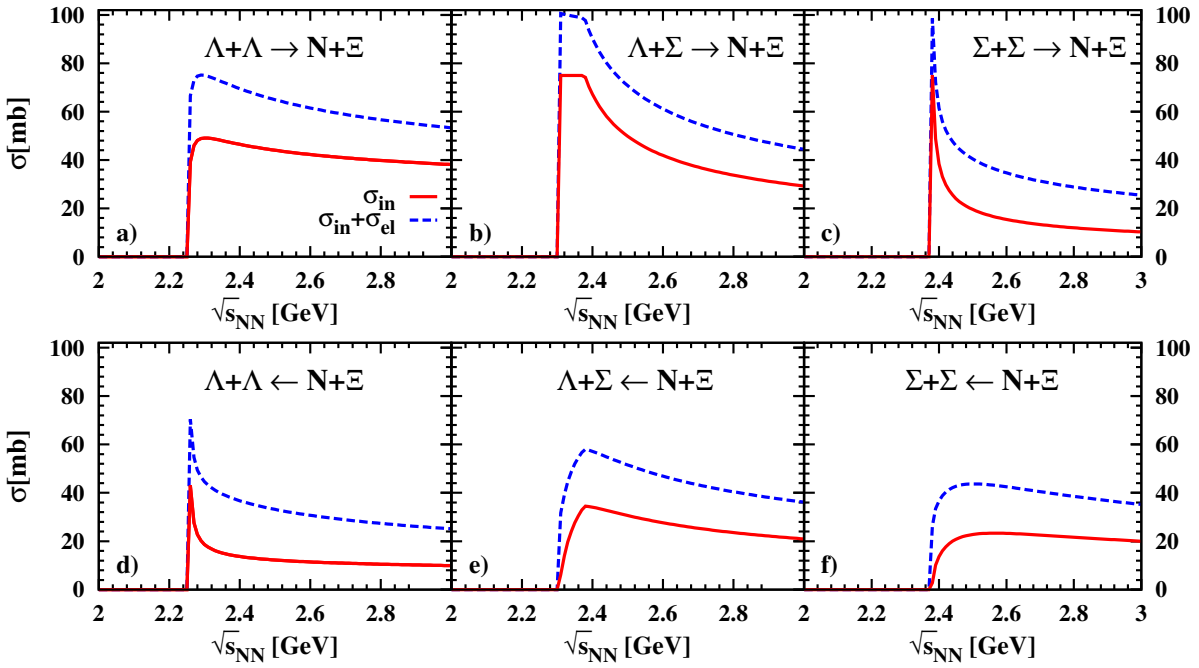

Figure 3.1: The cross-sections as a function of the center-of-mass energy $\sqrt{s_{NN}}$ of the flavor exchange reactions $\Lambda\Lambda \to N\Xi$, $\Lambda\Sigma \to N\Xi$, $\Sigma\Sigma \to N\Xi$ in panels (a), (b), (c), respectively, and of the corresponding backward channels $\Lambda\Lambda \leftarrow N\Xi$, $\Lambda\Sigma \leftarrow N\Xi$, $\Sigma\Sigma \leftarrow N\Xi$ in panels (d), (e), (f), respectively. These cross-sections are parametrized according to 3.3-3.9 and have been provided by Ref. [117]. A cut at 75 mb has been applied. The solid red lines represent the inelastic cross-sections, while the dashed blue lines refer to the total cross-sections.

where p_Σ is the momentum of the Σ particle in the center-of-mass frame and the numerical factors on the right hand side are given by isospin combinations.
We mention that the UrQMD transport model uses different parametrizations for the same reaction channels [119], in particular the cross-sections considered in PHSD are isospin-averaged, while in UrQMD they are isospin-dependent.

3.2 Implementation in PHSD

In this section, we explain in detail how we extend the Baryon-Baryon (B-B) hadronic cascade in PHSD to include the hyperon-hyperon ($Y + Y$) scattering of the Λ and Σ particles. For the flavor exchange reactions we adopt the parametrizations given in Eqs. 3.3-3.9, provided by Ref. [117], that are shown as a function of the invariant energy in Fig. 3.1. The cross-sections for the forward flavor exchange reactions $Y + Y \to N + \Xi$ are plotted using solid red lines in panels (a), (b), (c), while the cross-sections for the associated backward channels

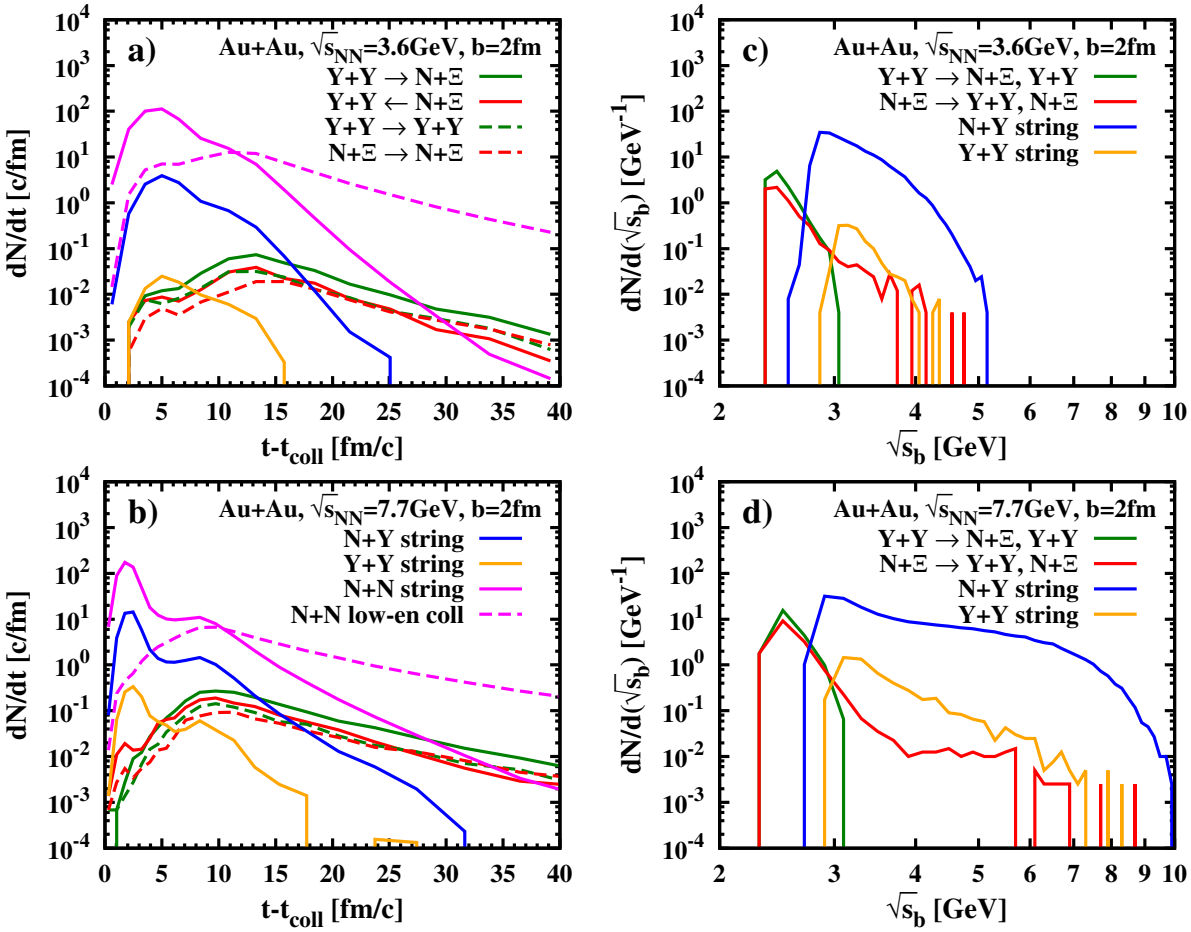

Figure 3.2: (l.h.s.) The collision rate dN/dt as a function of the time rescaled according to the collision time t_{coll} in central $Au + Au$ collisions at $\sqrt{s_{NN}} = 3.6, 7.7$ GeV in panels (a) and (b), respectively. The collision rates for different channels are shown (see legend on the plot). (r.h.s.) The collision rate $dN/d\sqrt{s_b}$ as a function of the center-of-mass energy of the colliding particles $\sqrt{s_b}$ in central $Au + Au$ collisions at $\sqrt{s_{NN}} = 3.6, 7.7$ GeV in panels (c) and (d), respectively (see legend on the plot).

$Y + Y \leftarrow N + \Xi$ are plotted with the same coding of the lines in panels (d), (e), (f). We apply a cut at 75 mb on the cross-sections $\Lambda\Sigma \rightarrow N\Xi$, $\Sigma\Sigma \rightarrow N\Xi$ in order to prevent them to exceed a total cross-section of $\sigma_{ref} = 102$ mb in the inclusive $Y + Y \rightarrow X + X$ scattering. The considered σ_{ref} corresponds to a maximum interaction radius of ≈ 1.8 fm, which takes into account screening effects due to the high densities reached in heavy-ion collisions. These flavor exchange reactions are activated at different center-of-mass energy in correspondence to the associated energy threshold $\sqrt{s_0}$ (see Eq. 3.6). All the cross-sections shown in Fig. 3.1 present a maximum close to the threshold and then a smooth decrease as a function

of $\sqrt{s_{NN}}$. Differently from $\Lambda\Lambda \rightarrow N\Xi$, both $\Lambda\Sigma \rightarrow N\Xi$ and $\Sigma\Sigma \rightarrow N\Xi$ reaction channels are exothermal, since the sum of the initial masses is larger than the sum of the final masses: $\sum_m^{initial} = m_{\Lambda,\Sigma} + m_\Sigma = 2.378, 2.304\,\text{GeV}$ and $\sum_m^{final} = m_N + m_\Xi = 2.252\,\text{GeV}$. In addition to the inelastic cross-section of the flavor exchange reactions σ_{in}, we assign to the hyperon-hyperon interactions an elastic cross-section equal to the elastic cross-section σ_{el} associated to the nucleon-nucleon scattering. In Fig. 3.1 the dashed blue lines show this additional elastic contribution, which contribute with σ_{in} to the total $Y + Y$ scattering cross-section σ_{tot}^{YY}. Furthermore, we extend the string dynamics to include also the Λ and Σ particles. In particular, for the nucleon-hyperon (NY) string the employed cross-section is decreased with respect to the non-strange (NN) string by a factor depending on the number of valence light quarks of the colliding particles, *i.e.* $\sigma_{string}^{NY} = \sigma_{string}^{NN} \cdot (2/3)$, while for the $Y + Y$ string we use the above mentioned σ_{tot}^{YY}.

It is interesting to study the features of the $Y + Y$ interactions included in the hadronic rescattering as implemented in PHSD. On the l.h.s. of Fig. 3.2 we analyze the reaction rate dN/dt of the hyperon-hyperon scattering as a function of the time in central ($b = 2$ fm) Au+Au collisions at $\sqrt{s_{NN}} = 3.6\,\text{GeV}$ and $\sqrt{s_{NN}} = 7.7\,\text{GeV}$ (panel (a) and (b), respectively). We distinguish the following different channels: the flavor exchange reactions $Y + Y \rightarrow N + \Xi$ are represented by the solid green lines, while the dashed green lines stand for the elastic $Y + Y$ scatterings; the backward channels $\Lambda + \Lambda \leftarrow N + \Xi$ are represented by the solid red lines, while the dashed red lines stand for the elastic $N + \Xi$ scatterings; the solid blue lines refer to the $N + Y$ string interactions, the solid orange lines refer to the $Y + Y$ string interactions, the solid magenta lines refer to the string interactions between non-strange particles and the dashed magenta lines refer to the low-energy collisions between non-strange particles. The common trend is that dN/dt first increases (reaching a maximum) and then decreases with increasing time and that it increases with increasing collision energy (the maxima of the rates are higher and the slopes are harder for $\sqrt{s_{NN}} = 7.7\,\text{GeV}$ than for $\sqrt{s_{NN}} = 3.6\,\text{GeV}$). The string dynamics is dominant at small times independently of the reaction type ($N+N$ or $N+Y$ or $Y + Y$). In fact, the string interactions mainly occur during the passage time (defined in Section 2.4), as indicated by the peaks of the rate at $t - t_{coll} \approx 5$ fm/c and $t - t_{coll} \approx 2$ fm/c for $\sqrt{s_{NN}} = 3.6\,\text{GeV}$ and $\sqrt{s_{NN}} = 7.7\,\text{GeV}$, respectively. Furthermore, it is straightforward that the $Y + Y$ interactions present a short time delay with respect to the non-strange particle collisions, since they are secondary collisions in the hadronic cascade. This is more visible at $\sqrt{s_{NN}} = 3.6\,\text{GeV}$. The rate of the flavor exchange reactions and elastic scatterings, which do not proceed as string excitation, first increases with increasing time up to a maximum at $t \approx 14$ fm/c for $\sqrt{s_{NN}} = 3.6\,\text{GeV}$ and at $t \approx 9$ fm/c for $\sqrt{s_{NN}} = 7.7\,\text{GeV}$ and then it decreases as the system expands and the energy and baryon densities drop. For the largest collision

energy considered here, the nuclear passage time is shorter and the system evolution is faster than for $\sqrt{s_{NN}} = 3.6\,\text{GeV}$. This explains the fact that the maxima of the collision rates shift to lower times when the collision energy is larger. Since $\sigma_{in} > \sigma_{el}$, the rates of the $Y + Y$ and $N + \Xi$ scatterings are characterized by the same hierarchy and in the whole time interval the rates of the forward $Y + Y \rightarrow N + \Xi$ channels are larger than the rates for the corresponding backward channels, apart from a small deviation at small times for $\sqrt{s_{NN}} = 7.7\,\text{GeV}$. In general, the dN/dt rates associated to the interactions involving strange particles are significantly lower than the interactions involving non-strange particles, but they are not negligible. Consequently, we expect that the new included reaction channels in PHSD provide a relevant contribution to the final observables in HIC.
Finally, on the r.h.s. of Fig. 3.2 we investigate the energy distribution of the number of collisions $dN/d\sqrt{s_b}$ as a function of the invariant energy of the colliding particles for the same colliding energies considered above. We display the contributions associated to: the elastic and flavor exchange $Y + Y$ interactions (solid green line), the elastic and flavor exchange $N + \Xi$ interactions (solid red line), the $N + Y$ string interactions (solid blue lines) and the $Y + Y$ string interactions (solid orange lines). The new included $Y + Y$ interactions occur in the system at low energies in the range $\sqrt{s_b} = 2 - 3\,\text{GeV}$, while at larger values of $\sqrt{s_b}$ the collisions proceed as string excitations. In fact, we recall that within PHSD the string excitations can occur above the two$-\pi$ production threshold. We notice that the $N + \Xi$ scatterings take place at large energies differently from the hyperon-hyperon case. This is due to the fact that the Ξ particles are still not included as initial particles in the string mechanism. Thus, the Ξ can interact with the non-strange baryon either elastically or inelastically, producing a hyperon pair. Comparing the results for $\sqrt{s_{NN}} = 3.6\,\text{GeV}$ and $\sqrt{s_{NN}} = 7.7\,\text{GeV}$, the features of $dN/d\sqrt{s_b}$ for the $Y + Y$ reactions remain basically unchanged, while the $dN/d\sqrt{s_b}$ for the other types of collisions do not vanish at larger energies, e.g. $N + Y$ strings occur also at $\sqrt{s_b} \approx 10\,\text{GeV}$.

3.3 Results from heavy-ion collisions

We study the effects of the new $Y + Y$ interactions in the PHSD model on observables in heavy-ion collisions. As seen in Section 3.2, we expect a small but finite contribution from the new channels in the hadronic cascade which develops in HIC. We explore possible modifications in the rapidity spectra at intermediate energies ($E_{Lab} = 6, 30\,\text{AGeV}$) and at the low-energies ($E_{Lab} = 1.25, 1.76, 1.93\,\text{AGeV}$), in comparison with FOPI, KAOS and HADES data [112, 113, 115, 121, 122, 123, 124]. Finally, we focus on the Ξ abundances, which have been the main motivation for this implementation. We list the explored scenarios and the corresponding color code for the results shown in Figs. 3.3 - 3.9:

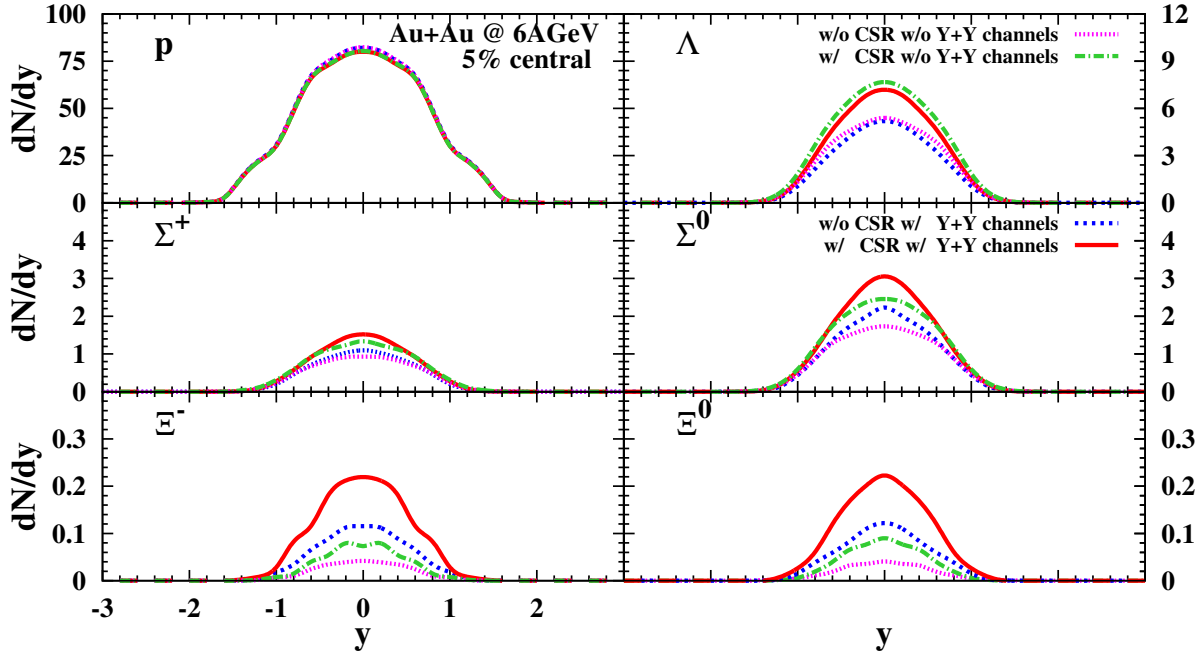

Figure 3.3: The rapidity distribution of protons, Λ's, Σ^+'s, Σ^0's, Ξ^-'s and Ξ^0's for 5% central Au+Au collisions at 6 AGeV. The solid red and the dashed blue lines show the results including the new $Y + Y$ channels with and without CSR, respectively, while the dash-dot green and the dotted magenta lines show the results excluding the new $Y + Y$ channels with and without CSR.

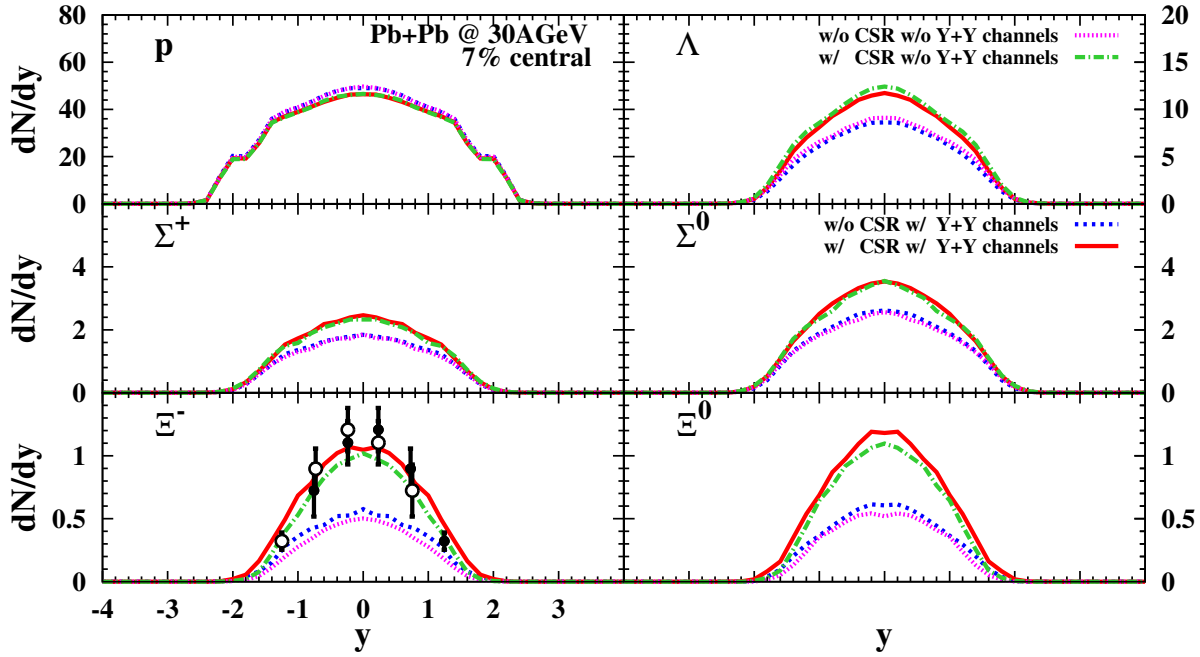

Figure 3.4: The rapidity distribution of protons, Λ's, Σ^+'s, Σ^0's, Ξ^-'s and Ξ^0's for 7% central Au+Au collisions at 30 AGeV. The coding of the lines is the same as in Fig. 3.3. The experimental data are taken from Ref. [120].

- PHSD including the new $Y + Y$ channels with Chiral Symmetry Restoration (CSR) displayed by the solid red line;
- PHSD including the new $Y + Y$ channels without CSR displayed by the dashed blue line;
- PHSD excluding the new $Y + Y$ channels with CSR displayed by the dash-dot green line;
- PHSD excluding the new $Y + Y$ channels without CSR displayed by the dotted magenta line.

Although in the following analysis we make some comments on the effects and possible signature of CSR, we defer a detailed discussion of these aspects to the Chapter 4.

3.3.1 Rapidity spectra at E_{Lab} = 6 and 30 AGeV

In Fig. 3.3 we present the rapidity spectra of protons, Λ's, Σ^+'s, Σ^0's, Ξ^-'s, Ξ^0's for 5% central Au+Au collisions at 6 AGeV. We do not display meson spectra, since they are marginally affected by the inclusion of the $Y + Y$ scatterings. The investigated scenarios do not show remarkable differences on the proton spectra, since the new reaction channels are rare events compared to the non-strange collisions, which determine the proton distributions. On the other hand, there are sizeable modifications in the strange baryon spectra. The inclusion of the $Y + Y$ scatterings decreases the multiplicity of the Λ particles, while it increases the multiplicity of the Σ and Ξ particles. The modification is more pronounced for the Σ^0 and Ξ particles, whose yields increase by about 15% and 30%, respectively. When we also introduce CSR in the calculations, we obtain even larger multiplicities for all the considered hyperons. We notice that the modifications associated to CSR are larger with respect to those related to the $Y + Y$ interactions in the spectra of the single-strange baryons, *i.e.* Λ and Σ. In fact, the lines referring to PHSD excluding the new $Y + Y$ channels with CSR (dash-dot green line) are above the lines referring to PHSD including the new $Y + Y$ channels without CSR (dashed blue line). We find the opposite hierarchy in the Ξ spectra, where the contribution of the flavor exchange interactions is larger than the modifications due to CSR.
At higher collision energies the role played by the new channels is not as significant as we have seen at E_{Lab} =6 AGeV. This is shown in Fig. 3.4, where we plot the rapidity spectra for 7% central Au+Au collisions at 30 AGeV of the same particle species displayed in Fig. 3.3. We recover similar features as described above for E_{Lab} =6 AGeV, but the modifications due to the inclusion of the $Y + Y$ scatterings are significantly smaller, e.g. for the Ξ the difference between the calculations with and without $Y + Y$ channels is $\approx$ 10%. Moreover, only when we consider CSR in our calculations we achieve a good reproduction of the experimental observations for the Ξ. A comparison with experimental data for the other particles will

be shown in Chapter 4 for a different centrality class. The fact that the particle spectra are less affected by the inclusion of the $Y + Y$ interactions is not surprising, since as seen in the Section 3.2 the flavor exchange channels are low energy interactions. At top SPS energies, the calculations of all 4 different scenarios merge, since the dynamics of the system is ruled by the partonic phase and the hadronic re-scattering in the late stages of the expansion is dominated by meson-baryon and meson-meson interactions because of the large meson density compared to the baryon density.

3.3.2 Particle spectra and ratios at E_{Lab} = 1.25, 1.76 and 1.93 AGeV

In this subsection we investigate the particle production at low energies, E_{Lab} =1.25, 1.76 and 1.93 AGeV, to compare our calculations to measurements from the FOPI, KAOS and HADES collaborations [112, 113, 115, 121, 122, 123, 124]. Unfortunately, in this energy regime it is really hard to measure multi-strange particle spectra because of the low production rate, thus we show particle spectra only for the most abundant particles, *i.e.* protons, $(\Lambda+\Sigma^0)$'s, charged pions and kaons. In Fig. 3.5 we present the predictions for the HADES Au+Au run at 1.25 AGeV. The centrality is fixed according to the preliminary analysis of the HADES collaboration (private communication), *i.e.* the calculations are performed for 10% central collisions for all particles, apart of the K^-, which are computed for the 20% centrality class. We show calculations from only two scenarios, PHSD including the new $Y + Y$ channels with and without CSR (solid red and dotted blue lines, respectively), since the inclusion of the $Y+Y$ scattering affects marginally the particle spectra considered here. We notice that also CSR does not sizably modify the particle spectra; we only see a small enhancement of the K^+ and of the $(\Lambda + \Sigma^0)$'s. The same considerations hold for the analogous particle spectra in Fig. 3.6 for central Ni+Ni collisions at 1.93 AGeV. In this case, there are data available from the FOPI and KAOS collaborations [115, 121, 122]; thus we calibrate our analysis according to the experimental analysis and acceptance ($b < 3.5$ fm for baryons and pions and $b < 4.5$ fm for kaons). Our results are in a good agreement with the data for the $(\Lambda+\Sigma^0)$ and K^- distributions, while they do not describe well the proton, pion and K^+ rapidity spectra. In particular, our calculations for the pions and K^+ overshoot the experimental observations by $\approx 30 - 40\%$. In fact, in this energy regime the particle production is expected to be sensitive to hadronic potentials. The repulsive kaon potential for example gives an increase of the effective kaon mass and consequently a decrease of the associated multiplicities. This was found in the analysis reported in Ref. [49] based on a previous version of HSD, where hadronic potentials have been incorporated in the particle production and propagation. There it was shown that HSD could reproduce the experimental data at $E_{Lab} = 1.93$ AGeV when the hadronic potentials are included. Thus, it is not surprising that the current version of PHSD, which includes

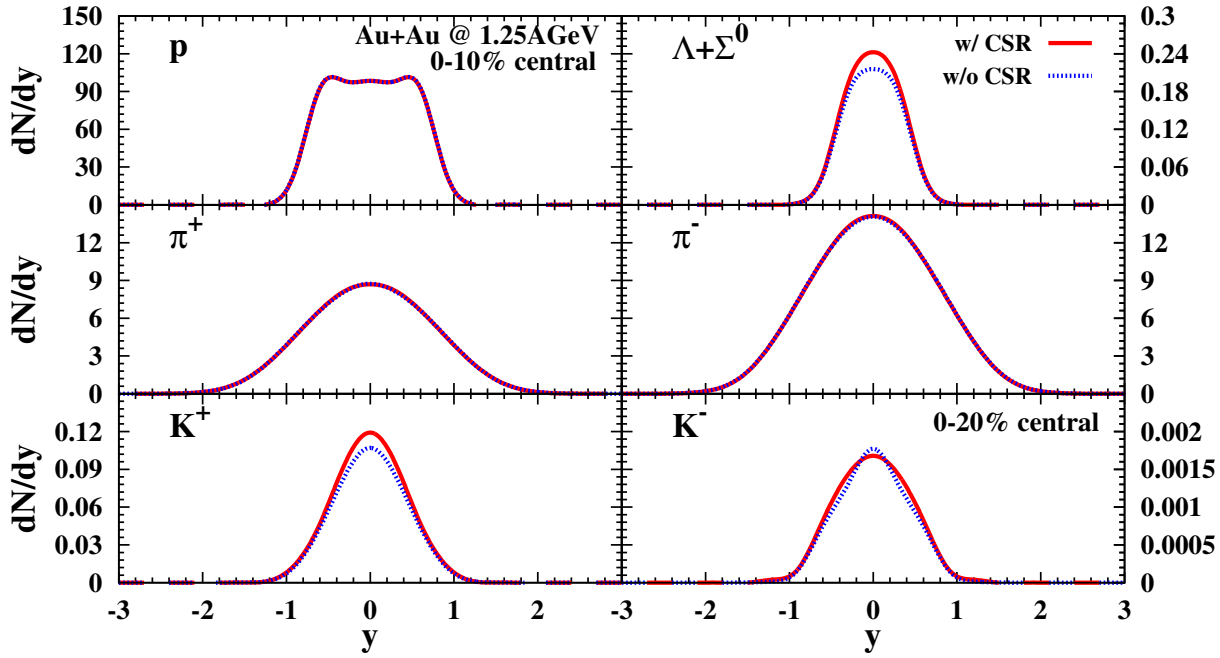

Figure 3.5: The rapidity distribution of protons, $(\Lambda+\Sigma^0)$'s, charged pions and K^+ for 10% central and K^- for 20% central Au+Au collisions at 1.25 AGeV. The solid red and the dotted blue lines show the results including the new $Y + Y$ channels with and without CSR, respectively.

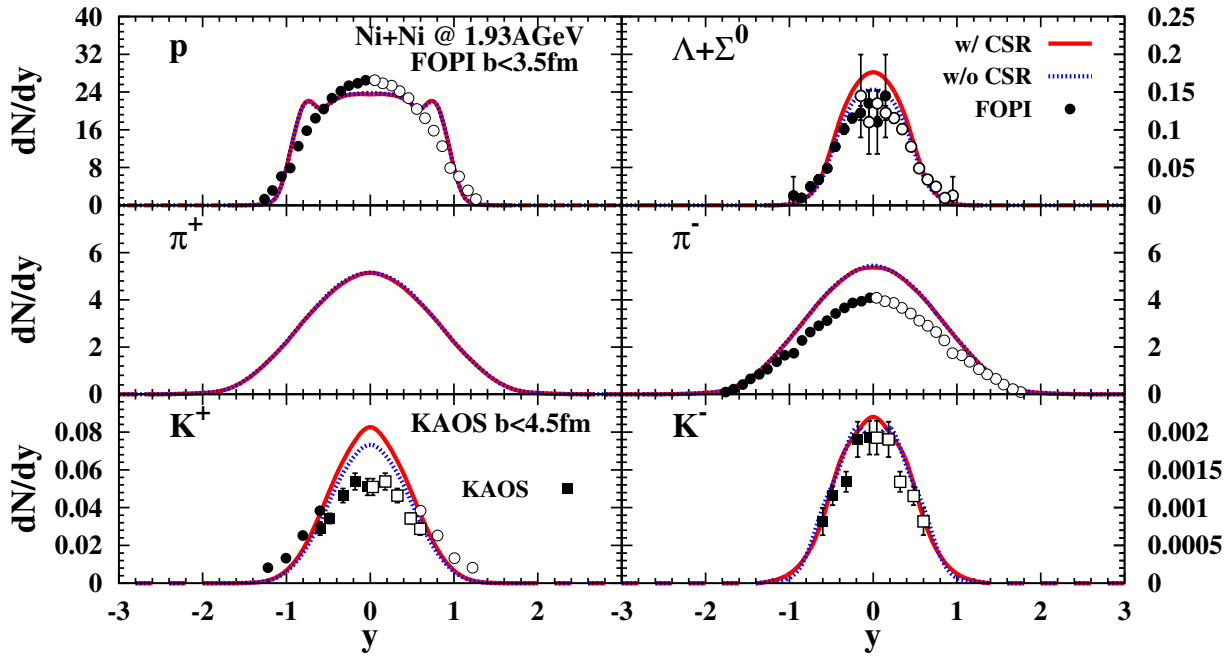

Figure 3.6: The rapidity distribution of protons, $(\Lambda+\Sigma^0)$'s, charged pions and kaons in central ($b < 3.5$ fm for baryons and pions and $b < 4.5$ fm for kaons) Ni+Ni collisions at 1.93 AGeV. The coding of the lines is the same as in Fig. 3.5. The experimental data are taken from Refs. [115, 121, 122].

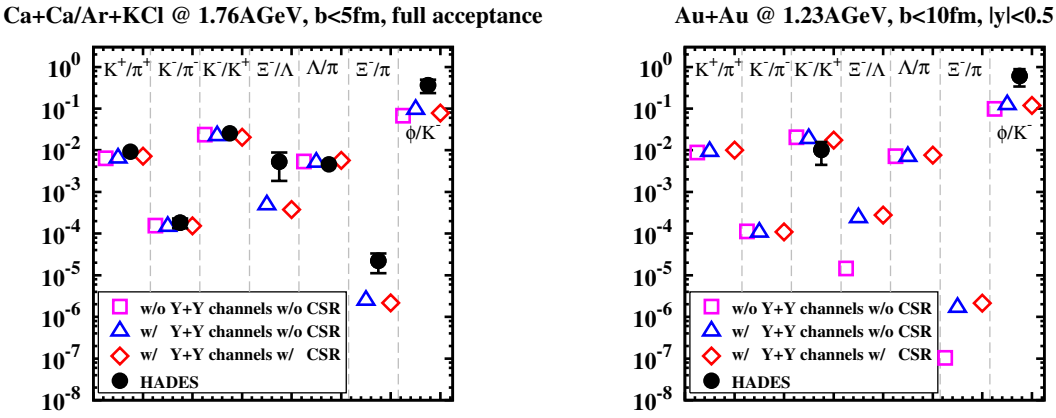

Figure 3.7: Different particle ratios in Ca+Ca collisions at 1.76 AGeV (for $b < 5$ fm and in full acceptance) on the l.h.s. and in Au+Au collisions at 1.23 AGeV (for $b < 10$ fm at mid-rapidity) on the r.h.s.. The Ca+Ca calculations are compared with the HADES observations for Ar+KCl collisions. The experimental data are taken from published and from preliminary results from the HADES collaboration [112, 113, 123, 124]. The magenta points refer to the PHSD calculations excluding the $Y + Y$ scatterings and without CSR, while the blue and red points refer to the PHSD results including the new $Y + Y$ channels with and without CSR, respectively.

the hadronic potentials only in the particle propagation and not in the particle production, is not able to describe the experimental rapidity spectra of the kaons in this energy regime. A consistent implementation of the hadronic potentials is currently under construction in PHSD. In Fig. 3.7 we show results on different particle ratios in Ca+Ca collisions at 1.76 AGeV (l.h.s.) and in Au+Au collisions at 1.23 AGeV (r.h.s.) in comparison with available published and preliminary data from the HADES collaboration [115, 121, 122]. The PHSD results from the explored scenarios (see legend of Fig. 3.7) do not present large differences between each other, apart from the Ξ^-/Λ and Ξ^-/π ratios. In Ca+Ca collisions at 1.76 AGeV the production of Ξ is basically negligible in PHSD if $Y + Y$ interactions are not included. The production of Ξ is investigated in more detail in the next subsection 3.3.3. Overall, our results are in a good agreement with the available data, with some discrepancies for the ratios Ξ^-/Λ, Ξ^-/π and ϕ/K^-. In fact, the PHSD calculations on these particle ratios are almost one order of magnitude lower than the experimental observations. It emerges that although the $Y + Y$ interactions are necessary in PHSD at intermediate energies (e.g. at $E_{Lab} = 6$ AGeV as it is shown in detail in the following Section 3.3.3), at these low energies there are probably some additional contributions for the close-to-threshold production mechanisms that are still missing in our approach. We mention that the UrQMD model proposes new decay channels

for high mass baryon resonances [125], whose inclusion seems to provide a good description of the high yields of ϕ and Ξ. In contrast to these suggestions, we report that, in a study of near-threshold incoherent ϕ photo-production [126], no remarkable contribution has been found to be associated with the high-mass resonance decays.

3.3.3 Ξ-abundances

In this Section we present a detailed study of the Ξ production. In Fig. 3.8 we show the centrality dependence of the full-acceptance Ξ^- and $(\Lambda + \Sigma^0)$ yields and of the corresponding $\Xi^-/(\Lambda+\Sigma^0)$ ratio in Au+Au collisions at 6 AGeV. Similarly to what we observed for the rapidity spectra in Fig. 3.3, the inclusion of $Y+Y$ interactions provides a strong enhancement of the Ξ^- multiplicity, which otherwise would be underestimated with respect to the experimental measurements (panel (a)). On the other hand, the $(\Lambda + \Sigma^0)$ yield is slightly decreased by the $Y + Y$ inelastic reactions (panel (b)). The inclusion of CSR in the string fragmentation (red lines) leads to a stronger enhancement of both considered hyperons which results in an overshoot of the data in the whole range of centrality. All four scenarios follow the experimental trend of the data as a function of centrality, *i.e.* the yields of the strange particles decrease with increasing impact parameter. Although none of the explored scenarios provides a satisfying description of both yields, the calculations of PHSD including the new $Y+Y$ channels without CSR seem to be in reasonable agreement with the data. The ratio $\Xi^-/(\Lambda + \Sigma^0)$ does not show a strong dependence on the centrality, as it is almost constant in the range $b = 2 - 4$ fm with a minor softening for $b > 4$ fm. Comparing the results of the $\Xi^-/(\Lambda+\Sigma^0)$ ratio with and without $Y + Y$ interaction, it is evident that the implementation of the new strange reaction channels plays an important role at E_{Lab} =6 AGeV. The PHSD calculations with the new $Y+Y$ channels and without CSR reproduce the experimental data quite well, while the calculations, which exclude the $Y + Y$ scatterings, are significantly lower than the data. If we include in the calculations only CSR and not the hyperon reactions, we obtain a small increase of the ratio (about 10%), since CSR provides an enhancement of both Ξ and $(\Lambda + \Sigma^0)$. Instead, the difference between the PHSD results including the new $Y+Y$ channels with and without CSR is about 40%, thus much larger than in the previous case. This is due to the fact that we have extended also the string dynamics to include the Λ and Σ particles, which in combination to the strangeness enhancement related to CSR, gives a larger abundance of the Ξ^- particles. As it emerges from the Ξ^- and $(\Lambda+\Sigma^0)$ yields, the scenario with $Y+Y$ scatterings and with CSR are above all other calculations and for the large centralities it overshoots the data. However, we stress that there is a non-negligible uncertainty related to the results from PHSD with CSR, due to the different parametrizations of the nuclear equation of state adopted in the calculations. This sensitivity to the nuclear equation of state will be discussed in more detail in Chapter 4. In the investiga-

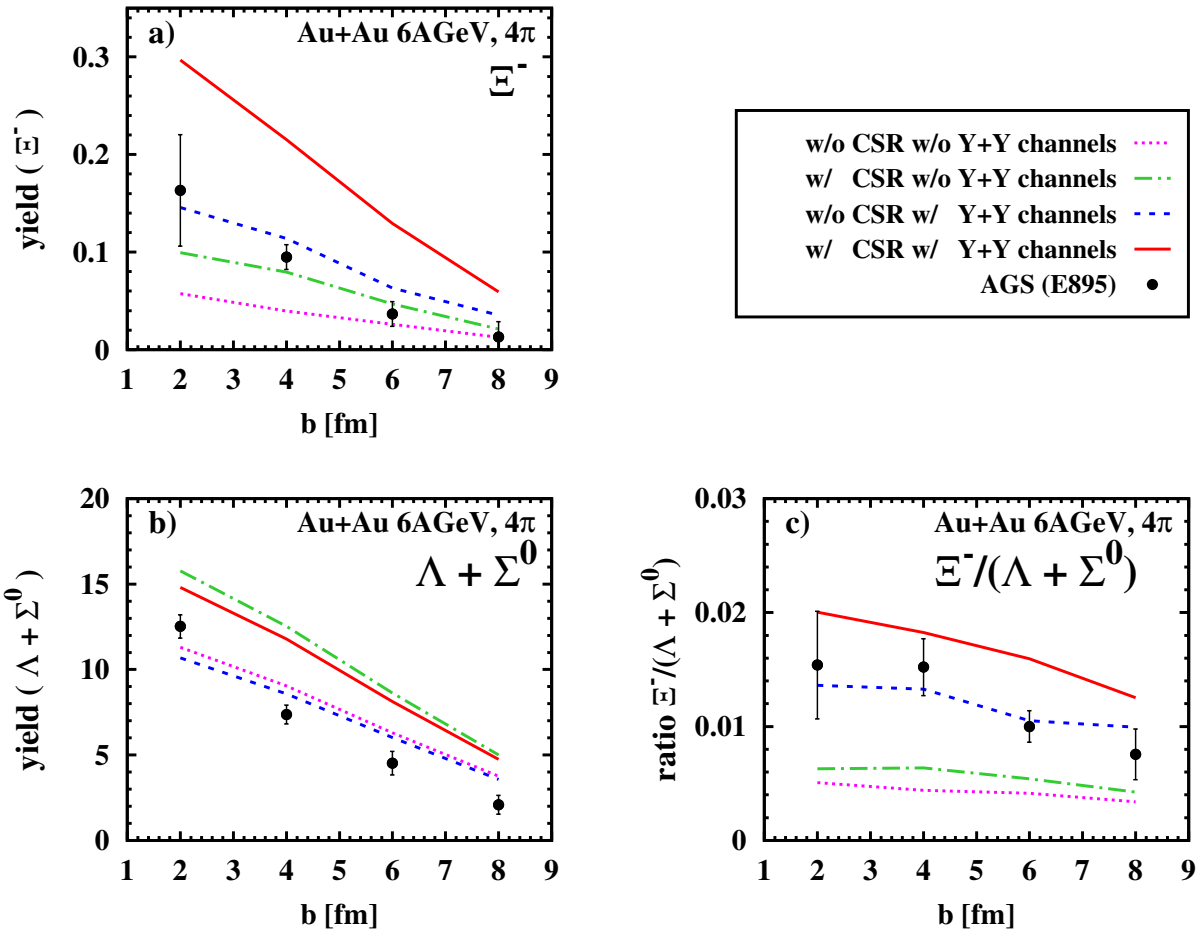

Figure 3.8: The full-acceptance yields of Ξ^- and $(\Lambda + \Sigma^0)$ in panels (a) and (b) and the ratio $\Xi^-/(\Lambda + \Sigma^0)$ in panel (c) as a function of the impact parameter b in Au+Au collisions at 6 AGeV. The solid red and the dashed blue lines show the results including the new $Y + Y$ channels with and without CSR, respectively, while the dash-dot green and the dotted magenta lines show the results excluding the new $Y + Y$ channels with and without CSR, respectively. The experimental data are taken from Ref. [127].

tions addressed in this Chapter we have considered the NL1 parametrization, which provides the largest strangeness enhancement with respect to the other explored parametrizations. In this way, the maximum effect from the CSR mechanism is shown. Different parametrizations give lower values of the $\Xi^-/(\Lambda+\Sigma^0)$ ratio, for example the results obtained with the parameter set NL3 are $\approx 10\%$ lower than the corresponding calculations with the NL1 parametrization. Finally, we present in Fig. 3.9 the excitation function of the $\Xi^-/(\Lambda + \Sigma^0)$ ratio for central Au+Au collisions in comparison with available data from Refs. [112, 120, 127, 128, 129, 130]. In this case, the NL3 parametrization is adopted for the PHSD calculations including

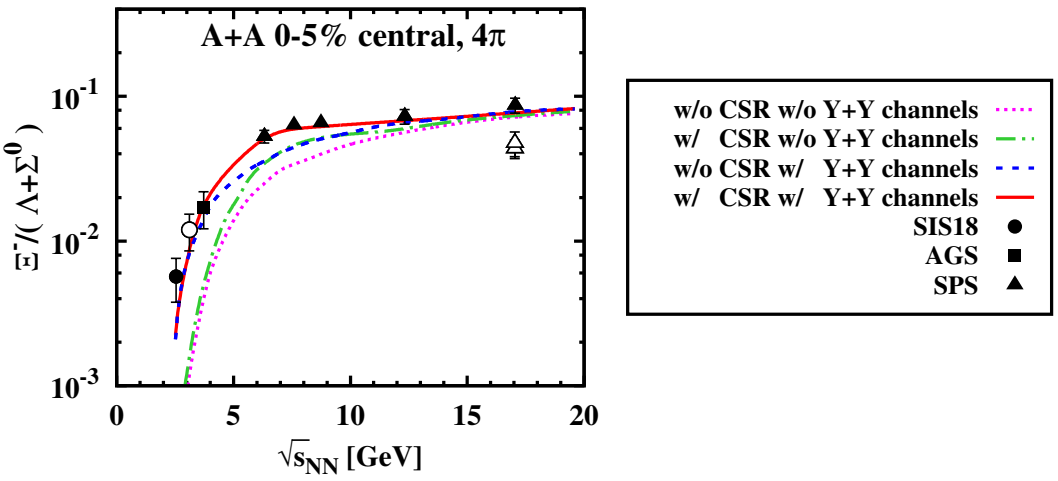

Figure 3.9: The full-acceptance ratio $\Xi^-/(\Lambda + \Sigma^0)$ as a function of the center-of-mass energy $\sqrt{s_{NN}}$ in central Au+Au collisions. The coding of the lines is the same as in Fig. 3.8. The filled symbols represent data for symmetric A+A collisions measured at SIS18 [112] (circle) at AGS [127] (square) and at SPS [120, 128] (triangles), while the open symbols are taken from Refs. [129, 130] and correspond to data measured in p+A collisions.

CSR, differently from the setting of the above analysis. The scenario of PHSD with $Y+Y$ channels and including CSR reproduces the experimental observation with a small discrepancy at low energies $\sqrt{s_{NN}} < 3\,\text{GeV}$. On the other hand, the alternative scenarios fail in describing the data apart from the top SPS point ($\sqrt{s_{NN}} = 17.2\,\text{GeV}$), where all calculations essentially merge. In fact, at $\sqrt{s_{NN}} = 17.2\,\text{GeV}$ the dominant production mechanism for hyperons is the hadronization of hadronic degrees of freedom and the contributions from flavor exchange reactions and CSR are negligible. Comparing the PHSD results with and without $Y+Y$ channels, we can infer that the $Y + Y$ channels give a significant contribution to the $\Xi^-/(\Lambda + \Sigma^0)$ ratio within the energy range $\sqrt{s_{NN}} = 2 - 6\,\text{GeV}$. The CSR mechanism is instead more effective in the dynamics for $\sqrt{s_{NN}} = 3 - 12\,\text{GeV}$, as the PHSD calculations with and without CSR do not overlap. Although the inclusion of the $Y+Y$ interaction does not provide a conclusive explanation of the extremely high Ξ^- yields measured by the HADES collaboration [112, 129] (SIS18 data points), it represents (within PHSD) a striking improvement of the hyperon production close to the threshold.

Chapter 4

Chiral symmetry restoration in heavy-ion collisions at intermediate energies

Heavy-ion collisions (HIC) are the unique experimental tool to probe nuclear matter at high temperatures and/or high densities. Experimentally, there is no direct insight to the collision process. One can detect only the final particle abundances and momentum distributions. Thus, it is not straightforward to relate the final observables to physical phenomena and to the production mechanisms happening during the different stages of the collision process. In this context, it is difficult to extract information about the restoration of chiral symmetry (CSR), that is expected to occur at high temperatures and/or high densities.
The crucial challenge is to identify signatures in the final particle distributions, which allow to understand if the system passed through a phase in which chiral symmetry is at least partially restored. In this Chapter we examine the role played by the restoration of chiral symmetry in the particle production as implemented in the PHSD approach. Then, we analyze particle abundances, spectra and ratios in A+A collisions in the energy range $\sqrt{s_{NN}} = 3 - 20\,\text{GeV}$.
This Chapter is based on the work published in Ref. [44, 82].

4.1 Scalar quark condensate

In this Section, we first investigate if in HIC the system undergoes a transition between a phase in which the chiral symmetry is broken to a phase in which the chiral symmetry holds. We recall that the scalar quark condensate $\langle\bar{q}q\rangle$ is an order parameter for this kind of transition. The scalar quark condensate $\langle\bar{q}q\rangle$ is expected to decrease from a non-vanishing value in the vacuum ($\langle\bar{q}q\rangle_V \approx -3.2\,\text{fm}^{-3}$) to $\langle\bar{q}q\rangle \approx 0$ corresponding to CSR at high density or temperature. In Fig. 4.1 we present the ratio $\langle\bar{q}q\rangle/\langle\bar{q}q\rangle_V$ expressed in Eq. A.1 as a function of x and z (for $y = 0$) at different times t for a central Au+Au collision at 30 AGeV. Before the

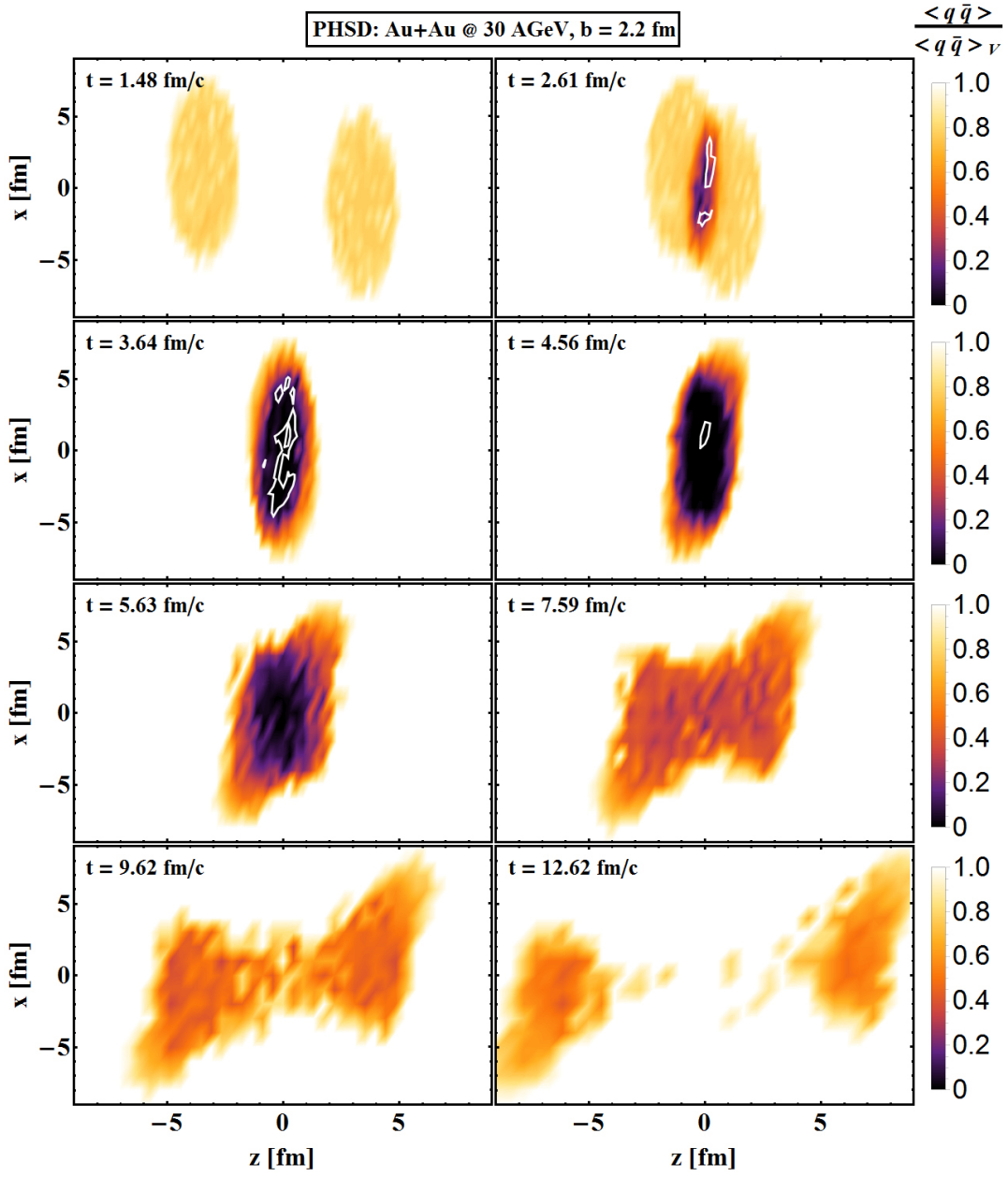

Figure 4.1: The ratio ratio $\langle\bar{q}q\rangle/\langle\bar{q}q\rangle_V$ expressed in Eq. A.1 as a function of x and z (for $y = 0$) at different times t for a central Au+Au collision at 30 A GeV employing the parameter set NL3 for the nuclear equation of state. The white borderline separates the space-time regions of deconfined matter to hadronic matter.

collision, the two impinging nuclei are characterized by a high value for the ratio $\langle\bar{q}q\rangle/\langle\bar{q}q\rangle_V$ ($\approx$ 70%). During the passage time (defined in Section 2.4) from about 2.6 fm/c to 6 fm/c, the overlap region reaches the highest values of baryon density and the scalar quark condensate practically vanishes. In the following expansion, the system dilutes and cools down, so

$\langle \bar{q}q \rangle$ recovers to the vacuum value. The white border-lines highlighted in Fig. 4.1 in the time interval between 2.61 fm/c to 4.56 fm/c separate the space-time regions of deconfined matter from those of hadronic matter. We find that in HIC a transition to CSR occurs and, in case of central collisions, a large volume is affected by CSR for a relatively long time interval lasting ≈ 4 fm/c. Similar considerations can be made for HIC at different energies, however, with some distinctions. At lower colliding energies, e.g. at 10.7 AGeV, the densities achieved in the overlap region are smaller. However, the passage time is larger compared to 30 AGeV. Overall, the system produced in low-energy collisions is considerably affected by CSR. At larger colliding energies, e.g. at 158 AGeV, the passage time is shorter, while the systems reaches larger densities. Thus, the scalar quark condensate vanishes, however, a larger region of the system is occupied by deconfined partons in the PHSD. Despite the high densities, the effect of CSR at 158 AGeV is expected to be negligible, since the CSR mechanism within PHSD is incorporated in the string decay and no strings can be formed in the QGP phase because of the vanishing string tension.
The results for $\langle \bar{q}q \rangle$ at 30 AGeV show that CSR takes place in HIC at the early stages of the collisions, but it is not possible to directly measure the scalar quark condensate in experiments. The CSR mechanism (as implemented in PHSD) affects the particle production via the string dynamics. Thus, we need to find indirect effects of CSR on experimentally measurable quantities.

4.2 Time evolution of the strange particle multiplicities

In this Section, we analyze the effect of CSR on the particle production in HIC focusing on the strange multiplicities. We provide in Fig. 4.2 an illustration of the time evolution of the strangeness content in central heavy-ion collisions. In panels (a), (c), (e) we show the number of particles N_s containing s-quarks (green lines) as a function of time (rescaled according to the collision time t_{coll}) in central Au+Au collisions at bombarding energies of 8, 30, 158 AGeV, respectively, while in panels (b), (d), (f) we plot the associated rates dN_s/dt of strange particles. The solid lines refer to the results of PHSD including CSR with NL1 parameters and the dashed lines refer to the results of PHSD without CSR. We see that at AGS and SPS energies the strange particle production takes place at the early stages of the collision process. More than $\approx 90\%$ of the strange content of the system is created in the time interval between 0 fm/c and 4 fm/c after the collision and already at about 10 fm/c the production of strange particles essentially ceases. Comparing the results at the different energies, we can see that the strangeness production is slower at lower energies. In fact, the peak of the total dN_s/dt shifts to smaller times with increasing energies, and for $E_{Lab} = 158$ AGeV the whole strangeness

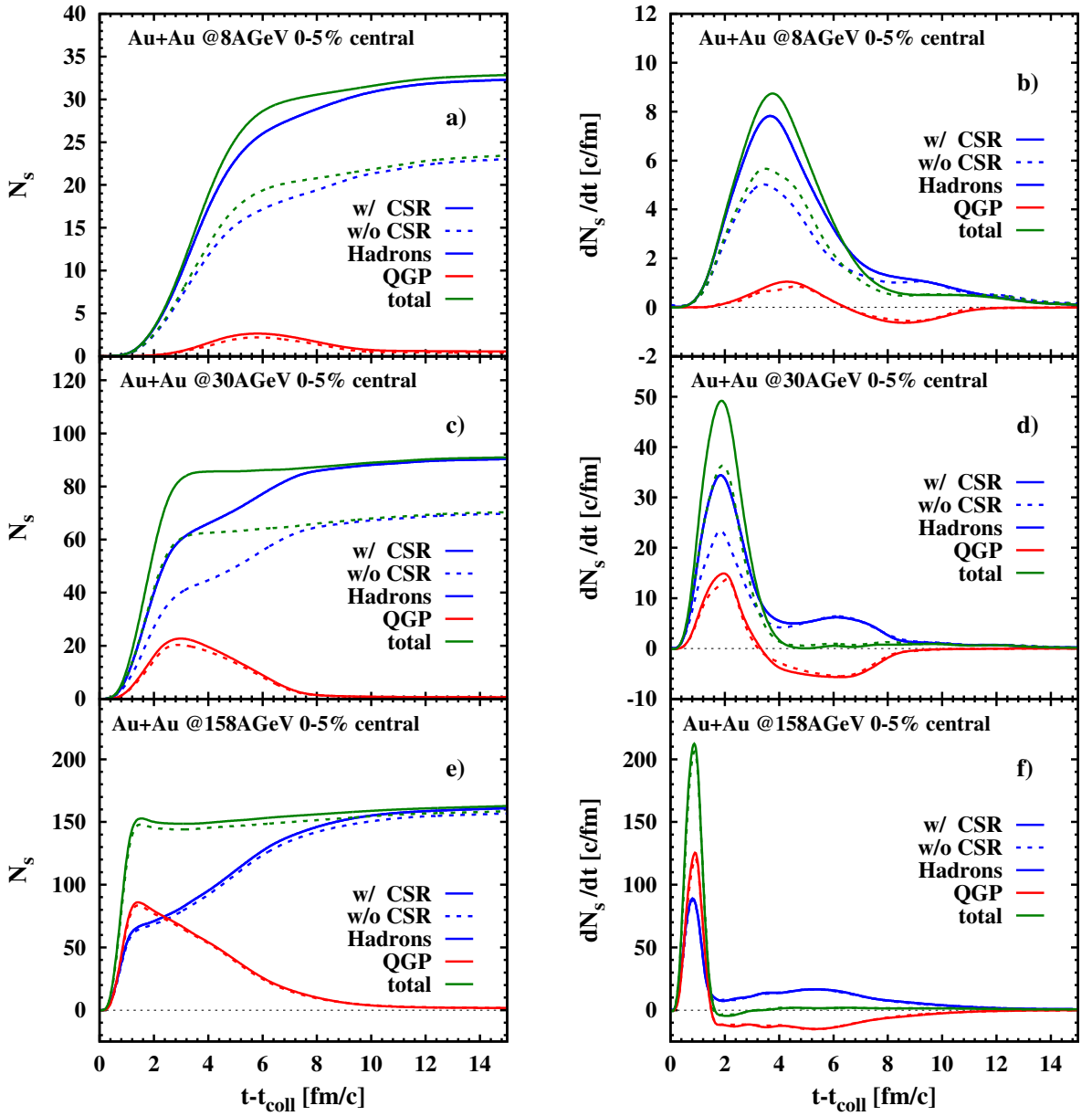

Figure 4.2: (l.h.s.) The strange particle number N_s as a function of time (rescaled according to the collision time t_{coll}) in 5% central Au+Au collisions at 8, 30, 158 AGeV in panels (a), (c), (e), respectively. (r.h.s.) The strangeness rate dN_s/dt as a function of $t - t_{coll}$ in 5% central Au+Au collisions at 8, 30, 158 AGeV in panels (b), (d), (f), respectively. The solid lines show the results from PHSD including CSR with NL1 parameters, while the dashed lines show the results from PHSD without CSR. The green lines refer to the total number of strange particles, while the blue and red lines refer to the hadronic and partonic contributions of the strangeness content, respectively.

production occurs within 2 fm/c. In Fig. 4.2 the total number of strange particles has also been separated in the corresponding hadronic and partonic contributions, represented by the blue and red lines, respectively. At the energies of 8 AGeV and 30 AGeV, the hadronic strangeness content is dominant relative to the partonic one. At 30 AGeV of collision energy, the partonic contribution reaches $\approx 28\%$ of the total strangeness content in correspondence of the maximum value of the partonic fraction. The production rate associated to the partonic degrees of freedom supersedes the hadronic one only for $E_{Lab} = 158$ AGeV. The strange quarks in the partonic phase do not appear immediately after the collision, as for the case $E_{Lab} = 30$ AGeV when they appear after about 1 fm/c. In fact, the primary interactions within the PHSD are realized via string excitation and after that, in the cells with energy density $\varepsilon > 0.5$ GeV/fm^3, the hadrons are dissolved into partons and mean-field energy. The partonic N_s distribution initially increases as a function of time, reaching a maximum at about 6 fm/c for $E_{Lab} = 8$ AGeV and at smaller times for larger bombarding energies. Then, at larger times, the energy density of the system decreases; as a result the partons hadronize by dynamical coalescence. We notice though that during the hadronization the total strange particle number is basically fixed, since there is no new creation of strangeness but a relocation of strangeness content from partonic to hadronic degrees of freedom. Moreover, further hadronic scattering processes do not create additional strangeness in the system, but they are only responsible for strange flavor exchange. We stress that the rates dN_s/dt include production as well as losses either due to dissolution of hadrons in the QGP or due to hadronization of strange partons. Accordingly, these rates become negative when dissolution or hadronization dominates. The total strange particle rate remains positive during the entire time evolution in panels (b) and (d) and shows a small negative rate only for $E_{Lab} = 158$ AGeV due to the dissolution of strange hadrons in the QGP. On the other hand, the partonic rate becomes negative at larger times since the hadronization ('loss') supersedes the strange quark production. The negative rate on the partonic content is balanced by the positive rate on the hadronic content due to strangeness conservation. The duration of the hadronization process becomes longer at higher bombarding energies, where a larger volume of the systems turns into the QGP phase, e.g. the hadronization lasts about 5 fm/c for $E_{Lab} = 30$ AGeV and about 8 fm/c for $E_{Lab} = 158$ AGeV.

Finally, we compare the strange particle amount computed in PHSD including (solid lines) and excluding (dashed lines) CSR in the string dynamics. The restoration of chiral symmetry causes a sizable increase ($\approx 30\%$) of the total strangeness content. We notice that CSR does not modify the time evolution of both $N_s(t)$ and dN_s/dt, but it only affects the hadronic contribution to the strange particle production. There is a small difference between the partonic results with and without CSR since the strange particle number in the partonic phase is slightly higher when including CSR. However, this is not due to a higher strangeness production in

the QGP, but stems from particles which are produced by string decay in the hadronic corona and travel to cells with energy density above ε_c during their propagation. Thus, such strange particles, although produced by the string decay, dissolve into partonic degrees-of-freedom. In this respect, the enhancement of the strange particle number in the hadronic phase drives a small increase also in the partonic contribution. The strangeness enhancement associated to CSR is most clearly visible at lower energies while at 158 AGeV it is very moderate. We find similar features in the results of the final particle rapidity spectra (see Section 4.3).
We infer that at 8 AGeV and 30 AGeV the steep increase of the number of strange particles as a function of time has to be attributed predominantly to the hadronic production, which occurs in PHSD via string formation and decay. Thus, CSR is found to play a crucial role in the strange particle production in HIC at AGS and low SPS energies. At higher energies, such as E_{Lab} = 158 AGeV, the dynamics and evolution of the system is ruled by partonic scattering process and mean-field energies. In general, the strangeness production occurs at the early stages and after $\approx$ 12 fm/c the strangeness content is entirely fixed and within PHSD the creation of strange particles ceases.

4.3 Rapidity spectra at AGS and SPS energies

In this Section we present results obtained within the PHSD for the rapidity distribution of the most abundant particles at AGS and SPS energies. We explore the following scenarios in order to disentangle the role of the CSR as well as the role of the partonic degrees of freedom:

- Scenario 1: PHSD calculations without CSR in dotted blue lines;
- Scenario 2: PHSD calculations including CSR with NL3 as parameter set for the nuclear EoS in solid red lines;
- Scenario 3: PHSD calculations including CSR with NL1 as parameter set for the nuclear EoS in dashed green lines;
- Scenario 4: HSD calculations without CSR in dash-dot orange lines;
- Scenario 5: HSD calculations including CSR with NL3 as parameter set for the nuclear EoS in solid orange lines.

We present in Figs. 4.3 – 4.5 the results of PHSD for the rapidity distribution of protons, $(\Lambda + \Sigma^0)$'s, pions and kaons for central nucleus-nucleus collisions at different energies (from AGS to top SPS energies) in comparison to the experimental data from Refs. [120, 131, 132, 133, 134, 135, 136, 137].

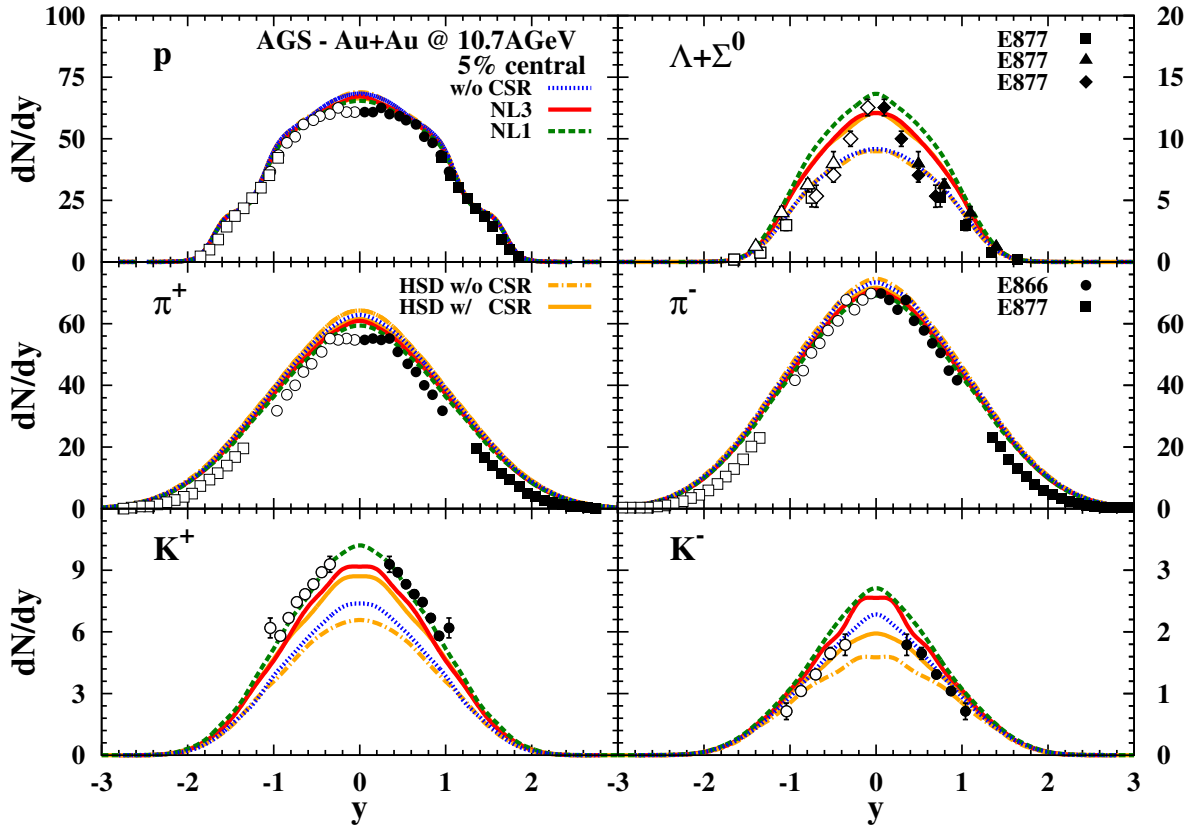

Figure 4.3: The rapidity distribution of protons, $(\Lambda + \Sigma^0)$'s, pions and kaons for 5% central Au+Au collisions at 10.7 AGeV in comparison to the experimental data from Refs. [131, 132]. The solid red lines show the results from PHSD including CSR with NL3 parameters, the dashed green lines show the results from PHSD including CSR with NL1 parameters, the dotted blue lines show the result from PHSD without CSR and the solid and dash-dot orange lines show the results from HSD with and without CSR, respectively.

In Figs. 4.3 and 4.4 the HSD results without CSR (Scenario 4) severely underestimate the K^+ and Λ production at the lower energies while overproducing pions. The inclusion of partonic degrees of freedom (Scenario 1) does not significantly change the rapidity distributions of the baryons compared to HSD at these energies. Actually this rough equivalence also holds for PHSD and HSD when including CSR (Scenarios 2 and 5, respectively) at 10.7 A GeV. The PHSD results from Scenarios 2,3 correctly reproduce the experimental observations of the $K^{\pm}$ and $(\Lambda + \Sigma^0)$ distributions. The restoration of chiral symmetry gives an enhancement of the strange particle yields both for mesons and baryons at 10.7 and 30 AGeV. On the other hand, it produces a slight decrease in the number of pions at midrapidity due to the suppression of pions in the string decays in favor of strange hadrons. The proton rapidity spectra do not

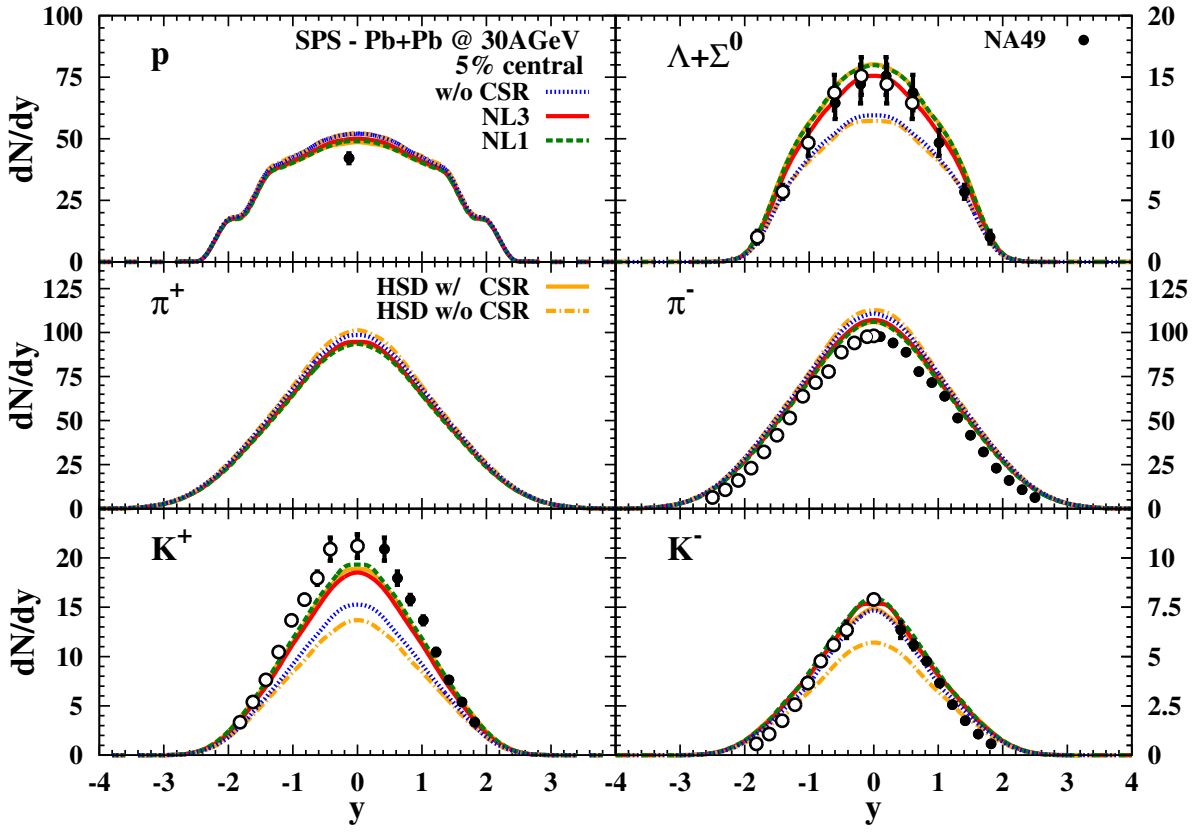

Figure 4.4: The rapidity distribution of protons, $(\Lambda + \Sigma^0)$'s, pions and kaons for 5% central Au+Au collisions at 30 AGeV in comparison to the experimental data from Ref. [120, 133, 134]. The coding of the lines is the same as in Fig. 4.3.

present any sensible variation. In fact, the CSR as implemented in PHSD modifies essentially the chemistry of the newly produced particles in the string decay and has a minor impact on the dynamics of the nucleons, which in the string picture are associated to the string ends of the primary interactions in the system. Furthermore, our calculations for the proton rapidity spectra are in good agreement with experimental observation at $E_{Lab} = 10.7$ AGeV, while at $E_{Lab} = 30$ AGeV both protons and pions are minimally overestimated at midrapidity in all explored scenarios which suggests that there is a small overestimation of the nuclear stopping. The hadronic equation of state also plays an important role. The effect of the different parametrizations NL1 and NL3 is investigated in PHSD in Scenarios 2 and 3, respectively. The results in Figs. 4.3 and 4.4 show a similar enhancement in the strangeness sector for both parametrizations. In particular, the NL1 set provides larger values for all strange particle rapidity spectra at midrapidity consistently with the discussion of Fig. 2.10 (r.h.s.). The difference between the two parametrizations represents the uncertainty of our results related to CSR as imple-

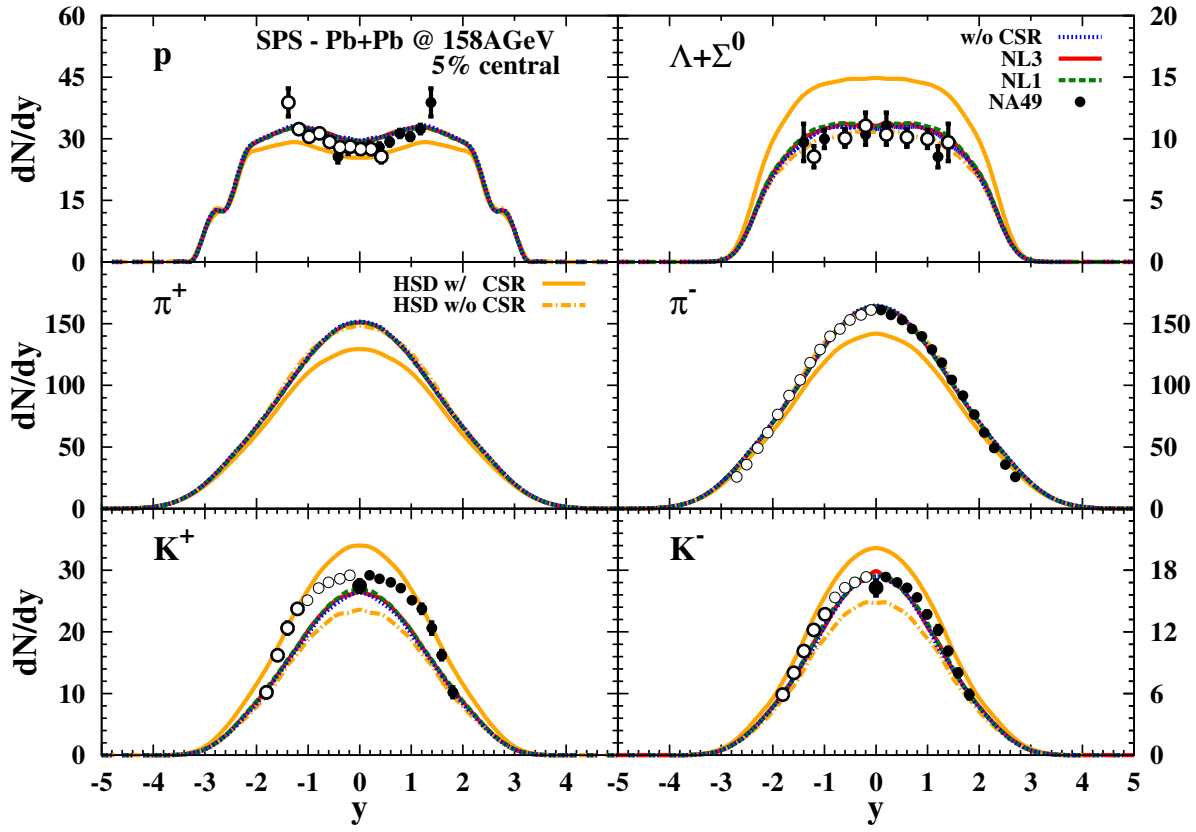

Figure 4.5: The rapidity distribution of protons, $(\Lambda + \Sigma^0)$'s, pions and kaons for 5% central Au+Au collisions at 158A GeV in comparison to the experimental data from Ref. [135, 136, 137]. The coding of the lines is the same as in Fig. 4.3.

mented in PHSD. We stress that this is not an attempt to tune the parameters of the equation of state in order to fit the data, but we employ different nuclear EoS to compute the scalar density (as explained in Section 2.5.2) in order to explore the uncertainties of our approach. At E_{Lab} = 30 AGeV (Fig. 4.4) the difference between the Scenarios 2 and 3 are slightly smaller compared to the corresponding results for E_{Lab} = 10.7 AGeV (Fig. 4.3). At the top SPS energy E_{Lab} = 158 AGeV (Fig. 4.5) the CSR does not play a significant role, since the dynamics is dominated by the QGP phase. This is clear when comparing the results from HSD (Scenarios 4, 5) with PHSD (Scenarios 1, 2, 3). Moreover, there is no appreciable difference between the results with and without CSR for the two different EoS. Our results for K^+ are lower with respect to the experimental data, however, the $(\Lambda + \Sigma^0)$ and K^- as well as the protons and the π^- are correctly reproduced. It is presently unclear where these final differences stem from, since strangeness conservation is exactly fulfilled in the PHSD calculations.

As additional investigation for the hadronic EoS, we consider NL2 as further parameter set.

	NL1	NL2	NL3
p	47.6	48.2	48.5
π^+	91.1	91.7	92.5
π^-	102.7	103.3	104.2
K^+	18.6	18.1	17.6
K^-	7.58	7.45	7.34
$\Lambda + \Sigma^0$	15.6	15.1	14.7
K^+/π^+	0.204	0.197	0.190
K^-/π^-	0.0738	0.0721	0.0704
$(\Lambda + \Sigma^0)/\pi$	0.0537	0.0516	0.0498

Table 4.1: Particle abundances and strange to non-strange particle ratios at midrapidity ($|y| \leq 0.5$) from 5% central Pb+Pb collisions at 30 AGeV for different parametrizations of the nuclear equation of state.

As we have seen in Fig. 2.9 in Chapter 2 the results for the strangeness ratio $\gamma_s(\varepsilon)$ are very similar for the parameter sets NL1 and NL2 for nuclear matter at $T = 0$. However, in HIC the different compression modulus leads to a slightly different baryon dynamics which also has an impact on the meson abundances and spectra. We provide in Table 4.1 the midrapidity yields for protons, pions, K^+, K^- and $(\Lambda + \Sigma^0)$ and associated ratios for the parameter sets NL1, NL2 and NL3 in case of central Pb+Pb collision at 30 AGeV. This is done to quantify the difference on the particle abundances between NL2 and the other two parametrizations, where the effect from CSR is most pronounced. There is a correlation between the proton and pion multiplicities. A higher stopping entails a higher proton and pion density with the order NL3 > NL2 > NL1. On the other hand, the strangeness abundances at midrapidity are anti-correlated with the proton density: the corresponding hierarchy is NL1 > NL2 > NL3. Although the hadron multiplicities do not dramatically depend on the parameter set, there is an enhanced effect in the ratios K^+/π^+, K^-/π^- and $(\Lambda + \Sigma^0)/\pi$ in the order NL1 > NL2 > NL3. We find that the calculations with the NL2 parametrization is always in between NL1 and NL3, hence we show on the final observables only the results corresponding to NL1 and NL3. Since any realistic nuclear EoS is expected to provide results within the limits of the parameter sets NL1 and NL3, we expect to obtain reliable limits on the uncertainties with respect to the nuclear EoS.
We have shown that the inclusions of the CSR and of the partonic degrees of freedom are essential ingredients in order to correctly reproduce the experimental data on the particle ra-

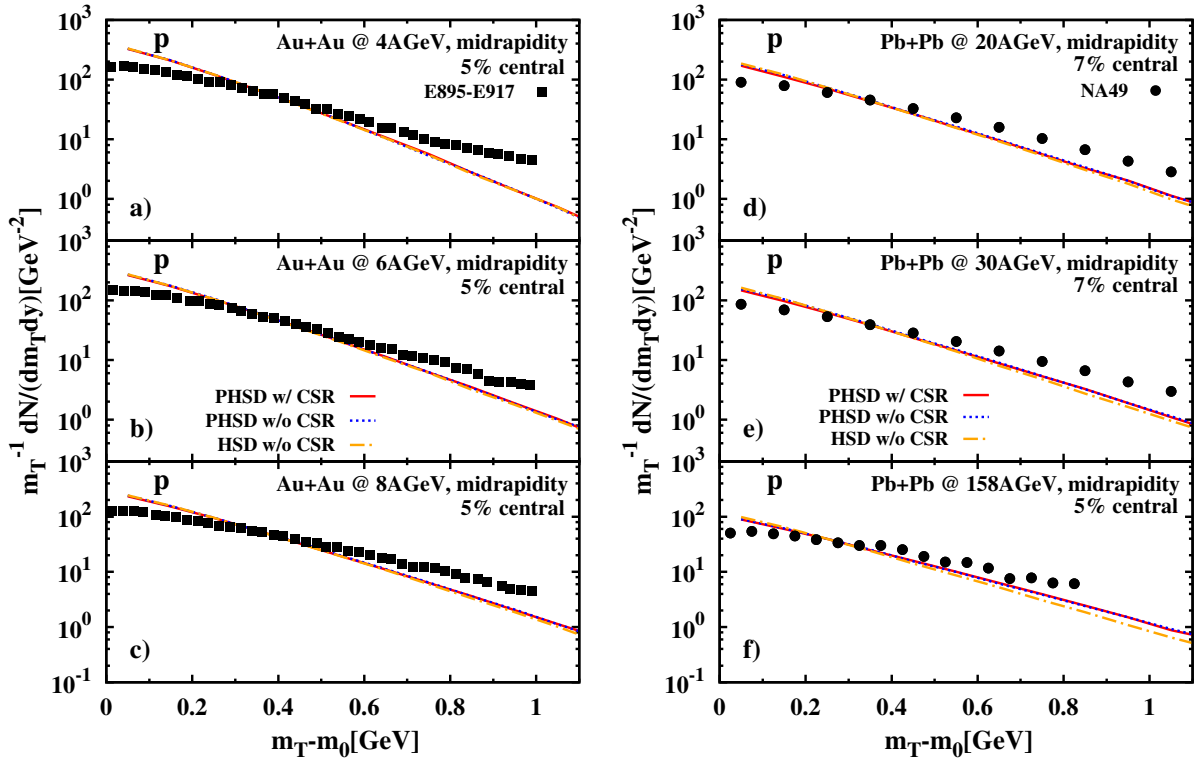

Figure 4.6: (l.h.s.) The transverse mass spectra of protons for 5% central Au+Au collisions at 4, 6, 8 AGeV in comparison to the experimental data from Ref. [138]. (r.h.s.) The transverse mass spectra of protons for 7% and 5% central Pb+Pb collisions at 20, 30, 158 AGeV in comparison to the experimental data from Ref. [139]. We show the results from PHSD including CSR with NL3 parameters by solid red lines, the results from PHSD without CSR by dotted blue lines and the results from HSD without CSR by dash-dot orange lines.

pidity spectra at $E_{Lab} = 10.7, 30, 158$ AGeV, as we can see especially for $(\Lambda + \Sigma^0)$ hyperons and K^+ mesons.

4.4 Transverse mass spectra at AGS and SPS energies

In this Section, we show the PHSD results for the transverse mass spectra of protons, pions and kaons for different energies in central Au+Au and Pb+Pb collisions in Figs. 4.6 and 4.7 in comparison with AGS and SPS data, respectively. We present here results from the Scenarios 1, 2, 4. The results on this observable are insensitive to the parameter set used for the EoS, so that Scenarios 2 and 3 are equivalent and we just present those from Scenario 2.
At AGS (l.h.s. of Fig. 4.6) and SPS (r.h.s. of Fig. 4.6) energies our calculations for the proton spectra (Fig. 4.6) show the same trend as the experimental data. However, we observe that

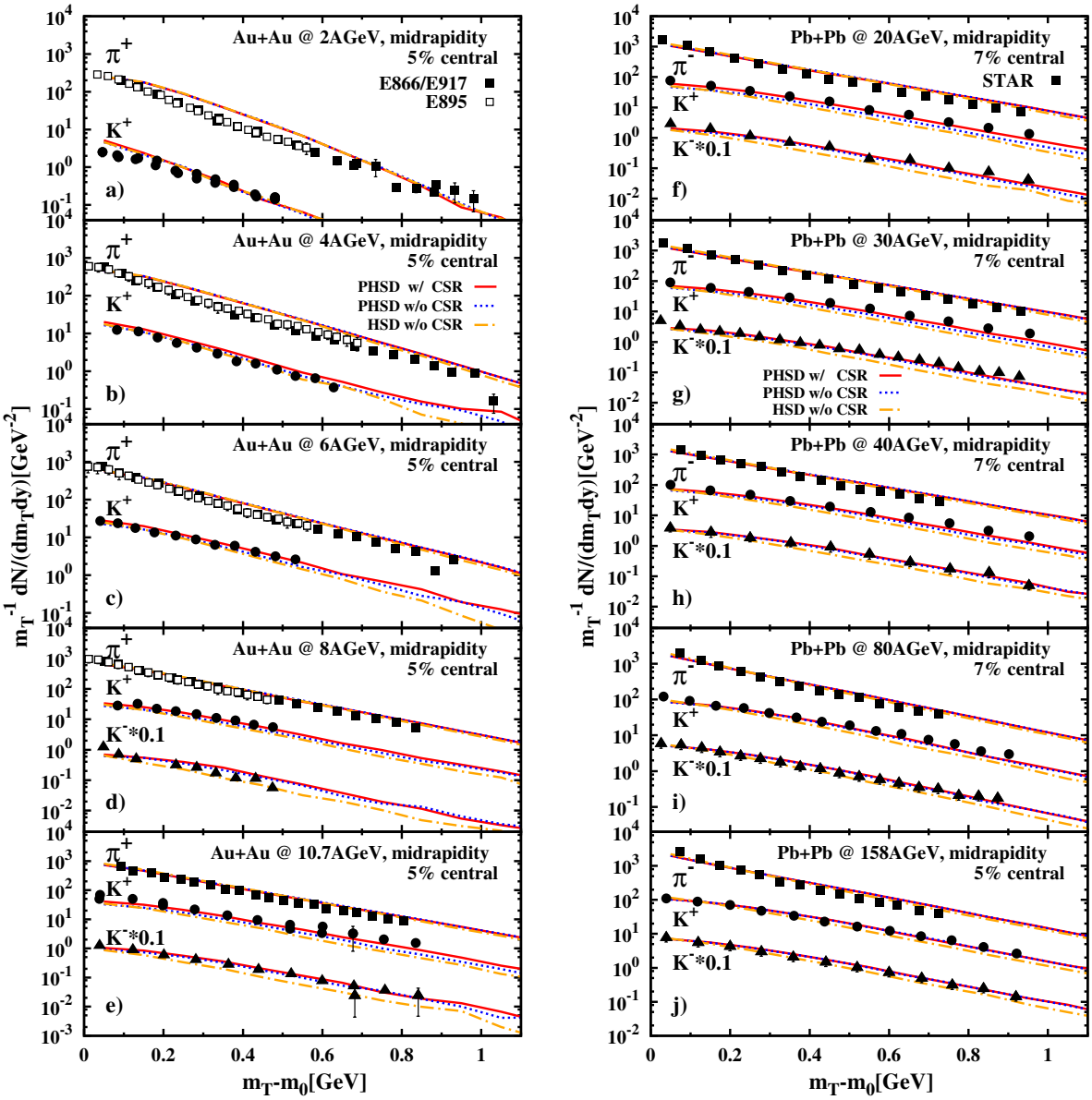

Figure 4.7: (l.h.s.) The transverse mass spectra of pions and kaons (K^- multiplied by 0.1) for 5% central Au+Au collisions at 2, 4, 6, 8, 10.7 AGeV in comparison to the experimental data from Refs. [140, 141, 142, 143]. (r.h.s.) The transverse mass spectra of pions and kaons (K^- multiplied by 0.1) for 7% and 5% central Pb+Pb collisions at 20, 30, 40, 80, 158 AGeV in comparison to the experimental data from Ref. [133, 135, 144]. The coding of the lines is the same as in Fig. 4.6.

the computed spectra are softer than the experimental data in this energy range. In fact, our results overestimate the data at low transverse mass m_T and underestimate the data at larger

m_T. We mention, however, that in our present calculations hadronic potentials have not been included and their inclusion can modify our results at AGS energies. Instead at SPS energies, the final particle spectra are insensitive to hadronic potentials, since the baryon densities in the final hadronic phase (after the hadronization of the partonic degrees of freedom) are rather low. We notice that CSR produces no change in the transverse mass spectra of protons, both at AGS energies and at SPS energies. The HSD calculations underestimate the data of the Pb+Pb collisions at SPS energies, while at AGS energies the difference between the HSD and PHSD results is smaller.

In Fig. 4.7 (l.h.s. and r.h.s.) we display the transverse mass spectra for pions and kaons in central Au+Au collisions at AGS energies and in Pb+Pb collisions at SPS energies, respectively. We focus on the role played by the CSR on the mesons transverse mass spectra. At the lower energies, $E_{Lab} = 2$ AGeV, there is no appreciable difference between the calculation with and without CSR, since the energy density reached by the system is not high enough to produce a vanishing scalar quark condensate. Instead, in the energy range $E_{Lab} = 4-40$ AGeV, we notice a small difference between Scenarios 1 and 2. As already mentioned, the CSR acts directly on the chemistry and not so much on the dynamics of the Schwinger mechanism, thus the effect of the partial restoration of chiral symmetry is rather small on the transverse mass spectra. The kaon spectra are harder when CSR is included, while the pion spectra remain essentially unchanged. At the higher SPS energies $E_{Lab} = 80, 158$ AGeV the dynamics of the system is ruled predominantly by the QGP phase and our calculations do not show any sensitivity to the inclusion of CSR. The agreement of our PHSD calculations with the data in Fig. 4.7 is good in all cases studied.

4.4.1 Strange particle abundances and ratios

The strangeness enhancement in A+A collisions with respect to elementary p+p collisions is considered as a signature of the creation of a QGP during the early stages of HIC [147, 148]. Gazdzicki and Gorenstein [6] identified the excitation function of the K^+/π^+ ratio as a clear observable to spot out the production of deconfined matter. In fact, they suggest that the horn feature in the behavior of the K^+/π^+ ratio as a function of the center-of-mass energy is due to the appearance of a QGP phase at $\sqrt{s_{NN}} \approx 7$ GeV.

In Fig. 4.8 we show the excitation function of the particle ratios K^+/π^+, K^-/π^- and $(\Lambda + \Sigma^0)/\pi$ at midrapidity from 5% central Au+Au collisions. We present calculations from all scenarios introduced in Section 4.3. The shaded area displays the uncertainties of our calculations emerging from the difference between Scenarios 2 and 3. The results from PHSD and HSD merge for $\sqrt{s_{NN}} < 4$ GeV and fail to describe the data in the conventional scenario without incorporating the CSR (Scenarios 1 and 4, respectively). Especially the rise of the computed

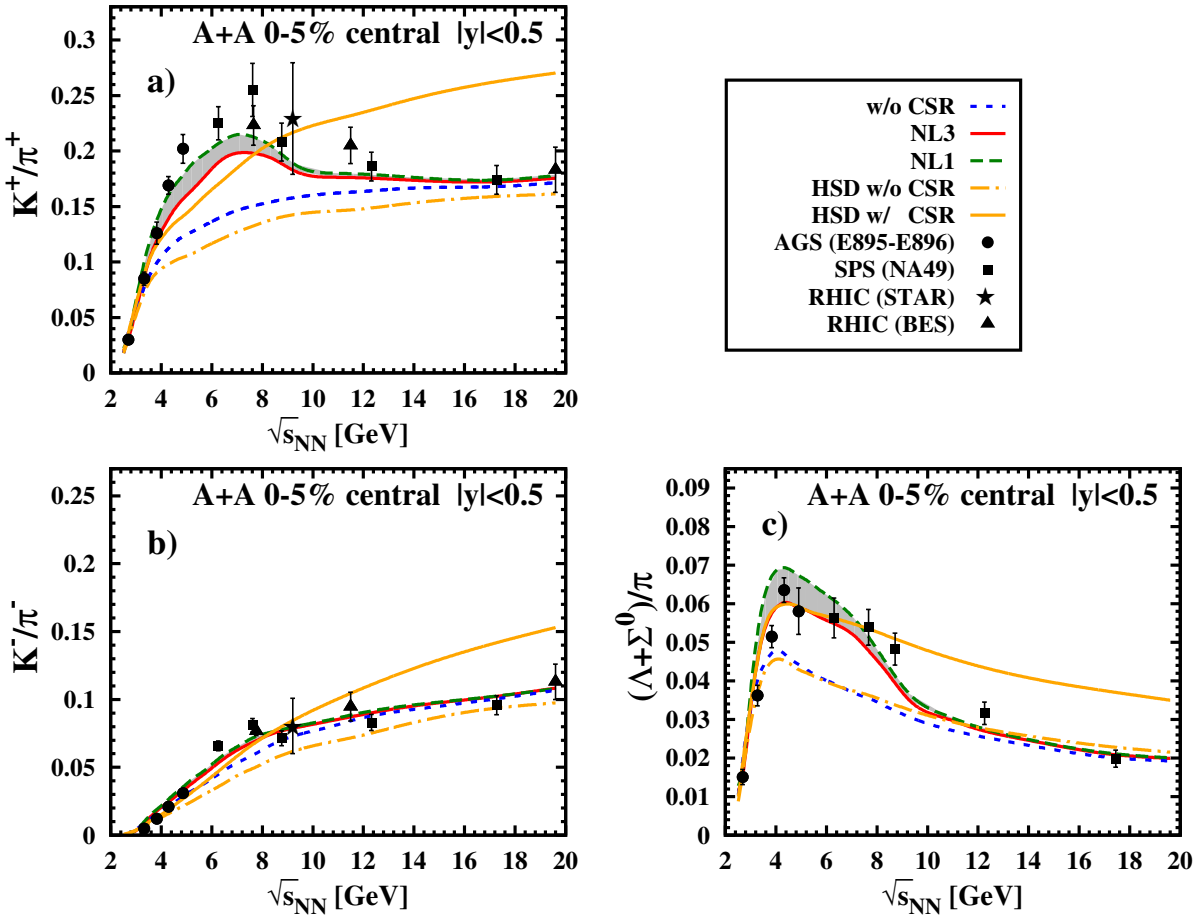

Figure 4.8: The ratios K^+/π^+, K^-/π^- and $(\Lambda + \Sigma^0)/\pi$ at midrapidity from 5% central Au+Au collisions as a function of the invariant energy $\sqrt{s_{NN}}$ up to the top SPS energy in comparison to the experimental data from [120, 143, 145, 146]. The coding of the lines is the same as in Fig. 4.5. The gray shaded area represents the results from PHSD including CSR taking into account the uncertainty from the parameters of the $\sigma - \omega$ model for the EoS.

K^+/π^+ ratio at low bombarding energies follows closely the experimental excitation function when incorporating CSR (Scenarios 2, 3 and 5). However, the drop in this ratio at ≈ 7 GeV is due to deconfinement since at higher bombarding energies the string decays in a hadronic medium cease. This is clearly seen in the case of HSD with CSR (Scenario 5) which overshoots the data substantially at high bombarding energy. The experimental observations of the ratio $(\Lambda + \Sigma^0)/\pi$ show a "horn"structure similar to the K^+/π^+ excitation function, which is reproduced by the PHSD calculations with CSR (Scenarios 2 and 3). At AGS energies, the energy dependencies of the ratios K^+/π^+ and $(\Lambda + \Sigma^0)/\pi$ are closely connected, since K^+

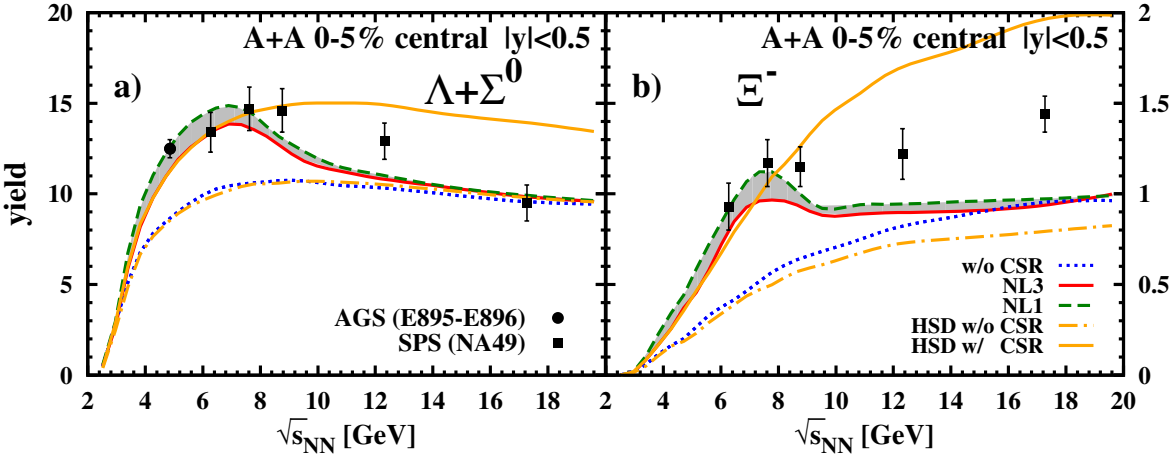

Figure 4.9: The yields of $(\Lambda + \Sigma^0)$ and Ξ^- at midrapidity from 5% central Au+Au collisions as a function of the invariant energy $\sqrt{s_{NN}}$ up to the top SPS energy in comparison to the experimental data from Refs. [120, 132]. The coding of the lines is the same as in Fig. 4.5 and for the shaded area see caption of Fig. 4.8.

and Λ (or Σ^0) are mostly produced in pairs due to strangeness conservation. As anticipated by the considerations in Sec. 2.5.2, the NL1 parameter set produces a sharper peak both in the K^+/π^+ and in the $(\Lambda + \Sigma^0)/\pi$ excitation functions with a $\approx$ 10% maximum increase with respect to the results with NL3. We point out that even adopting different parametrizations for the $\sigma - \omega$ model, we recover the same "horn"feature. This supports the reliability of the CSR mechanism as implemented in the PHSD model. Finally, the excitation function of the K^-/π^- ratio does not show any peak, but it smoothly increases as a function of $\sqrt{s_{NN}}$. In fact, especially at AGS energies, the antikaon production differs substantially from the production of K^+ and Λ, which occurs predominantly via string formation. In fact, the antikaons are produced mainly via secondary meson-baryon interactions by flavor exchange and their production is suppressed with respect to the Λ hyperons that carry most of the strange quarks. This is the reason why the inclusion of chiral symmetry restoration provides a substantial enhancement of the K^+/π^+ and $(\Lambda+\Sigma^0)/\pi$ excitation functions and a smaller change for the K^-/π^- ratio. We also notice that there is no sizeable difference between the NL1 and NL3 results for the K^-/π^- ratio. At top SPS energies the strangeness is produced predominantly by the hadronization of partonic degrees-of-freedom, thus our results for all the ratios do not show an appreciable sensitivity to the nuclear EoS and the calculations with and without CSR tend to merge at $\sqrt{s_{NN}} \approx 20$ GeV.

In Fig. 4.9 we present additionally the yields of $(\Lambda+\Sigma^0)$ and Ξ^- at midrapidity from 5% central Au+Au collisions as a function of the invariant energy $\sqrt{s_{NN}}$ in comparison to the available

data from Refs. [120, 132]. We recover a "horn"structure, similar to that shown in Fig. 4.8 for the energy dependence of the strange to non-strange particle ratios. A sensitivity on the nuclear model parametrizations persists at low energy, while in the top SPS energy regime the results corresponding to the Scenarios 1-3 merge. The comparison with the available data for $\sqrt{s_{NN}} < 8\,\mathrm{GeV}$ supports the validity of the CSR picture, while at larger energies we underestimate the experimental observations. Nevertheless, this discrepancy is not due to the CSR mechanism, since it does not play an essential role in the high-energy regime as pointed out above.

In conclusion, we attribute the strangeness enhancement, seen in the observables at AGS and low SPS energies, to the approximate restoration of chiral symmetry at high baryon density. Within the PHSD approach, the horn feature emerges in the energy-dependence of the K^+/π^+ and $(\Lambda + \Sigma^0)/\pi$ ratios. This is due both to CSR, which is responsible for the steep rise at low energies, and to the appearance of a deconfined partonic medium at higher energies, which is responsible for the drop at top SPS energies. This interpretation is in contrast to the early expectation in Refs. [6, 147] that the enhancement of strangeness should be attributed uniquely to the formation of deconfined matter.

Chapter 5

Directed flow

In Chapter 4 we have investigated particle abundances and spectra for A+A collisions. In this Chapter, we explore a different aspect of heavy-ion collision (HIC) observables, *i.e.* collectivity. A nucleus–nucleus collision should not be considered simply as a superposition of independent nucleon–nucleon collisions, but a collective behavior of the produced particles emerges due to the multiple collision processes. This Chapter is mainly devoted to the study of the directed flow, which is the first type of collective motion identified in heavy-ion collisions [149]. Moreover, we show the recent improvements achieved in the description of the differential hadron spectra produced in p+p collisions in the energy range between $E_{Lab} = 6\,\mathrm{GeV}$ and 158 GeV. This is needed also as a crucial ingredient for heavy-ion reactions.

5.1 Collectivity in HIC

The appropriate observable to study the collective phenomena is the azimuthal angular distribution $dN/d\phi$ of particles produced at a given transverse momentum p_T. If the nucleus–nucleus collision develops as a superposition of independent nucleon–nucleon collisions, the produced particles would be uniformly distributed in momentum space. On the contrary, experimental observations show asymmetries in the final momentum distribution of the particles, suggesting the existence of a collective behavior of the expanding system. In Fig. 5.1 we show a sketch of a heavy-ion collision to illustrate the anisotropies of the system, both in space (l.h.s.) and in momentum (r.h.s.) reference frame. Assuming z to be the beam axis, the reaction plane is defined by the z direction and the impact parameter b of the two colliding nuclei. During the passage time (defined in Section 2.4), the interaction between the participant nucleons generates a strong pressure gradient, which drives the system into an asymmetric configuration. This is more evident when the colliding nuclei have a non-vanishing impact parameter. While the system expands, the asymmetries in configuration

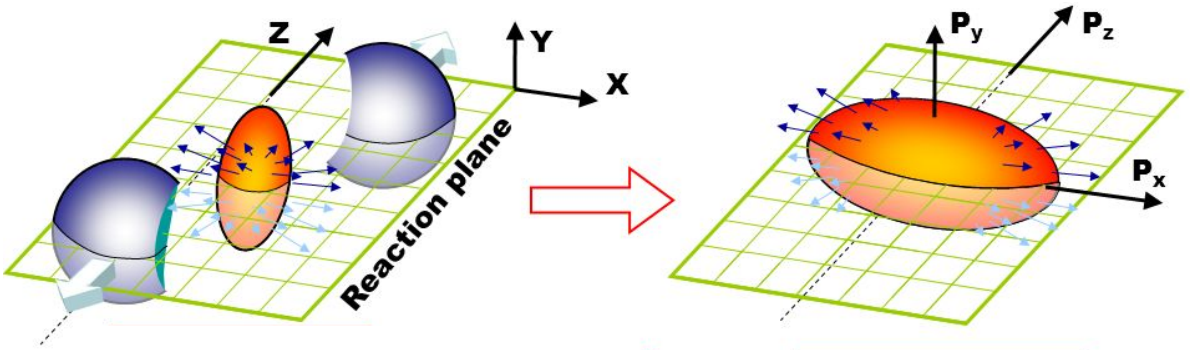

Figure 5.1: A sketch of a heavy-ion collision to illustrate that the asymmetries in configuration space (l.h.s.) are translated during the time evolution of the system into asymmetries in momentum space (r.h.s.). Courtesy by Hiroshi Masui (2008).

space (l.h.s. of Fig. 5.1) are translated into asymmetries in momentum space (r.h.s. of Fig. 5.1), which can be measured experimentally. These anisotropies in the momentum distribution of the produced particles can be conveniently described in terms of a Fourier expansion:

$$E\frac{d^3N}{d^3p} = \frac{1}{2\pi}\frac{d^2N}{p_T dp_T dy}\Big(1 + 2\sum_{n=1}^{+\infty} v_n \cos[n(\varphi - \psi_{RP})]\Big), \tag{5.1}$$

where E is the energy of the particle, p the momentum, φ the azimuthal angle, y the rapidity, and ψ_{RP} is the true reaction plane angle defined by the impact parameter and the beam axis in each single event and with $v_n = \langle cos[n(\varphi - \psi_{RP})]\rangle$ for $n = 1, 2, 3\ldots$. In this Fourier decomposition, the sine terms vanish due to the reflection symmetry with respect to the reaction plane. The first two coefficients v_1 and v_2 are called directed and elliptic flow, respectively:

$$v_1 = \left\langle \frac{p_x}{p_T} \right\rangle, \tag{5.2}$$

$$v_2 = \left\langle \frac{p_x^2 - p_y^2}{p_T} \right\rangle, \tag{5.3}$$

where $p_T = \sqrt{p_x^2 + p_y^2}$ is the transverse momentum.
The directed flow v_1 represents the deflection of the produced particles in the reaction plane with respect to the beam axis and it can be seen as a result of the bounce off of the particles in the heavy-ion collision. The directed flow as a function of the rapidity y can be approximated at midrapidity by a linear function, whose slope F is defined as:

$$F = \left.\frac{dv_1}{dy}\right|_{y=0}. \tag{5.4}$$

The magnitude of the absolute value of F is considered as an estimate of the intensity of the directed flow: the larger is $|F|$, the stronger is the flow. In addition, it is possible to distinguish the “normal flow”behavior, when the slope is positive, and the "antiflow" behavior, when the slope is negative. On the other hand, the elliptic flow v_2 measures the “squeeze-out”of the system: $v_2 > 0$ corresponds to a preferential emission of particles in the reaction plane, while $v_2 < 0$ refers to an out-of-plane emission, *i.e.* perpendicular to the reaction plane. Both the directed and the elliptic flows can provide valuable information about the Equation of State (EoS), the matter properties like hadronic potentials and Quark Gluon Plasma (QGP) viscosity. In particular, the beam energy dependence of v_1 has been suggested as a signature of the phase transition from nuclear matter to the QGP [150, 151, 152]. In fact, a first order phase transition gives a softening of the EoS, leading to a time-delayed expansion of the system. This feature would appear evident as a minimum in the excitation function of the directed flow, as suggested by hydrodynamical models [150, 151, 152]. In addition, the directed flow should also be sensitive to the pre-equilibrium stages of heavy-ion collisions since its onset occurs during the nuclear passage time [153]. The importance of these issues, already investigated in Refs. [154, 155], has been reconsidered in recent measurements from the STAR collaboration [156]. The inability of present theoretical models [150, 157, 158] to describe the observed behavior of the directed flow is called “directed flow puzzle”. In the following Sections, a study of the directed flow is addressed within the PHSD framework in comparison with data whenever possible.

5.2 The p_T-kick and the string rotation

A reliable description of the collective behavior of heavy-ion reactions requires a correct characterization of p+p collisions. In particular, a good reproduction of the transverse momentum spectra of hadrons produced in p+p collisions is needed for a robust determination of v_1 in A+A collisions, since the transverse momentum p_T is an essential ingredient for the calculation of the anisotropy coefficients like v_1 (see Eq. 5.2). In this respect, we introduce a p_T-kick to the constituent quarks and diquarks in the string interaction (see Chapter 2), which is the dominant particle production mechanism in nucleus-nucleus collisions at AGS and SPS energies. Throughout the fragmentation of the string, a transverse momentum is assigned to the string ends according to a probability distribution function, which by default is a Gaussian distribution in FRITIOF [159]. The inclusion of the p_T-kick corresponds to the use of the parametrization $f_{kick}(p_T)$ for the probability distribution function of the transverse momentum. This parametrization, which has been introduced in the transport approaches by Refs. [41, 42],

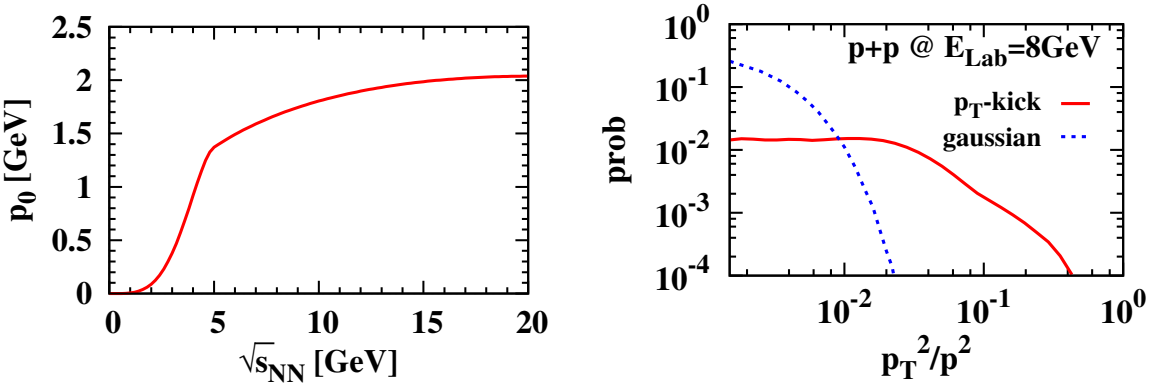

Figure 5.2: (l.h.s.) The maximum value of the transverse momentum p_0 of the parametrization $f_{kick}(p_T)$ (Eq. 5.5) as a function of the center-of-mass energy $\sqrt{s_{NN}}$.(r.h.s.) The probability distribution of the ratio of the square of transverse momentum transfer p_T^2 and the square to total momentum p^2 in the string interaction in p+p collisions at $E_{Lab} = 8\,\text{GeV}$. The solid red line refers to the p_T-kick recipe and the dashed blue line refers to the default Gaussian prescription of FRITIOF [159].

is expressed as:

$$f_{kick}(p_T) = (p_T^2 + c_1^2)(p_T^2 + p_0^2)(1 + e^{(p_T - p_0)/c_2})^{-1}, \tag{5.5}$$

where p_0 is the maximum value that can be assigned to the transverse momentum p_T and the two parameters are fixed to $c_1 = 0.1\,\text{GeV}$, $c_2 = 0.4\,\text{GeV}$ in agreement with Refs. [41, 42]. The value of p_0 is usually set to a constant value $p_0 = 1.4\,\text{GeV}$ [42] in order to describe the particle transverse mass spectra at large momentum in p+p collisions in the energy range $E_{Lab} = 10 - 20\,\text{GeV}$. In order to apply our approach in a broader range of energies, we extend the probability distribution function $f_{kick}(p_T)$ using an energy-dependent function for the maximum value of the transverse momentum $p_0(\sqrt{s_{NN}})$, that is displayed in the l.h.s. of Fig. 5.2. The parametrization $p_0(\sqrt{s_{NN}})$ is derived attaining m_T-scaling [161] of the hadron transverse mass spectra in p+p collisions in the energy range $E_{Lab} = 2 - 160\,\text{GeV}$. The value of p_0 smoothly increases as a function of $\sqrt{s_{NN}}$, reaching a saturation value of about 2 GeV at $\sqrt{s_{NN}} \approx 20\,\text{GeV}$. On the r.h.s. of Fig. 5.2, we show the probability distribution of the ratio of the square of transverse momentum transfer p_T^2 to the square of total momentum p^2 in the string interaction in p+p collisions at $E_{Lab} = 8\,\text{GeV}$, adopting both the $f_{kick}(p_T)$ parametrization (solid red line) and the default Gaussian prescription of FRITIOF [159] (dotted blue line). Compared to the Gaussian prescription, the $f_{kick}(p_T)$ parametrization provides a smaller value of the probability at low momenta and increases the probability at large momenta. As a consequence, the p_T-kick recipe gives a hardening of the transverse momentum spectra of the

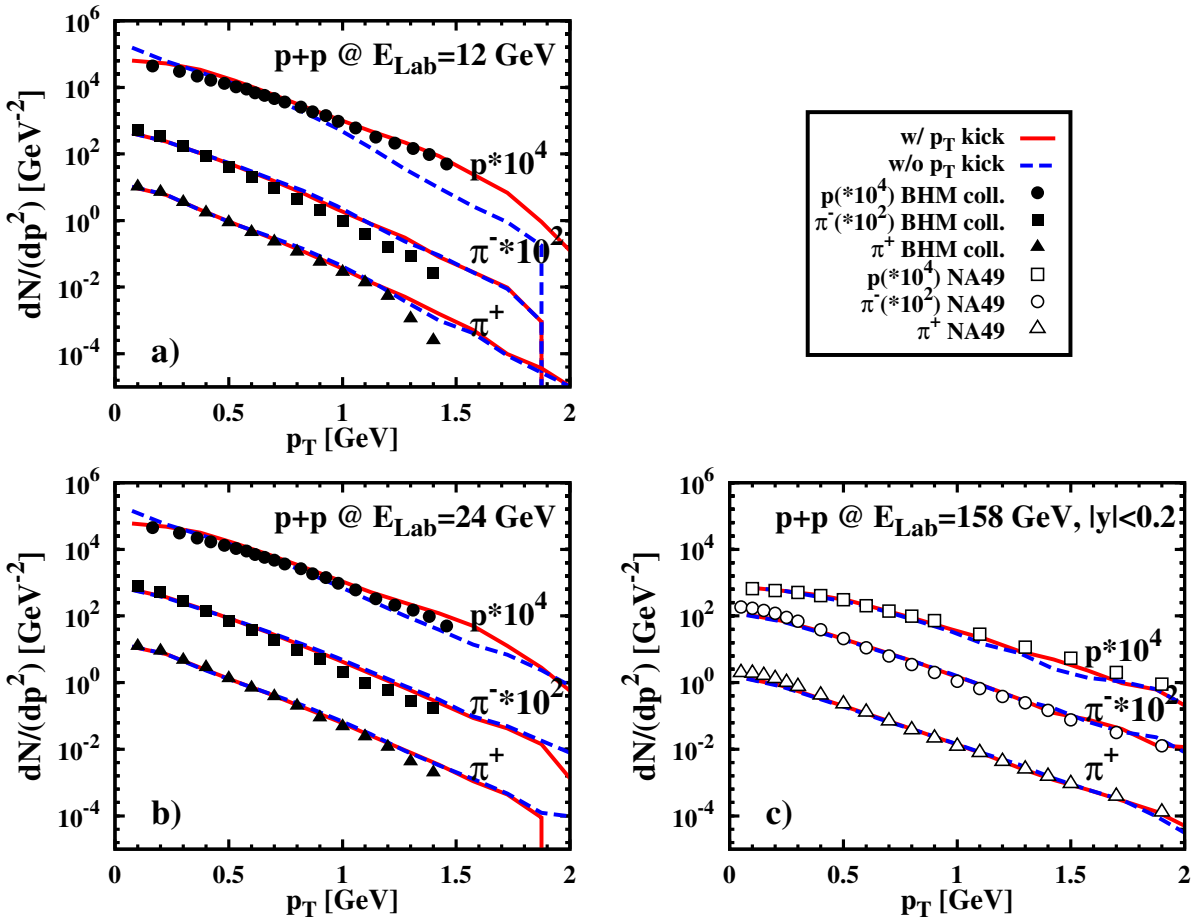

Figure 5.3: The transverse momentum spectra of protons (scaled by a factor of 10^4) and of the positive and negative (scaled by a factor of 10^2) pions for p+p collisions at E_{Lab} = 12, 24, 158 GeV (in panel (a), (b), (c) respectively) in comparison to the experimental data from Ref. [160]. The coding of the lines is the same as in Fig. 5.2.

produced hadrons in p+p collisions. This feature is essential to correctly describe the experimental data, which the default prescription of FRITIOF fails to reproduce. This is shown in Fig. 5.3, where we plot the transverse momentum spectra of protons and pions for p+p collisions at E_{Lab} = 12, 24, 158 GeV (in panel (a), (b), (c) respectively) in comparison to the experimental data from Ref. [160]. The hardening of the proton p_T-spectra is stronger at low energies (e.g. E_{Lab} = 12 GeV), while the pions are marginally affected by the p_T-kick. This is due to the fact that in the baryon-baryon string interaction the transverse momentum of the produced mesons, *i.e.* mostly pions, is given at the fragmentation of the string (via JETSET) while the p_T-kick acts on the soft momentum transfer of the string ends, that become the constituents of the final baryons, *i.e.* dominantly protons and neutrons. The hardening of the

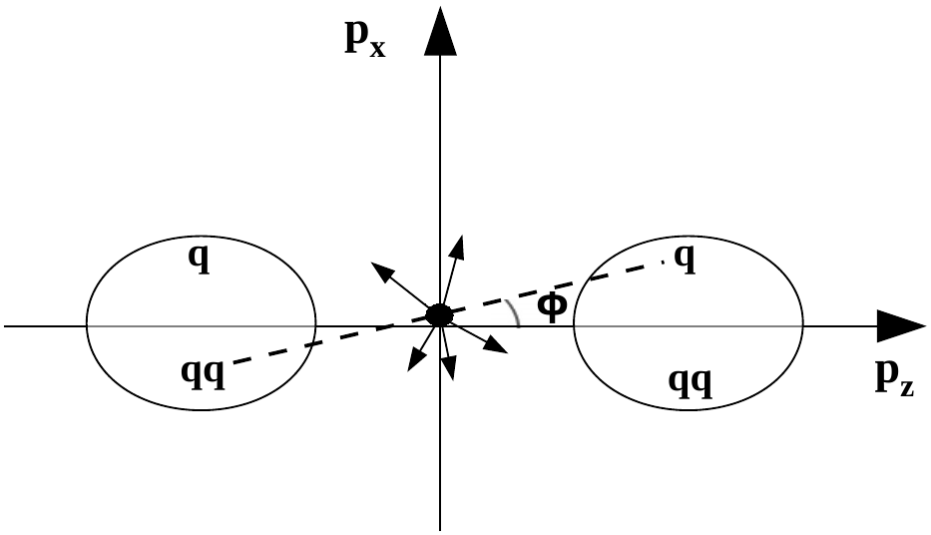

Figure 5.4: An illustration of one baryon-baryon string interaction in momentum space. The beam axis is fixed as the z-axis and we consider $p_y = 0$ for simplicity. The excited string is displayed by the dashed line connecting the diquark of the first nucleon with the quark of the second nucleon. The arrows starting from the middle of the string represent the particles emerging from the fragmentation of the string. The momentum rest frame of the string is rotated with respect to the center-of-mass frame of the two colliding nucleons by the angle ϕ.

transverse momentum spectra due to the p_T-kick in the nucleon-nucleon collisions is naturally translated in an analogous effect in heavy-ion reactions.
In addition to the p_T-kick, we distinguish a further source of hardening of the p_T-spectra in nucleus-nucleus collisions. Once a string interaction occurs in the PHSD simulation of nucleus-nucleus collisions, it is important to consider consistently the configuration of the excited string in momentum space. In fact, the momentum rest frame of the string is most likely rotated with respect to the center-of-mass frame of the two colliding nucleons, as it is illustrated in Fig. 5.4. Here the excited string is displayed by the dashed line connecting the diquark of the first nucleon with the quark of the second nucleon. The momentum rest frame of the string is rotated with respect to the center-of-mass frame of the two colliding nucleons by the angle ϕ. Within PHSD, the string dynamics and fragmentation are described within FRITIOF in the rest frame of the string. Consequently, it is necessary to calculate the momentum of the produced particles in the center-of-mass frame of the two colliding nucleons applying in each event the associated Lorentz transformation. This transformation is essentially a rotation in momentum space by the angle ϕ, as depicted in Fig. 5.4, and we refer to this procedure as "string rotation".
In Fig. 5.5 we analyze the role of both the p_T-kick and of the string rotation in the final trans-

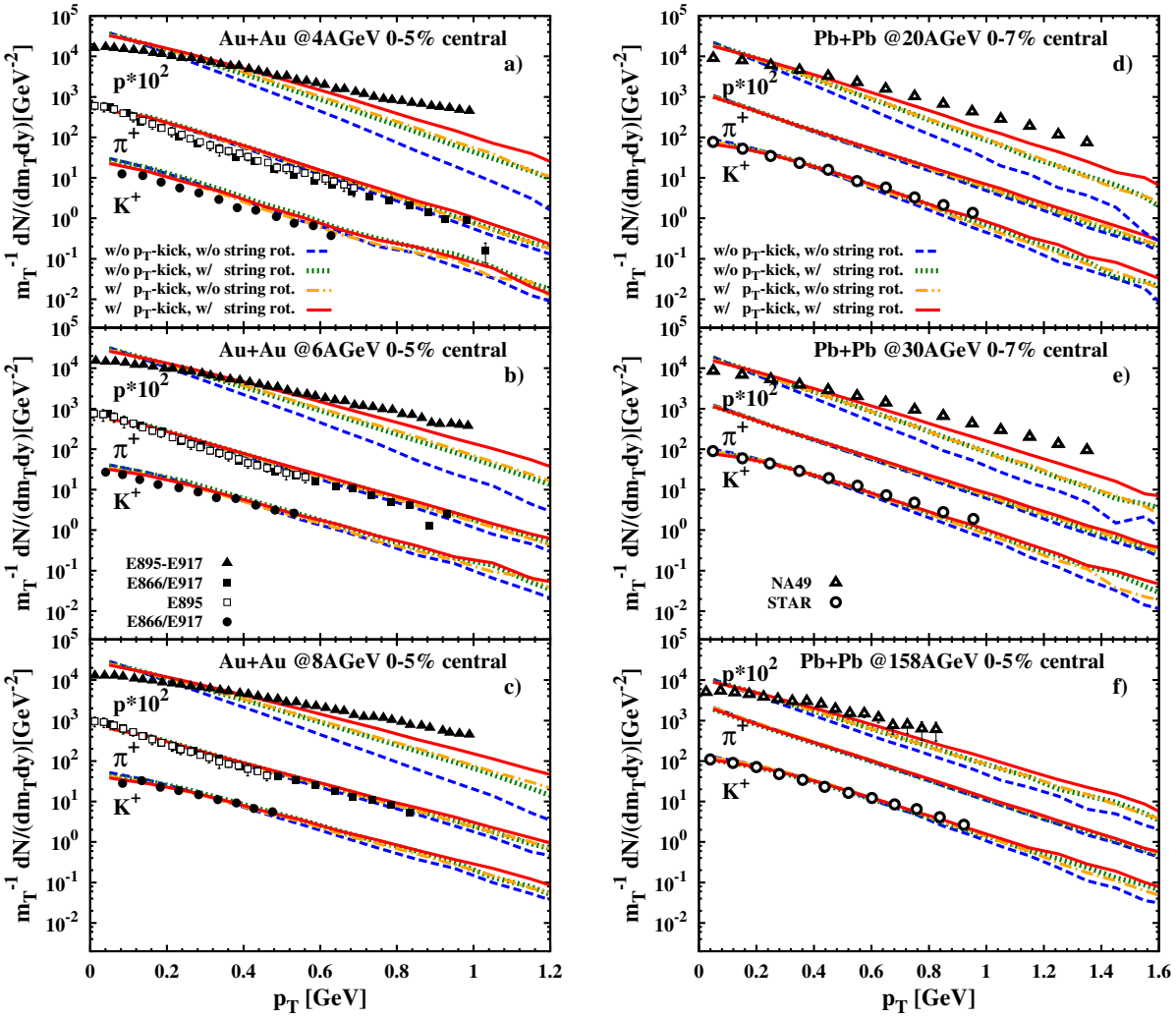

Figure 5.5: The transverse momentum spectra of protons (scaled by a factor of 10^2) and of the positive pions and kaons for central Au+Au collisions at $4, 6, 8$ AGeV (in panel (a), (b), (c), respectively) and for central Pb+Pb collisions at $E_{Lab} = 20, 30, 158$ AGeV (in panel (d), (e), (f), respectively). The dashed blue lines refer to the calculations excluding both the p_T-kick and the string rotation, the dotted green lines refer to the calculations including the string rotation but excluding the p_T-kick, the orange dash-dot lines refer to the calculations including the p_T-kick but excluding the string rotation, the solid red lines refer to the calculations including both the p_T-kick and the string rotation. We compare our results with experimental data from Refs. [138, 140, 141, 142, 143] for Au+Au collisions and from Refs. [133, 135, 139, 144] for Pb+Pb collisions.

verse mass spectra in central Au+Au collisions at $E_{Lab} = 4, 6, 8$ AGeV and in central Pb+Pb collisions at $E_{Lab} = 20, 30, 158$ AGeV. Both the p_T-kick and the string rotation produce a

hardening of the m_T-spectra at all investigated energies. Their effect is visible especially in the proton spectra. We notice that, differently from the p+p collisions shown in Fig. 5.3, the meson spectra are sizably modified by the inclusion of the p_T-kick. In fact, in A+A collisions not only baryon-baryon string interactions occur, but also meson-baryon and meson-meson string interactions take place and these are affected by the p_T-kick, too. Our calculations for pions and kaons show a good agreement with the data. On the other hand, the proton m_T-spectra are still softer than the experimental observations, but the inclusion of both the p_T-kick and the string rotation remarkably improve our calculations. Finally, we conclude that the p_T-kick and the string rotation are fundamental ingredients in the string dynamics within PHSD for the description of the momentum of particles produced in p+p and A+A collisions.

5.3 Time evolution of the particle momentum

It has already been mentioned that the directed flow develops at the early stages of heavy-ion collisions, basically during the nuclear passage time [153, 158]. Nevertheless, it is interesting to study in detail how the directed flow evolves in time and what is the behavior of v_1 among the particle species. In this respect, we calculate the average value of the x-component of the momentum $\langle p_x \rangle$ in semi-central (impact parameter $b = 6$ fm) Au+Au collisions at center-of-mass energies $\sqrt{s_{NN}} = 3.6, 7.7, 17.3, 62.4$ GeV. We recall that the directed flow differs from $\langle p_x \rangle$ only by the transverse momentum in the denominator (see Eq. 5.2), thus $\langle p_x \rangle$ and v_1 are characterized by the same time evolution. In Fig. 5.6 we show $\langle p_x \rangle$ at rapidity $|y| = 0.75$ for protons, pions and kaons. For $\sqrt{s_{NN}} = 3.6$ GeV (panel (a)) the protons (solid green line) acquire non-vanishing p_x during the nuclear passage time (defined in Section 2.4) of about 8 fm/c and the final value of $\langle p_x \rangle$ is reached essentially at $t - t_{coll} \approx 10$ fm/c. The following re-scattering marginally distorts the proton flow, which is then fixed almost entirely by the primary nucleon-nucleon collisions (so within PHSD by the string interactions). Increasing the energy, the nuclear passage time decreases, for example at $\sqrt{s_{NN}} = 7.7$ GeV (panel (b)) it is about 4 fm/c. In this case the proton $\langle p_x \rangle$ shows similar features to the corresponding results for $\sqrt{s_{NN}} = 3.6$ GeV. We notice though that the proton $\langle p_x \rangle$ marginally fluctuates up to $t - t_{coll} \approx 20$ fm/c. This is related to an increase of the meson-baryon interaction rate in addition to a non-vanishing contribution from the decay of heavy baryon resonances. At the larger energies $\sqrt{s_{NN}} = 17.3, 62.4$ GeV (panels (c) and (d)) the proton flow is established at later times $t - t_{coll} \approx 20$ fm/c, while the nuclear passage time is really short, $t - t_{coll} < 2$ fm/c. In fact, at large collision energies a large volume of the system undergoes firstly a phase transition to partonic degrees of freedom and secondly the hadronization, which lasts up to $t - t_{coll} \approx 10$ fm/c in case of $\sqrt{s_{NN}} = 17.3$ GeV (see Fig. 4.2 of Chapter 4). Next to this stage, the proton $\langle p_x \rangle$

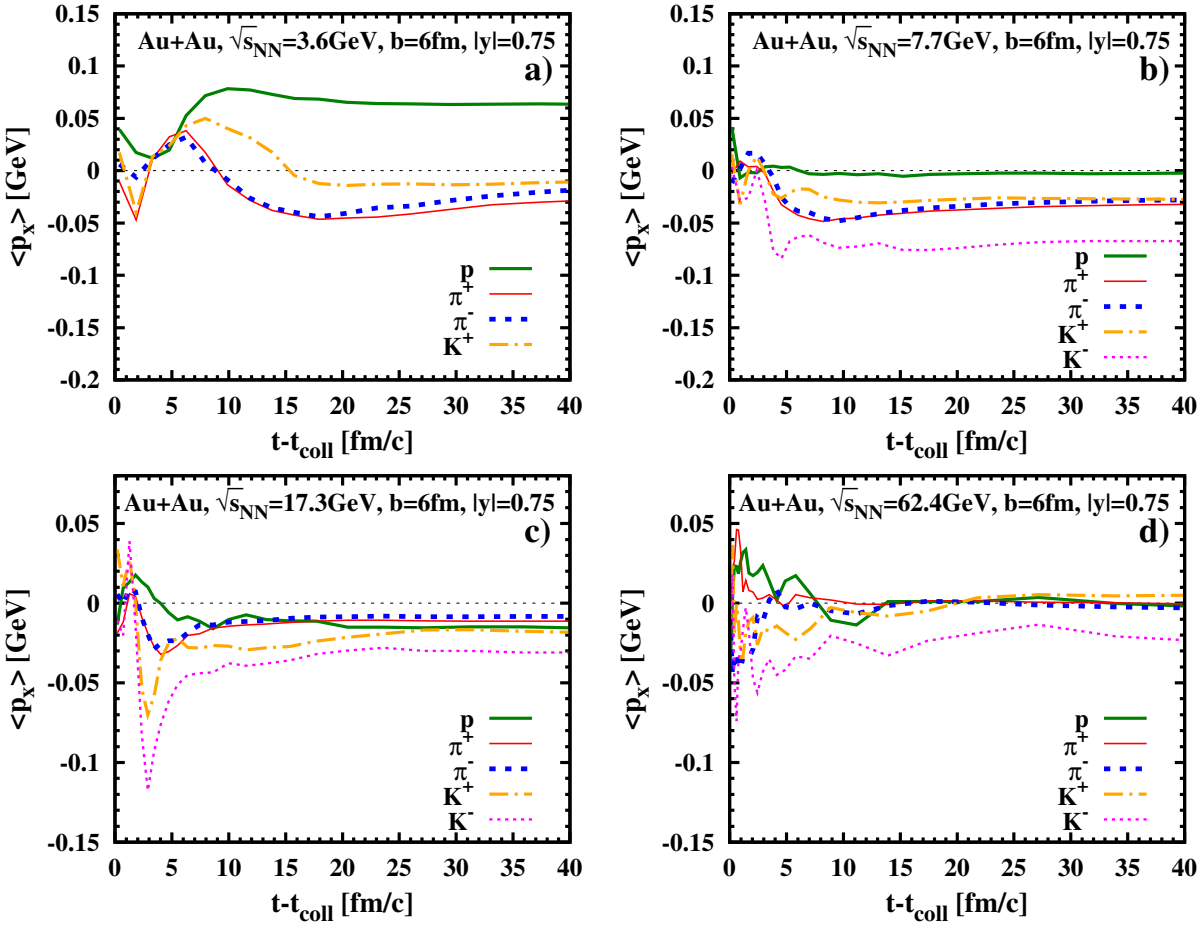

Figure 5.6: The time evolution of the average value of the x-component of the momentum $\langle p_x \rangle$ at rapidity $|y| = 0.75$ in Au+Au collisions with impact parameter $b = 6$ fm at center-of-mass energies $\sqrt{s_{NN}} = 3.6, 7.7, 17.3, 62.4$ GeV in panels (a), (b), (c), (d), respectively. The solid green line refers to the proton, the thin solid red line refers to the π^+, the dashed blue line refers to the π^-, the dash-dot orange line refers to the K^+, the dotted magenta line refers to the K^- meson. The time t is rescaled according to the collision time t_{coll}.

is still modified by the re-scattering especially by the meson-baryon interactions. Moreover, the final value of the proton $\langle p_x \rangle$ is positive at low energies, e.g. at $\sqrt{s_{NN}} = 3.6$ GeV, it almost vanishes at $\sqrt{s_{NN}} = 7.7$ GeV and it is negative at high energies $\sqrt{s_{NN}} = 17.3, 62.4$ GeV. Differently from protons, the mesons, both pions and kaons, are characterized by a negative final value of the flow for the all energies investigated. At the lower energy ($\sqrt{s_{NN}} = 3.6$ GeV, panel (a)) the $\langle p_x \rangle$ of the mesons initially highly fluctuates because of the low multiplicities of these particles which start appearing in the system. After this first stage, the flow of pions and kaons is positive and rises during the nuclear passage time, then it drops and turns to negative values

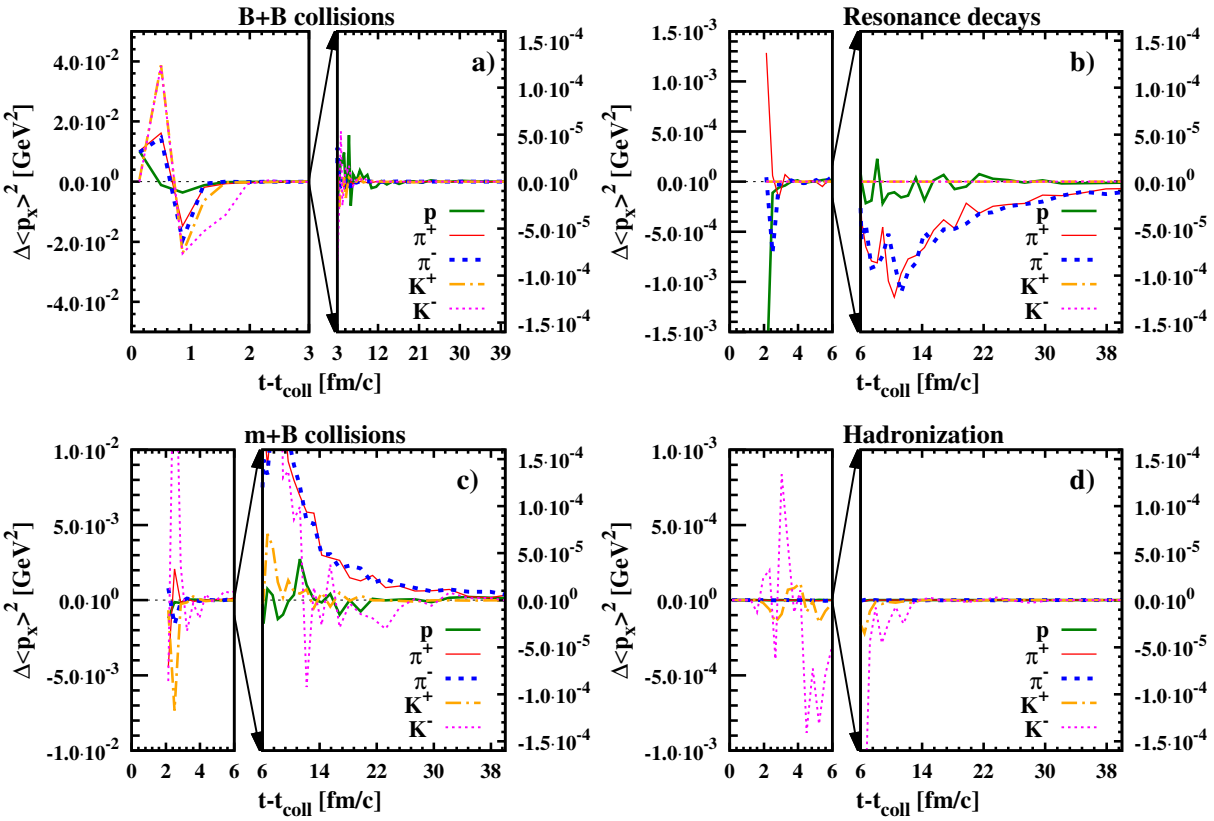

Figure 5.7: The time evolution of the variation of the square of the average x-component of the momentum $\Delta\langle p_x\rangle^2$ at rapidity $|y| = 0.75$ in Au+Au collisions with impact parameter $b = 6$ fm at the center-of-mass energy $\sqrt{s_{NN}} = 7.7$ GeV. We show the variation $\Delta\langle p_x\rangle^2$ due to baryon-baryon collisions in panel (a), to resonance decays in panel (b), to meson-baryon collisions in panel (c) and to the hadronization process in panel (d). Each panel is divided into two parts: on the left hand side $\Delta\langle p_x\rangle^2$ is shown at short times in a wide scale, on the right hand side $\Delta\langle p_x\rangle^2$ is shown at longer times in a small scale (the arrows indicate the change of the vertical range). The coding of the lines is the same as in Fig. 5.6.

as a result of the hadronic re-scattering. As a results, the $\langle p_x\rangle$ of kaons and pions achieves the final value at later times, $t - t_{coll} \approx 20$ fm/c and 30 fm/c, respectively, compared to the $\langle p_x\rangle$ of the protons. We mention that we did not include calculations for K^- at $\sqrt{s_{NN}} = 3.6$ GeV, since reliable results would need a considerable large amount of statistics due to the low multiplicities. We notice that the final values of $\langle p_x\rangle$ of the positive and negative pions differ of about $\approx 40\%$, while at $\sqrt{s_{NN}} = 7.7$ GeV they become almost equal. This is explained by the fact that at high energies a large fraction of the pions originates from the hadronization, where the momentum of the produced particles does not depend on the electric charge. On the other

hand, at low energies, the system proceeds as a chain of hadronic scatterings and particles with opposite electric charge can develop differently. At $\sqrt{s_{NN}} = 7.7\,\text{GeV}$ the mesons flow develops similarly to what we have found for $\sqrt{s_{NN}} = 3.6\,\text{GeV}$, while at $\sqrt{s_{NN}} = 17.3, 62.4\,\text{GeV}$ the meson flow is negative all along the time evolution of the system, apart from some low-multiplicities deviations. At high energies no excited strings can be formed and the behavior of the mesons $\langle p_x \rangle$ is determined by the hadronization of the partonic degrees of freedom, which generate a negative flow. Finally, the positive ad negative kaons share similar time evolutions but they exhibit different values of $\langle p_x \rangle$ in all cases investigated. This is due to the fact that they have different production mechanisms. In particular, at low energies most of K^- are produced in the hadronic re-scattering by flavor exchange reaction channels, while K^+ are produced dominantly by string fragmentation.

To understand the origin of $\langle p_x \rangle$, we address in Fig. 5.7 how the different reaction channels contribute in the change of the square of the average x-component of the momentum $\Delta\langle p_x \rangle^2$ as the system evolves in time. We show calculations for protons, pions and kaons in Au+Au collisions at $\sqrt{s_{NN}} = 7.7\,\text{GeV}$ with impact parameter $b = 6\,\text{fm}$ at rapidity $|y| = 0.75$ associated to baryon-baryon (B+B) collisions, to resonance decays, to meson-baryon (m+B) collisions and to the hadronization process in panel (a), (b), (c), (d), respectively. The B+B collisions (panel (a)) take place in the first time steps of the collision process and they produce modifications of $\langle p_x \rangle$ for all the particles studied. The B+B collisions are the main source of finite transverse momentum for the protons, which are moderately affected by the other reaction channels. The resonance decays (panel (b)) include the decays of the heavy resonances, *i.e.* Δ, $N(1440)$, $N(1535)$, Σ^* and Ξ^*, into lighter baryons and pions. Thus, kaons are not produced via these reactions and their corresponding $\Delta\langle p_x \rangle^2$ vanishes. Instead the $\langle p_x \rangle$ of both protons and pions is strongly modified by the resonance decays. For $t - t_{coll} < 4\,\text{fm/c}$ the variation in momentum of both protons and pions is large, with a maximum of about 10^{-3}, and at later times the $\Delta\langle p_x \rangle^2$ gets smaller, with a maximum of about 10^{-4} in case of pions. We notice that the resonance decays do not occur for times $t - t_{coll} < 2\,\text{fm/c}$, since the heavy resonances have to be created and they are mostly produced via string interaction with a formation time of $\tau_f \approx 0.8\,\text{fm/c}$. Moreover, we point out that the $\Delta\langle p_x \rangle^2$ associated to resonance decays is smaller than the one associated to the B+B collisions, but it does not vanish at later times as the $\Delta\langle p_x \rangle^2$ of B+B collisions. The m+B collisions (panel (c)) produce larger modifications for the $\langle p_x \rangle$ of mesons than for the $\langle p_x \rangle$ of protons. The $\Delta\langle p_x \rangle^2$ of both pions and kaons is finite and not vanishing almost in the whole time range investigated. Consequently, the m+B collisions are responsible for the fluctuations of the meson $\langle p_x \rangle$ (the final value of $\langle p_x \rangle$ is achieved at later times with respect to the proton case), as already mentioned above referring to Fig. 5.6. Finally, the hadronization process (panel (d)) does not change considerably

the transverse momentum of protons and pions, while kaons undergo larger modifications, although still much smaller compared to the other processes discussed above. Because of the low production rate of K^-, the results concerning this particle are affected by large statistical fluctuations. This might be diminished running long and computationally expensive simulations. However, studies on K^- at $\sqrt{s_{NN}} = 7.7, 17.3\,\text{GeV}$ indicate that the analysis presented here correctly describes the main features of the time evolution of $\Delta\langle p_x\rangle^2$. The major contribution to the transverse momentum of the particles coming from the hadronization arise within the time interval $2\,\text{fm/c} < t - t_{coll} < 12\,\text{fm/c}$.

5.4 Hadronic potentials

We have seen in Section 5.3 how the transverse momentum of particles originates from the different scattering processes. There is an additional source that can modify the particle momenta during the time evolution of the system. In fact, the produced particles propagate in a medium and they are sensitive to mean-field potentials. The impact of the hadronic potentials on the directed flow have been already studied in the past by transport models [155, 162, 163, 164, 165]. Here, it has been found that at SIS and AGS energies the directed flow (and even more the elliptic flow) shows a sensitivity to potentials and to the parametrizations of the equation of state adopted for the mean-field description. In addition, it has been suggested that these potentials show a dependence on the momentum of the particle for kinetic energies $E_{kin} > 200\,\text{MeV}$ (energies that can be achieved by the particles produced in HIC). In this Section, we introduce the potentials that we have incorporated in the particle propagation within PHSD and we address the main effects of this implementation on HIC observables.
In PHSD, the adopted mean-field model is the non-linear $\sigma - \omega$ model, that we have presented in Chapter 2, with different parametrizations for the nuclear equation of state, *i.e.* NL1, NL2 and NL3. Within this model, we can compute the scalar and vector contributions of the potential at fixed baryon density. The nucleon potential is then defined in terms of the Schrödinger-equivalent potential U_{sep} and expressed as:

$$U_{sep}(E_{kin}) = U_S + U_0 + \frac{1}{2M}(U_S^2 - U_0^2) + \frac{U_0}{M}E_{kin}, \tag{5.6}$$

where U_S is the scalar potential, U_0 is the time component of the vector potential, M is the nucleon mass and E_{kin} is the nucleon kinetic energy with respect to the local rest frame of the medium.
As mentioned above, an explicit-momentum dependence is established and we employ the following parametrizations f_S and f_V for the scalar and vector contributions, respectively:

$$f_S = \frac{1}{1 + p_{rel}/a}, \tag{5.7}$$

$$f_V = \frac{1}{1 + p_{rel}^2/b}, \tag{5.8}$$

where p_{rel} is the nucleon relative momentum with respect to the local rest frame of the medium, the parameter a is fixed as a =1 GeV and 2 GeV for the NL1 and NL3 equation of state, respectively, while the parameter $b = 1.7\,\mathrm{GeV}^2$ is the same for both NL1 and NL3.
These parametrizations describe the nucleon optical potential for $E_{kin} < 1$ GeV [166] and they are in fair agreement with previous studies in Refs. [155, 164] and with Dirac-Brueckner calculations [167, 168]. On the l.h.s. of Fig. 5.8 we plot the proton mean-field U_{sep} as a function of the momentum p_{rel}, as computed in PHSD with NL1 and NL3 parametrizations for the nuclear equation of state, for different baryon densities and at temperature $T = 0$ (the following considerations hold also in case of finite temperature). On the r.h.s. of Fig. 5.8 the effective potential extracted from Ref. [169] is shown. This parametrization for the potential follows the same momentum dependence of the NL3 equation of state given by Eqs. 5.7 and 5.8. We emphasize that experimental data on the nucleon optical potential are avaliable only for $E_{kin} \leq 1$ GeV. Consequently, extrapolations to larger momenta have to be considered with care. The explored scenarios for U_{sep} share similar features. With decreasing baryon density the potential decreases at fixed momentum (apart from a deviation in case of the effective potential at $\rho = \rho_0/2$ for low momenta)[1]. The proton potential increases with increasing momentum up to $p_{rel} = 1$ GeV and then it smoothly decreases with increasing p_{rel}. The results obtained with the three different settings are comparable at $\rho = \rho_0$. Despite these similarities, we detect some significant differences. For densities larger than the nuclear matter density, the lines associated to NL1 are below the corresponding results for NL3. Thus, the NL3 parametrization produces a much stronger repulsive potential than NL1. Moreover, the NL1 and NL3 paremetrizations (l.h.s. of Fig. 5.8) exhibit in the whole range of momenta only a repulsive behavior of the potential for $\rho \geq 2\rho_0$, while the effective potential (r.h.s. of Fig. 5.8) is characterized by an attractive behavior at low momenta even for large densities. Only for the largest density investigated here the effective potential results to be repulsive at low momenta. Our aim is now to probe the effect on HIC observables when including these parametrizations for the potentials in the particle propagation in PHSD. The potentials introduced above are incorporated in the baryonic sector and weighted according to the light quark content of the baryon.
First, we analyze the effects of the potential on the directed flow of proton and pions. In

[1]The normal nuclear density is $\rho_0 = 0.166\,\mathrm{fm}^{-3}$.

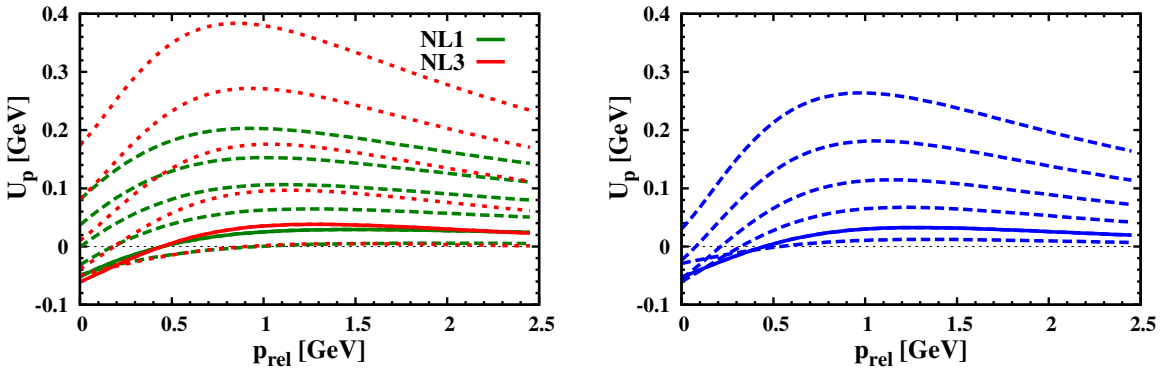

Figure 5.8: The mean-field proton U_{sep} as a function of the momentum p_{rel}. On the l.h.s. the potentials are computed within the non-linear $\sigma - \omega$ model adopting the NL1 (green lines) and NL3 (red lines) parametrizations. On the r.h.s. the effective potential extracted from Ref. [169] is shown. Each line refers to a fixed baryon density, increasing from $\rho_0/2$ (lowest line) to $3\rho_0$ (highest line) with steps of $\rho_0/2$. The solid lines refer to the calculations at ρ_0.

Fig. 5.9 we show v_1 as a function of y for protons and π^+ at $\sqrt{s_{NN}} = 3.6$ and 11.5 GeV. The potentials induce clear modifications of the directed flow only at the lowest energy. The PHSD calculations without potentials give a stronger proton flow than with potentials (the value of $|F|$ is larger in the former case than in the latter). Thus, we recognize altogether an attractive effect of both NL1 and the effective potential on v_1, but more pronounced in the second case. Instead, in the case of π^+ there are only fluctuations on the results and we are not able to isolate a specific modification caused by the inclusion of the baryon potentials. The small fluctuations observed in the directed flow of the π^+ arise since, even though pions are not directly affected by the potentials (included only in the baryon sector), they interact with protons, whose propagation is modified by the potentials as seen above. At larger collision energies (e.g. at $\sqrt{s_{NN}} = 11.5$ GeV) we do not detect any sensitivity on the hadronic potential since the system dynamics is dominated by the propagation of partonic degrees of freedom. In the partonic phase the mean-field properties of the system are given by the Dynamical Quasi-particle Model (DQPM) described in Chapter 2, and the potentials considered here do not apply. After the hadronization, the action played by the baryonic potential in the particle propagation is negligible due to the low baryon densities in the expanding system.

Second, we look at the possible contributions of the potential in the particle spectra. We restrict our analysis to the rapidity spectra of proton, $(\Lambda + \Sigma^0)$, π^+ and K^+ at $\sqrt{s_{NN}} = 3.6$ GeV, where we have found more remarkable effects of the potentials on v_1. The inclusion of the potentials (both for the NL1 and for the effective potentials) does not produce any sizable modifications of the particle spectra, as seen from Fig. 5.10. We only identify small fluctuations in the

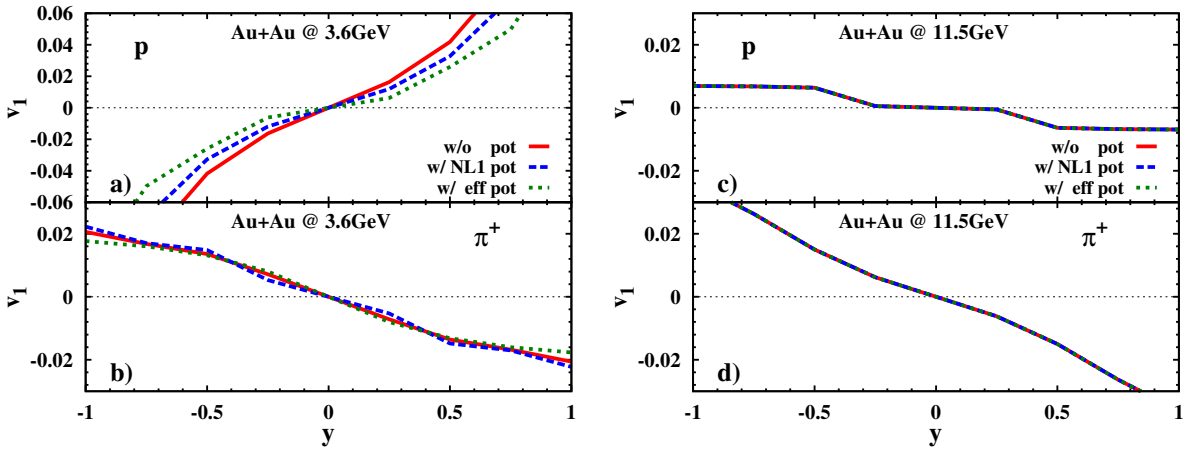

Figure 5.9: The directed flow v_1 of protons and positive pions as a function of the rapidity y for mid-central (10 - 40% centrality) Au+Au collisions at $\sqrt{s_{NN}}$ = 3.6 GeV (l.h.s.) and $\sqrt{s_{NN}}$ = 11.5 GeV (r.h.s.). The solid red lines refer to the calculations without hadronic potentials, while the dashed blue lines refer to the calculations including the hadronic potential with NL1 parametrizations and the dotted green lines refer to the calculations including the effective hadronic potential according to Ref. [169].

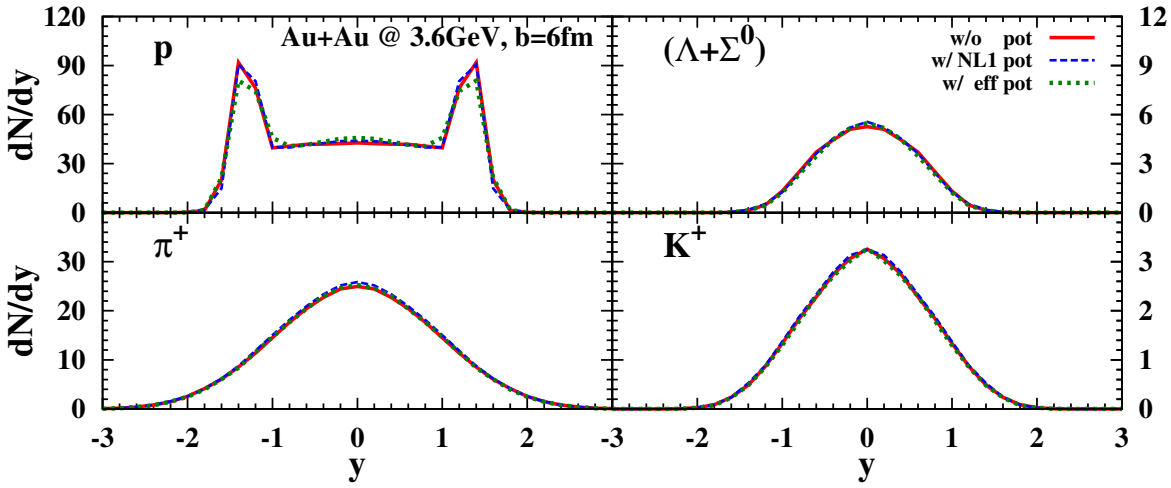

Figure 5.10: The rapidity distribution of protons, $(\Lambda + \Sigma^0)$'s, π^+ and K^+ for 10 - 40% central Au+Au collisions at $\sqrt{s_{NN}}$ = 3.6 GeV. The coding of the lines is the same as in Fig. 5.9.

proton spectra. We find that these considerations also hold for larger energies, e.g. at $\sqrt{s_{NN}}$ = 11.5 GeV.

We conclude that the proton directed flow is mildly sensitive to the baryonic potential at low energies, while the particle rapidity spectra are insensitive to a large extent. Further results on v_1 with and without potentials will be given in Section 5.6.

5.5 Experimental cuts and centrality dependence

In this section we study the sensitivity of the directed flow v_1 on analysis parameters and experimental settings. More specifically, we investigate the dependence of v_1 on experimental cuts and centrality. The aim is to understand if the experimental cuts (required to have a consistent comparison with experimental data) change the PHSD results on the directed flow. The following calculations from PHSD including Chiral Symmetry Restoration (CSR) are performed using hadronic potentials in the baryonic propagation according to the NL1 parametrization for the nuclear equation of state. All considerations below can be generalized to the other scenarios explored within PHSD, e.g. PHSD without CSR, PHSD without hadronic potentials etc..
The first aspect investigated here is how the PHSD results on v_1 are modified if we apply the cuts associated to the analysis of experimental measurements. The experimental cuts are finite ranges on the transverse momentum p_T due to the experimental acceptance [154]. For example, the STAR reconstruction analysis enforces the following cuts (see Ref. [156] for details):

- protons with $0.4\,\text{GeV} < p_T < 2.0\,\text{GeV}$;
- pions and kaons with $p_T > 0.2\,\text{GeV}$ and total momentum $p < 1.6\,\text{GeV}$.

We refer to these analysis settings as p_T-cuts.
In Fig. 5.11 we examine the sensitivity on the p_T-cuts for v_1 of the protons and positive pions as a function of the rapidity y for mid-central (10 - 40% centrality) Au+Au collisions at $\sqrt{s_{NN}} = 3.6\,\text{GeV}$ and $\sqrt{s_{NN}} = 11.5\,\text{GeV}$ (on the l.h.s. and r.h.s. respectively). We do not change the evolution dynamics within the PHSD simulation, but we solely modify the analysis procedure to compute v_1 at the end of the PHSD simulation, applying (or not) vetoes on the p_T of the examined particles. The results for v_1 are marginally modified when we include the p_T-cuts in the analysis, as seen from Fig. 5.11. Concerning the proton case, the p_T-cuts tilt the tails of the directed flow at large rapidities for the collision at $\sqrt{s_{NN}} = 3.6\,\text{GeV}$, while at 11.5 GeV there is no difference between the results with and without p_T-cuts. The results on the pion flow are modified by the inclusion of the p_T-cuts at both collision energies. At $\sqrt{s_{NN}} = 3.6\,\text{GeV}$ there is even a small change of the order of $\approx 10\%$ in the slope at midrapidity. At 11.5 GeV the inclusion of the p_T-cuts affects only the tails of the pion flow. In the results for the π^+, we notice that the order between the two calculations is reversed for $\sqrt{s_{NN}} = 11.5\,\text{GeV}$ with respect to $\sqrt{s_{NN}} = 3.6\,\text{GeV}$. In particular at the lower energy, the inclusion of the p_T-cuts decreases the value of $|F|$ of the pion flow. The small changes of the directed flow dictated by the different analysis techniques allow us to assert that the PHSD results are robust with

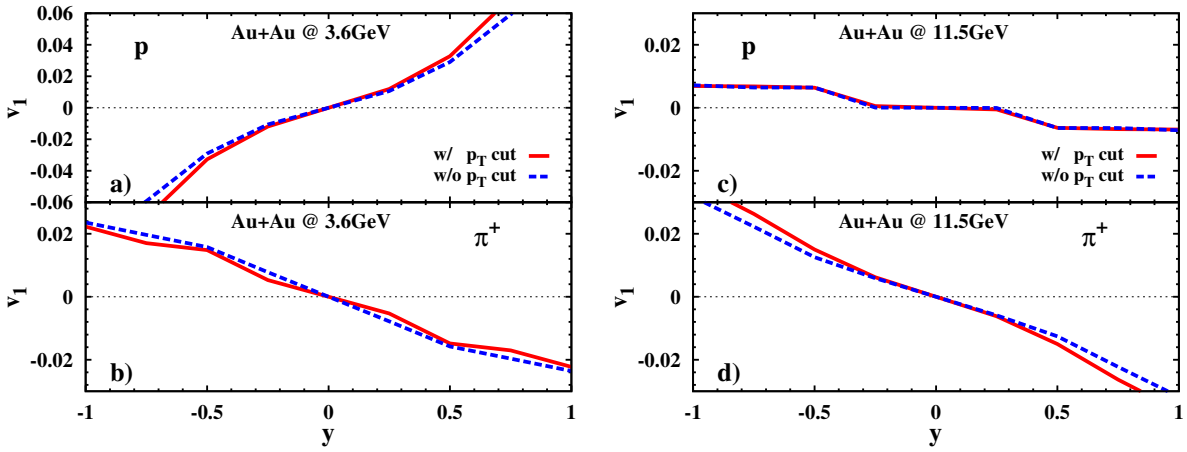

Figure 5.11: The directed flow v_1 of the protons and positive pions as a function of the rapidity y for mid-central (10 - 40% centrality) Au+Au collisions at $\sqrt{s_{NN}} = 3.6\,\text{GeV}$ (l.h.s.) and at $\sqrt{s_{NN}} = 11.5\,\text{GeV}$ (r.h.s.). The solid red lines refer to the results with p_T-cuts applied in the analysis, while the dashed blue lines refer to the results without p_T-cuts in the analysis.

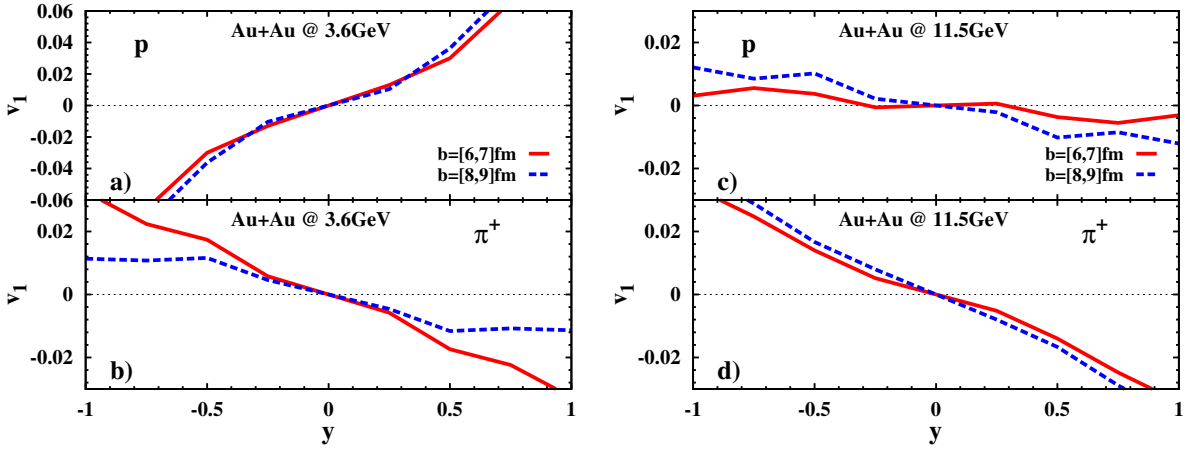

Figure 5.12: The directed flow v_1 of protons and positive pions as a function of the rapidity y in Au+Au collisions at $\sqrt{s_{NN}} = 3.6\,\text{GeV}$ (l.h.s.) and at $\sqrt{s_{NN}} = 11.5\,\text{GeV}$ (r.h.s.). The solid red lines are associated to impact parameter $b = 6 - 7$ fm, while the dashed blue lines to $b = 8 - 9$ fm.

respect to the analysis procedure. Thus, the results on v_1 presented below entirely emerge from the evolution of the system created at the collision and there is no alteration due to the analysis procedure. We specify that in the study of the beam energy scan of the directed flow (see Section 5.6), possible deviations arising from the p_T cuts (for example deviations of the order of $\approx 10\%$ found for the pion flow at $\sqrt{s_{NN}} = 3.6\,\text{GeV}$) are not neglected, but they are contained in the uncertainty range associated to the fitting procedure to extract the slope.

The second aspect studied here is the dependence of the directed flow on the centrality of the collision. As explained in Section 5.1, the directed flow is a manifestation in momentum space of the anisotropies of the system due to asymmetric configurations of the colliding system. A finite value of the impact parameter b between the two colliding nuclei is required to generate a non-vanishing v_1. Moreover, for larger b the flow increases and $|F|$ becomes larger at midrapidity. These considerations are evident in the measurements from the STAR collaborations for the proton and pion flow in Au+Au collisions [156]. Three centrality classes have been analyzed[2]: most central collisions ($0-10\%$), collisions at intermediate centrality ($10-40\%$), and peripheral collisions ($40-80\%$). The experimental observation of the directed flow follows this order: the lower values of $|F|$ are associated to the most central collisions and the larger values of $|F|$ to the peripheral ones. We study the variation of the directed flow, as computed in PHSD, within one experimental centrality class to understand the uncertainty associated to our results. In this respect, we show in Fig. 5.12 the directed flow v_1 of proton and π^+ as a function of the rapidity in Au+Au collisions at $\sqrt{s_{NN}} = 3.6\,\text{GeV}$ and $\sqrt{s_{NN}} = 11.5\,\text{GeV}$ for $b = 6-7\,\text{fm}$ and $b = 8-9\,\text{fm}$. These ranges of b represent two subclasses which compose the $10-40\%$ intermediate centrality class. We notice a sizable difference between the calculations at $b = 6-7\,\text{fm}$ and at $b = 8-9\,\text{fm}$, which is most significant at midrapidity for π^+ at $\sqrt{s_{NN}} = 3.6\,\text{GeV}$. At the lowest energy ($3.6\,\text{GeV}$), the results on the proton v_1 for $b = 6-7\,\text{fm}$ and for $b = 8-9\,\text{fm}$ basically overlap for $|y| < 0.5$ and differ for $|y| \geq 0.5$. In particular, the calculation associated to $b = 6-7\,\text{fm}$ presents smaller values for v_1 at positive rapidities compared to the corresponding result for $b = 8-9\,\text{fm}$. This shows that increasing the value of the impact parameter we obtain a stronger flow, as mentioned above. However, these considerations hold for the v_1 of protons, while the v_1 of pions shows the opposite behavior. One possible explanation is that the pion flow develops in close connection to the proton flow, since the dominant production mechanisms for the pions are string decays and low energy pion-nucleon scatterings. Thus, the change of the proton flow directly affects the pion flow, tilting the pion line in the same direction of the proton flow. As a results, the pion slope at midrapidity becomes smaller in modulus for larger impact parameter. At $\sqrt{s_{NN}} = 11.5\,\text{GeV}$, the calculations for $b = 8-9\,\text{fm}$ are characterized by a stronger flow than those for $b = 6-7\,\text{fm}$ both in the proton and in the pion case. In fact, at this energy the pions are predominantly produced from the hadronization of the partonic degrees of freedom and in the particle re-scattering; consequently there is no strong correlation with the proton dynamics. The conclusion drawn here for π^+ can be extended to other mesons, e.g. π^- and kaons. In order to achieve a reliable comparison with the STAR data, we need to simulate the collision for one collision energy over different b ranging inside the desired centrality class.

[2] We refer to Ref. [156] for the centrality selection criteria.

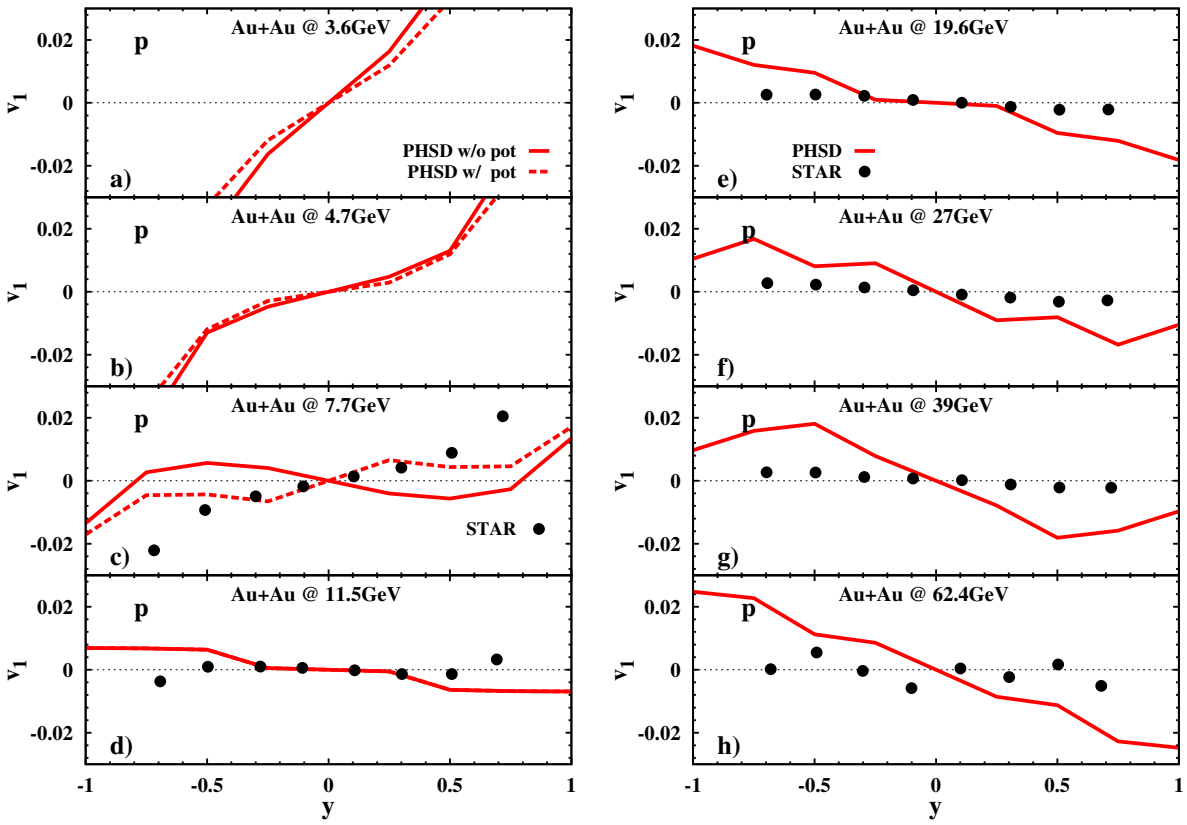

Figure 5.13: The directed flow v_1 of the protons as a function of the rapidity y for mid-central (10 - 40% centrality) Au+Au collisions at the center-of-mass energies $\sqrt{s_{NN}}$ = 3.6, 4.7, 7.7, 11.5, 19.6, 27, 39, 64.2 GeV (in panels (a), (b), (c), (d), (e), (f), (g), (h), respectively). The solid red and dashed red lines represent the results from PHSD without and with the baryonic potentials in the particle propagation, respectively. The experimental data are taken from Ref. [156].

The final PHSD result for the specific centrality class is then obtained as the average of these calculations (weighted by b).

5.6 Beam energy scan of the directed flow

In this Section, we study the directed flow of protons and pions in the energy range $\sqrt{s_{NN}} = 3 - 100$ GeV and we investigate the effects of the baryonic potentials introduced in Section 5.4. The following results for the directed flow from PHSD are computed at intermediate centrality (10 – 40%) according to the STAR experimental measurements [156] adopting the p_T-cuts introduced in Section 5.5. In Figs. 5.13 and 5.14 the directed flow v_1 of protons and

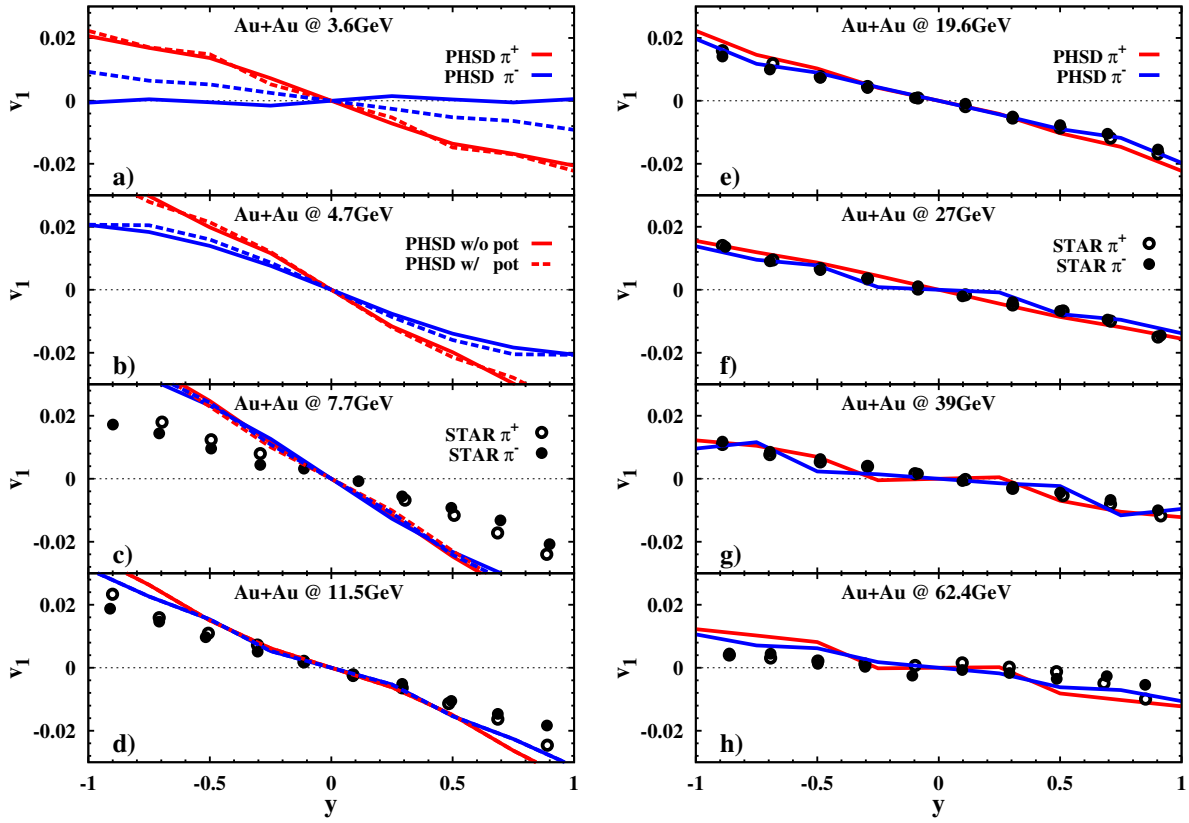

Figure 5.14: The directed flow v_1 of π^+ (red lines) and of the π^- (blue lines) as a function of the rapidity y for mid-central (10 - 40% centrality) Au+Au collisions at the center-of-mass energies $\sqrt{s_{NN}} = 3.6, 4.7, 7.7, 11.5, 19.6, 27, 39, 64.2$ GeV (in panels (a), (b), (c), (d), (e), (f), (g), (h), respectively). The solid and dashed lines represent the results from PHSD without and with the baryonic potentials in the particle propagation, respectively. The experimental data are taken from Ref. [156].

charged pions, respectively, is plotted as a function of the rapidity y for mid-central Au+Au collisions at different energies, in comparison with STAR data [156] whenever possible. The proton flow is characterized by a peculiar "S-shape", which is more visible at low energies (panels (a), (b), (c) of Fig. 5.13). There is a moderate sensitivity to the hadronic potentials in the particle propagation at low energies $\sqrt{s_{NN}} < 11.5$ GeV, while at large energies the results with and without potentials merge. For this investigation, we have adopted the potential according to the NL1 parametrization for the nuclear equation of state. The potential gives an attractive contribution to the proton v_1 for $\sqrt{s_{NN}} = 3.6, 4.7$ GeV, while it produces a repulsive effect at $\sqrt{s_{NN}} = 7.7$ GeV. At midrapidity ($|y| \leq 0.5$), the v_1 of protons is approximately linear in rapidity and it has a normal flow behavior at small energies ($\sqrt{s_{NN}} = 3.6, 4.7$ GeV) and an

antiflow behavior at high energies ($\sqrt{s_{NN}} \geq 11.5\,\text{GeV}$). At $\sqrt{s_{NN}} = 7.7\,\text{GeV}$, the inclusion of the potential induces a change in the proton flow: the result of PHSD without potential shows a normal flow behavior, while the result of PHSD including the potential shows an antiflow behavior. The experimental data seem to support the latter scenario. The inclusion of the potential at the lowest collision energies studied here ($\sqrt{s_{NN}} = 3.6, 4.7\,\text{GeV}$) does not cause a change of the behavior of v_1 at mid-rapidity, which is of the normal flow type. In particular, the difference between the two PHSD scenarios emerges only as a small decrease of the slope F at midrapidity. Overall, the PHSD results show the same trend as the STAR data. Whereas the agreement is quite well in the AGS and SPS energy range ($\sqrt{s_{NN}} < 20\,\text{GeV}$), the deviations become larger for the higher RHIC energies.

Differently from the case of protons, pions (π^+ in red lines and π^- in blue lines) are characterized by an antiflow in the whole energy range, apart from the π^- at $\sqrt{s_{NN}} = 3.6\,\text{GeV}$ (panel (a) of Fig. 5.14) which presents a vanishing flow when potentials are not included. As found above for the proton flow, the inclusion of the potential modifies our results only at small energies ($\sqrt{s_{NN}} < 11.5\,\text{GeV}$). Moreover, we observe a repulsive contribution from the potential and this is more pronounced for the π^- at $\sqrt{s_{NN}} = 3.6\,\text{GeV}$. We notice that the results for positive and negative pions differ substantially only at low energies ($\sqrt{s_{NN}} = 3.6, 4.7\,\text{GeV}$ in panels (a), (b) of Fig. 5.14). In particular, the π^+ has a stronger antiflow with respect to the π^- case. Increasing the energy the flows of the pions tend to merge, as an effect of the dominant role played by the QGP phase in the dynamics of the system. Our results on the pion v_1 are in good agreement with the data at high energies, while at small energies ($\sqrt{s_{NN}} = 7.7, 11.5\,\text{GeV}$ in panels (c), (d) of Fig. 5.14) the PHSD antiflow is too large.

In order to estimate the intensity of the directed flow, we extract in all cases the associated slope F defined in Eq. (5.4). We perform two fits of our results to take into account the uncertainty on the value of the slope F:

- a fit using the linear function $v_1(y) = Fy$ for $|y| < 0.5$;
- a fit using the cubic function $v_1(y) = Fy + Cy^3$ for $|y| < 1$.

In Fig. 5.15 we present the excitation function of the slope F for protons (panel (a)) and pions (π^+ in panel (b) and π^+ in panel (c)) for mid-central Au+Au collisions. We investigate different scenarios:

- Scenario 1: PHSD including CSR with the NL1 parametrization for the equation of state in red,
- Scenario 2: PHSD including both CSR and hadronic potential with the NL1 parametrization for the equation of state in green,

- Scenario 3: PHSD without CSR in blue,

- Scenario 4: HSD with CSR with the NL1 parametrization for the equation of state in orange.

As already described above, the proton slope (panel (a) of Fig. 5.15) is positive at small energies and then turns negative at $\sqrt{s_{NN}} \approx 6 - 9\,\text{GeV}$. The proton F becomes negative when more protons are produced in the direction opposite to the spectators of the collisions[3] rather than aligned with them. The energy range of the potential influence can be clearly distinguished in two regions, one of repulsive and one of attractive nature. The former corresponds to $\sqrt{s_{NN}} = 3 - 5\,\text{GeV}$, where the green band referring to PHSD calculations with potentials is below the red band referring to PHSD calculations without potentials. The latter corresponds to $\sqrt{s_{NN}} = 5 - 10\,\text{GeV}$, since the green band (Scenario 2) is above the red band (Scenario 1). Moreover, the PHSD calculations without potential give a negative value of the proton slope at energies lower than the case in which the potential is considered. The experimental data support a softening of the slope F of the proton in line with the PHSD calculations including both CSR and the hadronic potential. The only inclusion of the CSR mechanism does not modify the energy dependence of the proton flow (the red and blue band almost overlap). All scenarios investigated merge at large energies $\sqrt{s_{NN}} > 10\,\text{GeV}$, apart from the HSD result, which exhibits lower values for the slope with respect to the results of PHSD. The calculations seem to overlap again at large energies $\sqrt{s_{NN}} \approx 60\,\text{GeV}$, but this behavior must be considered carefully. In fact, we have shown in Chapter 4 that at energies $\sqrt{s_{NN}} \approx 60\,\text{GeV}$ PHSD and HSD simulations do not produce comparable results on many observables (e.g. excitation function of particle ratios) and the HSD scenario is ruled out by the comparison with experimental data. Overall, our calculation of the proton slope from Scenario 2 is in good agreement with the data, apart from a deviation at large energies. Comparing our results to those from the UrQMD model, PHSD describes better the experimental trend up to $\sqrt{s_{NN}} \approx 20\,\text{GeV}$, while UrQMD shows a good agreement with the data at the higher energies. This is quite surprising since the UrQMD model, as a pure hadronic transport approach, should describe the experimental trend better at low energies, where a QGP is not created during the collisions, and drift apart from the data at large energies, where a QGP is observed to appear in the system. Differently from protons, the slopes associated to the flow of both charged pions (panels (b) and (c) of Fig. 5.15) remains negative in all the energy range. First, F decreases with increasing energy, reaching a minimum at $\sqrt{s_{NN}} \approx 8\,\text{GeV}$, then it increases with increasing $\sqrt{s_{NN}}$.

[3]The spectators are the nucleons located outside the overlap region of the two colliding nuclei and they are not involved in the interactions, consequently, during the expansion of the system, they travel basically unaffected along the beam axis.

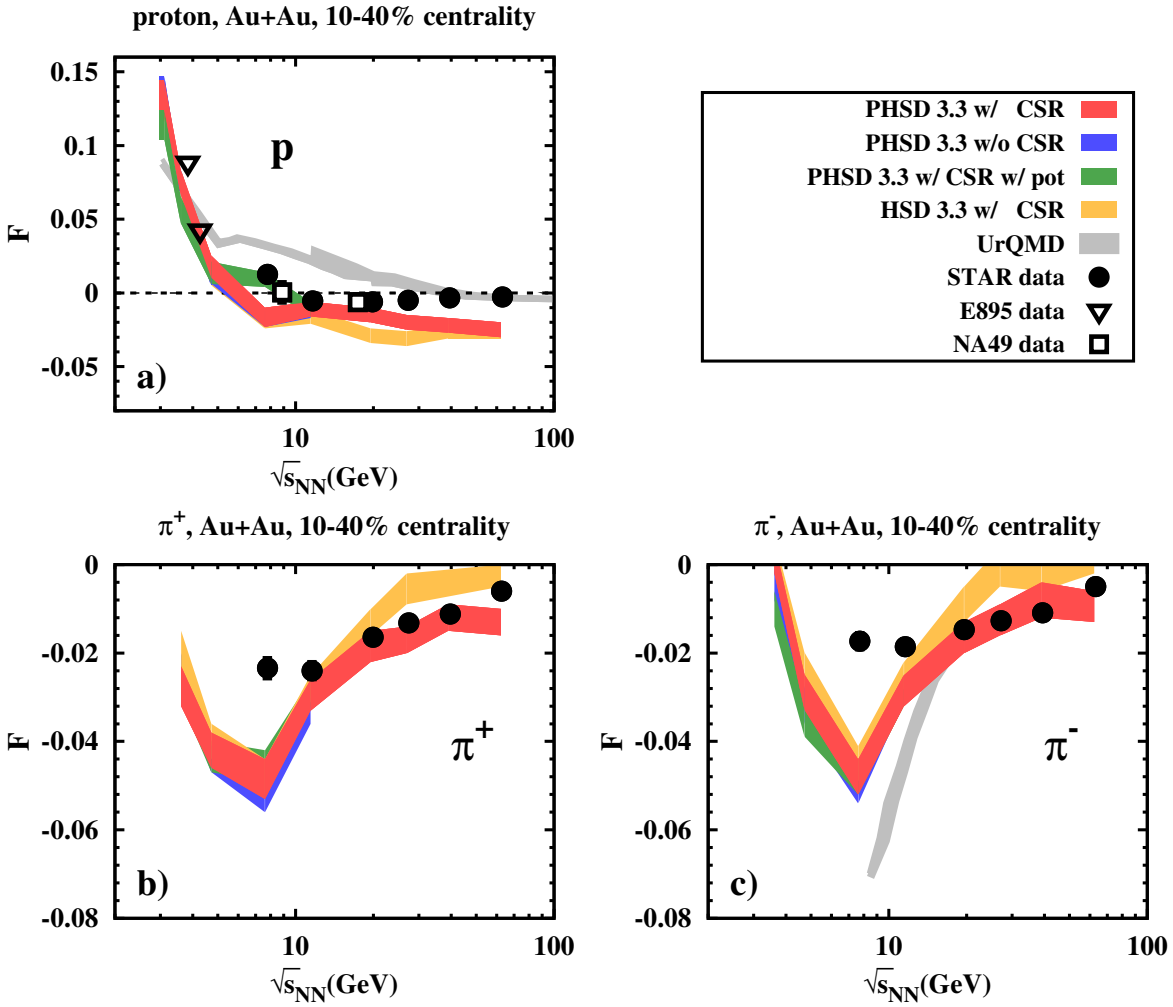

Figure 5.15: The excitation function of the directed flow slopes F of protons (panel (a)) and charged pions (π^+ in panel (b) and π^- in panel (c)) as a function of the center-of-mass energy $\sqrt{s_{NN}}$. The experimental data points and the UrQMD calculations (gray band) are taken from Refs. [154, 156, 170, 171]. The red band refers to the PHSD calculations including CSR with the NL1 parameter set, the green band refers to the PHSD calculations including CSR and potential with the NL1 parameter set, the blue band refers to the PHSD calculations without CSR and the orange band refers to the HSD calculations with CSR.

The PHSD scenarios provide similar results, so that it is hard to disentangle contributions coming from the inclusion of CSR and baryonic potential. We can only comment that the inclusion of the potential produces slightly smaller slopes for π^- at low energies. The HSD and PHSD results are comparable for $\sqrt{s_{NN}} < 10\,\text{GeV}$ and they differ at larger energies. Among these results, the PHSD calculations achieve a better agreement with the data. Consequently, in our

model partonic degrees of freedom are necessary in the evolution of the colliding system at the energies $\sqrt{s_{NN}} > 10\,\text{GeV}$ to correctly describe the pion v_1. Although we obtain a good agreement with data at large energies, we notice that PHSD fails to describe the pion flow at $\sqrt{s_{NN}} = 7.7\,\text{GeV}$, since our results from the different scenarios are lower than the experimental points by a factor of ≈ 2.5. Currently, the reason of this finding is not clear, especially in relation to the fact that the PHSD result of the proton v_1 (including potential) is in good agreement with the data in the same energy range. We expect that the inclusion of momentum-dependent potentials in the propagation of mesons can modify the pion F, but additional experimental information at this and lower energies are necessary to better understand the excitation function of the pion slope. We notice that, although the UrQMD results are in fair agreement with the STAR data for $\sqrt{s_{NN}} > 20\,\text{GeV}$ (similarly to PHSD), this model severely underestimates the experimental observations at lower energies, while the inconsistency of PHSD calculations is only of a factor of ≈ 2.5.

We propose the existence of a correlation between the minimum in the excitation function of the pion slope and change of sign of the proton flow as a function of $\sqrt{s_{NN}}$. In fact, these features of v_1 emerge in the same energy interval $\sqrt{s_{NN}} = 7 - 9\,\text{GeV}$. We suggest that this is due to a smooth transition from a hadronic- to a partonic-dominated system. This consideration can be reasonably related to the drop in the excitation function of the ratio K^+/π^+, analyzed in Chapter 4. However, we are not able to draw a robust interpretation, since we detect no significant differences between HSD and PHSD calculations on the proton and pion slope F in the energy range $\sqrt{s_{NN}} = 7 - 9\,\text{GeV}$. Further studies are needed to solve this issue.

Chapter 6

Predictions for FAIR and NICA

In the recent past the heavy-ion facilities pushed to higher and higher collision energies. First, RHIC reached a center-of-mass energy of $\sqrt{s_{NN}} = 200\,\text{GeV}$ in Au+Au collisions. In 2010, the Large Hadron Collider (LHC) at CERN started the heavy-ion program and managed to strike the TeV limit, running Pb–Pb collisions up to $\sqrt{s_{NN}}$ =5.02 TeV. In this energy range, it is possible to extract important information about the quark matter in the high temperature regime. Nevertheless, the interest of the heavy-ion physics community moved to the exploration of less hot and more dense systems. The characterization of the deconfinement phase transition at large baryon chemical potential and the search for a possible critical point in the QCD phase diagram are the goals of the new experimental programs. In this context, it is crucial to access a wider region of the $T - \mu_B$ plane by varying the beam energy. Thus, the investigation of lower energies, compared to the LHC and top RHIC energies, has become the new challenge for Heavy-Ion Collision (HIC) research. For example, the beam energy scan (BES) performed at RHIC is currently studying the energies of $\sqrt{s_{NN}} = 5.5, 7.7, 11.5, 19.6, 27, 39, 62.4\,\text{GeV}$. Moreover, new heavy-ion facilities, the Nuclotron-based Ion Collider fAcility (NICA) at the Joint Institute for Nuclear Research, the Facility for Antiprotons and Ion Research (FAIR) at GSI Helmholtzzentrum für Schwerionenforschung and the Japan Proton Accelerator Research Complex (J-PARC), are under construction to explore even lower energies. The planned energy ranges are $\sqrt{s_{NN}} = 4 - 11\,\text{GeV}$ for NICA and $\sqrt{s_{NN}} = 4 - 9\,\text{GeV}$ for FAIR.

In this section, our aim is to provide detailed predictions for observables in ultra-relativistic collisions that the FAIR and NICA facilities can measure experimentally in the near future. As a fundamental reference, we provide particle rapidity spectra in the FAIR-NICA energy range. In addition, we explore new aspects of CSR. Firstly, the dependence of the strange to non-strange particle ratios on the size of the colliding system. Secondly, the effects of CSR on the strange particle yields for different centralities in Au+Au collisions.

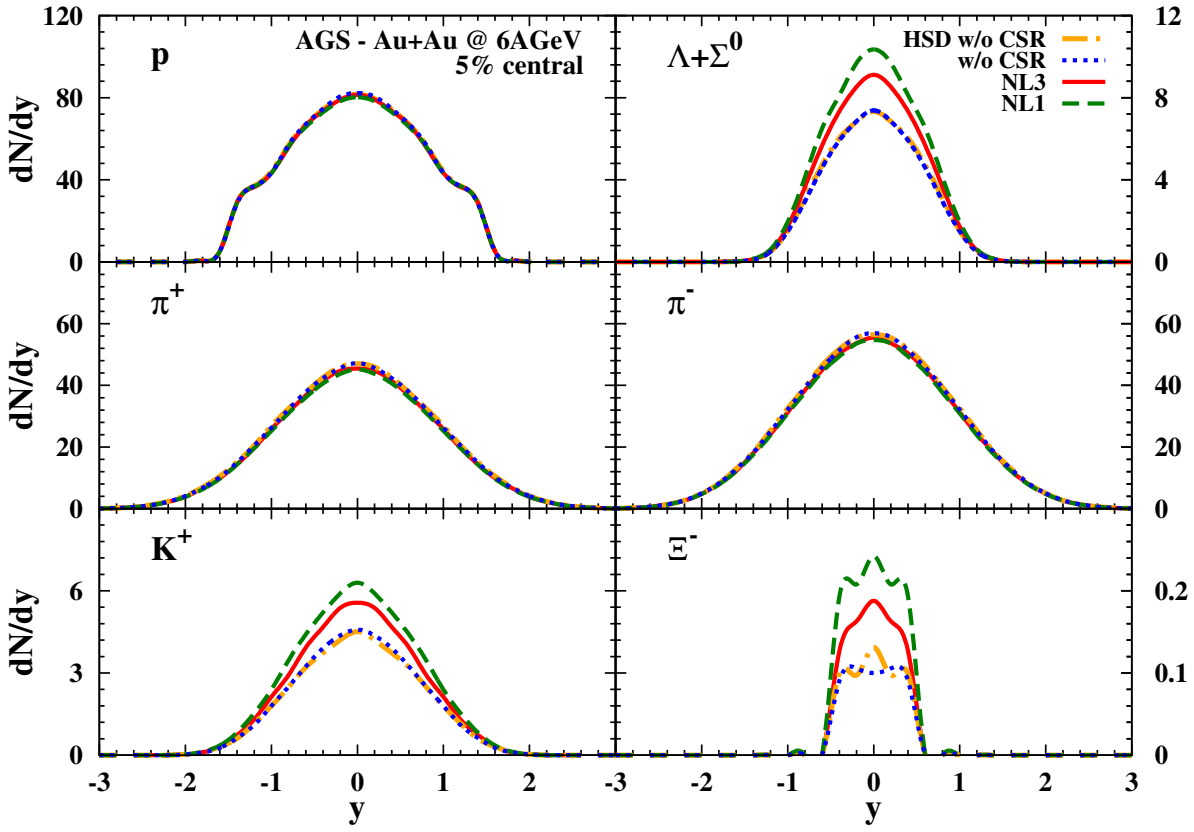

Figure 6.1: The rapidity distribution of protons, $(\Lambda + \Sigma^0)$'s, pions and K^+'s and Ξ^-'s for 5% central Au+Au collisions at $E_{Lab} = 6$ AGeV. The solid red lines show the results from PHSD including CSR with NL3 parameters, the dashed green lines show the results from PHSD including CSR with NL1 parameters, the dotted blue lines show the result from PHSD without CSR, the dash-dot orange lines show the result from HSD without CSR.

6.1 Particle spectra

The energy range which will be scanned by the FAIR and NICA facilities is altogether $E_{Lab} = 2 - 63.5$ AGeV. We expect that the system created in collisions at these energies achieves energy and baryon densities that enable the restoration of chiral symmetry as already discussed in Chapter 4. Among the experimental observables studied in Chapter 4, we have found that particle rapidity spectra are suitable probes to study CSR. Moreover, the rapidity spectrum represents one of the most investigated observables in HIC. Thus, we provide particle rapidity spectra in the FAIR-NICA energy range, as fundamental reference for the future experiments.

In Figs. 6.1 and 6.2 we show rapidity distribution of protons, $(\Lambda + \Sigma^0)$'s, pions and K^+'s and Ξ^-'s for 5% central Au+Au collisions at 6 AGeV and 8 AGeV, respectively. These correspond

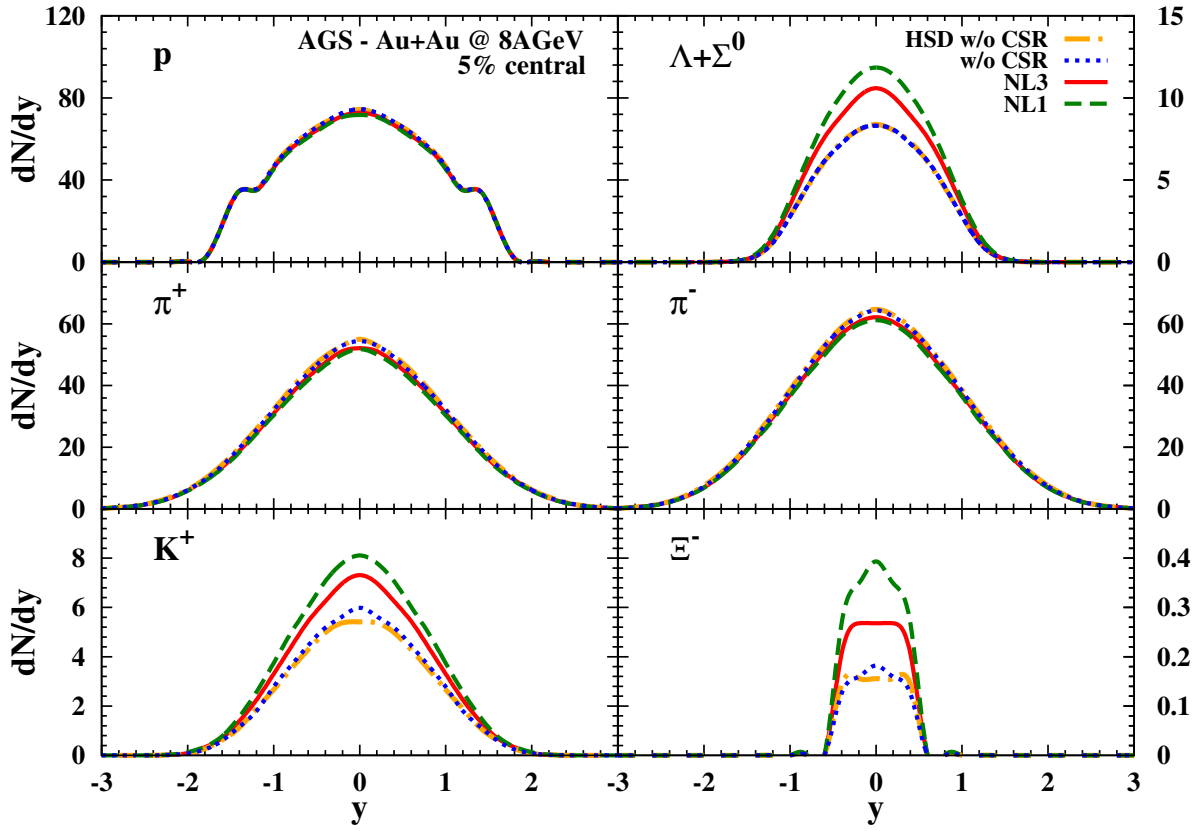

Figure 6.2: The rapidity distribution of protons, $(\Lambda + \Sigma^0)$'s, pions and K^+'s and Ξ^-'s for 5% central Au+Au collisions at E_{Lab} = 8 AGeV. The coding of the lines is the same as in Fig. 6.1.

to the lower collisions energies planned for FAIR and NICA experiments. We investigate the following scenarios: PHSD including CSR with NL3 parameters (solid red lines), PHSD including CSR with NL1 parameters (dashed green lines), PHSD without CSR (dotted blue lines), HSD without CSR (dash-dot orange lines). As already discussed in Chapter 4, the inclusion of CSR produces an increase of the strange particle yields. The enhancement in the $(\Lambda + \Sigma^0)$ and K^+ spectra is of the order of $\approx 25\%$ and $\approx 40\%$ for E_{Lab} = 6 AGeV and 8 AGeV, respectively. At the same energies the increase in the Ξ^- distributions is of the order of 45%. We highlight that at these low energies (Figs. 6.1 and 6.2) there is basically no contribution to the spectra coming from the QGP. In fact, we see that the calculations from PHSD and HSD without CSR (dotted blue and dashed dotted orange lines, respectively) show a small difference only for the K^+ spectra at E_{Lab} = 8 AGeV and in the Ξ^- spectra at 6 and 8 AGeV. In fact, QGP 'droplets' can be created in the system because of the high baryon and energy densities, but they disappear in short time. Consequently, they do not give a sizeable contribution to the final particle multiplicities. The comparison with experimental observation at these energies will then allow the identification of the features of the CSR in the hadronic dense medium

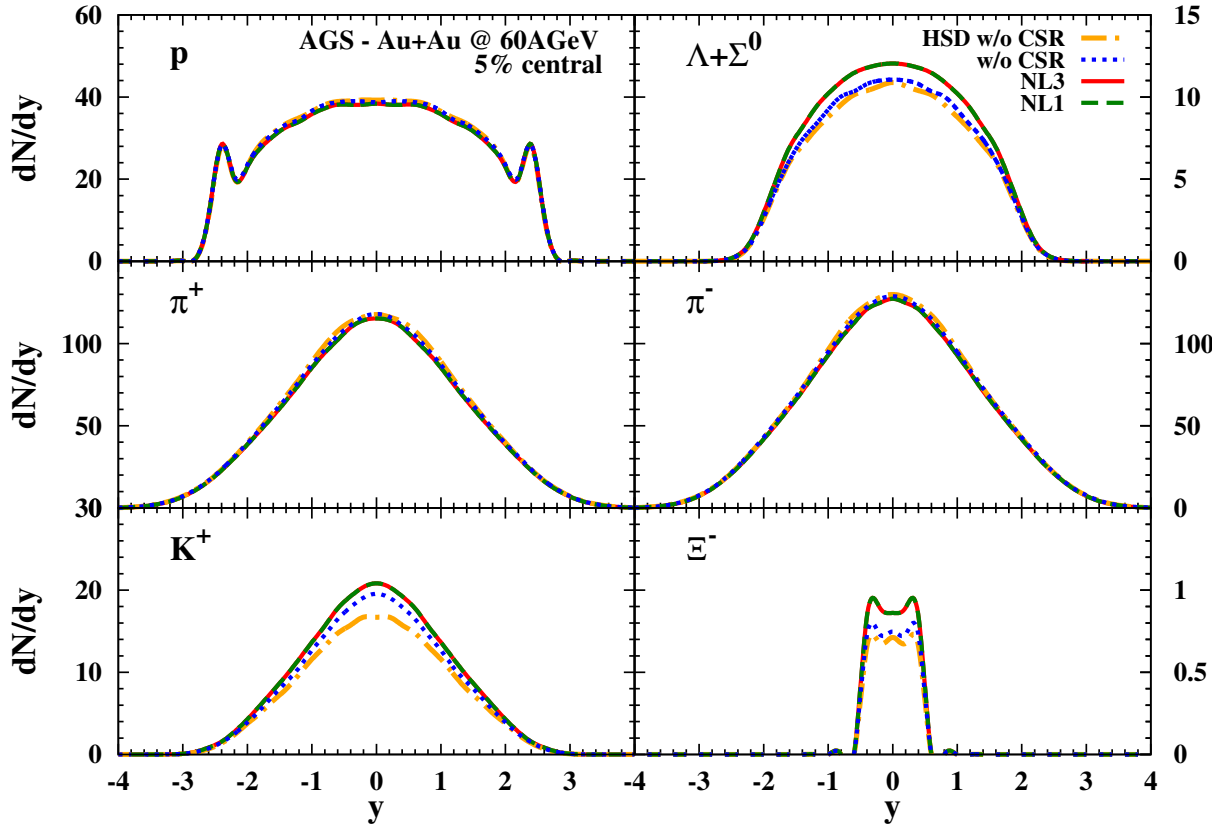

Figure 6.3: The rapidity distribution of protons, $(\Lambda + \Sigma^0)$'s, pions and K^+'s and Ξ^-'s for 5% central Au+Au collisions at $E_{Lab} = 60$ AGeV. The coding of the lines is the same as in Fig. 6.1.

produced in heavy-ion collisions more clearly than at higher energies. In fact, at AGS and SPS energies the final particle production is the result of many contributions (string production, hadronization of partonic degrees of freedom, hadronic re-scattering), so it is not trivial to isolate the role of CSR. Hence, we support the idea that the low-energy collisions in the FAIR and NICA regime are suited to isolate the role of CSR and to establish if CSR occurs in HIC before the onset of the QGP phase.

Finally, we display in Fig. 6.3 analogous calculations at 60 AGeV, which represents the top beam energy of the NICA program. At this collision energy, the final particle multiplicities originate predominantly from the hadronization of partonic degrees of freedom, however, the contribution from the string decay is non-negligible. In fact, in Fig. 6.3 the inclusion of CSR produces sizeable modifications of the rapidity spectra. We addressed in Chapter 4 the study of intermediate colliding energies in the FAIR-NICA regime, e.g. we have shown the rapidity spectra for $E_{Lab} = 10.7, 30$ AGeV in Figs. 4.3 and 4.4. In conclusion, the FAIR and NICA experiments will perform a beam energy scan which is optimal to study CSR in the hadronic sector and its "interplay"with the QGP phase.

6.2 System size dependence of strangeness production in HIC

The aim of this section is to explore how the variation of the size of the system modifies the excitation functions of the particle ratios K^+/π^+, K^-/π^- and $(\Lambda + \Sigma^0)/\pi$ shown in section 4.4.1 of Chapter 4 (cf. also Ref. [172]). In Fig. 6.4 we display the calculations for ^{197}Au + ^{197}Au in blue, for ^{40}Ca + ^{40}Ca in green and for ^{12}C + ^{12}C in red. The scenarios considered here are the default PHSD without CSR (dashed lines) and PHSD including CSR with NL1 as parameter set for the nuclear equation of state from the non-linear $\sigma - \omega$ model (solid lines). The inclusion of CSR gives a strangeness enhancement also in case of smaller system size with respect to Au+Au collisions and this holds for all three particle ratios. In fact, when considering central collisions, a sizeable volume of the system is affected by the partial restoration of chiral symmetry even in case of light ions. We notice that, for the K^+/π^+, K^-/π^- ratios, the discrepancy between the calculations with and without CSR remains significant even at high SPS energies for Ca+Ca and C+C collisions. In particular, the spread between the scenarios with and without CSR is larger when the size of the system is smaller. This can be explained by the fact that in Ca+Ca and C+C collisions the fraction of the system which performs a phase transition to the QGP is smaller with respect to Au+Au collisions, and the string excitations and decays still have a large strangeness production rate even at large energies. These characteristics are evident also in the observation that at large energies the ratio K^+/π^+ is smaller for the Au+Au collisions and larger in C+C collisions. In fact, we recall that the drop of the K^+/π^+ ratio in Fig. 4.8 is due to the appearance of the QGP, since the strangeness production in the QGP phase is suppressed with respect to the hadronic production at fixed energy density. Concerning the "horn"structure in the K^+/π^+ ratio, we notice that the peak of the excitation function becomes less pronounced in case of Ca+Ca and it disappears completely in case of C+C collisions. With decreasing system size the low energy rise of the excitation functions becomes less steep. We can see also that the peak for Ca+Ca is shifted to larger energies with respect to the Au+Au case.

Differently from the K^+/π^+, the $(\Lambda + \Sigma^0)/\pi$ ratio preserves the same structure for all three colliding systems. In order to produce Λ's the threshold energy of $\sqrt{s_{th}} = 2.55\,\text{GeV}$ (for Σ^0 $\sqrt{s_{th}} = 2.62\,\text{GeV}$) must be reached, so the $(\Lambda + \Sigma^0)/\pi$ ratio increases when the system easily exceeds this value. The peak of the Λ production is not exactly in correspondence of the threshold energy, since we are considering A+A collisions where the available collision energy is distributed among the participants and where secondary and even higher order interactions take place. However, it is interesting to notice that the peak position in this excitation function does not move for different systems, different from the K^+/π^+ ratios. At large energies the $(\Lambda + \Sigma^0)/\pi$ ratio decreases as a function of the energy, since the pion production is enhanced in the hadronic re-scattering.

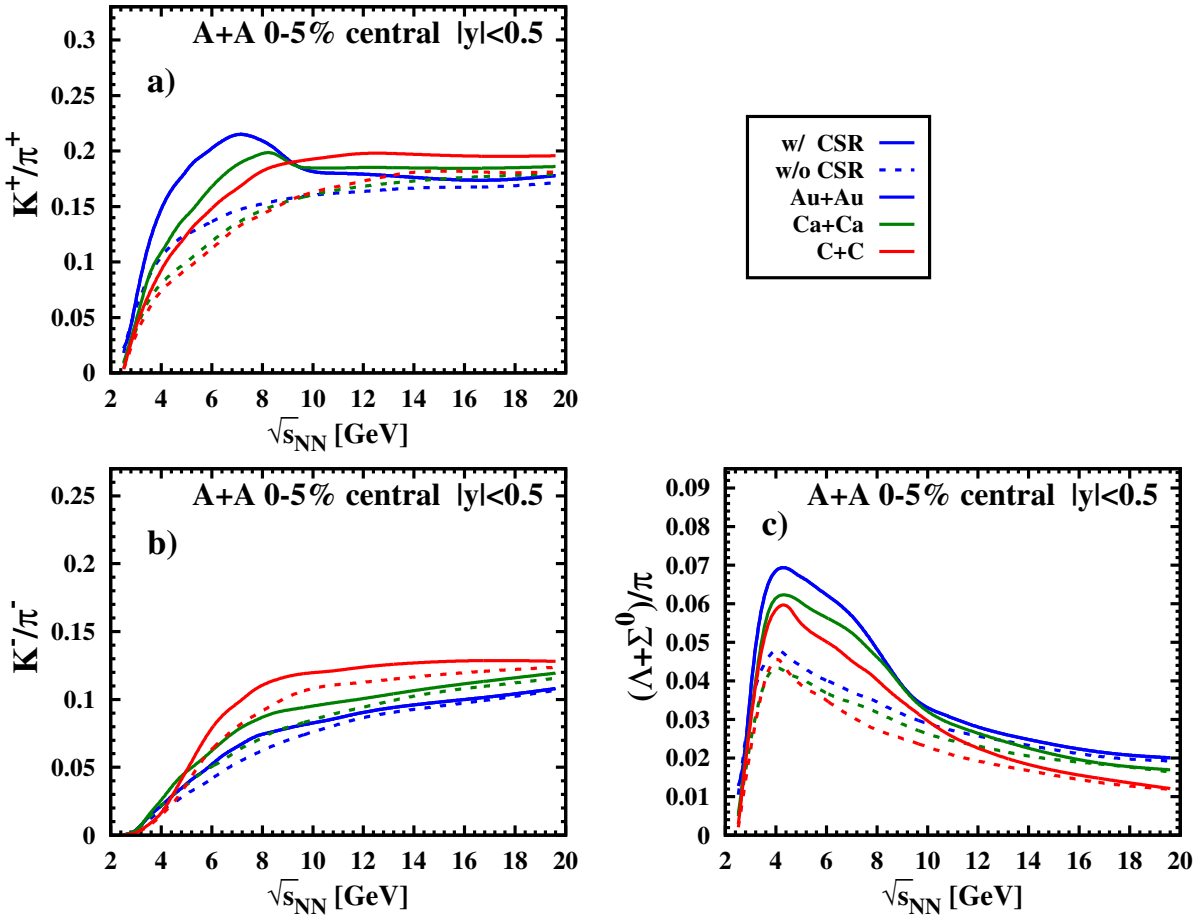

Figure 6.4: The ratios K^+/π^+, K^-/π^- and $(\Lambda+\Sigma^0)/\pi$ at midrapidity from 5% central symmetric A+A collisions as a function of the invariant energy $\sqrt{s_{NN}}$. The solid lines show the results from PHSD including CSR with NL1 parameters, the dashed lines show the result from PHSD without CSR. The blue lines refer to Au+Au collisions, the green lines to Ca+Ca collisions and the red lines to C+C collisions.

Finally, we observe no peak structure in the energy dependence of the K^-/π^- ratio in any of the scenarios studied. We notice that the results for the different sizes of the system present an opposite hierarchy with respect to the K^+/π^+ and the $(\Lambda + \Sigma^0)/\pi$ ratios. In fact, for C+C and Ca+Ca collisions the pion production is suppressed, since in the small systems the hadronic re-scattering cannot develop as in Au+Au collisions.

In Fig. 6.5, we consider even smaller colliding systems than the one considered in Fig. 6.4. The blue line refers to Au+Au, the green line to p+p collisions, the orange line to p+C collisions, the purple lines to p+Ca and the red lines to p+Au collisions. Apart from the Au+Au system, whose results are computed at mid-rapidity, the calculations in all other cases corre-

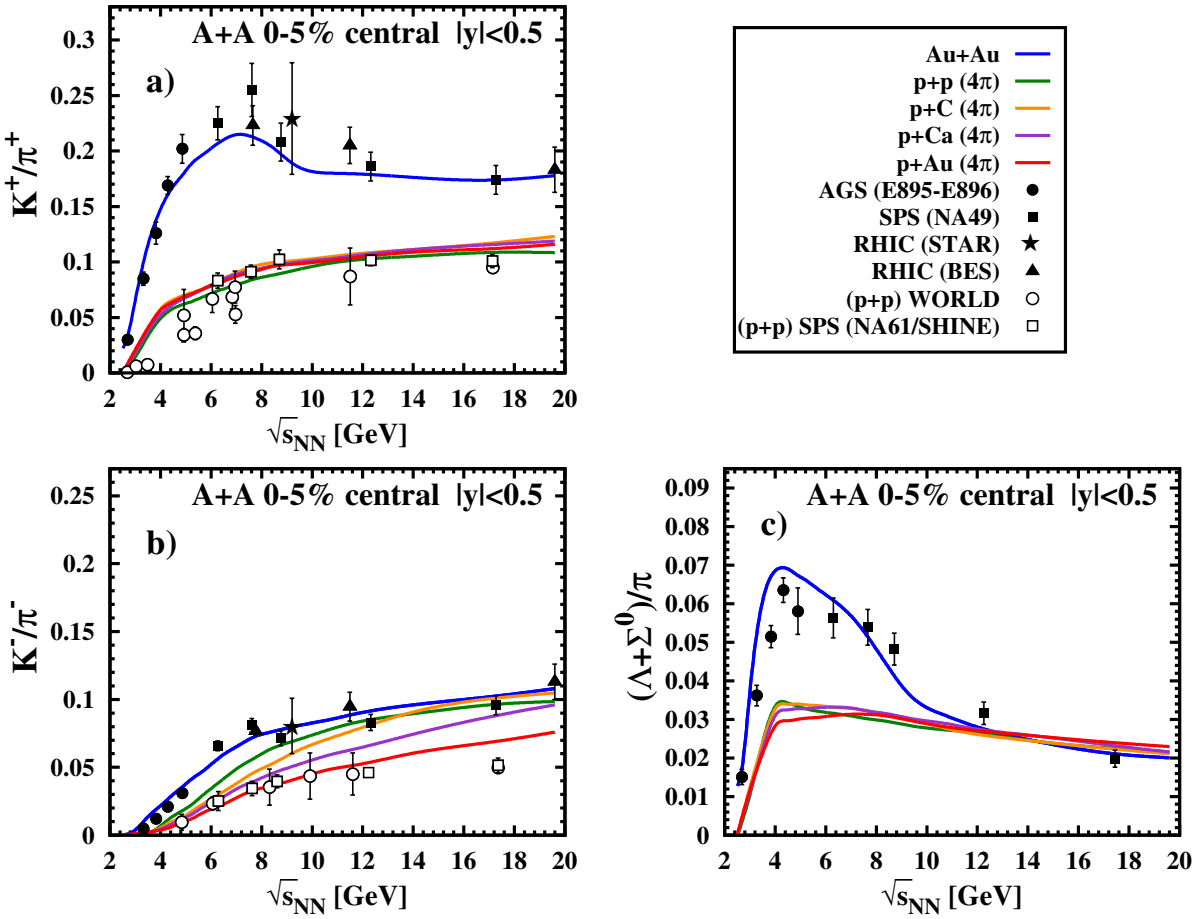

Figure 6.5: The ratios K^+/π^+, K^-/π^- and $(\Lambda + \Sigma^0)/\pi$ at midrapidity from 5% central symmetric Au+Au and the 4π calculations for p+p and p+A collisions as a function of the invariant energy $\sqrt{s_{NN}}$. The solid lines show the results from PHSD including CSR with NL1 parameters. The blue line refers to Au+Au, the green line to p+p collisions, the orange line to p+C collisions, the purple lines to p+Ca and the red lines to p+Au collisions. The experimental data are extracted from Refs. [120, 143, 145, 146] for Au+Au collisions and from Ref. [173] for p+p collisions (open symbols).

spond to full acceptance. We do not differentiate between the results with and without CSR, since the small colliding systems do not reach the high densities needed for the CSR mechanism to develop. In case of the Au+Au system, we show the result from PHSD including CSR with NL1 parametrization. In the K^+/π^+ excitation function, the newly studied colliding systems show a smooth increase of the particle ratio, without the peculiar peak emerging in the Au+Au collisions. There is no sizeable difference among the different results of the p+A collisions, while the p+p calculation is slightly below and is in good agreement with the avail-

able experimental data (open symbols).
In case of the excitation function of K^-/π^-, one can better distinguish among the results of the different colliding configurations. Apart from the case for Au+Au collisions, for smaller colliding systems the value of the K^-/π^- ratio increases. We notice that the PHSD calculation for p+p collisions shows the same trend as the data but is slightly above. On the other hand, the p+Au line exhibits an almost perfect match with the p+p experimental observations. It is unclear why the PHSD result for p+p collisions agrees with the data for the K^+/π^+ ratio, while it does not reproduce the K^-/π^- ratio. In relation to this issue, we stress that PHSD strictly fulfills the conservation laws of the quantum numbers (the baryon and strange numbers and the electric charge) and there is no inconsistency between the kaon and pion production. This means that the PHSD calculations should in principle reproduce the K^-/π^- ratio as it does for the K^+/π^+ ratio. Besides, the available data from Ref. [173] are dated measurements, that should be verified by new experiments with modern detectors and more precise reconstruction techniques, before we can extract a conclusive interpretation of these results.
Similarly to the K^+/π^+ and K^-/π^- ratios, the excitation functions of the $(\Lambda + \Sigma^0)/\pi$ for all explored systems are not characterized by a sharp peak. The $(\Lambda + \Sigma^0)/\pi$ ratio increases up to $\sqrt{s_{NN}} \sim 4\,\text{GeV}$, then it smoothly decreases nearly merging at $\sqrt{s_{NN}} \sim 12\,\text{GeV}$ with the Au+Au calculations. Although there is no big difference between the p+p and p+A lines, we notice a hierarchy at $\sqrt{s_{NN}} \sim 20\,\text{GeV}$: for larger system size, the value of $(\Lambda + \Sigma^0)/\pi$ increases (apart from the line associated to Au+Au collisions, which is below all the other ones due to the larger pion production).
In conclusion, the appearance/disappearance of the "horn"-structure in the strange to non-strange particle ratios as a function of the system size is found to be a signature of CSR. This features have to investigated in more detail and addressed by future experimental programs.

6.3 Centrality dependence of strangeness production in HIC

In this section, we investigate the centrality dependence of strangeness production in HIC, with a special focus on the CSR contribution. We vary the impact parameter in Au+Au collisions within an interval, where the most central configuration corresponds to the $0 - 10\%$ centrality class and the most peripheral configuration to the $45 - 50\%$ centrality class. The centrality of the collision can be expressed in terms of the number of participants N_{part}[1]: large values of N_{part} correspond to central collisions, while low values of N_{part} correspond to periph-

[1]The nucleons of the colliding nuclei can be distinguished according to the Glauber model [174] in participants and spectators. The former are located in the overlap region of the nuclei and interact, while the latter are not affected by interactions.

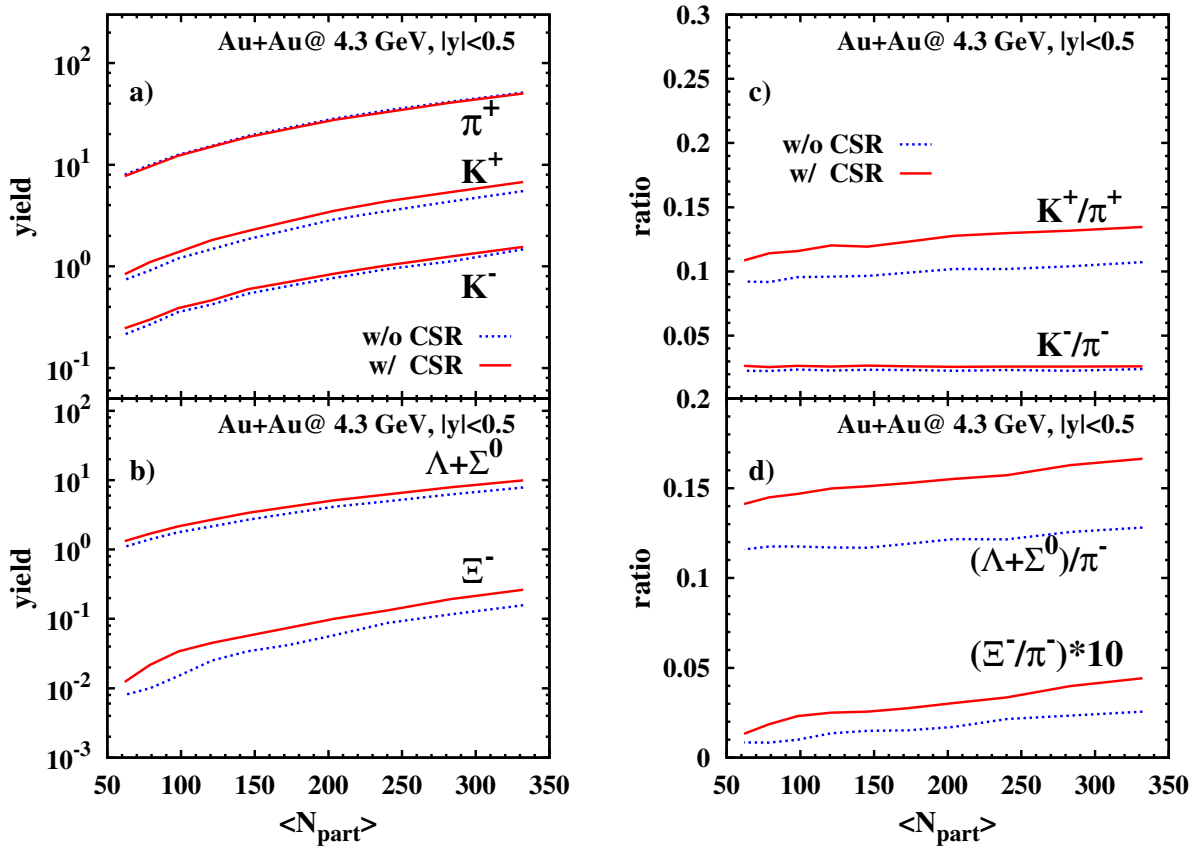

Figure 6.6: (l.h.s.) The particle yields of π^+, K^+, K^-, $(\Lambda + \Sigma^0)$ and Ξ^- at midrapidity from Au+Au collisions at $\sqrt{s_{NN}} = 4.3\,\text{GeV}$ as a function of the number of participants. (r.h.s.) The particle ratios K^+/π^+, K^-/π^-, $(\Lambda + \Sigma^0)/\pi^-$ and Ξ^-/π^- (the latter increased by 10 for comparison) at midrapidity in Au+Au collisions at $\sqrt{s_{NN}} = 4.3\,\text{GeV}$ as a function of $\langle N_{\text{part}} \rangle$. The solid red lines show the results from PHSD including CSR with NL3 parameters, the dotted blue lines show the results from PHSD without CSR.

eral collisions. We adopt the correlation between the centrality class and the average number of participants $\langle N_{\text{part}} \rangle$ as given by the STAR collaboration for $\sqrt{s_{NN}} = 7.7\,\text{GeV}$ in Ref. [175]. In Fig. 6.6 we plot on the l.h.s. the abundances of pions, kaons and the most abundant hyperons and on the r.h.s. the ratios K^+/π^+, K^-/π^-, $(\Lambda + \Sigma^0)/\pi^-$ and Ξ^-/π^- as a function of $\langle N_{\text{part}} \rangle$ at midrapidity from Au+Au collisions at $\sqrt{s_{NN}} = 4.3\,\text{GeV}$ (the ratio Ξ^-/π^- is multiplied by 10 to be visualized on the same scale of $(\Lambda + \Sigma^0)/\pi^-$). The same observables are shown in Fig. 6.7 for $\sqrt{s_{NN}} = 7.7\,\text{GeV}$. We display the calculations from PHSD including CSR with NL3 as parameter set with solid red lines and the calculations from PHSD without CSR with dotted blue lines.

For both $\sqrt{s_{NN}} = 4.3\,\text{GeV}$ and $\sqrt{s_{NN}} = 7.7\,\text{GeV}$, all particle yields and the $(\Lambda + \Sigma^0)/\pi^-$ and

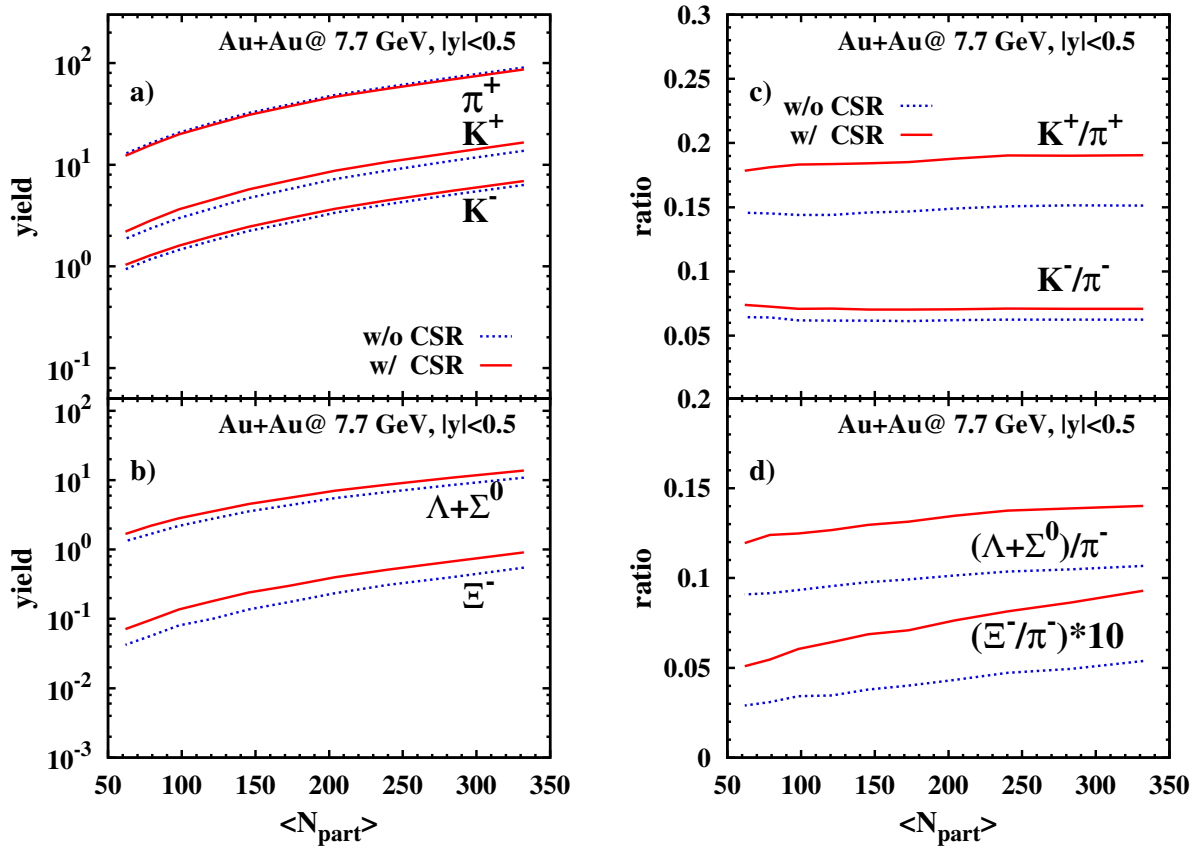

Figure 6.7: The particle yields of π^+, K^+, K^-, $(\Lambda + \Sigma^0)$ and Ξ^- and the associated strange to non-strange particle ratios at midrapidity from Au+Au collisions at $\sqrt{s_{NN}} = 7.7\,\text{GeV}$ as a function of the number of participants on the l.h.s. and r.h.s., respectively. The coding of the lines is the same as in Fig. 6.6.

Ξ^-/π^- ratios increase with increasing number of participants. On the other hand, the ratios K^+/π^+, K^-/π^- at $\sqrt{s_{NN}} = 7.7\,\text{GeV}$ and the ratio K^-/π^- at $\sqrt{s_{NN}} = 4.3\,\text{GeV}$ are almost constant as a function of the centrality for $\langle \text{N}_{\text{part}} \rangle > 50$. Moreover, the yields increase with a larger rate as a function of $\langle \text{N}_{\text{part}} \rangle$ than the ratios (notice the logarithmic scale on the l.h.s. with respect to the linear scale on the r.h.s. on the y axis). The inclusion of CSR produces a strangeness enhancement in the whole range of centralities. Note, however, that very peripheral reactions ($\langle \text{N}_{\text{part}} \rangle < 50$) are not considered, since we have selected the centrality classes according to Ref. [175]. Both at $\sqrt{s_{NN}} = 4.3$ and at $\sqrt{s_{NN}} = 7.7\,\text{GeV}$ the interaction volume of the two colliding nuclei reaches high energy densities such that practically all central cells are influenced by the CSR mechanism independently of the centrality of the collision. The centrality dependence of our results including CSR shows similar trends and features at low ($\sqrt{s_{NN}} = 4.3\,\text{GeV}$) and intermediate ($\sqrt{s_{NN}} = 7.7\,\text{GeV}$) energies.

We study the strangeness enhancement also in relation to the strange particle production in p+p collisions, especially for the hyperon production. The comparison between the particle production in A+A and in p+p collisions is usually expressed as a ratio of the particle yields in A+A collisions normalized to $\langle N_{part} \rangle$ to the corresponding quantities in p+p reactions at the same energy [130]:

$$\left(\frac{\text{yield}}{\langle N_{part} \rangle} \right)_{A+A} / \left(\frac{\text{yield}}{\langle N_{part} \rangle} \right)_{p+p}, \tag{6.1}$$

where $\langle N_{part} \rangle$ is equal to 2 in p+p collisions.

On the l.h.s. of Fig. 6.8 we compare the yield of $\Lambda + \Sigma^0$ and Ξ^- as produced in Au+Au and p+p collisions at $\sqrt{s_{NN}} = 4.3\,\text{GeV}$ and $\sqrt{s_{NN}} = 7.7\,\text{GeV}$ (in panels (a) and (c), respectively) as a function of the centrality. We mention that a p+p collision develops as an interaction in vacuum and the CSR does not occur (we do not distinguish the cases with and without CSR for the PHSD results for p+p collisions in Fig. 6.8). The hyperon production is larger in the nucleus-nucleus system with respect to the nucleon-nucleon system which is represented by the black diamond point. The difference is larger for the multi-strange particle Ξ^- than for the single-strange $(\Lambda + \Sigma^0)$. For example, in case of the most central collision ($\langle N_{part} \rangle \approx 330$), this enhancement in the PHSD calculation with CSR is of a factor ≈ 10 for Ξ^- and a factor of ≈ 2 for $(\Lambda + \Sigma^0)$ for $\sqrt{s_{NN}} = 7.7\,\text{GeV}$. The production of Ξ^- normalized to the one of p+p increases with $\langle N_{part} \rangle$, while the production of $(\Lambda + \Sigma^0)$ shows a much less pronounced increase.

In addition, we analyze the hyperon production in Au+Au and p+p collisions in terms of the particle ratios $\Lambda/\pi \equiv (\Lambda + \Sigma^0 + \overline{\Lambda} + \overline{\Sigma}^0)/(\pi^+ + \pi^-)$ and $\Xi/\pi \equiv (\Xi + \overline{\Xi})/(\pi^+ + \pi^-)$. This is shown as a function of the centrality on the r.h.s. of Fig. 6.8 at $\sqrt{s_{NN}} = 4.3\,\text{GeV}$ and $\sqrt{s_{NN}} = 7.7\,\text{GeV}$ in panels (b) and (d), respectively. As described above for the hyperon yields, the Ξ/π ratio relative to p+p smoothly rises with centrality, while the Λ/π is almost constant with $\langle N_{part} \rangle$. However, the enhancement with respect to the nucleon-nucleon scattering is smaller than what we find for the normalized yields. In particular, the Ξ/π ratio presents a maximum enhancement for the largest value of $\langle N_{part} \rangle$ of ≈ 75 at $\sqrt{s_{NN}} = 4.3\,\text{GeV}$ and of ≈ 8 at $\sqrt{s_{NN}} = 7.7\,\text{GeV}$.

Finally, we compare our results displayed in Fig. 6.8 at $\sqrt{s_{NN}} = 4.3\,\text{GeV}$ (panels (a) and (b)) and $\sqrt{s_{NN}} = 7.7\,\text{GeV}$ (panels (c) and (d)). The normalized strangeness enhancement appears larger in case of the lower collision energy. In fact, both the Ξ^- yield and the Ξ/π ratio at $\sqrt{s_{NN}} = 4.3\,\text{GeV}$ are approximately one order of magnitude larger than the corresponding quantities at $\sqrt{s_{NN}} = 7.7\,\text{GeV}$ over the entire range of centralities. This is explained by the fact that the flavor exchange channels $Y + Y \leftrightarrow N + \Xi$ have sizable production rates at low energy, while they are less effective at large energies (see Chapter 3 for details). Differently from Ξ^-, the calculations concerning Λ particles at $\sqrt{s_{NN}} = 4.3\,\text{GeV}$ and $\sqrt{s_{NN}} = 7.7\,\text{GeV}$ do not show significant differences, apart from the case of the Λ/π ratio. Specifically, the result

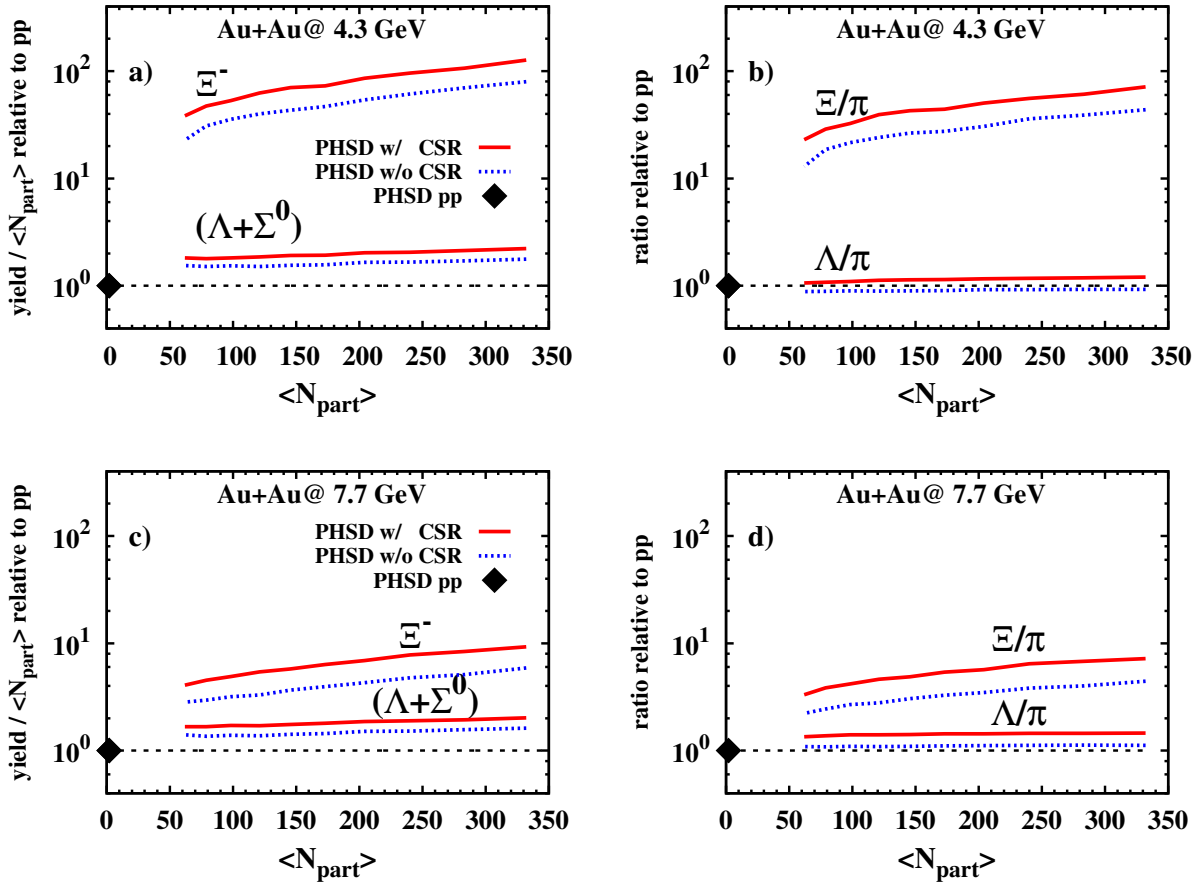

Figure 6.8: (l.h.s.) The full acceptance ratio of the yields of $(\Lambda + \Sigma^0)$ and Ξ^- normalized to $\langle N_{part} \rangle$ to the corresponding quantities in p+p collisions as a function of the number of participants in Au+Au collisions at $\sqrt{s_{NN}} = 4.3\,\text{GeV}$ and $\sqrt{s_{NN}} = 7.7\,\text{GeV}$ in panels (a) and (c), respectively. (r.h.s.) The full acceptance particle ratios Λ/π and Ξ/π from Au+Au collisions relative to p+p collisions as a function of $\langle N_{part} \rangle$ at $\sqrt{s_{NN}} = 4.3\,\text{GeV}$ and $\sqrt{s_{NN}} = 7.7\,\text{GeV}$ in panels (b) and (d), respectively. The black diamonds refer to the results from p+p collisions. The coding of the lines is the same as in Fig. 6.6.

of PHSD without CSR for the Λ/π ratio at $\sqrt{s_{NN}} = 4.3\,\text{GeV}$ is below unity which corresponds to the p+p result. This traces back to the flavor exchange channel $Y + Y \leftrightarrow N + \Xi$, whose associated rates are larger for the forward reactions $(Y + Y \rightarrow N + \Xi)$ than for the backward reactions $(Y + Y \leftarrow N + \Xi)$. As a result, the Λ/π ratio obtained in A+A collisions is smaller than in p+p collisions, where the hadronic re-scattering does not develop. On the other hand, the PHSD result with CSR for the Λ/π ratio at $\sqrt{s_{NN}} = 4.3\,\text{GeV}$ is above unity, because CSR increases the production of strange particles over the non-strange ones.

In the observables investigated in this section, the difference between the results from PHSD

with and without CSR is evident and it is more clearly seen in the particle ratios than in the single particle yields. This provides a way to disentangle the effects of CSR in small systems through the comparison between our calculations and experimental data for this kind of observables. In this respect, future heavy-ion collision experiments are expected to shed light on the centrality dependence of the CSR, too.

Conclusions

In this work we have presented a study of the Chiral Symmetry Restoration (CSR) in Heavy-Ion Collisions (HIC) adopting the Parton-Hadron-String Dynamics (PHSD) transport approach. PHSD represents a solid framework to describe HIC, that has been tested in a wide range of energies, from SIS (SchwerIonen Synchrotron) up to LHC (Large Hadron Collider) energies, providing good results . This model includes both a hadronic and a partonic phase, as well as a transition between the effective degrees of freedom. The partonic phase is modeled according to the Dynamical-Quasi-Particle Model (DQPM), which defines the properties of the degrees of freedom (masses and widths) in the partonic phase and which is conceived to reproduce lQCD results in thermodynamical equilibrium. We have extended PHSD to include essential aspects of CSR, that are incorporated in the Schwinger mechanism for the string decay. This implementation only affects the hadronic particle production and it does not imply modifications in the Quark-Gluon Plasma (QGP) phase.

In Chapter 2 we have shown that CSR induces an enhancement of the strange quark fraction $\gamma_s = s/u$ defined by the Schwinger formula for the string decay, while we predict no sensible changes in the diquark production. Different parametrizations (NL1, NL2, NL3) for the nuclear Equation of State (EoS) have been employed in order to estimate the uncertainty of our results. The role of the EoS is crucial in the calculation of the scalar density (and consequently in the calculation of the scalar quark condensate), which is performed according to a non-linear $\sigma - \omega$ model. Although the s/u ratio shows a moderate dependence on the EoS, its behavior as a function of the energy density is the same for all investigated parametrizations for the EoS: the s/u ratio increases with increasing energy density due to CSR. This strangeness enhancement entails an enhancement of the strange particle abundances with respect to the non-strange ones, that are detected at the end of the collision process. This effect is the signature that allows us to recognize that CSR occurs in HIC, even though we cannot directly measure the scalar quark condensate, which is the order parameter for the chiral phase transition.

In Chapter 3 we have analyzed the strange particle production in the low energy regime, especially close to the threshold of the multi-strange hyperons ($\sqrt{s_{NN}} = 2-3$ GeV). This investiga-

tion has mostly been driven by the open question concerning the large multiplicities of Ξ and ϕ measured by the HADES collaboration. We have addressed this issue extending PHSD to include hyperon-hyperon ($Y + Y$) interactions, as flavor exchange reactions, elastic scatterings and string excitations. The employed cross-sections have been taken from an effective model based on a gauged flavor SU(3)-invariant hadronic Lagrangian solved in the Born approximation (described in Appendix B). Results on rapidity spectra and particle abundances show that the $Y + Y$ channels produce a significant enhancement of the Ξ yield within the energy range $\sqrt{s_{NN}} = 2 - 6\,\text{GeV}$ and that the CSR mechanism is more effective in the dynamics for $\sqrt{s_{NN}} = 3 - 12\,\text{GeV}$. The inclusion of the $Y + Y$ interactions and of CSR do not provide a conclusive explanation of the extremely high Ξ^- and ϕ yields for collisions at $\sqrt{s_{NN}} < 3\,\text{AGeV}$, but a striking improvement of the PHSD description of the hyperon production close to the threshold has been achieved. Further studies are required on mean-field effects and on additional contributions from the close-to-threshold production mechanisms.

Chapter 4 contains a detailed study of the contribution of CSR in HIC observables at AGS and SPS energies. As mentioned above, the role of CSR in the collision dynamics emerges as a strangeness enhancement, which is visible and sizable in the particle spectra at AGS and lower SPS energies (e.g. at $E_{Lab} = 10.7 - 30\,\text{AGeV}$). Increasing further the collision energy, the contribution of CSR vanishes (e.g. at $E_{Lab} = 158\,\text{AGeV}$), since the dynamics of the system is dominated by the QGP phase where strings cannot be formed due to the vanishing string tension. The final results on the particle yields depend moderately on the parametrization for the Equation of State (EoS) adopted in the calculation (NL1, NL2, NL3). For example the maximum variation due to the different parametrization of the EoS is only $\approx 6\%$ for the K^+ yield in central Pb+Pb collisions at 30 AGeV. The strangeness enhancement observed in the particle abundances due to CSR develops in the order NL1 > NL2 > NL3 (the density of protons and pions shows the opposite hierarchy). The NL1 and NL3 fix reliable limits on the uncertainties associated to the CSR effects as implemented in PHSD and these uncertainties are only $\lesssim 10\%$ in the maximum case. Moreover, we have found that transverse mass spectra are relatively insensitive to the CSR mechanism. The results of PHSD including CSR are in a good agreement with the experimental observations of rapidity and transverse mass spectra and particle ratios. In particular, the PHSD calculations with CSR provide the first microscopic interpretation of the "horn"structure in the excitation functions of the K^+/π^+ and $(\Lambda+\Sigma^0)/\pi$ ratios in central Au+Au (or Pb+Pb) collisions. The steep rise of these ratios at AGS energies are associated to CSR, while the drop at higher SPS energies is due to the appearance of the QGP phase in an increasing volume of the interaction region.

The influence of the CSR on the collective dynamics is investigated in Chapter 5. The PHSD description of the differential hadron spectra in p+p and A+A collisions has been remarkably

improved by the implementation of the p_T-kick distribution function in the string dynamics and by the inclusion of the string rotation. Our analysis on the time evolution of the directed flow v_1 has shown that v_1 is established at the early stages of the collisions. In particular, protons acquire transverse momentum during the string interactions. This opens the possibility to detect an effect of CSR also in the directed flow of particles like protons and pions. However, the final result of v_1 extracted from PHSD simulations can be influenced by many factors (hadronic potentials, p_T-cuts), whose contributions have been analyzed in detail. We have incorporated baryon potentials in the particle propagation and have found that this inclusion modifies the proton v_1 only at low energies. The study of the influence of the p_T-cuts on our calculations has shown no severe alteration of our results (only small modifications with respect to the case in which no cuts are applied). Furthermore, we have performed a beam energy scan of the proton and pion flow and our results are in good agreement with the data with some deviations for $\sqrt{s_{NN}} > 20\,\text{GeV}$ for the protons and for $\sqrt{s_{NN}} \leq 11.5\,\text{GeV}$ for pions. The role of CSR on v_1 is negligible, while the inclusion of the partonic phase is essential for the proton and pion flow at RHIC energies. The dependence of v_1 on the baryon potentials manifests at low collision energy, where we find that the potential associated to the NL1 parametrization gives a repulsive effect within $\sqrt{s_{NN}} = 3-5\,\text{GeV}$ and an attractive effect within $\sqrt{s_{NN}} = 5-10\,\text{GeV}$. For $\sqrt{s_{NN}} = 7-9\,\text{GeV}$, the excitation function of the pion slope exhibits a minimum and the proton slope turns from positive to negative values. We suggest that this is due to a smooth transition from a hadronic- to a partonic-dominated system, but further studies are needed to draw a conclusive interpretation.

In Chapter 6 we have focused our attention on the energy range of the future FAIR and NICA facilities ($\sqrt{s_{NN}} = 4-11\,\text{GeV}$), with the aim of providing valuable predictions for observables sensitive to the CSR mechanism. The analysis of the rapidity spectra shows that the FAIR and NICA experiments will explore an energy regime where the QGP contribution is small and consequently the identification of the contribution associated to CSR is easier. From the investigation of the excitation functions of the K^+/π^+ and $(\Lambda + \Sigma^0)/\pi$ ratios we have found that the "horn"structure disappears in the K^+/π^+ ratio as the system size decreases, while it remains at the same energy in the ratio $(\Lambda + \Sigma^0)/\pi$. Furthermore, we have analyzed the particle multiplicities as a function of the number of participants in the collision, to investigate the centrality dependence of CSR. Our results on the strange particle yields and strange to non-strange particle ratios support the fact that CSR occurs in central collisions as well as in moderately peripheral collisions. We have also studied the strangeness enhancement in relation to the strange particle production in p+p collisions and have found an increase of the hyperon production in A+A collisions with respect to p+p collisions. This is more pronounced when CSR is included in the calculations and it is larger for the multi-strange particle Ξ^- than

for the single-strange ($\Lambda + \Sigma^0$).

In conclusion, our microscopic studies support the idea that CSR occurs in hadronic systems with high temperature and density before the deconfinement phase transition takes over. We have shown that many observables are suitable probes to study the properties of CSR in HIC. In this respect, the FAIR and NICA experiments will play an important role, since they will scan the energy regime which is optimal to study CSR and its interplay with the QGP phase.

Acknowledgments

In the first place, I would like to thank my thesis advisor Prof. Wolfgang Cassing for giving me the opportunity to join his research group and to work on this fascinating and stimulating topic. He gave me important advice, constant support and the opportunity to widen my professional horizons in many conferences during my PhD.
Next, I would like to thank Prof. Claudia Höhne for being the second examiner of this dissertation and for her interest in its content.
I am grateful to Prof. Elena Bratkovskaya for the helpful suggestions and discussions, that make me grow on a professional level.
I deeply thank Olena Linnyk, who has been my mentor and my first friend in Giessen.
Many thanks go to the current and former members of the PHSD group and collaborators V. Konchakovski, T. Steinert, E. Seifert, P. Moreau, D. Cabrera, T. Song, A. Ilner, R. Marty, V. Toneev and V. Voronyuk.
I would like to thank all my colleagues and the secretaries of the institute of theoretical physics at the University of Giessen and my friends M. Dhar, C. Hornung, C. Welzbacher and R. Williams.
I want to express my gratitude to R. Ehmann, P. Tebaartz, A. Wieck, Prof. Dr. Adriana del Rey and the SciMento team for their support.
Finally, I am grateful to my husband and my family, who have encouraged and helped me despite the distance.

This work was possible thanks to the computational resources of Loewe-CSC and the support of the Helmholtz International Center for FAIR (HIC for FAIR), the Helmholtz Graduate School for Hadron and Ion Research (HGS-HIRe), the Helmholtz Research School for Quark Matter Studies in Heavy-Ion Collisions (H-QM).

Appendix A

Chiral symmetry

A phase transition of the strong matter associated to the restoration of Chiral Symmetry (CS) is expected to occur at high temperature and/or density. The CS is defined as the invariance of the Quantum-Chromo-Dynamics (QCD) Lagrangian in the massless limit under a transformation of the group $U(N_f)_L \times U(N_f)_R$, where N_f denotes the number of flavors. This symmetry group is isomorphic to $SU(N_f)_L \times SU(N_f)_R \times U(1)_V \times U(1)_A$, where the $U(1)_V$ is associated to the baryon number conservation and the $U(1)_A$ is anomalously broken. In the following, we provide a brief introduction of CS and its features, focusing on the relevant part of CS for two flavors, *i.e.* the $SU(2)_L \times SU(2)_R$ symmetry.
The QCD Lagrangian can be written (flavor indices suppressed) as:

$$\mathscr{L} = -\frac{1}{4} G^a_{\mu\nu} G^{\mu\nu}_a + i\overline{\psi}_R \gamma^\mu D_\mu \psi_R + i\overline{\psi}_L \gamma^\mu D_\mu \psi_L - m(\overline{\psi}_R \psi_L + \overline{\psi}_L \psi_R), \tag{A.1}$$

where $D_\mu = \partial_\mu - i g_s A_\mu$ is the covariant derivative (g_s is the strong coupling constant and A_μ refers to the gluon fields), $G^a_{\mu\nu} = F^a_{\mu\nu} + g_s f^{abc} A_{b\mu} A_{c\nu} = \partial_\mu A^a_\nu - \partial_\nu A^a_\mu + g_s f^{abc} A_{b\mu} A_{c\nu}$ is the gluon field tensor with color index a (f^{abc} denotes the structure constants of SU(3)) and $\psi_{R,L}$ refer to the right- ψ_R and left-handed ψ_L components of the quark field, respectively:

$$\psi = \begin{pmatrix} \psi_R \\ \psi_L \end{pmatrix}. \tag{A.2}$$

The distinction of the quark field in ψ_R and ψ_L components is based on the chiral properties of the quarks, that, as massive fermions, can be right-handed when the sign of the projection of the spin vector onto the momentum vector is positive or left-handed in the opposite case. We can extract the right- and left-handed states by applying the following projectors on the quark field:

$$P_{L,R} = \frac{1}{2}(1 \mp \gamma^5) \tag{A.3}$$

where γ^5 is the Dirac matrix:

$$\gamma^5 = \begin{bmatrix} \mathbb{1}_2 & 0_2 \\ 0_2 & -\mathbb{1}_2 \end{bmatrix} \tag{A.4}$$

with $\mathbb{1}_2$ as 2×2 identity matrix.

In Eq. A.1 the components ψ_R and ψ_L mix only in the last term, *i.e.* in the mass term $m\overline{\psi}\psi = m(\overline{\psi}_R\psi_L + \overline{\psi}_L\psi_R)$. Consequently in case of massless quarks, the QCD Lagrangian fulfills CS, namely it is invariant under a generic transformation of the symmetry group $SU(2)_L \times SU(2)_R$:

$$\psi \rightarrow \psi' = e^{-i\frac{\vec{\tau}_a}{2}\vec{\Theta}_a P_L} e^{-i\frac{\vec{\tau}_b}{2}\vec{\Theta}_b P_R}\psi. \tag{A.5}$$

This transformation can also be re-written in terms of the transformation $\Upsilon_V \times \Upsilon_A$ of the group $SU(2)_V \times SU(2)_A$:

$$e^{-i\frac{\vec{\tau}_a}{2}\vec{\Theta}_a P_L} e^{-i\frac{\vec{\tau}_b}{2}\vec{\Theta}_b P_R}\psi \rightarrow e^{-i\frac{\vec{\tau}}{2}\vec{\Theta}_V} e^{-i\gamma_5\frac{\vec{\tau}}{2}\vec{\Theta}_A}\psi. \tag{A.6}$$

Consequently, if the CS holds, the vector and axial vector currents are equal.

In case of massive quarks, the CS is explicitly broken. For example, under a generic transformation Υ_A the change of the mass term reads:

$$\Upsilon_A : m(\overline{\psi}\psi) \rightarrow m(\overline{\psi}\psi) - 2im\vec{\Theta} \cdot (\overline{\psi}\frac{\vec{\tau}}{2}\gamma_5\psi). \tag{A.7}$$

However, CS is considered as an approximate symmetry of the QCD Lagrangian for energies larger than the quark masses, *i.e.* for energies (or high temperature and/or high density) at which the quark masses approximately vanish $m_q \approx 0$. The chiral condensate $\langle\overline{\psi}\psi\rangle$ represents the order parameter of the transition from a phase in which CS is broken to a phase in which CS is restored:

$$\langle\overline{\psi}\psi\rangle = \begin{cases} \neq 0 & \text{chiral symmetry is broken,} \\ = 0 & \text{chiral symmetry is restored.} \end{cases} \tag{A.8}$$

As mentioned above, the restoration of Chiral Symmetry (CS) is expected to occur at high temperature and/or density [93, 94, 176], as the chiral condensate is expected to decrease from the vacuum value $\langle\overline{\psi}\psi\rangle_V$ to $\langle\overline{\psi}\psi\rangle \approx 0$. This behavior of the chiral condensate as a function of the temperature is shown in Fig. A.1 from a lattice QCD calculation [176] for three flavors ($l = u, d$ and s) in terms of the subtracted chiral condensate $\Delta_{l,s}$:

$$\Delta_{l,s} = \frac{\langle\overline{\psi}\psi\rangle_l - m_l/m_s\langle\overline{\psi}\psi\rangle_s}{\langle\overline{\psi}\psi\rangle_{l,V} - m_l/m_s\langle\overline{\psi}\psi\rangle_{s,V}}. \tag{A.9}$$

Moreover, the breaking of the CS can be treated as a spontaneous symmetry breaking, that generates pseudo-Goldstone bosons, which are massive due to the fact that CS is not exact but

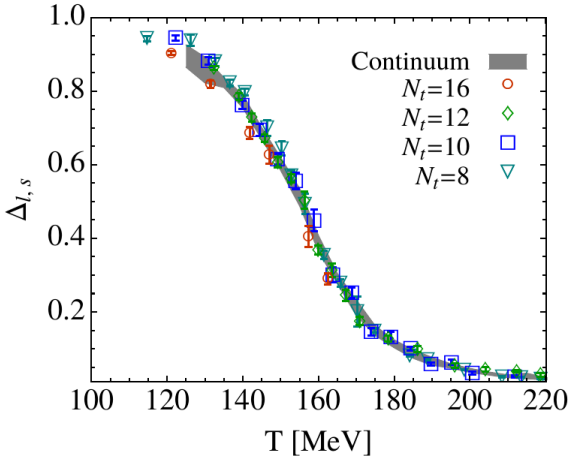

Figure A.1: Subtracted chiral condensate $\Delta_{l,s}$ as a function of the temperature (N_t denotes the temporal extent of the lattice). Figure taken from Ref. [176].

approximate. The pseudo-Goldstone bosons of CS are the pions and their mass m_π is found to be dependent on the quark condensate (considering the u and d flavors) via the Gell Mann Oakes Renner relation [107, 108, 109]:

$$m_\pi^2 f_\pi^2 = -(m_u^0 + m_d^0)\,\langle\overline{\psi}\psi\rangle = -\frac{1}{2}(m_u^0 + m_d^0)\cdot(\langle\overline{\psi}_u\psi_u\rangle + \langle\overline{\psi}_d\psi_d\rangle)\,, \tag{A.10}$$

where f_π is the pion decay constant, m_u^0 and m_d^0 are the bare masses of the u and d quarks, respectively.

Appendix B

Hyperon-hyperon interactions in a gauged flavor SU(3) hadronic model

Within the Parton-Hadron-String Dynamics (PHSD) transport approach, the cross-sections for the hyperon scattering of the types $Y + Y \leftrightarrow N + \Xi$ and $Y + \bar{K} \leftrightarrow \Xi + \pi$ are employed according to the hadronic model described in Refs. [116, 117, 177]. This model is introduced here with a particular focus on the derivation of the cross-sections for the $Y + Y \leftrightarrow N + \Xi$ scatterings, which have been recently implemented in PHSD as reported in Chapter 3.
The hadronic model [177] is based on a gauged flavor SU(3)-invariant hadronic Lagrangian $\mathscr{L}$ for pseudoscalar mesons and baryons:

$$\mathscr{L} = iTr(\overline{B}\partial\!\!\!/ B) + Tr[(\partial_\mu P^\dagger \partial^\mu P)] + g'\{Tr[(2\alpha - 1)\overline{B}\gamma^5\gamma^\mu B\partial_\mu P + \overline{B}\gamma^5\gamma^\mu(\partial_\mu P)B]\}, \tag{B.1}$$

where g' represents the pseudoscalar coupling constant, α is a parameter and B and P refer to the baryon and pseudoscalar meson octets, respectively:

$$B = \begin{pmatrix} \frac{\Sigma^0}{\sqrt{2}} + \frac{\Lambda}{\sqrt{6}} & \Sigma^+ & p \\ \Sigma^- & -\frac{\Sigma^0}{\sqrt{2}} + \frac{\Lambda}{\sqrt{6}} & n \\ -\Xi^- & \Xi^0 & -\sqrt{\frac{2}{3}}\Lambda \end{pmatrix}, \tag{B.2}$$

$$P = \frac{1}{\sqrt{2}} \begin{pmatrix} \frac{\pi^0}{\sqrt{2}} + \frac{\eta_8}{\sqrt{6}} + \frac{\eta_1}{\sqrt{3}} & \pi^+ & K^+ \\ \pi^- & -\frac{\pi^0}{\sqrt{2}} + \frac{\eta_8}{\sqrt{6}} + \frac{\eta_1}{\sqrt{3}} & K^0 \\ -K^- & \overline{K}^0 & -\sqrt{\frac{2}{3}}\eta_8 + \frac{\eta_1}{\sqrt{3}} \end{pmatrix}. \tag{B.3}$$

In Eq. B.3, η_0 and η_8 are the singlet and octet η mesons, respectively. They correspond to combinations of the physical η and η' particles in terms of the mixing angle θ: $\eta_1 = -sin\theta\,\eta + cos\theta\,\eta'$, $\eta_8 = cos\theta\,\eta + sin\theta\,\eta'$.
The interactions between the pseudoscalar mesons and baryons with the vector meson octet V_μ

are included in the model via replacing in Eq. B.1 the partial derivative ∂_μ with the covariant derivative D_μ:

$$\partial_\mu \rightarrow D_\mu = \partial_\mu - \frac{i}{2} g[V_\mu,], \tag{B.4}$$

where g is a coupling constant. The 3×3 matrix representation of the vector meson octet is:

$$V = \frac{1}{\sqrt{2}} \begin{pmatrix} \frac{\rho^0}{\sqrt{2}} + \frac{\omega}{\sqrt{2}} & \rho^+ & K^{*+} \\ \rho^- & -\frac{\rho^0}{\sqrt{2}} + \frac{\omega}{\sqrt{2}} & K^{*0} \\ -K^{*-} & K^{*0} & \phi \end{pmatrix}. \tag{B.5}$$

Additionally, tensor interactions between baryons and vector mesons are incorporated according to the following interaction Lagrangian $\mathscr{L}^t$:

$$\mathscr{L}^t = \frac{g^t}{2m} Tr[(2a-1)\overline{B}\sigma^{\mu\nu} B \partial_\mu V_\nu + \overline{B}\sigma^{\mu\nu}(\partial_\mu V_\nu) B], \tag{B.6}$$

where g^t is the associated coupling constant and m is the SU(3) degenerate baryon mass.
The unknown couplings g, g' and g^t and the parameter α can be related to known couplings (e.g., to the pion-nucleon coupling $f_{\pi NN}$) using SU(3) relations and their values are extracted from empirical information (see Refs. [117, 177] for details). The values of the couplings and of the parameter α (estimated in Ref. [117]) are: $g = 13.0$, $g' = 14.4\,\mathrm{GeV}^{-1}$, $g^t/2m = 19.8/m_N$ (with m_N as nucleon mass), and $\alpha = 0.64$.
The cross-sections for the reactions $Y + Y \leftrightarrow N + \Xi$ are computed in the Born approximation and they are given by the tree-level t-channel and u-channel diagrams, which are displayed in Fig. B.1 on the l.h.s. and r.h.s., respectively.

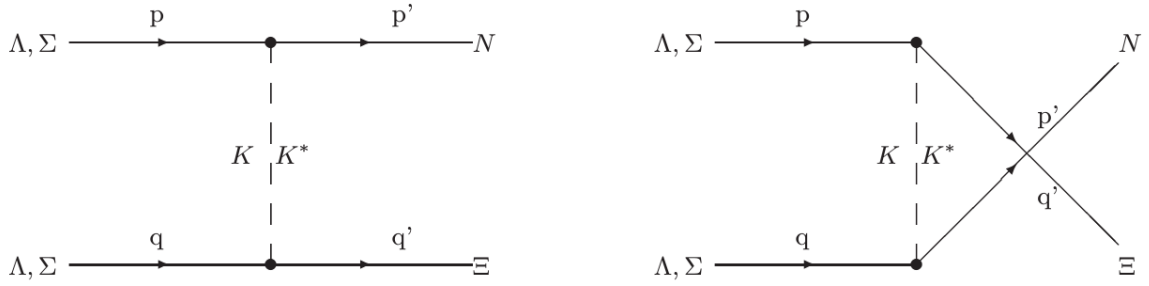

Figure B.1: The tree-level t-channel and u-channel diagrams for the reactions $Y + Y \leftrightarrow N + \Xi$ in the Born approximation on the l.h.s. and r.h.s., respectively. Figure taken from Ref. [117].

At the interaction vertices, form factors F have to be included due to the finite size of the hadrons. In the hadronic model considered here, the expression adopted for the form factors for all the interacting hadrons is:

$$F(\mathbf{q}, \lambda) = \frac{\lambda^2}{\lambda^2 + \mathbf{q}^2}, \tag{B.7}$$

where $\mathbf{q}$ is the 3-momentum transfer and λ is a parameter, which is taken to be $\lambda = 0.7\,\mathrm{GeV}$ for consistency with the cross-section of the $Y + \bar{K} \leftrightarrow \Xi + \pi$ reactions computed in Ref. [116] (the dependence on the parameter λ is investigated in Refs. [116, 117, 177]).
The cross-sections for the forward channels are given by:

$$\sigma_{YY\to N\Xi}(s) = \frac{1}{64\pi s p_i^2}\int dt\,\overline{|M|^2}, \tag{B.8}$$

where s and t are the Mandelstam variables, p_i is the momentum of the initial hyperons in their center-of-mass frame and $|M|^2$ is the spin-isospin averaged scattering amplitude squared. Finally, these cross-sections can be parametrized as follows:

$$\sigma_{\Lambda\Lambda\to N\Xi} = 37.15\frac{p_N}{p_\Lambda}(\sqrt{s} - \sqrt{s_0})^{-0.16} mb, \tag{B.9}$$

$$\sigma_{\Lambda\Sigma\to N\Xi} = 25.12(\sqrt{s} - \sqrt{s_0})^{-0.42} mb, \tag{B.10}$$

$$\sigma_{\Sigma\Sigma\to N\Xi} = 8.51(\sqrt{s} - \sqrt{s_0})^{-0.395} mb, \tag{B.11}$$

with p_N as the initial nucleon momentum and p_Λ as final momentum of the Λ, both expressed in the center-of-mass frame of the collision. The energy threshold $\sqrt{s_0}$ is the minimum energy needed for the reaction to occur: $\sqrt{s_0} = Max[(m_{\Lambda,\Sigma} + m_{\Lambda,\Sigma}), (m_N + m_\Xi)]$.
The cross-sections for the backward reactions are computed applying the detailed balance and they are expressed by the following relations:

$$\sigma_{N\Xi\to\Lambda\Lambda} = \frac{1}{4}\left(\frac{p_\Lambda}{p_N}\right)^2 \sigma_{\Lambda\Lambda\to N\Xi}, \tag{B.12}$$

$$\sigma_{N\Xi\to\Lambda\Sigma} = \frac{3}{4}\left(\frac{p_\Lambda}{p_N}\right)^2 \sigma_{\Lambda\Sigma\to N\Xi}, \tag{B.13}$$

$$\sigma_{N\Xi\to\Sigma\Sigma} = \frac{9}{4}\left(\frac{p_\Sigma}{p_N}\right)^2 \sigma_{\Sigma\Sigma\to N\Xi}, \tag{B.14}$$

where p_Σ is the momentum of the Σ particle in the center-of-mass frame and the numerical factors on the right-hand side are given by isospin combinations.

Bibliography

[1] G. S. F. Stephans. Probing the extremes of high baryon density nuclear matter: The BNL AGS program. *Nucl. Phys.*, A583:653C–662C, 1995.

[2] M. Gazdzicki. The SPS ion program and the first LHC data. *AIP Conf. Proc.*, 1422:98–103, 2012.

[3] Bedangadas Mohanty. STAR experiment results from the beam energy scan program at RHIC. *J. Phys.*, G38:124023, 2011.

[4] Jeffery T. Mitchell. The RHIC Beam Energy Scan Program: Results from the PHENIX Experiment. *Nucl. Phys.*, A904-905:903c–906c, 2013.

[5] Paul Romatschke and Ulrike Romatschke. Viscosity Information from Relativistic Nuclear Collisions: How Perfect is the Fluid Observed at RHIC? *Phys. Rev. Lett.*, 99:172301, 2007.

[6] Marek Gazdzicki and Mark I. Gorenstein. On the early stage of nucleus-nucleus collisions. *Acta Phys. Polon.*, B30:2705, 1999.

[7] W. Cassing and E. L. Bratkovskaya. Parton-Hadron-String Dynamics: an off-shell transport approach for relativistic energies. *Nucl. Phys.*, A831:215–242, 2009.

[8] N. Armesto and E. Scomparin. Heavy-ion collisions at the Large Hadron Collider: a review of the results from Run 1. *Eur. Phys. J. Plus*, 131(3):52, 2016.

[9] A. Andronic et al. Excitation function of elliptic flow in Au+Au collisions and the nuclear matter equation of state. *Phys. Lett.*, B612:173–180, 2005.

[10] P. Senger et al. The KAON spectrometer at SIS. *Nucl. Instrum. Meth.*, A327:393–411, 1993.

[11] G. Agakichiev et al. Dielectron production in C-12+C-12 collisions at 2-AGeV with HADES. *Phys. Rev. Lett.*, 98:052302, 2007.

[12] P. Spiller and G. Franchetti. The FAIR accelerator project at GSI. *Nucl. Instrum. Meth.*, A561:305–309, 2006.

[13] Alexander Sorin, Vladimir Kekelidze, Alexander Kovalenko, Richard Lednicky, Igor Meshkov, and Grigory Trubnikov. Heavy-ion program at NICA/MPD at JINR. *Nucl. Phys.*, A855:510–513, 2011.

[14] H. Sako et al. Towards the heavy-ion program at J-PARC. *Nucl. Phys.*, A931:1158–1162, 2014.

[15] V. Friese. The CBM experiment at GSI/FAIR. *Nucl. Phys.*, A774:377–386, 2006.

[16] Grazyna Odyniec. Future of the beam energy scan program at RHIC. *EPJ Web Conf.*, 95:03027, 2015.

[17] N. Cabibbo and G. Parisi. Exponential Hadronic Spectrum and Quark Liberation. *Phys. Lett.*, B59:67–69, 1975.

[18] L. McLerran. The Phase Diagram of QCD and Some Issues of Large N(c). *Nucl. Phys. Proc. Suppl.*, 195:275–280, 2009.

[19] Y. Aoki, Z. Fodor, S. D. Katz, and K. K. Szabo. The QCD transition temperature: Results with physical masses in the continuum limit. *Phys. Lett.*, B643:46–54, 2006.

[20] P. Petreczky. Lattice QCD at non-zero temperature. *J. Phys.*, G39:093002, 2012.

[21] Gert Aarts. Introductory lectures on lattice QCD at nonzero baryon number. *J. Phys. Conf. Ser.*, 706(2):022004, 2016.

[22] P. Senger *et al. Lect. Notes Phys. 814, 681*. Springer, 2011.

[23] Christian S. Fischer, Jan Luecker, and Christian A. Welzbacher. Phase structure of three and four flavor QCD. *Phys. Rev.*, D90(3):034022, 2014.

[24] Christian S. Fischer, Leonard Fister, Jan Luecker, and Jan M. Pawlowski. Polyakov loop potential at finite density. *Phys. Lett.*, B732:273–277, 2014.

[25] Tina K. Herbst, Jan M. Pawlowski, and Bernd-Jochen Schaefer. Phase structure and thermodynamics of QCD. *Phys. Rev.*, D88(1):014007, 2013.

[26] Gernot Eichmann, Helios Sanchis-Alepuz, Richard Williams, Reinhard Alkofer, and Christian S. Fischer. Baryons as relativistic three-quark bound states. *Prog. Part. Nucl. Phys.*, 91:1–100, 2016.

[27] Gernot Eichmann, Christian S. Fischer, and Christian A. Welzbacher. Baryon effects on the location of QCD's critical end point. *Phys. Rev.*, D93(3):034013, 2016.

[28] S. P. Klevansky. The Nambu-Jona-Lasinio model of quantum chromodynamics. *Rev. Mod. Phys.*, 64:649–708, 1992.

[29] Kenji Fukushima. Phase diagrams in the three-flavor Nambu-Jona-Lasinio model with the Polyakov loop. *Phys. Rev.*, D77:114028, 2008. [Erratum: Phys. Rev.D78,039902(2008)].

[30] Larry McLerran and Robert D. Pisarski. Phases of cold, dense quarks at large N(c). *Nucl. Phys.*, A796:83–100, 2007.

[31] Yoichiro Nambu and G. Jona-Lasinio. Dynamical Model of Elementary Particles Based on an Analogy with Superconductivity. 1. *Phys. Rev.*, 122:345–358, 1961.

[32] S. Wheaton and J. Cleymans. Statistical-thermal model calculations using THERMUS. *J. Phys.*, G31:S1069–S1074, 2005.

[33] F. Becattini, J. Manninen, and M. Gazdzicki. Energy and system size dependence of chemical freeze-out in relativistic nuclear collisions. *Phys. Rev.*, C73:044905, 2006.

[34] A. Andronic, P. Braun-Munzinger, and J. Stachel. Thermal hadron production in relativistic nuclear collisions: The Hadron mass spectrum, the horn, and the QCD phase transition. *Phys. Lett.*, B673:142–145, 2009. [Erratum: Phys. Lett.B678,516(2009)].

[35] Jean Letessier and Johann Rafelski. Hadron production and phase changes in relativistic heavy ion collisions. *Eur. Phys. J.*, A35:221–242, 2008.

[36] K. A. Bugaev, D. R. Oliinychenko, J. Cleymans, A. I. Ivanytskyi, I. N. Mishustin, E. G. Nikonov, and V. V. Sagun. Chemical Freeze-out of Strange Particles and Possible Root of Strangeness Suppression. *Europhys. Lett.*, 104:22002, 2013.

[37] Yu. B. Ivanov, V. N. Russkikh, and V. D. Toneev. Relativistic heavy-ion collisions within 3-fluid hydrodynamics: Hadronic scenario. *Phys. Rev.*, C73:044904, 2006.

[38] S. Teis, W. Cassing, M. Effenberger, A. Hombach, U. Mosel, and G. Wolf. Pion production in heavy ion collisions at SIS energies. *Z. Phys.*, A356:421–435, 1997.

[39] S. A. Bass et al. Microscopic models for ultrarelativistic heavy ion collisions. *Prog. Part. Nucl. Phys.*, 41:255–369, 1998. [Prog. Part. Nucl. Phys.41,225(1998)].

[40] C. Hartnack, Rajeev K. Puri, J. Aichelin, J. Konopka, S. A. Bass, Horst Stoecker, and W. Greiner. Modeling the many body dynamics of heavy ion collisions: Present status and future perspective. *Eur. Phys. J.*, A1:151–169, 1998.

[41] Xin-Nian Wang and Miklos Gyulassy. HIJING: A Monte Carlo model for multiple jet production in p p, p A and A A collisions. *Phys. Rev.*, D44:3501–3516, 1991.

[42] Y. Nara, N. Otuka, A. Ohnishi, K. Niita, and S. Chiba. Study of relativistic nuclear collisions at AGS energies from p + Be to Au + Au with hadronic cascade model. *Phys. Rev.*, C61:024901, 2000.

[43] L. V. Bravina et al. Equilibrium and nonequilibrium effects in relativistic heavy ion collisions. *Nucl. Phys.*, A661:600–603, 1999.

[44] A. Palmese, W. Cassing, E. Seifert, T. Steinert, P. Moreau, and E. L. Bratkovskaya. Chiral symmetry restoration in heavy-ion collisions at intermediate energies. *Phys. Rev.*, C94(4):044912, 2016.

[45] J. Cleymans, H. Oeschler, K. Redlich, and S. Wheaton. Transition from baryonic to mesonic freeze-out. *Phys. Lett.*, B615:50–54, 2005.

[46] A. Andronic, P. Braun-Munzinger, and J. Stachel. Hadron production in central nucleus-nucleus collisions at chemical freeze-out. *Nucl. Phys.*, A772:167–199, 2006.

[47] A. Andronic, P. Braun-Munzinger, and J. Stachel. Thermal hadron production in relativistic nuclear collisions: The Hadron mass spectrum, the horn, and the QCD phase transition. *Phys. Lett.*, B673:142–145, 2009. [Erratum: Phys. Lett.B678,516(2009)].

[48] Wojciech Broniowski, Francesco Giacosa, and Viktor Begun. Cancellation of the σ meson in thermal models. *Phys. Rev.*, C92(3):034905, 2015.

[49] E. E. Kolomeitsev et al. Transport theories for heavy-ion collisions in the 1-A-GeV regime. *J. Phys.*, G31:S741–S758, 2005.

[50] Dirk H. Rischke, Mark I. Gorenstein, Horst Stoecker, and Walter Greiner. Excluded volume effect for the nuclear matter equation of state. *Z. Phys.*, C51:485–490, 1991.

[51] V. Vovchenko, D. V. Anchishkin, and M. I. Gorenstein. Van der Waals Equation of State with Fermi Statistics for Nuclear Matter. *Phys. Rev.*, C91(6):064314, 2015.

[52] Fred Cooper and Graham Frye. Comment on the Single Particle Distribution in the Hydrodynamic and Statistical Thermodynamic Models of Multiparticle Production. *Phys. Rev.*, D10:186, 1974.

[53] D. Oliinychenko, P. Huovinen, and H. Petersen. Systematic Investigation of Negative Cooper-Frye Contributions in Heavy Ion Collisions Using Coarse-grained Molecular Dynamics. *Phys. Rev.*, C91(2):024906, 2015.

[54] Michael L. Miller, Klaus Reygers, Stephen J. Sanders, and Peter Steinberg. Glauber modeling in high energy nuclear collisions. *Ann. Rev. Nucl. Part. Sci.*, 57:205–243, 2007.

[55] A. V. Merdeev, L. M. Satarov, and I. N. Mishustin. Hydrodynamic modeling of deconfinement phase transition in heavy-ion collisions at NICA-FAIR energies. *Phys. Rev.*, C84:014907, 2011.

[56] Francois Gelis, Edmond Iancu, Jamal Jalilian-Marian, and Raju Venugopalan. The Color Glass Condensate. *Ann. Rev. Nucl. Part. Sci.*, 60:463–489, 2010.

[57] Peter F. Kolb and Ulrich W. Heinz. Hydrodynamic description of ultrarelativistic heavy ion collisions. arXiv: 0305084 [nucl-th], 2003.

[58] P. Huovinen and P. V. Ruuskanen. Hydrodynamic Models for Heavy Ion Collisions. *Ann. Rev. Nucl. Part. Sci.*, 56:163–206, 2006.

[59] K. H. Ackermann et al. Elliptic flow in Au + Au collisions at (S(NN))**(1/2) = 130 GeV. *Phys. Rev. Lett.*, 86:402–407, 2001.

[60] Miklos Gyulassy. The QGP discovered at RHIC. In *Structure and dynamics of elementary matter. Proceedings, NATO Advanced Study Institute, Camyuva-Kemer, Turkey, September 22-October 2, 2003*, pages 159–182, 2004.

[61] M. C. Chu. One-dimensional Hydrodynamics of Ultrarelativistic Heavy Ion Collisions. *Phys. Rev.*, D34:2764–2772, 1986.

[62] I. N. Mishustin, V. N. Russkikh, and L. M. Satarov. Ultrarelativistic Heavy Ion Collisions Within Two Fluid Model With Pion Emission. *Nucl. Phys.*, A494:595–619, 1989.

[63] Iu. Karpenko, P. Huovinen, and M. Bleicher. A 3+1 dimensional viscous hydrodynamic code for relativistic heavy ion collisions. *Comput. Phys. Commun.*, 185:3016–3027, 2014.

[64] Chun Shen, Ulrich Heinz, Pasi Huovinen, and Huichao Song. Radial and elliptic flow in Pb+Pb collisions at the Large Hadron Collider from viscous hydrodynamic. *Phys. Rev.*, C84:044903, 2011.

[65] Bjoern Schenke, Sangyong Jeon, and Charles Gale. (3+1)D hydrodynamic simulation of relativistic heavy-ion collisions. *Phys. Rev.*, C82:014903, 2010.

[66] Huichao Song and Ulrich W. Heinz. Suppression of elliptic flow in a minimally viscous quark-gluon plasma. *Phys. Lett.*, B658:279–283, 2008.

[67] Hannah Petersen, Jan Steinheimer, Gerhard Burau, Marcus Bleicher, and Horst Stocker. A Fully Integrated Transport Approach to Heavy Ion Reactions with an Intermediate Hydrodynamic Stage. *Phys. Rev.*, C78:044901, 2008.

[68] Huichao Song, Steffen A. Bass, and Ulrich Heinz. Viscous QCD matter in a hybrid hydrodynamic+Boltzmann approach. *Phys. Rev.*, C83:024912, 2011.

[69] H. Niemi and G. S. Denicol. How large is the Knudsen number reached in fluid dynamical simulations of ultrarelativistic heavy ion collisions? arXiv: 1404.7327 [nucl-th], 2014.

[70] L. P. Kadanoff and G. Baym. *Quantum Statistical Mechanics*. Benjamin, 1962.

[71] Torbjorn Sjostrand, Stephen Mrenna, and Peter Z. Skands. PYTHIA 6.4 Physics and Manual. *JHEP*, 05:026, 2006.

[72] Bo Nilsson-Almqvist and Evert Stenlund. Interactions Between Hadrons and Nuclei: The Lund Monte Carlo, Fritiof Version 1.6. *Comput. Phys. Commun.*, 43:387, 1987.

[73] Bo Andersson, G. Gustafson, and Hong Pi. The FRITIOF model for very high-energy hadronic collisions. *Z. Phys.*, C57:485–494, 1993.

[74] Torbjorn Sjostrand and Mats Bengtsson. The Lund Monte Carlo for Jet Fragmentation and e+ e- Physics. Jetset Version 6.3: An Update. *Comput. Phys. Commun.*, 43:367, 1987.

[75] Bo Andersson, G. Gustafson, and B. Nilsson-Almqvist. A Model for Low p(t) Hadronic Reactions, with Generalizations to Hadron - Nucleus and Nucleus-Nucleus Collisions. *Nucl. Phys.*, B281:289–309, 1987.

[76] W. Cassing. Anti-baryon production in hot and dense nuclear matter. *Nucl. Phys.*, A700:618–646, 2002.

[77] Rainer J. Fries, Vincenzo Greco, and Paul Sorensen. Coalescence Models For Hadron Formation From Quark Gluon Plasma. *Ann. Rev. Nucl. Part. Sci.*, 58:177–205, 2008.

[78] E. L. Bratkovskaya, W. Cassing, V. P. Konchakovski, and O. Linnyk. Parton-Hadron-String Dynamics at Relativistic Collider Energies. *Nucl. Phys.*, A856:162–182, 2011.

[79] W. Cassing. From Kadanoff-Baym dynamics to off-shell parton transport. *Eur. Phys. J. ST*, 168:3–87, 2009.

[80] W. Cassing. Dynamical quasiparticles properties and effective interactions in the sQGP. *Nucl. Phys.*, A795:70–97, 2007.

[81] O. Linnyk, E. L. Bratkovskaya, and W. Cassing. Effective QCD and transport description of dilepton and photon production in heavy-ion collisions and elementary processes. *Prog. Part. Nucl. Phys.*, 87:50–115, 2016.

[82] W. Cassing, A. Palmese, P. Moreau, and E. L. Bratkovskaya. Chiral symmetry restoration versus deconfinement in heavy-ion collisions at high baryon density. *Phys. Rev.*, C93:014902, 2016.

[83] Wim Botermans and Rudi Malfliet. Quantum transport theory of nuclear matter. *Phys. Rept.*, 198:115–194, 1990.

[84] Y. Aoki, Szabolcs Borsanyi, Stephan Durr, Zoltan Fodor, Sandor D. Katz, Stefan Krieg, and Kalman K. Szabo. The QCD transition temperature: results with physical masses in the continuum limit II. *JHEP*, 06:088, 2009.

[85] Hamza Berrehrah, Wolfgang Cassing, Elena Bratkovskaya, and Thorsten Steinert. Quark susceptibility in a generalized dynamical quasiparticle model. *Phys. Rev.*, C93(4):044914, 2016.

[86] Hamza Berrehrah, Elena Bratkovskaya, Thorsten Steinert, and Wolfgang Cassing. A dynamical quasiparticle approach for the QGP bulk and transport properties. *Int. J. Mod. Phys.*, E25(07):1642003, 2016.

[87] T. Kodama, S. B. Duarte, K. C. Chung, R. Donangelo, and R. A. M. S. Nazareth. Causality and relativistic effects in intranuclear cascade calculations. *Phys. Rev.*, C29:2146–2152, 1984.

[88] Julian S. Schwinger. On gauge invariance and vacuum polarization. *Phys. Rev.*, 82:664–679, 1951.

[89] J. Geiss, W. Cassing, and C. Greiner. Strangeness production in the HSD transport approach from SIS to SPS energies. *Nucl. Phys.*, A644:107–138, 1998.

[90] L. Montanet et al. Review of particle properties. Particle Data Group. *Phys. Rev.*, D50:1173–1823, 1994.

[91] W. Cassing and E. L. Bratkovskaya. Hadronic and electromagnetic probes of hot and dense nuclear matter. *Phys. Rept.*, 308:65–233, 1999.

[92] Thomas D. Cohen, R. J. Furnstahl, and David K. Griegel. Quark and gluon condensates in nuclear matter. *Phys. Rev.*, C45:1881–1893, 1992.

[93] U. Vogl and W. Weise. The Nambu and Jona Lasinio model: Its implications for hadrons and nuclei. *Prog. Part. Nucl. Phys.*, 27:195–272, 1991.

[94] Michael C. Birse. Chiral symmetry in nuclei: Partial restoration and its consequences. *J. Phys.*, G20:1537–1576, 1994.

[95] Volker Koch. Aspects of chiral symmetry. *Int. J. Mod. Phys.*, E6:203–250, 1997.

[96] James V. Steele, Hidenaga Yamagishi, and Ismail Zahed. Dilepton and photon emission rates from a hadronic gas. *Phys. Lett.*, B384:255–262, 1996.

[97] James V. Steele, Hidenaga Yamagishi, and Ismail Zahed. Dilepton and photon emission rates from a hadronic gas. 2. *Phys. Rev.*, D56:5605–5617, 1997.

[98] T. Ueda and Y. Ikegami. Separable representation of pi-N scattering amplitudes. *Prog. Theor. Phys.*, 91:85–104, 1994.

[99] G. E. Brown, C. M. Ko, Z. G. Wu, and L. H. Xia. Kaon production from hot and dense matter formed in heavy-ion collisions. *Phys. Rev.*, C43:1881–1892, 1991.

[100] V. Koch and G. E. Brown. Model of the thermodynamics of the chiral restoration transition. *Nucl. Phys.*, A560:345–364, 1993.

[101] Ralf Rapp. Dilepton Spectroscopy of QCD Matter at Collider Energies. *Adv. High Energy Phys.*, 2013:148253, 2013.

[102] B. Friman, W. Nörenberg, and V. D. Toneev. The Quark condensate in relativistic nucleus-nucleus collisions. *Eur. Phys. J.*, A3:165–170, 1998.

[103] J. M. Alarcon, J. Martin Camalich, and J. A. Oller. The chiral representation of the πN scattering amplitude and the pion-nucleon sigma term. *Phys. Rev.*, D85:051503, 2012.

[104] Martin Hoferichter, J. Ruiz de Elvira, Bastian Kubis, and Ulf-G. Meissner. High-Precision Determination of the Pion-Nucleon σ-term from Roy-Steiner Equations. *Phys. Rev. Lett.*, 115:092301, 2015.

[105] Gunnar S. Bali, Sara Collins, Daniel Richtmann, Andreas Schäfer, Wolfgang Söldner, and André Sternbeck. Direct determinations of the nucleon and pion σ terms at nearly physical quark masses. *Phys. Rev.*, D93(9):094504, 2016.

[106] Yi-Bo Yang, Andrei Alexandru, Terrence Draper, Jian Liang, and Keh-Fei Liu. πN and strangeness sigma terms at the physical point with chiral fermions. *Phys. Rev.*, D94(5):054503, 2016.

[107] Masako Bando, Taichiro Kugo, and Koichi Yamawaki. Nonlinear Realization and Hidden Local Symmetries. *Phys. Rept.*, 164:217–314, 1988.

[108] T. D. Cohen, R. J. Furnstahl, D. K. Griegel, and Xue-min Jin. QCD sum rules and applications to nuclear physics. *Prog. Part. Nucl. Phys.*, 35:221–298, 1995.

[109] J. Boguta and A. R. Bodmer. Relativistic Calculation of Nuclear Matter and the Nuclear Surface. *Nucl. Phys.*, A292:413–428, 1977.

[110] A. Lang, B. Blaettel, W. Cassing, V. Koch, U. Mosel, and K. Weber. Dynamical and thermal aspects of relativistic heavy-ion collisions. *Z. Phys.*, A340:287–295, 1991.

[111] Torbjorn Sjostrand. The Lund Monte Carlo for Jet Fragmentation and e+ e- Physics: Jetset Version 6.2. *Comput. Phys. Commun.*, 39:347–407, 1986.

[112] G. Agakishiev et al. Deep sub-threshold Xi- production in Ar+KCl reactions at 1.76A-GeV. *Phys. Rev. Lett.*, 103:132301, 2009.

[113] G. Agakishiev et al. Hyperon production in Ar+KCl collisions at 1.76A GeV. *Eur. Phys. J.*, A47:21, 2011.

[114] J. L. Ritman et al. On the transverse momentum distribution of strange hadrons produced in relativistic heavy-ion collisions. *Z. Phys.*, A352:355–357, 1995.

[115] D. Best et al. K+ production in the reaction Ni-58 + Ni-58 at incident energies from 1-A/GeV to 2-A/GeV. *Nucl. Phys.*, A625:307–324, 1997.

[116] Lie-Wen Chen, Che Ming Ko, and Yiharn Tzeng. Cascade production in heavy-ion collisions at SIS energies. *Phys. Lett.*, B584:269–275, 2004.

[117] Feng Li, Lie-Wen Chen, Che Ming Ko, and Su Houng Lee. Contributions of hyperon-hyperon scattering to subthreshold cascade production in heavy-ion collisions. *Phys. Rev.*, C85:064902, 2012.

[118] E. E. Kolomeitsev, B. Tomasik, and D. N. Voskresensky. Strangeness Balance in HADES Experiments and the Ξ^- Enhancement. *Phys. Rev.*, C86:054909, 2012.

[119] G. Graef, J. Steinheimer, Feng Li, and Marcus Bleicher. Deep sub-threshold Ξ and Λ production in nuclear collisions with the UrQMD transport model. *Phys. Rev.*, C90:064909, 2014.

[120] C. Alt et al. Energy dependence of Lambda and Xi production in central Pb+Pb collisions at A-20, A-30, A-40, A-80, and A-158 GeV measured at the CERN Super Proton Synchrotron. *Phys. Rev.*, C78:034918, 2008.

[121] N. Bastid et al. K0 and Lambda production in Ni + Ni collisions near threshold. *Phys. Rev.*, C76:024906, 2007.

[122] M. Menzel et al. First measurement of anti-kaon phase space distributions in nucleus - nucleus collisions at subthreshold beam energies. *Phys. Lett.*, B495:26–32, 2000.

[123] G. Agakishiev et al. Phi decay: A Relevant source for K- production at SIS energies? *Phys. Rev.*, C80:025209, 2009.

[124] P. Tlusty et al. Charged pion production in C+C and Ar+KCl collisions measured with HADES. In *Proceedings, 47th International Winter Meeting on Nuclear Physics (Bormio 2009): Bormio, Italy, January 26-30, 2009*, 2009.

[125] Jan Steinheimer and Marcus Bleicher. Sub-threshold ϕ and Ξ^- production by high mass resonances with UrQMD. *J. Phys.*, G43(1):015104, 2016.

[126] Alvin Kiswandhi, Shin Nan Yang, and Yu Bing Dong. Near-threshold incoherent ϕ photoproduction on the deuteron: Searching for traces of a resonance. *Phys. Rev.*, C94(1):015202, 2016.

[127] P. Chung et al. Near threshold production of the multistrange Xi- hyperon. *Phys. Rev. Lett.*, 91:202301, 2003.

[128] F. Antinori et al. Energy dependence of hyperon production in nucleus nucleus collisions at SPS. *Phys. Lett.*, B595:68–74, 2004.

[129] G. Agakishiev et al. Subthreshold Xi- Production in Collisions of p(3.5 GeV)+Nb. *Phys. Rev. Lett.*, 114(21):212301, 2015.

[130] F. Antinori et al. Enhancement of hyperon production at central rapidity in 158-A-GeV/c Pb-Pb collisions. *J. Phys.*, G32:427–442, 2006.

[131] J. Stachel. Tests of thermalization in relativistic nucleus nucleus collisions. *Nucl. Phys.*, A610:509C–522C, 1996.

[132] S. Albergo et al. Lambda spectra in 11.6-A-GeV/c Au Au collisions. *Phys. Rev. Lett.*, 88:062301, 2002.

[133] C. Alt et al. Pion and kaon production in central Pb + Pb collisions at 20-A and 30-A-GeV: Evidence for the onset of deconfinement. *Phys. Rev.*, C77:024903, 2008.

[134] C. Alt et al. Energy and centrality dependence of anti-p and p production and the anti-Lambda/anti-p ratio in Pb+Pb collisions between 20/A-GeV and 158/A-Gev. *Phys. Rev.*, C73:044910, 2006.

[135] S. V. Afanasiev et al. Energy dependence of pion and kaon production in central Pb + Pb collisions. *Phys. Rev.*, C66:054902, 2002.

[136] T. Anticic et al. Centrality dependence of proton and antiproton spectra in Pb+Pb collisions at 40A GeV and 158A GeV measured at the CERN SPS. *Phys. Rev.*, C83:014901, 2011.

[137] T. Anticic et al. Lambda and anti-Lambda production in central Pb - Pb collisions at 40-A-GeV, 80-A-GeV and 158-A-GeV. *Phys. Rev. Lett.*, 93:022302, 2004.

[138] J. L. Klay et al. Longitudinal flow from 2-A-GeV to 8-A-GeV Au+Au collisions at the Brookhaven AGS. *Phys. Rev. Lett.*, 88:102301, 2002.

[139] C. Alt et al. Energy and centrality dependence of antiproton and proton production in relativistic Pb + Pb collisions at the CERN SPS. arXiv: 0512033 [nucl-ex], 2005.

[140] L. Ahle et al. Excitation function of K+ and pi+ production in Au + Au reactions at 2/A-GeV to 10/A-GeV. *Phys. Lett.*, B476:1–8, 2000.

[141] L. Ahle et al. An Excitation function of K- and K+ production in Au + Au reactions at the AGS. *Phys. Lett.*, B490:53–60, 2000.

[142] L. Ahle et al. Kaon production in Au + Au collisions at 11.6-A-GeV/c. *Phys. Rev.*, C58:3523–3538, 1998.

[143] J. L. Klay et al. Charged pion production in 2 to 8 AGeV central Au+Au collisions. *Phys. Rev.*, C68:054905, 2003.

[144] C. Alt et al. Strangeness from 20-A-GeV to 158-A-GeV. *J. Phys.*, G30:S119–S128, 2004.

[145] B. I. Abelev et al. Identified particle production, azimuthal anisotropy, and interferometry measurements in Au+Au collisions at s(NN)**(1/2) = 9.2- GeV. *Phys. Rev.*, C81:024911, 2010.

[146] M. M. Aggarwal et al. Strange and Multi-strange Particle Production in Au+Au Collisions at $\sqrt{s_{NN}}$ = 62.4 GeV. *Phys. Rev.*, C83:024901, 2011.

[147] Johann Rafelski and Berndt Müller. Strangeness Production in the Quark - Gluon Plasma. *Phys. Rev. Lett.*, 48:1066, 1982. [Erratum: Phys. Rev. Lett.56,2334(1986)].

[148] R. Stock. Strange quarks in matter. *J. Phys.*, G28:1517–1526, 2002.

[149] K. G. R. Doss et al. Composite particles and entropy production in relativistic nuclear collisions. *Phys. Rev.*, C32:116–123, 1985.

[150] Horst Stoecker. Collective flow signals the quark gluon plasma. *Nucl. Phys.*, A750:121–147, 2005.

[151] J. Brachmann, S. Soff, A. Dumitru, Horst Stoecker, J. A. Maruhn, W. Greiner, L. V. Bravina, and D. H. Rischke. Antiflow of nucleons at the softest point of the EoS. *Phys. Rev.*, C61:024909, 2000.

[152] L. P. Csernai and D. Rohrich. Third flow component as QGP signal. *Phys. Lett.*, B458:454, 1999.

[153] H. Sorge. Elliptical flow: A Signature for early pressure in ultrarelativistic nucleus-nucleus collisions. *Phys. Rev. Lett.*, 78:2309–2312, 1997.

[154] H. Liu et al. Sideward flow in Au + Au collisions between 2-A-GeV and 8-A-GeV. *Phys. Rev. Lett.*, 84:5488–5492, 2000.

[155] P. K. Sahu and W. Cassing. Differential flow of protons in Au+Au collisions at AGS energies. *Nucl. Phys.*, A712:357–369, 2002.

[156] L. Adamczyk et al. Beam-Energy Dependence of the Directed Flow of Protons, Antiprotons, and Pions in Au+Au Collisions. *Phys. Rev. Lett.*, 112(16):162301, 2014.

[157] J. Steinheimer, J. Auvinen, H. Petersen, M. Bleicher, and H. Stöcker. Examination of directed flow as a signal for a phase transition in relativistic nuclear collisions. *Phys. Rev.*, C89(5):054913, 2014.

[158] V. P. Konchakovski, W. Cassing, Yu. B. Ivanov, and V. D. Toneev. Examination of the directed flow puzzle in heavy-ion collisions. *Phys. Rev.*, C90(1):014903, 2014.

[159] Hong Pi. An Event generator for interactions between hadrons and nuclei: FRITIOF version 7.0. *Comput. Phys. Commun.*, 71:173–192, 1992.

[160] V. Blobel et al. Multiplicities, topological cross-sections, and single particle inclusive distributions from p p interactions at 12-GeV/c and 24-GeV/c. *Nucl. Phys.*, B69:454–492, 1974.

[161] M. Deutschmann et al. Transverse spectra in pi+- p and K- p interactions between 8-GeV/c and 16-GeV/c. *Nucl. Phys.*, B70:189–204, 1974.

[162] Tomoyuki Maruyama, Wolfgang Cassing, Ulrich Mosel, Stefan Teis, and Klaus Weber. Study of a high-energy heavy-ion collisions in a relativistic BUU approach with momentum dependent mean fields. *Nucl. Phys.*, A573:653–675, 1994.

[163] K. Weber, B. Blaettel, W. Cassing, H. C. Doenges, V. Koch, A. Lang, and U. Mosel. A Relativistic effective interaction for heavy-ion collisions. *Nucl. Phys.*, A539:713–751, 1992.

[164] P. K. Sahu, W. Cassing, U. Mosel, and A. Ohnishi. Baryon flow from SIS to AGS energies. *Nucl. Phys.*, A672:376–386, 2000.

[165] J. Aichelin, A. Rosenhauer, G. Peilert, Horst Stoecker, and W. Greiner. Importance of Momentum Dependent Interactions for the Extraction of the Nuclear Equation of State From High-energy Heavy-Ion Collisions. *Phys. Rev. Lett.*, 58:1926–1929, 1987.

[166] S. Hama, B. C. Clark, E. D. Cooper, H. S. Sherif, and R. L. Mercer. Global Dirac optical potentials for elastic proton scattering from heavy nuclei. *Phys. Rev.*, C41:2737–2755, 1990.

[167] T. Gross-Boelting, C. Fuchs, and Amand Faessler. Covariant representations of the relativistic Bruckner T matrix and the nuclear matter problem. *Nucl. Phys.*, A648:105–137, 1999.

[168] C. Fuchs, T. Waindzoch, Amand Faessler, and D. S. Kosov. Scalar and vector decomposition of the nucleon self-energy in the relativistic Brueckner approach. *Phys. Rev.*, C58:2022–2032, 1998.

[169] W. Cassing, E. L. Bratkovskaya, and S. Juchem. Excitation functions of hadronic observables from SIS to RHIC energies. *Nucl. Phys.*, A674:249–276, 2000.

[170] C. Alt et al. Directed and elliptic flow of charged pions and protons in Pb + Pb collisions at 40-A-GeV and 158-A-GeV. *Phys. Rev.*, C68:034903, 2003.

[171] Yadav Pandit. Directed Flow of Charged Kaons in Au+Au Collisions from the BES Program at RHIC. *J. Phys. Conf. Ser.*, 636(1):012001, 2015.

[172] J. Cleymans, B. Hippolyte, H. Oeschler, K. Redlich, and N. Sharma. Thermal Model Description of Collisions of Small Nuclei. arXiv: 1603.09553 [hep-ph], 2016.

[173] Szymon Puławski. Energy dependence of hadron spectra and multiplicities in p + p interactions. *PoS*, CPOD2014:010, 2015.

[174] D. R. Harrington. Multiple scattering, the glauber approximation, and the off-shell eikonal approximation. *Phys. Rev.*, 184:1745–1749, 1969.

[175] A. Adare et al. Transverse energy production and charged-particle multiplicity at midrapidity in various systems from $\sqrt{s_{NN}}$ = 7.7 to 200 GeV. *Phys. Rev.*, C93(2):024901, 2016.

[176] Szabolcs Borsanyi, Gergely Endrodi, Zoltan Fodor, Christian Hoelbling, Sandor Katz, Stefan Krieg, Claudia Ratti, and Kalman K. Szabo. Transition temperature and the equation of state from lattice QCD, Wuppertal-Budapest results. *J. Phys. Conf. Ser.*, 316:012020, 2011.

[177] C. H. Li and C. M. Ko. Cascade production from anti-kaon induced reactions on lambda and sigma. *Nucl. Phys.*, A712:110–130, 2002.

Erklärung

Ich habe die vorgelegte Dissertation selbständig und ohne unerlaubte fremde Hilfe und nur mit den Hilfen angefertigt, die ich in der Dissertation angegeben habe. Alle Textstellen, die wörtlich oder sinngemäß aus veröffentlichten Schriften entnommen sind, und alle Angaben, die auf mündlichen Auskünften beruhen, sind als solche kenntlich gemacht. Bei den von mir durchgeführten und in der Dissertation erwähnten Untersuchungen habe ich die Grundsätze guter wissenschaftlicher Praxis, wie sie in der *Satzung der Justus-Liebig-Universität Gießen zur Sicherung guter wissenschaftlicher Praxis* niedergelegt sind, eingehalten.

Gießen,

Alessia Palmese